AEROSOL PARTICLES IN THE SUMMERTIME ARCTIC LOWER TROPOSPHERE: CHEMICAL COMPOSITION, SOURCES, AND FORMATION

Dissertation
zur Erlangung des Grades
„Doktor der Naturwissenschaften“
am Fachbereich Physik, Mathematik und Informatik
der Johannes Gutenberg-Universität
in Mainz

FRANZISKA KÖLLNER

geboren in Bad Langensalza

Mainz, den 11. Juli 2019

1. Berichterstatter: Prof. Dr. Peter Hoor
2. Berichterstatter: PD Dr. Johannes Schneider und Prof. Dr. Thomas Palberg
3. Berichterstatter: Prof. Dr. Hartmut Herrmann

Tag der mündlichen Prüfung: 13. Dezember 2019

ABSTRACT

In the face of drastic climate changes in the Arctic (e.g., increasing near-surface air temperatures and sea ice loss), it is important to understand both key processes driving these changes and related future implications. The coupling of aerosol, clouds, and radiation plays an important role in the Arctic climate system. However, our knowledge of summertime Arctic aerosol and related processes is limited, in part owing to a lack of airborne observations in the Arctic summer. This study focuses on natural and anthropogenic sources as well as formation processes controlling particle chemical composition in the summertime Arctic lower troposphere. Airborne in-situ measurements of aerosol particle chemical composition with diameters between 300 nm and 900 nm were performed in the Arctic summer using the single particle aerosol mass spectrometer ALABAMA. The ALABAMA particle composition analysis is complemented by trace gas measurements, satellite data, and air mass history modeling.

Several pieces of evidence suggest the importance of both primary emissions and secondary processes in controlling the abundance of organic particulate matter in the summertime marine Arctic boundary layer. Single particle analysis shows that primary sea spray particles, including sodium, chloride, magnesium, and calcium, were internally mixed with organic matter. Alongside with these primary sea-to-air emissions, marine-biogenic sources contributed to secondary aerosol formation by trimethylamine, methanesulfonic acid, and/or sulfate. These particles were externally mixed from sea spray aerosol and their abundance correlated with time spent over Arctic open waters prior to sampling. In contrast, chemically aged particles, containing elemental carbon, nitrate, and/or dicarboxylic acids, dominated single particle composition above the Arctic boundary layer. The presence of these particle types was driven by transport of aerosol and precursor gases from mid-latitudes to Arctic regions. Based on air mass history analysis, mid-latitude sources included anthropogenic emissions in Europe, North America, and East Asia as well as vegetation fires in northern Canada. Together, these findings improve our knowledge of mid-latitude and regional sources that influence the vertical structure of aerosol properties in the Arctic summer. This work further provides new insights into the marine-biogenic control of composition and growth of summertime Arctic aerosol that is likely to change in future as sea ice retreats.

ZUSAMMENFASSUNG

Im Hinblick auf die drastischen Klimaveränderungen in der Arktis, wie die Erwärmung der bodennahen Atmosphäre und der Rückgang des Meereises, ist es unerlässlich die zugrundeliegenden Ursachen und zukünftigen Folgen besser zu verstehen. Eine wichtige Rolle spielt hierbei das Zusammenwirken von Aerosolen, Wolken und Strahlung. Unser Wissen über Aerosole im arktischen Sommer und damit verbundene Prozesse ist allerdings begrenzt, was sich zum Teil darauf zurückführen lässt, dass bisher nur wenige flugzeuggetragene Beobachtungen während des Sommers in der Arktis stattgefunden haben. Im Rahmen dieser Arbeit wurden deshalb flugzeuggetragene Messungen mit dem Einzelpartikel-Aerosolmassenspektrometer ALABAMA durchgeführt, welches die chemische Zusammensetzung von Aerosolpartikeln in einem Größenbereich zwischen 300 nm und 900 nm analysiert. Weitere Analysemethoden basieren auf Messungen von Spurengasen, Satellitendaten und der Modellierung der Luftmassenherkunft. In der vorliegenden Arbeit wurden somit der Einfluss von natürlichen und anthropogenen Quellen auf die chemische Zusammensetzung der Aerosolpartikel in der arktischen unteren Troposphäre sowie deren Bildung untersucht.

Die Messungen zeigen, dass Aerosolpartikel aus organischem Material sowohl durch primäre Emissionen als auch durch sekundäre Prozesse in der marinen arktischen Grenzschicht gebildet wurden. Basierend auf den Einzelpartikelanalysen stellte sich heraus, dass primäre Seesalzpartikel, bestehend aus Natrium, Chlorid, Magnesium und Calcium, zusätzlich intern mit organischen Substanzen gemischt waren. Marine biogene Quellen haben außerdem zur sekundären Bildung von Aerosolpartikeln, bestehend aus Trimethlyamin, Methansulfonsäure und/oder Sulfat, beigetragen. Die sekundären Aerosolpartikel waren extern gemischt mit Seesalzpartikeln und ihr Auftreten korrelierte mit der vergangenen Aufenthaltszeit der Luftmasse über arktischen marinen Quellen. In Gegensatz dazu dominierten chemisch gealterte Aerosolpartikel, bestehend aus elementarem Kohlenstoff, Nitrat und/oder Dicarboxylsäuren, die chemische Zusammensetzung der Einzelpartikel in Höhen oberhalb der Grenzschicht. Das Auftreten dieser Partikeltypen kann auf den Transport von Aerosolen und Vorläufergasen aus den mittleren Breiten in die Arktis zurückgeführt werden. Die Analyse der Luftmassenherkunft hat außerdem gezeigt, dass die Quellen in den mittleren Breiten vor allem durch anthropogene Emissionen in Europa, Nordamerika und Ostasien sowie durch Biomasseverbrennung im nördlichen Kanada bestimmt waren. Zusammenfassend wurden im Rahmen dieser Arbeit weiterführende Erkenntnisse über regionale und weiter entfernte Quellen des arktischen Aerosols und deren chemische Zusammensetzung gewonnen. Es wurden außerdem neue Einblicke in marine biogene Quellen und deren Einfluss auf die sekundäre Bildung von Aerosolpartikeln im arktischen Sommer ermöglicht.

CONTENTS

1

INTRODUCTION

1.1 MOTIVATION

Despite the remoteness and the small fraction of the globe, the Arctic plays an important role in our climate system, yet climate relevant processes within the Arctic are poorly understood (e.g., Serreze and Barry, 2011). One characteristic feature of Arctic climate is the haze phenomenon in late winter and early spring. Following early descriptions of visibility-reducing haze (Nordenskiöld, 1883; Greenaway, 1950), comprehensive analysis of Arctic haze began in the 1970s (Shaw, 1975; Rahn et al., 1977; Rahn and McCaffrey, 1980; Heintzenberg, 1980; Barrie, 1986; Dreiling and Friederich, 1997). These early studies suggested that Arctic air pollution is associated with anthropogenic mid-latitude emissions. Further research activities have been devoted to characterize Arctic haze, however, its radiative forcing impact is still not well quantified (Shaw, 1995; Quinn et al., 2007). Nowadays, in the face of rapid climate changes in the Arctic (IPCC, 2014), polar research has attracted renewed interests with regard to the key processes driving these changes (Chapman and Walsh, 1993; Serreze and Francis, 2006; Serreze et al., 2007; Serreze et al., 2009; Serreze and Barry, 2011). The observed amplified Arctic warming in recent decades and the coupled rapid sea ice retreat have been attributed to various causes, including increases in greenhouse gases and local feedback mechanisms, such as the the snow/ice-albedo feedback (Curry et al., 1995; Holland and Bitz, 2003; Serreze et al., 2007; Serreze and Barry, 2011; Flanner et al., 2011; Stroeve et al., 2012).

Understanding the Arctic climate system further requires studying the coupling between aerosol, clouds, and radiation. Modeling studies for example could show the control of anthropogenic aerosol on temperature changes in the Arctic in recent decades (Shindell and Faluvegi, 2009; Serreze and Barry, 2011; Fyfe et al., 2013; Flanner, 2013; Najafi et al., 2015; Acosta Navarro et al., 2016; Breider et al., 2017). However, interactions between aerosol, clouds, and radiation are complex by a combination of unique features in the Arctic atmosphere, such as shallow stable boundary layer, high surface albedo, frequent appearance of low level clouds (Curry et al., 1995; Lubin and Vogelmann, 2006; Garrett and Zhao, 2006; Quinn et al., 2008; Kay and Gettelman, 2009; Boucher et al., 2013), and seasonality in aerosol chemical and physical properties (Sirois and Barrie, 1999; Ström et al., 2003; Engvall et al., 2008; Sharma et al., 2012;

Breider et al., 2014; Leaitch et al., 2013; Tunved et al., 2013). Exemplary, in the summertime pristine Arctic environment, new particle formation and subsequent growth can strongly impact low-level clouds and thus the surface radiation budget (Mauritsen et al., 2011; Moore et al., 2013; Leaitch et al., 2016; Croft et al., 2016b).

Arctic warming in turn can have significant implications on Arctic aerosol. Several studies suggested that prospective changes in biosphere-atmosphere interactions will alter aerosol and cloud properties (Struthers et al., 2011; Liu et al., 2012; Paasonen et al., 2013; Browse et al., 2014). Along these natural changes, emerging anthropogenic activities in Arctic regions, owing to socioeconomic interests, likely influence atmospheric composition. Rapid sea ice retreat for example leads to an easier exploration of undiscovered oil and gas reservoirs (Gautier et al., 2009; Peters et al., 2011; Roiger et al., 2015) and to an easier accessibility of efficient high-latitude shipping routes (e.g., Granier et al., 2006; Paxian et al., 2010; Khon and Mokhov, 2010; Corbett et al., 2010; Peters et al., 2011).

Together, causes and implications of Arctic warming and sea ice retreat are complex and poorly constrained (Chapin et al., 2005; Serreze et al., 2007; Bhatt et al., 2010; Overland et al., 2016; Gilgen et al., 2018; Wendisch et al., 2019). Despite the importance to understand the Arctic climate system, our detailed chemical and physical knowledge of summertime Arctic aerosol is incomplete, in part owing to a paucity of observations in summer Arctic regions. In particular, airborne observations that provide crucial in-situ data on aerosol vertical and spatial distributions are sparse (Paris et al., 2009; Schmale et al., 2011; Quennehen et al., 2011; Kupiszewski et al., 2013; Lathem et al., 2013; Creamean et al., 2018). The current thesis focuses on processes and sources controlling summer Arctic aerosol by using vertically resolved measurements of aerosol properties and trace gases, together with modeling of air mass history, to address a portion of this challenging puzzle.

1.2 CURRENT KNOWLEDGE OF SUMMERTIME ARCTIC AEROSOL

This section summarizes our current understanding of sources, formation processes, and transport mechanisms of summertime Arctic aerosol. Remaining knowledge gaps are identified with emphasis on those that are relevant for this study. A further detailed review on Arctic aerosol is given by Willis et al. (2018). The following questions are addressed in this section:

- What characterizes summer Arctic aerosol properties?

- Which processes and sources control these properties?
- Which gaps exist in our understanding of summer Arctic aerosol?

Arctic aerosol in the lower troposphere is characterized by a strong annual cycle in aerosol mass concentrations, size distribution[1], and composition (e.g., Rahn and McCaffrey, 1980; Quinn et al., 2002, 2007; Engvall et al., 2008; Tunved et al., 2013; Leaitch et al., 2013; Freud et al., 2017). In summer, nucleation and Aitken mode particles dominate the size distribution, whereas in winter and spring accumulation mode particles are prevalent, often referred to as Arctic haze. In addition, winter and springtime aerosol is characterized by higher concentrations of black carbon, organic carbon, and sulfate compared to summer, whereas methanesulfonic acid (MSA) from northern marine sources is more important in summer months (e.g., Quinn et al., 2002; Leaitch et al., 2013). This seasonality is partly controlled by a combination of transport and removal mechanisms, as explained in the following sections.

1.2.1 *Characteristics of long-range transport*

Early studies suggested that tropospheric transport to Arctic regions is largely realized by applying an isentropic perspective (e.g., Carlson, 1981; Iversen, 1984). Thus, air parcels when transported to Arctic regions preferentially follow isolines of potential temperature (θ), i.e. isentropic surfaces (e.g., Carlson, 1981; Iversen, 1984). These low-level isentropes slope upwards towards polar regions leading to the conclusion that the Arctic boundary layer (BL) resides under a dome-like structure, which later became known as the polar dome (Klonecki et al., 2003; Law and Stohl, 2007). Following this concept, only surface emissions within the dome could affect the Arctic BL composition. Emissions outside the dome with rather high values of potential temperature could not penetrate into the Arctic BL due to the absence of diabatic processes (Carlson, 1981; Iversen, 1984; Barrie, 1986). The polar dome associated transport barrier is often characterized by the location of the Arctic front (Klonecki et al., 2003; Law and Stohl, 2007). In addition, a recent study applied measurements of trace gas gradients for identification (Bozem et al., 2019).

In recent years modeling studies suggested a stronger role of diabatic processes, opening pathways from the mid-latitudes to Arctic regions (e.g., Klonecki et al.,

---

[1] Aerosol sizes span several orders of magnitude. Nucleation and Aitken mode are defined as particles below 0.01 µm and between 0.01 and 0.1 µm in diameter, respectively. In parallel, particles below 0.1 µm are summarized as ultrafine particles. Accumulation mode is comprised of particles with diameters between 0.1 and 1 µm. Coarse mode includes particles beyond 1 µm in diameter (Boucher, 2015).

2003; Stohl, 2006). In particular, this further helped to understand the seasonality of Arctic aerosol properties with Arctic haze pollution being evident in winter/spring. In summer, the input of aerosol from lower latitudes exhibits a minimum that is mainly related to three factors. First, the Arctic front retreats northward with the beginning of summer, thus, the polar dome surface area is smaller compared to winter, excluding northern latitude pollution sources (Klonecki et al., 2003; Stohl, 2006; Jiao and Flanner, 2016). Second, northern latitude surfaces act as net source of heat, thus, diabatic cooling is nearly absent (Klonecki et al., 2003; Stohl, 2006). As a result, the northward transport of air is associated with a lifting either at the Arctic front (dark red arrow in Fig. 1.1) or near source regions (light red arrow in Fig. 1.1), followed by high-level transport and eventually mixing of air into the polar dome by radiative cooling (Stohl, 2006). Third, both summertime routes include uplift of moist air that is likely associated with cloud formation and thus latent heat release (Fig. 1.1). Therefore, summertime transport of pollutants to Arctic regions is related to efficient aerosol wet removal within and outside the polar dome (blue arrows in Fig. 1.1; Garrett et al., 2010; Browse et al., 2012; Croft et al., 2016b).

Consequently, summertime Arctic near-surface regions ($\theta < 290\,\mathrm{K}$, see Fig. 1.1) are largely isolated from the rest of the atmosphere by a combination of a far northern location of the Arctic front and absence of diabatic surface-cooling. In contrast, regions aloft ($\theta > 290\,\mathrm{K}$, see Fig. 1.1) can be episodically influenced by air originating in mid-latitudes. However, wet scavenging is a dominant process along summertime transport routes leading to efficient aerosol removal.

1.2.2 *Transport related aerosol processes*

Arctic aerosol particles affected by long-range transport reside in the atmosphere for several days up to weeks (Klonecki et al., 2003; Stohl, 2006; Shindell et al., 2008; Hirdman et al., 2010). During this time, aerosol and precursor gases can undergo several processes that alter physicochemical aerosol properties (red arrow in Fig. 1.2), thereby lifetime and aerosol climate impacts (e.g., Boucher, 2015; Willis et al., 2018). One main process is the formation of secondary aerosol by oxidation of gas phase species forming lower-volatility products and subsequent new particle formation or condensation on pre-existing particles (e.g., Kroll and Seinfeld, 2008; Boucher, 2015; Seinfeld and Pandis, 2016). As a result, an overall increase in particle size and mass as well as changes in particle composition are observed (e.g., Schmale et al., 2011; Quennehen et al., 2012). Likewise, particle coagulation (e.g., Hinds, 1999) shifts particle size distribution to larger sizes and increases particle mixing state (e.g., Fiebig et al.,

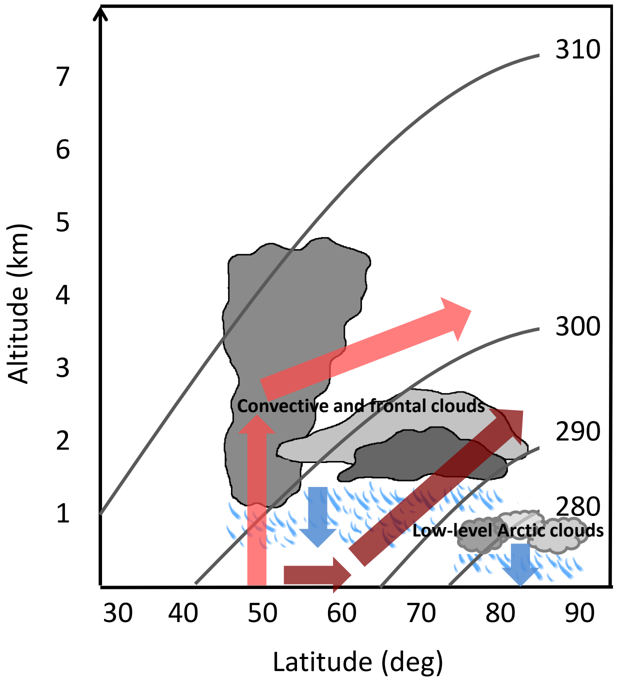

Figure 1.1: Schematic overview of major summertime transport pathways to Arctic regions indicated by red arrows in a latitude-altitude system. Clouds and blue arrows indicate the presence of aerosol removal processes by liquid- and mixed-phase precipitation scavenging. Grey lines present zonal mean averaged summertime isentropes, whereby numbers show associated potential temperatures (θ) in K. This figure is partly adapted from Browse et al. (2012).

2003; Petzold et al., 2007; Quennehen et al., 2012). Few modeling studies that focused on Arctic aerosol processes demonstrated a strong impact on particle losses in the Aitken mode by coagulation of interstitial aerosol with liquid cloud droplets (Pierce et al., 2015; Croft et al., 2016b). Furthermore, aqueous phase oxidation of dissolved gases, such as sulfur dioxide (SO_2), water-soluble organics, ammonia, and nitric acid (e.g., Sorooshian et al., 2006; Ervens et al., 2011; Seinfeld and Pandis, 2016), alter aerosol properties (Kupiszewski et al., 2013; Croft et al., 2016b) as droplets evaporate and release the pre-existing cloud condensation nuclei with all non-volatile material collected during cloud lifetime (e.g., Hoppel et al., 1994; Boucher, 2015; Schneider et al., 2017). Moreover, plume dilution by mixing with surrounding air leads to a reduction of aerosol number and mass (e.g. DeCarlo et al., 2010), which have been directly observed with increasing plume age during Arctic pollution studies (Paris et al., 2009; Brock et al., 2011; Quennehen et al., 2012). Finally, scavenging by liquid- and mixed-phase precipitation at lower latitudes and along transport

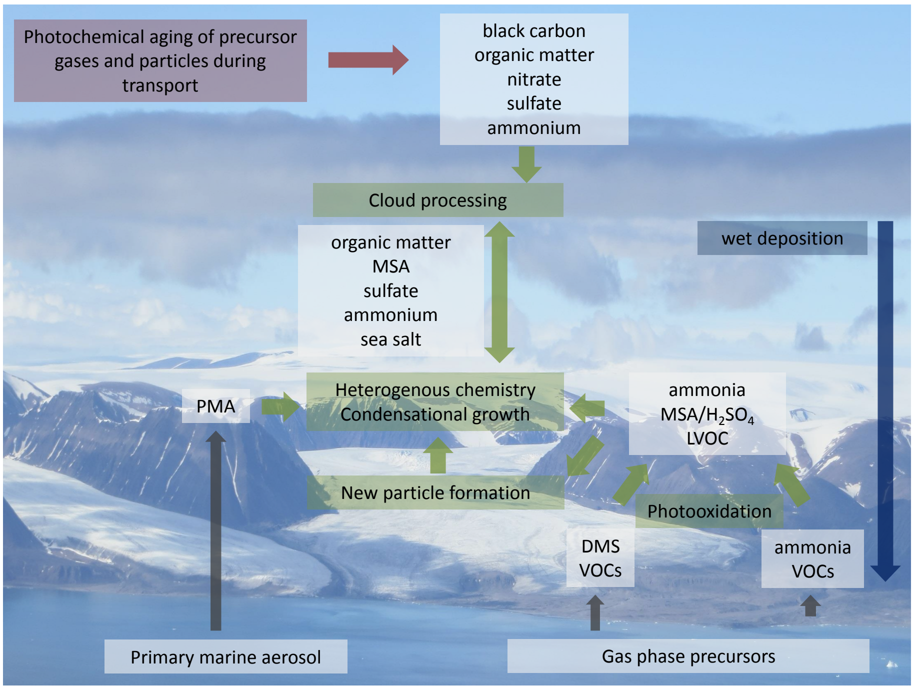

Figure 1.2: Main processes controlling aerosol properties in the summertime marine Arctic lower troposphere. Grey arrows represent emissions of primary aerosol and precursor gases. Green arrows indicate physical and chemical processing of aerosol and precursor gases. Red arrow represents aerosol long-range transport (see Fig. 1.1) and related photochemical processes. Blue arrow represents the main aerosol removal processes by liquid- and mixed-phase precipitation scavenging (see Fig. 1.1). Acronyms are defined as follows: DMS = dimethylsulfide; VOCs = volatile organic compounds; MSA = methanesulfonic acid; LVOC = low-volatile organic compounds; PMA = primary marine aerosol.

constitute the main aerosol removal processes in summer (e.g., Garrett et al., 2010; Browse et al., 2012; Croft et al., 2016b; Mahmood et al., 2016).

Taken together, size distribution and composition of aerosol transported to Arctic regions are complex due to a combination of source emissions, particle processing as well as raining and non-raining cloud effects. However, northward transport and related processes control the abundance of accumulation and Aitken mode particles in pristine summertime Arctic regions (e.g., Croft et al., 2016b). The current understanding of Arctic aerosol composition affected by transport and thus by pollution in lower latitudes is described in the following sections.

1.2.3 *Anthropogenic aerosol*

Anthropogenic pollution sources include energy production (fossil and biofuel combustion), industrial production (e.g., sinter, steel), and waste treatment. Those sources emit a variety of primary aerosol and precursor gases that can be transported to Arctic regions and thus contribute to Arctic pollution. Anthropogenic aerosol in Arctic regions is mainly given by sulfate, black carbon (BC), and organic matter (OM)[2] (Fig. 1.2; e.g., Schmale et al., 2011; Breider et al., 2014).

Sulfate concentrations in the summertime Arctic free troposphere are largely influenced by anthropogenic sources in northern Eurasia, North America, and East Asia (Shindell et al., 2008; Hirdman et al., 2010; Kuhn et al., 2010; Bourgeois and Bey, 2011; Schmale et al., 2011; Yang et al., 2018; Sobhani et al., 2018). Sulfate is formed by gas or aqueous phase oxidation of the precursor gas SO_2 (e.g., Seinfeld and Pandis, 2016) that in turn is primarily emitted by anthropogenic sources (e.g., Smith et al., 2001). Depending on the availability of ammonia, sulfate exists in acidic, partially or completely neutralized form (see Sect. 1.2.4; Fisher et al., 2011; Brock et al., 2011; Seinfeld and Pandis, 2016). However, studies of aerosol acidity in the Arctic are sparse and, if available, focused on spring (Barrie and Barrie, 1990; Quinn et al., 2009; Fisher et al., 2011; Brock et al., 2011), on the Arctic BL (see Sect. 1.2.6), or on the influence of vegetation fires (see Sect. 1.2.4).

In Arctic summer, organic aerosol significantly contributes to submicron aerosol mass (e.g., Schmale et al., 2011; Chang et al., 2011; Lathem et al., 2013; Breider et al., 2014; Leaitch et al., 2018; Lange et al., 2018). Boreal fires and to a lesser extent anthropogenic activities in North America and northern Eurasia, can strongly influence the organic aerosol burden in the summer Arctic free troposphere (Hirdman et al., 2010; Schmale et al., 2011; Lathem et al., 2013; Breider et al., 2014). Organic particulate matter summarizes a tremendous variety of chemical compounds[3] that are either directly emitted by sources (primary organic aerosol (POA)) or can be formed in the atmosphere by condensation of lower-volatility products resulting from hydrocarbon photooxidation (secondary organic aerosol (SOA))[4] (e.g., Hoffmann and Warnke, 2007;

---

[2] Organic carbon refers to only a fraction of organic matter. The rest is hydrogen, oxygen, nitrogen etc. (Seinfeld and Pandis, 2016).

[3] Compounds identified in ambient aerosol include alkanes, alkenes, alcohols, aromatic compounds, carbonylated compounds, organic acids, amines etc. (e.g., Boucher, 2015; Seinfeld and Pandis, 2016).

[4] Secondary aerosol formation further include heterogeneous reactions on particle surfaces and in-cloud processing (e.g., Hoffmann and Warnke, 2007).

Hallquist et al., 2009; Seinfeld and Pandis, 2016). Organic molecular composition of aerosol varies significantly with Arctic sites, related to differences in sources and chemical processing (e.g., Fu et al., 2013a; Hansen et al., 2014; Leaitch et al., 2018). However, alkanes, acids, alcohols, and organic sulfates in summertime Arctic aerosol can be associated with combustion-related sources, including fossil fuel and biomass (see Sect. 1.2.4; e.g., Kawamura et al., 2012; Fu et al., 2013a; Hansen et al., 2014; Leaitch et al., 2018). Exemplary, phthalic acid from aromatic hydrocarbon oxidation has been used as an anthropogenic tracer for Arctic aerosol (Kawamura et al., 1996; Kawamura et al., 2012; Fu et al., 2013a; Hansen et al., 2014).

Black carbon[5] is formed during the incomplete combustion of carbon-based fuel (e.g., Bond et al., 2013; Boucher, 2015). The summertime Arctic BC burden is largely influenced by vegetation fires (see Sect. 1.2.4), whereas anthropogenic sources contribute less to the overall transport of BC to Arctic regions (Bourgeois and Bey, 2011; Breider et al., 2014). Nevertheless, anthropogenic BC sources in northern Eurasia can have important contributions to Arctic near surface concentrations, whereby South Asian BC layers are present in the Arctic middle and upper troposphere (Singh et al., 2010; Huang et al., 2010; Bourgeois and Bey, 2011; Sobhani et al., 2018). Regarding high-latitude anthropogenic sources, recent studies demonstrated gas flaring and shipping to significantly impact the lower tropospheric BC, organic, and sulfate aerosol burdens (e.g., AMAP, 2010; Chang et al., 2011; Stohl et al., 2013; Eckhardt et al., 2013; Breider et al., 2014; Sand et al., 2016; Ferrero et al., 2016; Winiger et al., 2017; Xu et al., 2017; Gunsch et al., 2017; Leaitch et al., 2018; Creamean et al., 2018; Kirpes et al., 2018).

1.2.4 *Aerosol from vegetation fires*

Emissions from boreal fires in North America and Siberia can efficiently be transported to Arctic regions (Fig. 1.2) and thus influence Arctic aerosol background concentrations below and above approximately 2 km, respectively (e.g., Singh et al., 2010; Breider et al., 2014; Xu et al., 2017). Organic matter dominates vegetation fire aerosol (Kondo et al., 2011; Schmale et al., 2011; Quennehen et al., 2011; Hecobian et al., 2011) caused by large emissions of primary aerosol and organic precursors at the source (e.g., Andreae and Merlet, 2001). The latter leading to the formation of SOA during transport, although the contribution of SOA remains poorly constrained (Hecobian et al., 2011; Cubison

---

[5] Terminology of this aerosol type is complex by a combination of various measurement methods and aerosol properties (Petzold et al., 2013). However, unless otherwise is noted, the term black carbon is used.

et al., 2011; Quennehen et al., 2012; Lathem et al., 2013). Along with transport, organic aerosol particles become more water soluble (e.g., Jimenez et al., 2009; Lathem et al., 2013) and less volatile as a result of intense oxidative aging (Jimenez et al., 2009; Schmale et al., 2011; Cubison et al., 2011; Chang et al., 2011; Lathem et al., 2013).

Organic molecular composition of Arctic aerosol particles is thus largely characterized by water-soluble organics, including acids (see Sect. 1.2.6), carbonyls, and carbohydrates like levoglucosan (e.g., Fu et al., 2013a; Hansen et al., 2014; Nguyen et al., 2014; Leaitch et al., 2018). Levoglucosan, a thermal decomposition product of cellulose, is a key organic tracer for biomass combustion (Simoneit et al., 1999). Despite the potential for oxidation of levoglucosan during transport (Hoffmann et al., 2010; Hennigan et al., 2010), several studies show levoglucosan from biomass burning in Arctic aerosol (Fu et al., 2009a,b; Hu et al., 2013; Fu et al., 2013a; Yttri et al., 2014; Nguyen et al., 2014). Potassium is considered as another commonly used tracer for vegetation fires (e.g., Andreae, 1983; Silva et al., 1999), but can be also measured, albeit to a smaller extent, in emissions from fossil fuel combustion (e.g., Guazzotti et al., 2003), potash mining (e.g., Orris et al., 2014), and oceans (e.g., Hawkins and Russell, 2010). Potassium has been previously reported to be associated with aerosol from biomass and fossil fuel combustion in Arctic regions (e.g., Iziomon et al., 2006; Brock et al., 2011; Quennehen et al., 2012; Sierau et al., 2014; Leaitch et al., 2018).

Vegetation fires are a major source of black carbon in Arctic summer (e.g., Stohl, 2006; Iziomon et al., 2006; Paris et al., 2009; Stohl et al., 2013; Breider et al., 2014; Mahmood et al., 2016; Xu et al., 2017; Creamean et al., 2018), often even dominate the atmospheric burden (e.g., Hirdman et al., 2010; Singh et al., 2010; Bourgeois and Bey, 2011; Sobhani et al., 2018). Several observational studies show that BC particles from vegetation fires are thickly coated with organics and inorganics, again indicative for intense aerosol processing during transport (e.g., Singh et al., 2010; Kondo et al., 2011; Lathem et al., 2013).

Further, vegetation fires also contribute to the presence of Arctic secondary inorganic aerosol, namely nitrate, ammonium, and sulfate, that develop while transported over long distances (see Fig. 1.2; e.g., Fisher et al., 2011; Breider et al., 2014). Ammonium nitrate and sulfate are formed by initial oxidation of precursor gases nitrogen oxides ($\mathrm{NO_x}$) and $\mathrm{SO_2}$, respectively, and subsequent reactions with ammonia, predominantly in aqueous phase (e.g., Seinfeld and Pandis, 2016). The abundance of ammonium nitrate strongly depends on the excess ammonia, since it will only form after acidic sulfate/sulfuric acid has been completely neutralized (e.g., Fisher et al., 2011; Seinfeld and Pandis, 2016). Notably, nitrate and sulfate can further exist in the form of organic nitrates (e.g., Hao et al., 2014; Kiendler-Scharr et al., 2016; Zare et al., 2018) and organic sulfates (e.g., Hallquist et al., 2009; Froyd et al., 2010), which both have been observed in Arctic aerosol (e.g., Kuhn et al., 2010; Hansen et al., 2014). In summer Arctic regions, background concentrations of ammonium and nitrate are low compared to sulfate (Quinn et al., 2002; Kuhn et al., 2010; Chang et al., 2011; Schmale et al., 2011; Quennehen et al., 2011; Hamacher-Barth et al., 2016; Lange et al., 2018). However, episodic and localized transport of vegetation fire emissions, including ammonia and nitrogen oxides (Andreae and Merlet, 2001; Seinfeld and Pandis, 2016; Lutsch et al., 2016), to Arctic regions can perturb background concentrations and thus contribute to more neutralized aerosol in summer Arctic free troposphere (Nance et al., 1993; Hecobian et al., 2011; Brock et al., 2011; Fisher et al., 2011; Lathem et al., 2013; Breider et al., 2014). In contrast, ammonium concentrations in the summertime Arctic BL are dominated by natural sources (see Sect. 1.2.6; e.g., Wentworth et al., 2016).

To summarize, the vertical structure of Arctic summertime aerosol from long-range transport is impacted by a combination of lower latitude sources, transport and removal mechanisms as well as photochemical aging processes. However, our understanding of the aerosol vertical structure remains incomplete, largely owing to a lack of detailed airborne measurements that attribute aerosol physical and chemical properties to sources (e.g., Willis et al., 2018).

1.2.5 *Regional Arctic aerosol processes*

Summertime Arctic regions are largely a coastal marine and pristine environment, with limited anthropogenic contributions from high-latitude oil/gas extractions, shipping, and domestic activities (e.g., Aliabadi et al., 2015). Additionally, the boundary layer composition is largely unperturbed by mid-latitude pollution (see Sect. 1.2.1). As a result, natural regional sources strongly contribute to summertime Arctic aerosol (see Sect. 1.2.6), by cloud processing, primary emissions, and secondary chemical processes, including new particle formation (NPF)[6] and subsequent condensational growth (see Fig. 1.2; e.g., Browse et al., 2014; Croft et al., 2016a,b; Burkart et al., 2017; Croft et al., 2019).

New particle formation and subsequent growth events show a strong seasonality at Arctic long-term monitoring sites, with high frequency during summer

---

[6] New particle formation is also termed as nucleation in common literature.

and nearly absence in winter (e.g., Leaitch et al., 2013; Nguyen et al., 2016; Dall'Osto et al., 2017; Freud et al., 2017; Heintzenberg et al., 2017), reflecting the necessity of photochemistry and low aerosol surface area (e.g., Engvall et al., 2008; Collins et al., 2017). Recent studies show the complex interplay of several factors driving NPF and growth, beside the above mentioned, e.g., biological activity, cloud cover, sea ice extent, vicinity of anthropogenic emissions, and temperature, (e.g., Asmi et al., 2016; Burkart et al., 2017; Dall'Osto et al., 2017; Collins et al., 2017; Kolesar et al., 2017). Thus, particle formation and growth rates show large variations. Median values ($0.5\,\mathrm{cm}^{-3}\mathrm{s}^{-1}$ and $2.5\,\mathrm{nm}$ h^{-1}, respectively) are, however, comparable to those observed in boreal forest environments (Kerminen et al., 2018). In addition to NPF taking place in the Arctic BL, sources of sub-100 nm particles might also be entrainment from the free troposphere (Tunved et al., 2013; Croft et al., 2016b; Igel et al., 2017) and primary marine emissions (e.g., Leck and Bigg, 2005; Karl et al., 2013).

Taken together, the dominant Aitken mode in summertime Arctic size distribution is driven by northward transport (see Sect. 1.2.2), primary emissions, NPF and subsequent growth as well as wet removal processes (e.g., Leaitch et al., 2016). By a further condensational growth of this sub-100nm particles, accumulation mode particles can form (e.g., Croft et al., 2016b). When sub-100 nm particles are activated as cloud condensation nuclei, particles can further grow by cloud processing (see Sect. 1.2.2 and Fig. 1.2; e.g., Tunved et al., 2013; Leaitch et al., 2016; Croft et al., 2016b). However, summertime Arctic size distributions show a suppressed accumulation mode compared to other seasons caused by both efficient wet removal processes in Arctic low-level clouds (e.g., Browse et al., 2014) and less efficient transport of mid-latitude aerosol (see Sect. 1.2.1). Primary emissions are the dominant source process for Arctic coarse mode particles. The following section discusses a range of chemical species from natural, mainly regional, sources that have been linked to NPF and growth as well as to primary aerosol production.

1.2.6 *Natural aerosol*

Natural sources include oceans, soils, vegetation, sea birds, and volcanoes. Those sources provide a variety of primary aerosol species and precursor gases. Natural aerosol particles in summertime Arctic regions are thus characterized by a mixture of sea salt, organic matter, MSA, ammonium, sulfate, and mineral dust (Fig. 1.2), as explained in detail below.

Sea spray aerosol is a complex mixture of organic matter and inorganic salts, originating from primary sea-to-air emissions and atmospheric aging. Initially, wind-driven breaking waves at the water surface trap air that subsequently rises as bubbles. Rising air bubbles scavenge organic matter and inorganic salts from the surrounding sea water. At the sea surface, these bubbles burst and generate film and jet droplets. Once released to the atmosphere, these droplets evaporate and get enriched in substances that are non-volatile (e.g., Blanchard and Woodcock, 1980; O'Dowd and de Leeuw, 2007; Boucher, 2015). Thus, sodium, chloride, magnesium, and calcium are commonly used as tracers for inorganic sea salt (e.g., Prather et al., 2013; Sierau et al., 2014; Chi et al., 2015; Gunsch et al., 2017; Kirpes et al., 2018).

Arctic long-term records from ground-based monitoring stations illustrate minimum sea salt concentrations in summer when wind speeds are generally lower compared to winter/spring (e.g., Quinn et al., 2002; Lana et al., 2011; May et al., 2016; Leaitch et al., 2018). In contrast, organic matter have been observed to be enriched in sea spray aerosol with the coming of summer (e.g., Fu et al., 2013a; Fu et al., 2015; Leaitch et al., 2018), partly owing to a higher ocean productivity in summer compared to winter (e.g., Behrenfeld et al., 2016). Summertime Arctic studies show carbohydrate- and protein-like organics to incorporate in primary marine aerosol (see Fig. 1.2; e.g., Leck and Bigg, 2005; Karl et al., 2013; Fu et al., 2013a; Fu et al., 2015). Aged sea spray aerosol is characterized by an internal mixing with secondary organics, nitrate, and sulfate (e.g., Laskin et al., 2012; Sierau et al., 2014; Chi et al., 2015; Kirpes et al., 2018), due to reactions with organic, nitric, and sulfuric acids, respectively (Gard et al., 1998; O'Dowd et al., 1999; Sorensen et al., 2005; Laskin et al., 2012).

Organic matter in the summertime Arctic BL is not only of primary origin, but rather a result of both primary emissions and secondary chemical processes (see Fig. 1.2; e.g., Croft et al., 2019). Sources and identities of SOA are poorly characterized (Willis et al., 2018), nevertheless, recent studies show volatile organic precursor compounds, including isoprene, monoterpenes, and fatty acids, to originate from marine and terrestrial sources (see Fig. 1.2; e.g., Fu et al., 2009b; Schollert et al., 2014; Kramshøj et al., 2016; Kim et al., 2017; Mungall et al., 2017). Tracers of SOA, including a variety of dicarboxylic acids (DCA), had been detected at several Arctic sites (e.g., Kawamura et al., 1996; Kerminen et al., 1999; Fu et al., 2009b; Kawamura et al., 2012; Fu et al., 2013a; Hansen et al., 2014). Year-around Arctic measurements illustrate the strong control of solar irradiance on the abundance and composition of those DCA. Formation processes and abundance in the Arctic are complex by a variety of biogenic and anthropogenic organic precursor gases, intermediate oxidation products, and also primary sources (e.g., Kawamura et al., 1996; Kawamura et al., 2012;

Kawamura and Bikkina, 2016). However, several studies demonstrated that DCA are less abundant in summer than in spring, driven by diminished long-range transport of precursors and efficient aerosol wet removal. In parallel, natural regional sources become more important by sea ice melt and biological productivity (e.g., Kawamura et al., 1996; Kerminen et al., 1999; Kawamura et al., 2010; Kawamura et al., 2012). Notably, previous studies on Arctic DCA made use of ground-based and shipborne measurements. Due to the largely isolated nature of the Arctic BL compared to the rest of the atmosphere, this raises the question of the representativeness of these near-surface studies of Arctic aerosol composition. For this reason, vertically resolved measurements of DCA are necessary for characterizing sources and abundances in Arctic summer.

Dimethylsulfide (DMS) released by marine biota controls concentrations of sulfate and MSA in the summertime Arctic BL (see Fig. 1.2; e.g., Breider et al., 2014; Yang et al., 2018; Lange et al., 2018). Vegetation fires and lake sources can further contribute, albeit to a localized extent, to DMS abundance in the Arctic (e.g., Sharma et al., 1999; Akagi et al., 2011). Once in the atmosphere, DMS is oxidized by various reaction pathways to MSA and sulfate/sulfuric acid (see Fig. 1.2; e.g., Seinfeld and Pandis, 2016). Both oxidation products can contribute to NPF in Arctic regions (e.g., Leaitch et al., 2013; Park et al., 2017; Dall'Osto et al., 2017), however, the ability of MSA is much lower by its higher saturation vapor pressure (e.g., Seinfeld and Pandis, 2016). Thus, the importance of MSA to aerosol formation may restricted to particle condensational growth (see Fig. 1.2; e.g., Leaitch et al., 2013; Willis et al., 2016). Long-term monitoring stations in the Arctic demonstrated MSA concentrations to increase in spring and decrease in autumn, related to the annual cycle in solar irradiance (e.g., Quinn et al., 2002; Sharma et al., 2012; Leaitch et al., 2013). The acidity of Arctic BL aerosol from DMS is discussed in a few observational and modeling studies (Quinn et al., 2002; Breider et al., 2014; Wentworth et al., 2016; Giamarelou et al., 2016). Results showed a range from partial to full neutralization. Differences are partly caused by an incomplete understanding of gas phase neutralizing agents, mainly ammonia and amines, in Arctic regions.

Few summer Arctic measurements illustrated the importance of natural sources, such as sea bird colonies and vegetation fires on ammonia concentrations, while marine waters in Arctic regions can act as a net sink (e.g., Johnson and Bell, 2008; Wentworth et al., 2016; Lutsch et al., 2016). Regarding amines, very little is known about sources and abundance in Arctic regions. Measurements at Mace Head, Irleand, showed amines from polar marine air masses (Dall‘Osto et al., 2012). Scalabrin et al. (2012) reported marine influences on amino acids in Arctic aerosol. Recently, Gunsch et al. (2017, Supplement) briefly mentioned the detection of particulate amines at a coastal Alaskan site in summer. Lower latitude observations showed marine biota to release gas phase amines to the atmosphere, which subsequently may contribute to aerosol chemistry (e.g., Van Neste et al., 1987; Gibb et al., 1999; Facchini et al., 2008; Ge et al., 2011a; Healy et al., 2015). In addition, ammonia and amines play a crucial role in NPF by stabilizing sulfuric acid clusters, as evident from numerous chamber studies and lower latitude observations (e.g., Almeida et al., 2013; Kürten et al., 2016). However, only a few Arctic studies exists that show the importance of ammonia to NPF in the Arctic (Giamarelou et al., 2016; Wentworth et al., 2016; Croft et al., 2016a).

Along with NPF, amines may further contribute to secondary aerosol formation in several ways. First, amines can be oxidized, leading to the formation of species such as amides, nitramines, and imines[7]. The resulting lower-volatility products can form secondary organic aerosol (SOA) (e.g., Angelino et al., 2001; Murphy et al., 2007; Ge et al., 2011b). Second, amines may dissolve in cloud water, owing to their high water-solubility, where subsequent aqueous phase acid-base reactions can occur (e.g., Rehbein et al., 2011; Erupe et al., 2011; Ge et al., 2011b; Dawson et al., 2012; Yu et al., 2012; Jen et al., 2014; Glasoe et al., 2015; Youn et al., 2015; Pankow, 2015; Jen et al., 2016). Amines compete with ammonia in neutralizing acidic aerosol. The base that is favoured by these reactions depends on several parameters, such as acidity of the aerosol, Henry's law coefficient, and concentrations of both substances in the atmosphere (e.g., Pratt et al., 2009b; Barsanti et al., 2009).

Natural sulfate from volcanic sulfur emissions may contribute episodically to Arctic middle and upper tropospheric burden (Fisher et al., 2011; Breider et al., 2014; Yang et al., 2018), related to high injection heights and transport pathways (Yang et al., 2018). However, few observations at long-term monitoring stations showed volcanic influences also on surface concentrations (e.g., Breider et al., 2014; Leaitch et al., 2018). Natural sulfur emissions from the Smoking Hills in northern Canada may further impact Arctic sulfate concentrations (Radke and Hobbs, 1989; Hirdman et al., 2010; Leaitch et al., 2018).

Mineral dust aerosol originates from wind-blown bulk-to-particle conversion in arid and semi-arid regions (e.g., Boucher, 2015). It thus consists of an internal mixture of crustal material, such as Si, Al, Mg, Fe, K, and organic material (e.g., Hoffmann and Warnke, 2007). Mean tropospheric dust concentrations are

---

[7] Amides, nitramines, and imines are characterized by functional groups of -R=O, $-NO_2$, and -N=R, respectively.

minimum in Arctic summer (VanCuren et al., 2012; Fan, 2013), related to a less efficient transport from distant sources (mainly Gobi and Sahara deserts) compared to spring (Quinn et al., 2007; Huang et al., 2015). Nevertheless, high-latitude dust sources, primarily in northern North America, become more important in summer (Bullard et al., 2016), particularly impacting Arctic surface concentrations (Breider et al., 2014; Groot Zwaaftink et al., 2016; Sobhani et al., 2018).

Taken together, the pronounced seasonal cycle in Arctic aerosol properties is driven by a combination of processes occurring along transport and within Arctic regions. As a result, understanding both anthropogenic sources as well as natural aerosol processes are crucial for Arctic climate studies. Although considerable advances have been achieved in recent years (e.g., Willis et al., 2018), knowledge gaps about the natural influence on Arctic aerosol particles as well as related primary and secondary processes remain.

1.3 OBJECTIVES AND STRUCTURE OF THE THESIS

This study focuses on the understanding of sources and formation processes contributing to summertime Arctic aerosol abundance. Previous findings show that our picture of Arctic aerosol properties and related processes is incomplete, partly owing to a lack of summertime airborne observations (e.g., Willis et al., 2018). In Chapter 1, remaining gaps relevant to this study in our current understanding of summertime Arctic aerosol were presented. To summarize, first, the relative importance of lower latitude sources and regions to Arctic aerosol composition are not well characterized. Second, our knowledge of the natural and related primary as well as secondary processes influencing aerosol properties in the pristine Arctic summer is incomplete. However, a detailed chemical and physical understanding of processes controlling summertime Arctic aerosol is crucial for a predictive understanding of the Arctic climate system. Thus, the following questions are addressed in this study:

- Which compounds characterize the vertically resolved single particle chemical composition?
- Which processes control the vertical abundance of aerosol compounds?
- Which compounds are related to anthropogenic, natural, and/or vegetation fire sources?

To the author's knowledge, this is the first study to conduct in-situ airborne single particle composition measurements in the summertime Arctic and thus to investigate the vertical structure of aerosol particle mixing state. Information on particle mixing state are of particular interest for a detailed understanding of secondary and primary aerosol formation processes. This study further provides new insights into the vertical abundance of organic functional groups, such as carboxylic acids and amines. In addition, a combination of aerosol and trace gas measurements as well as air mass history modeling allows a comprehensive analysis of Arctic aerosol source attribution.

The thesis is organized as follows: In Chapter 2, measurement and modeling methods used in this work are presented. This part includes laboratory studies to characterize the main instrument, the Aircraft-based single particle aerosol mass spectrometer (ALABAMA), for airborne measurements. Complementary measurement techniques are briefly described. Further, descriptions of air mass history modeling and potential aerosol source inventories are given. In Chapter 3, a new approach to infer the mixing state of aerosol particles from single particle mass spectrometer data is introduced. This part further includes laboratory measurements aimed to identify ion markers of particles that are relevant for this study. In Chapter 4, findings of the Arctic airborne measurements conducted in summer 2014 are presented with focus on aerosol composition, sources, and formation processes. The key results of this research and an outlook on potential future research activities in Arctic regions are summarized in Chapter 5.

2

EXPERIMENTAL AND MODELING METHODS

This chapter introduces the main instrument used in this study to measure the particle chemical composition in the summertime Arctic: the Aircraft-based single particle aerosol mass spectrometer (ALABAMA). The performance of the instrument during the Arctic field experiment in July 2014 and during laboratory measurements in September/October 2017 is characterized in this chapter. The ALABAMA particle composition analysis is complemented by gas and additional aerosol instrumentation, air mass history modeling, and aerosol source inventories.

2.1 LASER ABLATION/IONIZATION AEROSOL MASS SPECTROMETER ALABAMA

2.1.1 *Working principle*

The ALABAMA (Brands et al., 2011) was deployed on the Polar 6 aircraft during the Arctic field experiment, to provide in-situ airborne measurements of single particle chemical composition. Figure 2.1 shows schematically the working principle of the ALABAMA. Particles enter the system through a critical orifice (here, constant pressure inlet (CPI)). The following Liu-type aerodynamic lens focuses particles into a narrow beam (Liu et al., 1995a,b; Liu et al., 2007). Further, particles are optically detected by scattering light when passing through two orthogonal detection laser beams (InGaN laser diodes, $\lambda = 405\,\text{nm}$). The scattered light is focused by elliptical mirrors and further detected by photomultiplier tubes. This setup allows to determine the particle's time of flight and thus its velocity. The particle vacuum-aerodynamic diameter (d_{va}) in turn can be derived from the velocity, using a calibration with particles of known size, density, and shape (e.g., monodisperse polystyrene latex (PSL) particles). The ALABAMA analyzes particles in a size range[1] between approximately 270 nm and 1900 nm (d_{va}). Further, the successfully detected and sized particles are ablated and ionized in the high-vacuum region by a single triggered laser shot (frequency-quadrupled Nd:YAG laser, $\lambda = 266\,\text{nm}$,

---

[1] The size range is defined by the 50 % collection efficiency of PSL particles at 2.5 hPa lens pressure, as described in detail in Sect. 2.1.4. However, during the Arctic field experiment (see Ch. 4), the ALABAMA size range was between approximately 300 nm and 900 nm, owing to several instrumental modifications (see details in Sect. 2.1.4).

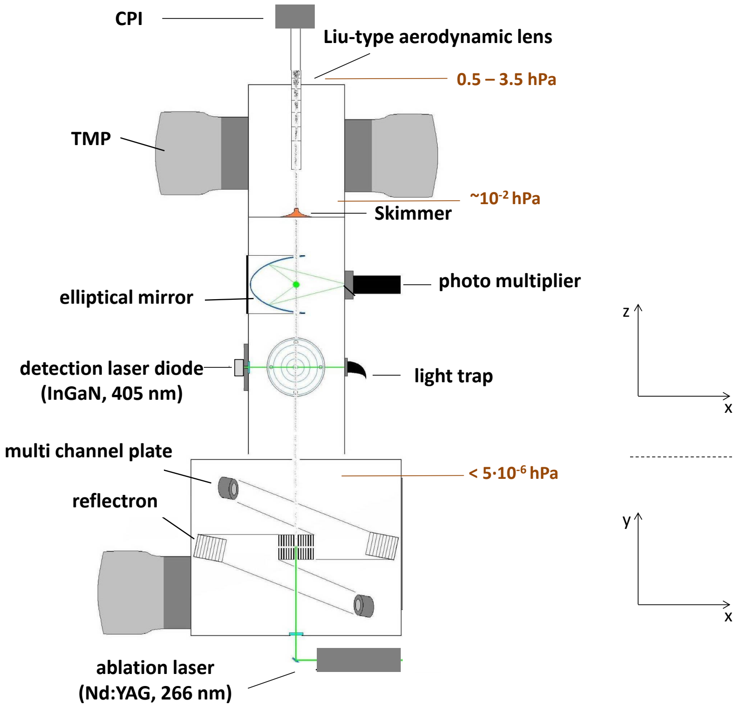

Figure 2.1: Schematic overview of the ALABAMA (adapted from Brands et al. (2011)). Acronyms are defined as follows: CPI = constant pressure inlet (see Sect. 2.1.2); TMP = turbo molecular pump. The view of the scheme changes from the upper to the lower part, indicated by the two coordinate systems on the right-hand side. Pressure regimes for the aerodynamic lens as well as for the first and second pumping stage are given from top to bottom, respectively.

pulse length ∼ 6 ns, maximum repetition rate = 20 Hz; Quantel, 2008). Finally, generated ions are guided into a Z-shaped Time of Flight mass spectrometer that provides bipolar mass spectra of individual particles, up to ion mass to charge ratio (m/z) 250. Together, the ALABAMA instrumental setup obtains on-line size and chemical composition of each particle being analyzed.

In practice, the laser-induced ablation/ionization process shows both technical advantages and disadvantages, compared to other aerosol mass spectrometer techniques (see Sect. 2.2.3). For example, the molecular identification of compounds, in particular organics, can be challenging due to fragmentation of molecules and ions (e.g., Sullivan and Prather, 2005; Murphy et al., 2007). Further, quantification of aerosol mass concentration is complex (e.g., Suess and Prather, 1999; Pratt and Prather, 2012) and practically not possible by highly variable ion signals (e.g., Sullivan and Prather, 2005; Roth, 2009, 2014), owing to the following reasons. First, particles in the ablation and ionization region can pass different laser intensities, by a combination of particle beam divergence and Gaussian laser beam profile as well as inhomogeneities within the spatial profile of the laser beam (e.g., Wenzel and Prather, 2004; Brands, 2009). Second, the fraction of an individual particle that is ablated by the laser can vary, depending on particle size, composition, and structural heterogeneity as well as laser intensity (e.g., Weiss et al., 1997; Bhave et al., 2002; Cai et al., 2006; Zhou et al., 2006; Sultana et al., 2017b). Third, the ionization efficiency is composition-dependent (e.g., Bhave et al., 2002). Fourth, matrix effects, mainly related to charge exchange reactions in the ablation plume, can cause suppressions of ion signals from major compounds by less concentrated compounds (e.g., Reilly et al., 2000; Gross et al., 2000; Zhou et al., 2006). In general, the ablation/ionization mechanism of those small particles in vacuum is complex and not fully understood (e.g., Suess and Prather, 1999; Drewnick, 2000; Murphy et al., 2007). Nonetheless, single-particle technique provides the unique opportunity to directly analyze the distribution of aerosol chemical components within an aerosol population, the so-called mixing state (e.g., Sullivan and Prather, 2005). In parallel, a wide range of organic and inorganic species, including refractory material such as minerals, metals, and elemental carbon, can be studied, in contrast to other aerosol mass spectrometer techniques. Finally, number concentrations of the ALABAMA particle types can be estimated by scaling the measured particle fraction with concurrent quantitative measurements (see Sect. 3.2; Sullivan and Prather, 2005).

2.1.2 *Characterizing the inlet transmission efficiency*

The ALABAMA inlet for airborne sampling requires a special design due to varying atmospheric pressure and temperature. For stationary ground-based measurements, aerosol mass spectrometers typically use a fixed critical orifice with approximately 100 µm diameter. The fixed critical orifice ensures constant volumetric flow rate into the instrument, while mass flow rate varies with air density during airborne sampling. This in turn leads to a variable pressure inside the aerodynamic lens (p_{lens}) and, thus, to variable particle velocity and particle transmission efficiency of the aerodynamic lens (Liu et al., 1995a,b; Liu et al., 2007), both of which are not convenient too handle. The Instrumental development and Electronics Department of the Max Planck Institute for Chemistry (MPIC) developed a new device (Fig. 2.2), the so-called constant pressure inlet (CPI) for airborne measurements. A flexible orifice (O-ring) is either pinched or relaxed, depending on upstream pressure (p_{upstream}), by a bottom and top plate that are connected to a rotor. Thus, the CPI maintains a constant lens pressure by adjusting the orifice diameter, thereby changing the volumetric flow into the instrument. The new device was successfully applied for several airborne experiments (Molleker et al., 2019).

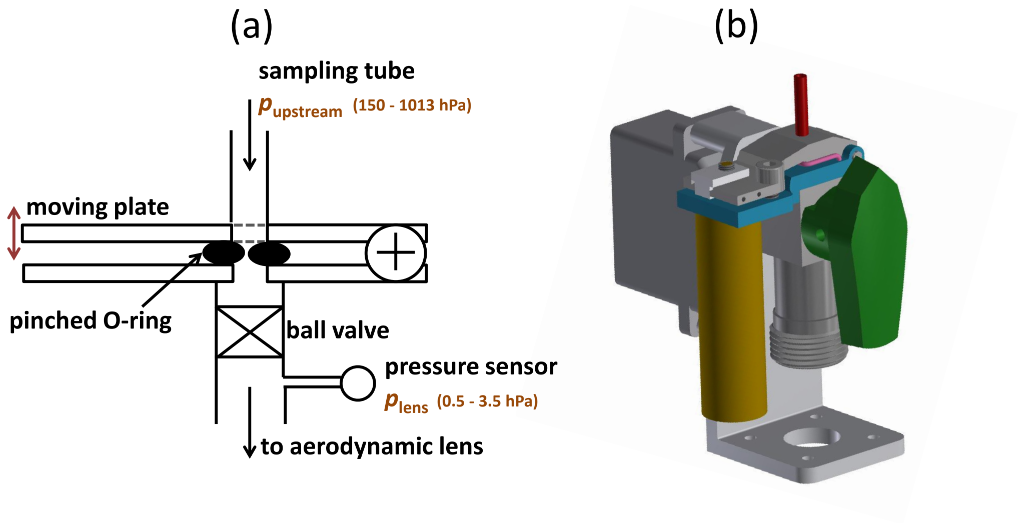

Figure 2.2: (a) Schematic (adapted from Molleker et al., 2019) and (b) technical drawing of the constant pressure inlet (CPI; designed by the Instrumental development and Electronics Department of the MPIC). Regimes of upstream pressure (p_{upstream}) and lens pressure (p_{lens}) are indicated.

Laboratory measurements with the ALABAMA were conducted to characterize the inlet particle transmission efficiency as a function of upstream pressure. The experimental setup to characterize the inlet transmission efficiency is as follows. Monodisperse PSL particles of various sizes mixed with purified water were nebulized with an aerosol generation system, forming tiny droplets. The droplets passed through a diffusion dryer filled with silica gel to remove water. Further, the dried particles passed through a differential mobility analyzer (DMA) with the classifier set at the appropriate voltage to extract the nominal particle size. This setup allowed to check if the PSL geometric diameter, specified by the manufacturer, altered due to aging of the sample. The particle vacuum-aerodynamic diameter (d_{va}) of PSL is then calculated as follows:

$$d_{\text{va}} = \frac{\rho_{\text{PSL}}}{\rho_0} \cdot S_{\text{PSL}} \cdot d_{\text{mob}}, \tag{1}$$

with the PSL particle density (ρ_{PSL}) of 1.05 g cm^{-3}, the standard particle density (ρ_0) of 1.0 g cm^{-3}, the dimensionless Jayne shape factor (S_{PSL}) of 1, and the particle mobility diameter (d_{mob}) given by the DMA[2] (Jayne et al., 2000; DeCarlo et al., 2004). Section 2.1.5 provides further detailed information on

---

[2] For PSL particles larger than 1 µm, the DMA was used as a filter, removing a second particle mode appearing at smaller sizes, rather than selecting the nominal PSL size. Thus, the

d_{va}. Further, the particles were guided into the ALABAMA and the additional reference instrument. In this section, the optical particle counter (OPC) model 1.129 was used as reference instrument due to its ability to operate down to 150 hPa upstream pressure (GRIMM Aerosol Technik, 2008; Bundke et al., 2015). Briefly, the OPC measures particle number concentrations based on particle's scattering light signals. The experimental setup included also in-line orifices[3] upstream of both instruments were used to provide p_{upstream} between 700 hPa and 170 hPa (Fig. 2.3). As a result, the experimental setup in this section imitated the performance of the ALABAMA down to 170 hPa operational pressure level.

The inlet transmission efficiency (TE_{Inlet}) is defined as follows:

$$TE_{\mathrm{Inlet}} = \frac{N_0}{N_{\mathrm{reference}}}, \tag{2}$$

with the particle number concentration monitored by the reference instrument ($N_{\mathrm{reference}}$) and particle number concentration detected by the ALABAMA first optical detection stage (N_0). The position of the aerodynamic lens was aligned to ensure maximum N_0 for particles present in ambient air. By the experimental setup together with the definition in Eq. 2, the inlet transmission efficiency refers only to the CPI transmission efficiency and the lens transmission efficiency. The lens transmission efficiency in turn is constant for varying upstream pressure, owing to the CPI ability to maintain a constant lens pressure.

The CPI particle transmission efficiency is dependent on upstream atmospheric pressure caused by particle impaction losses within the CPI (Fig. 2.3). In theory, the air flow converges in front of the CPI causing particles to perform a curvelinear motion. Curvelinear motions are typically characterized by the dimensionless Stokes number (Stk) (Hinds, 1999):

$$Stk = \frac{\tau \cdot V_g}{L_c}, \tag{3}$$

with the characteristic length (L_c), the gas velocity (V_g), and the relaxation time (τ) that is defined as follows:

$$\tau = \frac{\rho_p \cdot d_p^2 \cdot C_c}{18 \cdot \eta}, \tag{4}$$

---

geometric diameter, provided by the manufacturer, instead of d_{mob}, was used to calculated PSL d_{va}.

[3] Orifice diameters ranged between 0.5 mm and 0.25 mm in 4 steps that are equivalent to p_{upstream} of 700 hPa to 170 hPa.

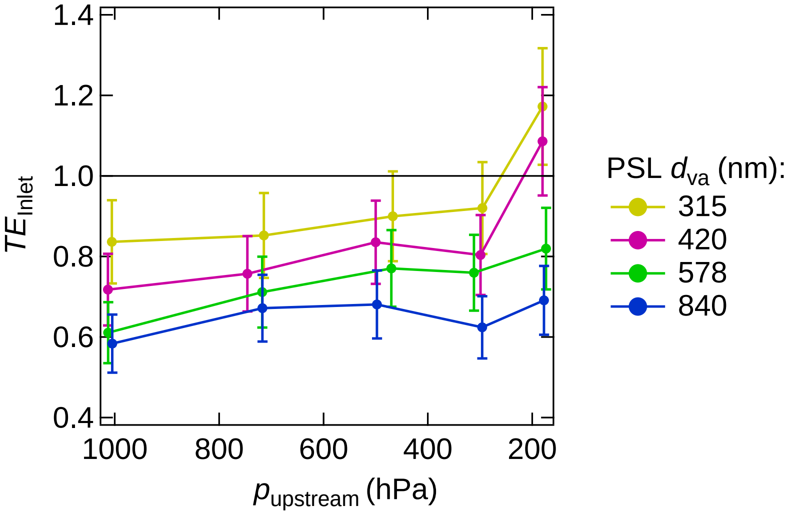

Figure 2.3: Inlet transmission efficiency (TE_{Inlet}) as a function of both upstream pressure (p_{upstream}) and particle size (d_{va}) at 2.5 hPa lens pressure. Upstream pressure of approximately 1013 hPa to 170 hPa is equivalent to a CPI orifice diameter (d_{CPI}) of 150 µm to 340 µm, respectively (see Sect. A.1). The detection efficiency is given in STP, as defined in Sect. A.1. Uncertainty analyses are given in Sect. A.2.

with the particle density (ρ_p), the particle diameter (d_p), the coefficient of dynamic viscosity (η), and the Cunningham slip correction factor (C_c) that can be parametrized as:

$$C_c = 1 + \frac{2.52 \cdot \lambda_{\mathrm{g}}}{d_p} \tag{5}$$

with gas mean free path (λ_{g}) of 0.066 µm at 293 K and 1013 hPa (Hinds, 1999). The relaxation time characterizes the time a particle requires to adjust its velocity to the new conditions of forces. The Stokes number can be understood as the ratio of particle relaxation time to the transit time available for the adjustment. When the Stokes number $\ll 1$, particles perfectly follow the gas streamlines; when the Stokes number $\gg 1$, particles resist changing their directions and further move in a straight line. Thus, the Stokes number characterizes impaction of particles onto surfaces based on particle inertia when flow direction is changed, so-called inertial impaction (Hinds, 1999).

Exemplary, considering the movement of a PSL particle with 0.8 µm diameter (d_p) and 1.05 g cm^{-3} density (ρ_p) in upstream conditions of approximately 1000 hPa (p_{upstream}), the relaxation time of the particle is approximately 2.4 µs. Particle Stokes number is further determined by the characteristic length (L_c) (Liu et al., 1995a; Bahreini et al., 2008) that is here given by the equivalent CPI orifice diameter (d_{CPI}) of 150 µm (see Sect. A.1). The equivalent CPI orifice diameter is introduced as the pinching of the O-ring leads to an irregular and non-reproducible O-ring shape, indicated by pictures from a microscopic view in Schulz (2019) and Molleker et al. (2019). Thus, the equivalent CPI orifice diameter can be thought of as an orifice diameter of a circular shaped O-ring that provides the same orifice area as the orifice of interest. The upstream gas velocity (V_g) is 14.7 cm s^{-1}, determined by using upstream volumetric flow rate (f_{upstream}) of 2.9 cm^3 s^{-1} in a tube of 5 mm inner diameter (see Sect. A.1). As a result, the particle Stokes number is $2.3{\cdot}10^{-3}$. The Stokes number is even smaller than $2.3{\cdot}10^{-3}$, when considering particles smaller than 0.8 µm in upstream pressure below 1000 hPa. Thus, impaction losses for particles up to 0.8 µm upstream of the CPI are unlikely.

However, compared to an inlet with a fixed orifice diameter, O-rings have a larger dimension in flow direction, which is described hereafter as a channel. Particle motion through the CPI channel is likely along a curved path by the irregular shape of the O-ring while pinching. In contrast to upstream conditions described above, V_g increases by passing the CPI channel[4]. Assuming that the particle relaxation time (τ) and the characteristic length (L_c) remain constant (2.4 µs and 150 µm, respectively), the Stokes number of a particle passing the CPI channel is approximately 2.6. Thus, it is likely that the available time for the particle to adjust to the new conditions is less than their relaxation time, leading to impaction losses within the CPI curved channel. The assumption of keeping τ constant does not consider that the gas mean free path (λ_{g}) in the CPI channel is larger compared to upstream conditions, since the pressure in the CPI channel is smaller than upstream pressure. However, an increasing λ_{g} will cause an increasing τ that in turn lead to even larger particle Stokes numbers.

Taken together, upstream pressure determines the strength of the O-ring pinch and thereby the CPI orifice diameter and shape of the CPI channel. The O-ring pinch in turn can lead to particle impaction losses within the CPI channel. This theoretical approach is confirmed by measurements illustrated in Fig. 2.3: when p_{upstream} decreases, d_{CPI} increases, thus, the O-ring is less pinched such that the CPI particle transmission increases. This effect is less pronounced for larger particles (Fig. 2.3), which is somewhat counterintuitive. Reasons for this remain unclear. The inlet transmission efficiency above 1 for particles smaller than 420 nm might caused by two reasons. First, systematic uncertainties, for example given by the instrument's flow accuracy, are not considered in the depicted uncertainty bars (see Sect. A.2). Second, the particle counting efficiency of the OPC compared to the ALABAMA might be lower for this size range.

---

[4] V_g is approximately 164 m s^{-1}, corresponding to f_{upstream} of approximately 2.9 cm^3 s^{-1} with the 150 µm CPI equivalent diameter.

Particle losses by the CPI likely influence airborne particle measurements. However, the inlet transmission efficiency obtained in this study cannot be applied to correct particle concentrations measured by instruments using the CPI, owing to several factors. Material fatigue, non-reproducible O-ring shape (see Sect. A.2), and different CPI designs make it difficult to compare measurements of different instruments using this device and measurements of the same instrument using the CPI at different times and temperatures. The CPI O-ring design was improved meanwhile (see Table 6 in Sect. A.3 and Molleker et al., 2019). The new custom made O-ring with a smaller inner diameter of 0.5 mm requires less pinching to conduct measurements in high upstream pressure conditions. Still, the new O-ring with smaller inner diameter can maintain the instrument operational pressure level down to 150 hPa (Molleker et al., 2019).

2.1.3 *Characterizing the particle detection efficiency*

Measurements of single particle chemical composition require the prior successful particle detection. The instrument performance thus depends largely on the particle detection efficiency (DE). The ALABAMA particle detection efficiency was characterized by both laboratory and atmospheric measurements after and during the Arctic field experiment, respectively. The particle DE is here defined as the fraction of the particle number concentration detected by both optical detection stages within a pre-defined time interval (N_{coinc}) to the particle number concentration monitored by the reference instrument ($N_{\text{reference}}$):

$$DE = \frac{N_{\text{coinc}}}{N_{\text{reference}}}. \tag{6}$$

Defined in this manner, the efficiency depends on the performance of several instrumental parts: the CPI transmission efficiency, the aerodynamic lens transmission efficiency, and the optical detection. These parts are in turn dependent on several parameters, such as p_{upstream} (see Sect. 2.1.2), pressure inside the aerodynamic lens (p_{lens}), particle size, and particle shape (e.g., Jayne et al., 2000; Zhang et al., 2002, 2004; Huffman et al., 2005; Liu et al., 2007; Kamphus et al., 2008; Brands, 2009; Brands et al., 2011; Klimach, 2012). Brands et al. (2011) reported the ALABAMA detection efficiency as a function of particle size and shape. Meanwhile, several instrumental parts were modified and improved, e.g., the optical detection setup (Roth, 2014; Schmidt, 2015) and the inlet setup (see Sect. 2.1.2) such that further laboratory measurements focusing on the ALABAMA DE as a function of particle size and lens pressure (see Sect. A.3) had to be conducted. This section presents the measurements of DE as a function of particle size.

The laboratory setup is described in Sect. 2.1.2. The condensation particle counter (CPC) model 5.403 and the OPC model 1.129 (GRIMM Aerosol Technik, 2003, 2008, respectively) were used as reference instruments, measuring particles smaller and larger than 1 µm, respectively. Similar to the OPC, the CPC measures particle number concentrations based on particle's scattering light signals. In contrast to the OPC, the CPC detects particles smaller than 250 nm by prior enlarging particles to a detectable size by butanol condensation (GRIMM Aerosol Technik, 2003). The position of aerodynamic lens was adjusted prior to measurements to achieve maximum N_{coinc} for 400 nm PSL particles. The lens position was not readjusted for each particle size, to create realistic atmospheric measurement conditions.

Figure 2.4 presents the particle size-dependent detection efficiency at 3.5 hPa lens pressure and approximately 1013 hPa upstream pressure. The ALABAMA DE curve results primarily from a combination of two effects: the aerodynamic lens transmission efficiency (e.g., Zhang et al., 2002) and the so-called effective detection laser beam width (Klimach, 2012). Briefly, the Liu-type aerodynamic aerosol focusing lens consists of a series of apertures of different orifice sizes (3 mm to 5 mm) providing an alternating converging-diverging flow field. Based on particle inertia when flow direction is changed, either a displacement towards the symmetry axis or inertial impaction onto the orifice front surface occurs (see Sect. 2.1.2). The first of the two effects leads to a highly collimated particle beam close to the centerline. Impaction in turn affects particle losses in the lens (e.g., Liu et al., 1995a,b; Zhang et al., 2002; Liu et al., 2007; Zhang et al., 2004). Taken together, the decreasing detection efficiency with increasing particle size can be explained by impaction losses in the aerodynamic lens, associated with an excess of particle inertia, and thus a lower lens transmission efficiency (Liu et al., 2007).

In parallel, the decreasing DE for particles smaller than 400 nm can be explained with the concept of the effective detection laser beam width (Klimach, 2012). The effective detection laser beam width describes the maximum distance between the particle and the center of the laser beam (approximately Gaussian intensity profile) that the particle can still be detected by its scattered light signals (Klimach, 2012). Considering an optical detection geometry similar to the ALABAMA[5], Klimach (2012) reported that the total intensity of the scattered light signal decreases with decreasing particle size. As a result, the effective laser beam width strongly depends on particle size. Smaller particles need to be closer to the center of the laser beam to produce enough scattered light signal to be detected. For particles below approximately 100 nm,

---

[5] The solid angle of the elliptical mirror is 3° to 177°.

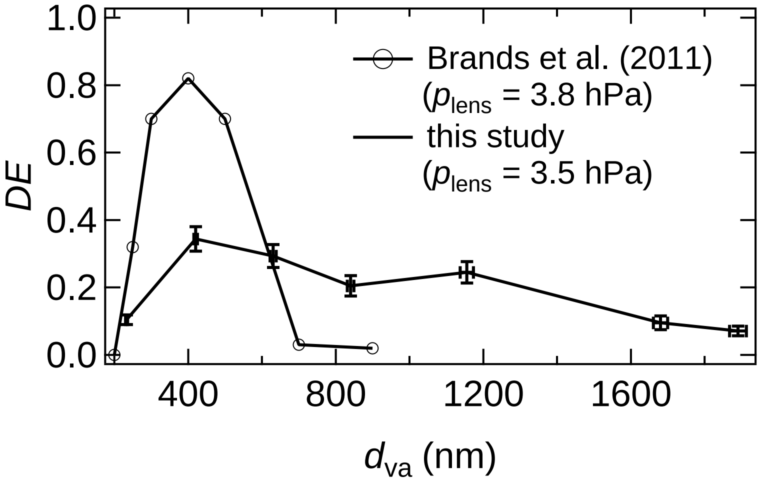

Figure 2.4: Detection efficiency (DE) as a function of particle size (d_{va}) at 3.5 hPa lens pressure (p_{lens}) compared to results in Brands et al. (2011) at 3.8 hPa lens pressure. Uncertainty analyses are given in Sect. A.2.

the effective laser beam width decreases strongly towards 0 mm.

By comparing results in Fig. 2.4 with measurements conducted in Brands et al. (2011), three differences are obvious. First, the maximum DE is about half of the value measured in Brands et al. (2011) for 400 nm particles. This might be caused by several modifications of the ALABAMA and differences in the general experimental setup. In detail, the constant pressure inlet (CPI) cannot explain the discrepancy, as the new custom made O-ring that was used for this measurement shows a particle transmission efficiency close to 1 (Molleker et al., 2019). Nevertheless, it might be that the CPI orifice was partly clogged, which could lead to additional particle losses. Further, Brands et al. (2011) used a Nd:YAG continuous wave laser diode ($\lambda = 532$ nm) for particle detection. Additionally, the detection efficiency largely depends on lens alignment, as indicated by comparing Figs. 2.3 and 2.4 (lens aligned to obtain maximum N_{coinc} and lens aligned to obtain maximum N_0, respectively). However, lens alignments for experiments conducted in this study and in Brands et al. (2011) cannot be reproduced. Micrometer screws that provide the exact lens position were not implemented in the ALABAMA. Together, reasons for the discrepancy remain unclear.

Second, the DE decline towards smaller particles is less pronounced in this study. This is likely caused by improving both the optical detection setup and the alignment of the elliptical mirrors (Roth, 2014; Schmidt, 2015). Third, the decline towards larger particles is less pronounced in this study. Brands et al. (2011) used a 90° bent tubing behind the 100 µm inlet orifice, which likely

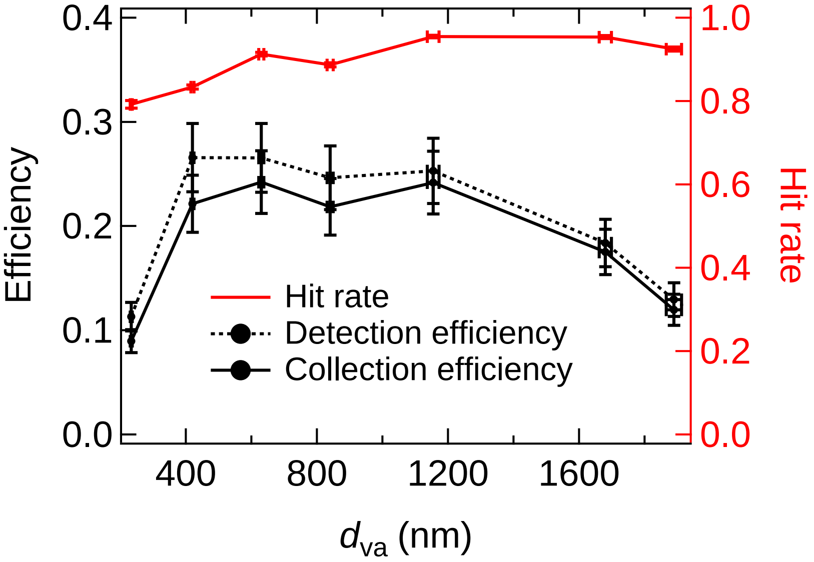

Figure 2.5: Hit rate (red line), detection efficiency (black dashed line), and collection efficiency (black solid line) as a function of particle size (d_{va}) at 2.5 hPa lens pressure (obtained in September/October 2017). Uncertainty analyses are given in Sect. A.2.

caused a significant fraction of particles larger than 600 nm to impact onto the tube wall in the bend. The inlet setup was modified, by removing the bend and using the CPI (see Sect. 2.1.2).

2.1.4 *Particle collection efficiency*

The overall performance of the ALABAMA is described here as the collection efficiency (CE):

$$CE = DE \cdot HR, \tag{7}$$

accounting for both the detection efficiency (DE) and the efficiency of the laser ablation/ionization process, the so-called hit rate (HR)[6]. The instrument hit rate is defined as the number of particles that are successfully ionized by the ablation laser and that create a mass spectrum (N_{hits}) relative to the number of laser shots (N_{shots}):

$$HR = \frac{N_{\text{hits}}}{N_{\text{shots}}}. \tag{8}$$

The triggered shot requires that the particle velocity was prior successfully determined and that the laser was ready to shoot[7] (Brands et al., 2011). The particle hit rate is dependent on several factors, such as particle size (e.g., Kane et al., 2001; Brands et al., 2011), shape (e.g., Moffet and Prather, 2009), chem-

---

[6] Section A.4 presents a side topic on hit rate variability.

[7] The maximum shot repetition rate of the Nd:YAG laser was set to 12 Hz.

ical composition (e.g., Thomson et al., 1997; Kane et al., 2001; Brands et al., 2011), and charge (Su et al., 2004) as well as the laser intensity (e.g., Thomson et al., 1997; Kane et al., 2001; Brands et al., 2011). Detailed characterization of the ALABAMA particle hit rate will be part of the PhD thesis of H.-C. Clemen (Clemen, 2020) and was earlier discussed in Brands et al. (2011). Hit rate measurements were simultaneously conducted with measurements in Sect. 2.1.3. The ablation laser was prior aligned to achieve maximum hit rate for 400 nm PSL particles and the position was kept constant for each particle size. The ablation laser intensity was approximately $3.7{\cdot}10^{9}\,\mathrm{W\,cm^{-2}}$ (see Table 7 in Sect. B.1).

The size-dependent collection efficiency provides the particle size range that the ALABAMA can efficiently analyze. The size range is derived by the upper and lower 50 % values of the collection efficiency averaged between 420 nm and 1155 nm. Further, the CE was linearly interpolated between 233 nm and 420 nm to obtain the 50 % lower size cut-off. As a result, the size range that the ALABAMA can efficiently analyze is between 267 nm and 1890 nm, respectively, given for PSL particles and at 2.5 hPa lens pressure. 2.5 hPa is maximum operating lens pressure, limited by the maximum pressure in the mass spectrometer of $5{\cdot}10^{-6}$ hPa to operate high voltages. To note, the Arctic field experiment in July 2014 was conducted at 3.2 hPa lens pressure, owing to a smaller skimmer orifice diameter (Fig. 2.1) built in the ALABAMA at this time (see Table 6 in Sect. A.3).

The measurement performance of the ALABAMA during the Arctic field experiment in July 2014 was additionally investigated (Fig. 2.6), as several instrumental parts were modified between July 2014 and the September/October 2017 laboratory measurements presented in Fig. 2.5 (see Table 6 in Sect. A.3 and Clemen, 2020). Detection efficiency, hit rate, and collection efficiency are calculated according to Eqs. 6, 8, and 7, respectively. $N_{\mathrm{reference}}$ is provided by the UHSAS number concentration in the size range between 320 nm and 870 nm, simultaneously measured onboard the airborne platform (for instrumental details see Sect. 2.2.2). The selected UHSAS lower and upper size cut-offs refer to the ALABAMA size range that include 98 %[8] of all particles collected during the Arctic field experiment (see Fig. A.8). To note, the different measurement principals of the ALABAMA and the UHSAS result in different definitions for the particle equivalent diameter: the particle vacuum-aerodynamic diameter (d_{va}) and the particle optical diameter (d_{opt}), respectively. Thus, the com-

---

[8] The 1 % and 99 % percentiles define the lower and upper size cut-offs, respectively. The value 98 % is chosen, as almost the overall sample is included and at the same time outliers are excluded.

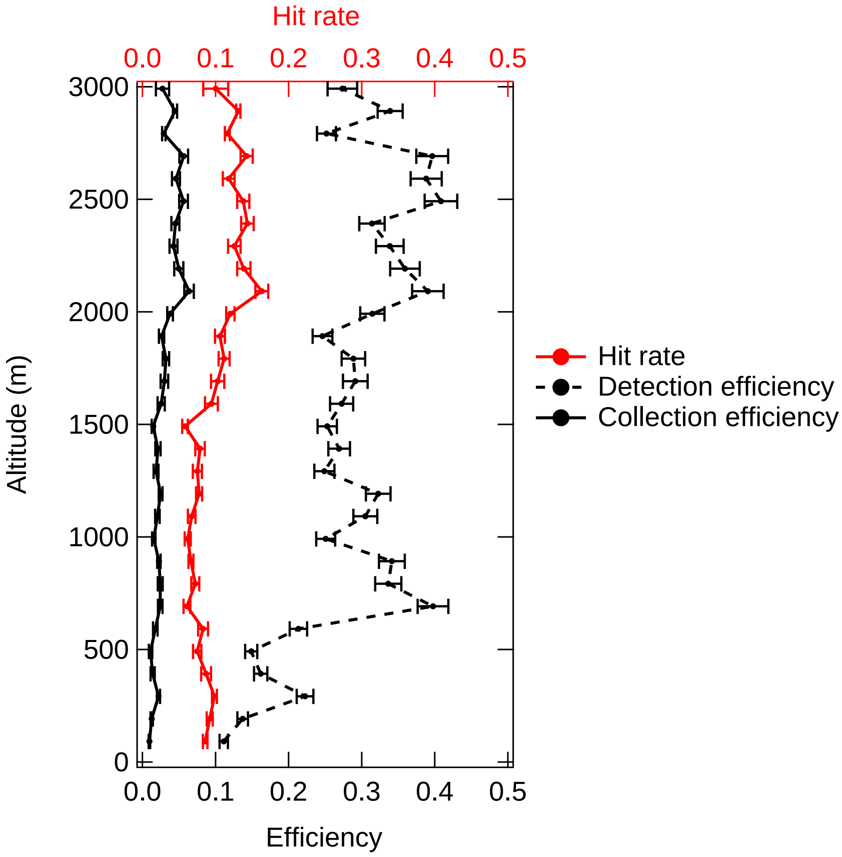

Figure 2.6: Detection efficiency (black dashed line), hit rate (red line), and collection efficiency (black line) as a function of altitude at 3.2 hPa lens pressure during the Arctic field experiment in July 2014 (NETCARE 2014). The bottom x-axis presents the detection and collection efficiencies. Uncertainty analyses are given in Sect. A.2

parison between the ALABAMA and the UHSAS size ranges should solely be considered as an approximation.

Figure 2.6 presents the vertically resolved detection efficiency, hit rate, and collection efficiency of the ALABAMA during the Arctic field experiment. The detection efficiency increased with altitude, which can likely be explained by two possibilities. First, the CPI particle transmission efficiency was found to increase with decreasing atmospheric pressure (see Sect. 2.1.2). Second, it might be that particles present below 500 m altitude were predominantly smaller than 400 nm, thus, were less efficiently detected by the ALABAMA optical detection stages compared to larger particles (see Sect. 2.1.3). Two additional points should also be considered when discussing the ALABAMA *DE* during the Arctic field experiment. First, the UHSAS number concentration and in turn the resulting ALABAMA detection efficiency are largely dependent on the chosen UHSAS lower size cut-off (here, 320 nm d_{opt}). The d_{opt} and d_{va} measured by the UHSAS and the ALABAMA, respectively, are here assumed to be approximately equal (see discussion above). Second, the aerodynamic lens was held in a bipod (see Fig. A.3), which was susceptible to vibrations. This may caused a varying DE during airborne operations. Nevertheless, the particle detection efficiencies in July 2014 and September/October 2017 were comparable by values between 10 % and 40 % (compare Figs. 2.4 and 2.6).

In parallel, the hit rate increased by a factor of 2 to 3 with altitude (Fig. 2.6), which can be likely explained by varying particle properties with altitude (see above). The hit rate was on average 10 %, which is approximately a factor of 9 smaller than the hit rate obtained during the laboratory experiment (compare Figs. 2.5 and 2.6). This can be explained by several instrumental modifications that were conducted by H.-C. Clemen after July 2014 to improve the ALABAMA hit rate (Clemen, 2020). Together, the particle collection efficiency by the ALABAMA during the Arctic field experiment varied between 1 % and 6 % (Fig. 2.6)

2.1.5 *Particle sizing*

Particles of different sizes acquire different velocities while exiting the aerodynamic lens (e.g., Jayne et al., 2000; Brands et al., 2011). The particle velocity (V_p) is determined by the time-resolved optical detection of the particle in the vacuum chamber, using the time counter value between the two detection events (*upcount*), together with the known flight distance of 0.07 m and the 25 MHz processor clock (Klimach, 2012; Roth, 2014):

$$V_p = \frac{0.07\,\mathrm{m} \cdot 25\,\mathrm{MHz}}{upcount}. \tag{9}$$

Thus, one *upcount* step corresponds to 40 ns. The size-dependent velocity is further a function of particle shape and density (e.g., Wang and McMurry, 2006). Since most atmospheric particles are non-spherical and have a non-standardized density, the equivalent vacuum-aerodynamic diameter (d_{va}) is introduced to characterize the particle size. The aerodynamic diameter is defined as the diameter of a spherical particle with a density of $1\,\mathrm{g\,cm^{-3}}$ that travels at the same V_p as the particle of interest (e.g., Hinds, 1999; DeCarlo et al., 2004). The aerodynamic diameter in the free-molecular regime is called the vacuum-aerodynamic diameter (DeCarlo et al., 2004).

The diameter of atmospheric particles is calibrated by measuring the velocity of monodisperse, spherical PSL particles of various sizes. The experimental

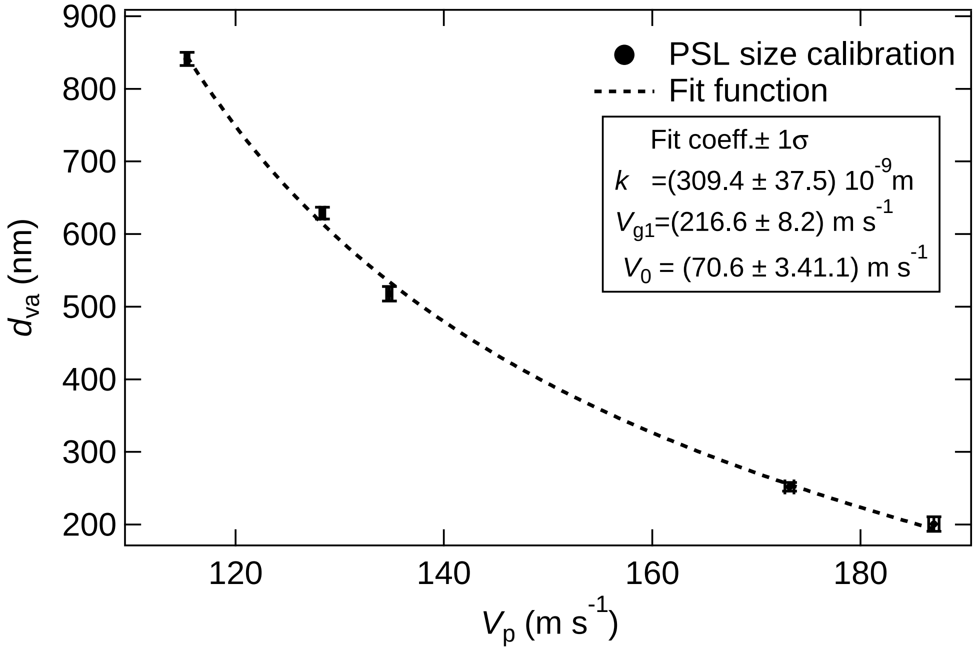

Figure 2.7: Vacuum-aerodynamic diameter (d_{va}) as a function of particle velocity (V_p) derived from the PSL size calibration conducted during the Arctic field experiment (NETCARE 2014) at 3.2 hPa lens pressure. Uncertainty analyses are given in Sect. A.2. The fit function (dashed line), based on Eq. 10, considers only the uncertainty of d_{va} and not that of V_p by negligible small values. The text box presents the associated fit coefficients. Fit residuals can be found in Fig. A.14.

setup for calibration is described in Sect. 2.1.2. Klimach (2012) derived a mathematical relation between d_{va} and V_p as follows:

$$d_{\mathrm{va}} = \frac{k}{\ln\left(\frac{V_{\mathrm{g1}}-V_0}{V_{\mathrm{g1}}-V_{\mathrm{p}}}\right)} \tag{10}$$

with the particle velocity before the gas expansion $(V_0)^9$, the gas velocity after the gas expansion (V_{g1}), and the size calibration factor (k). V_0 and V_{g1} specify the lower and upper limit of V_p, respectively. Together, the ALABAMA size calibration, which is used to calculate d_{va} from the measured V_p, is described by three fit coefficients: k, V_{g1}, and V_0.

For this study, the size calibration was conducted during the Arctic field experiment in July 2014. The particle velocity is calculated using Eq. 9 together with the modal *upcount* value derived from the histograms in Fig. A.9. Finally, the application of Eq. 10 provides fit coefficients k, V_{g1}, and V_0 (Fig. 2.7). More information on the fitting method are given in Sect. A.6.

---

[9] Gas expansion occurs when the air exists the last orifice of the aerodynamic lens and enters the vacuum (see Fig. 2.1).

2.2 COMPLEMENTARY METHODS

Single particle chemical composition by the ALABAMA is complemented by aerosol number and mass concentrations as well as by trace gases, meteorological parameters, and air mass history modeling, to provide a comprehensive analysis on summertime Arctic aerosol composition and sources. This section briefly describes the basic working principles of the additional instrumentation. Table 1 summarizes the complementary data and associated instrumentation. This section further introduces the modeling tool FLEXPART together with aerosol source inventories to study the air mass history.

2.2.1 *Measurement platform and inlets*

Airborne measurements of aerosol physical and chemical properties, trace gases as well as meteorological parameters were performed onboard the Alfred Wegener Institute (AWI) Polar 6 aircraft, a DC-3 aircraft modified to a Basler BT-67 for operation in cold and harsh environments (Fig. 2.8; Herber et al., 2008). Flight altitude was limited to 6 km due to the non-pressurized aircraft cabin. The ALABAMA was switched off at altitudes above 3.5 km to avoid damages in such low pressure conditions. The aircraft survey speed was maintained at approximately $75\,\mathrm{m\,s^{-1}}$, with ascent and descent rates of 150 to $300\,\mathrm{m\,min^{-1}}$ for vertical profiling (Willis et al., 2016).

Aerosol particles were sampled through a shrouded forward-facing inlet diffuser with a diameter of 0.35 cm at intake point (Fig. 2.8). Inside the cabin, the inlet was connected to a 2.3 cm inner diameter stainless steel manifold, of which stainless steel sample lines were directed to the various particle instruments employing angled branches ($\leq 90°$). The manifold exhaust flowed freely into the cabin back to keep the aerosol main inlet from being over-pressured. As a result, the inlet total flow varied with true air speed. With the survey speed noted above, the particle transmission efficiency by the intake is near unity for particles from 20 nm to $\leq 1\,\mu\mathrm{m}$ (Leaitch et al., 2016). Further, based on the total flow drawn by the particle instruments ($\sim 35\,\mathrm{l\,min^{-1}}$) and the measured manifold exhaust flow ($\sim 20\,\mathrm{l\,min^{-1}}$), the total flow through the shrouded intake was nearly isokinetic with $55\,\mathrm{l\,min^{-1}}$ (Leaitch et al., 2016).

Trace gases were sampled through a separate inlet line, consisting of a forward-facing 0.40 cm outer diameter (OD) Teflon tube. Using the aircraft forward motion, ambient air was pushed into the line in combination with a rear-facing 0.95 cm OD exhaust tube that reduced the pressure in the sampling line (Fig. 2.8). An inlet flow of approximately $12\,\mathrm{l\,min^{-1}}$ was maintained.

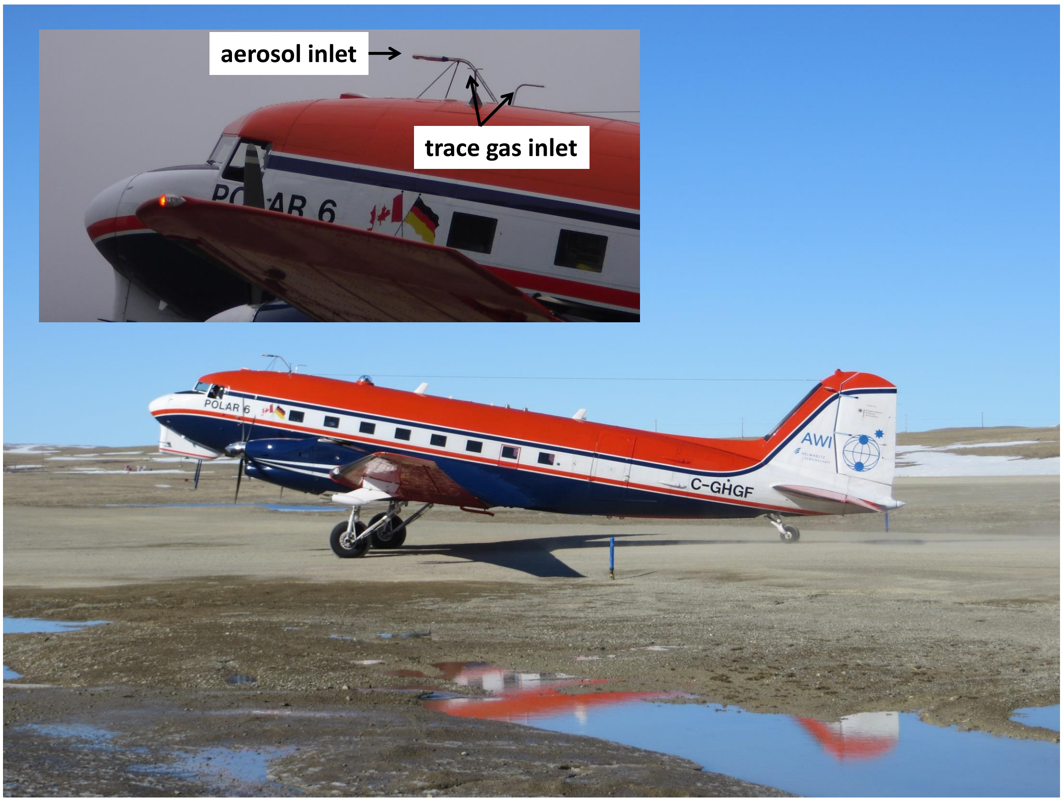

Figure 2.8: Polar 6 aircraft from AWI. The inset shows an expanded image of the inlets located at the top front of the aircraft. The images are courtesy of H. Bozem and J. Schneider.

2.2.2 *Aerosol number concentrations*

Number concentrations of particles between 85 nm and 1000 nm were measured with the Ultra-High Sensitivity Aerosol Spectrometer (UHSAS), manufactured by Droplet Measurement Technologies (DMT). The instrument is based on particle light scattering technique. Particles that cross the beam of a laser ($\lambda = 1054$ nm) are detected and counted by their scattering signals. The intensity of the scattered light provides information on the d_{opt} (e.g., Cai et al., 2008; Schulz et al., 2019). Hereafter, only number concentration of particles greater than 100 nm in diameter ($N_{>100}$) and number concentrations of particles greater than 320 nm in diameter ($N_{>320}$) are used, as discussed in detail in Sect. 2.1.4.

Number concentrations of particles larger than 5 nm in diameter ($N_{>5}$) were measured by the TSI water-based ultrafine condensation particle counter (UCPC) model 3787, sampling at a flow rate of 0.6 l min^{-1} (TSI Incorporated, 2013). Particles are detected and counted by their scattering light signals. To also detect Aitken and nucleation mode, particles are prior enlarged by water condensation.

2.2.3 *Aerosol mass concentrations*

Sub-micron ensemble aerosol composition was measured by an Aerodyne high-resolution time-of-flight aerosol mass spectrometer (HR-ToF-AMS), complementary to the ALABAMA single particle analysis. The HR-ToF-AMS is based on particle thermal vaporization by contact with a heated surface ($\sim 650\,^{\circ}\mathrm{C}$) followed by electron impact ionization (e.g., DeCarlo et al., 2006), in contrast to the ALABAMA laser-induced ablation/ionization process. The HR-ToF-AMS allows quantitative mass concentration measurements of non-refractory aerosol particle components. In practice, organic matter (OM), nitrate, sulfate, ammonium, and MSA are detected (Willis et al., 2016; Willis et al., 2017).

Concentration of particles containing refractory black carbon (rBC) were acquired with a Single Particle Soot Photometer (SP2) manufactured by DMT (Schwarz et al., 2006; Gao et al., 2007). The instrument includes a continuous intra-cavity Nd:YAG laser ($\lambda = 1064\,\mathrm{nm}$) to classify particles as incandescent. The peak incandescence signal is linearly related to rBC mass.

2.2.4 *Trace gas data*

Carbon monoxide (CO) mixing ratios were measured by an Aero-Laser ultra-fast CO monitor (model AL 5002), based on the fluorescence of CO in the vacuum ultraviolet (VUV) at 150 nm (Scharffe et al., 2012; Aero-Laser GmbH, 2013; Wandel, 2015; Bozem et al., 2019). Here, CO is used as an indicator of air mass influenced by combustion sources, including fossil fuel and biomass burning combustion (Andreae and Merlet, 2001).

Water vapor (H_2O) and carbon dioxide (CO_2) measurements were conducted using a LI-7200 closed CO_2/H_2O analyzer, manufactured by LI-COR Biosciences GmbH, based on H_2O and CO_2 infrared absorption (Kluschat, 2016; Bozem et al., 2019). The H_2O mixing ratio by volume ($\mathrm{VMR}_{\mathrm{H2O}}$) together with the temperature (T) and the atmospheric pressure (p_{air}), measured by the AIMMS-20 instrument were used to calculate the relative humidity (RH) and the pseudoequivalent potential temperature (θ_{e}) (see Sect. C.2).

2.2.5 *Atmospheric state parameters and wind data*

The Aircraft Integrated Meteorological Measurement System (AIMMS)-20 by Aventech Research Inc., integrated on the Polar 6 aircraft, delivered meteorological and state parameters. The module Air-Data Probe provides T, p_{air}, RH, wind direction, wind speed, and the three-dimensional aircraft-relative flow vector (true air speed, angle of attack, and side slip). The second module, a Global Positioning System (GPS), processes satellite navigation signals and determines aircraft three-dimensional position and altitude (Aventech, 2018).

2.2.6 *Air mass history modeling*

Air mass history analysis is crucial for understanding aerosol sources and transport processes, both of which controlling aerosol properties in Arctic regions. In this study, the Lagrangian FLEXible PARTicle dispersion model (FLEXPART), version 10.0, is used. FLEXPART is a comprehensive tool for modeling atmospheric transport (e.g., Stohl, 1998; Stohl et al., 2003, 2005) and is widely used in Arctic studies (e.g., Stohl, 2006; Paris et al., 2009; Hirdman et al., 2010; Kuhn et al., 2010; Schmale et al., 2011; Quennehen et al., 2011). The model calculates trajectories of a multitude of hypothetical particles[10] based on the following equation:

$$X(t+\Delta t) = X(t) + v(X,t)\cdot\Delta t, \tag{11}$$

with particle position vector (X), time (t), time increment (Δt), and wind vector (v) (Stohl et al., 2005). Trajectory calculations treat advection and include parametrizations for turbulent diffusion and convection (Stohl et al., 2003, 2005). Grid scale winds from meteorological data sets are used and superimposed by sub-grid scale turbulent as well as convective transport (Stohl et al., 2003, 2005).

In this study, FLEXPART was operated backward in time with operational data from the European Centre for Medium-Range Weather Forecast (ECMWF) with 0.125° horizontal and 3 hours temporal resolution as well as with 137 vertical hybrid sigma-pressure levels. Tracer particles are released from a certain receptor location and followed for 15 days backward in time (Stohl et al., 2003; Seibert and Frank, 2004; Stohl et al., 2005). The receptor location depends on airborne sampling location. In detail, releases were repeatedly initialized each 10-min sampling interval along flight track. By this approach, between 16 and 29 releases were created at each flight, depending on flight duration.

---

[10] Particles need not necessarily to be real particles, but rather infinitesimal small air parcels (Stohl et al., 2005).

Table 1: Complementary data and associated instrumentation used in this study along with additional information.

Instrument	Data used in this study [unit]	Particle size range[a]	Time resolution	T: total uncertainty R: reproducibility A: accuracy CE: collection efficiency	Ref.	Operator
UHSAS	$N_{>320}$ [cm^{-3} (STP)[b]]	320 nm - 870 nm	1 s	CE: 95 %	[c]	AWI
	$N_{>100}$ [cm^{-3} (STP)[b]]	100 nm - 1 µm				
UCPC	$N_{>5}$ [cm^{-3} (stdP)[d]]	5 nm - $\leq$3 µm	1 s	A: 10 %	[e]	UofT
HR-ToF-AMS	ammonium, sulfate, nitrate, OM, MSA [µg m^{-3} (stdP)[d]]	70 - 900 nm	20 - 30 s	T: 33 - 37 %	[f]	UofT
SP2	rBC [µg m^{-3} (STP)[b]]	85 - 700 nm	1 s	R: 10 %	[g]	AWI
CO analyzer	CO [ppb$_v$]		1 s	T: 4.7 ppb$_v$	[h]	IPA
H_2O/CO_2 analyzer	VMR$_{\mathrm{H2O}}$ [ppm$_v$]		1 s	T: 18.5 ppm$_v$	[i]	IPA
AIMMS-20	T [°C], p_{air} [Pa], wind speed [m s^{-1}]		1 s	A: 0.3 °C, A: 100 Pa + 0.05 %, A: 0.5 m s^{-1}	[j]	AWI, ECCC

---

[a] The upper particle size cut-off is approximately 1 µm owing to the particle transmission efficiency of the main aerosol inlet (Sect. 2.2.1), although some instruments might have a higher upper cut-off.

[b] Data by the UHSAS and SP2 are presented at standard temperature and pressure (STP) 273.15 K and 1013.25 hPa (Schulz et al., 2019)

[c] Cai et al. (2008) and Schulz et al. (2019)

[d] Data by the CPC and HR-ToF-AMS are presented at standard pressure (stdP) 1013.25 hPa, since no temperature measurements inside the inlet line are available.

[e] TSI Incorporated (2013) and Leaitch et al. (2016)

[f] DeCarlo et al. (2006), Bahreini et al. (2008), Willis et al. (2016), and Willis et al. (2017)

[g] Schwarz et al. (2006), Gao et al. (2007), Laborde et al. (2012), Dahlkötter et al. (2014), and Schulz et al. (2019)

[h] Scharffe et al. (2012), Aero-Laser GmbH (2013), Wandel (2015), and Bozem et al. (2019)

[i] Kluschat (2016) and Bozem et al. (2019)

[j] Aventech (2018)

Maximum/minimum latitude, longitude, and altitude within the 10-min sampling interval specify the boundaries of the release volume (blue boxes in Fig. 2.9a). In backward mode, FLEXPART calculates the sensitivity of substances, sampled at the receptor, to source emissions (Seibert and Frank, 2004; Stohl et al., 2005; Hirdman et al., 2010). This so-called potential emission sensitivity (PES) function (Fig. 2.9a) is provided every six hours, with uniform horizontal grid spacing of 0.25°, and with five vertical levels (400, 1000, 2000, 5000, and 15000 m; Fig. 2.10). Essentially, the PES value in a particular output grid cell is proportional to the particle's residence time in this cell (Seibert and Frank, 2004; Hirdman et al., 2010) and given in unit of seconds (Fig. 2.10) by assuming contribution of a source with unit strength in this cell and transport of an inert tracer[11] (Stohl et al., 2003; Hirdman et al., 2010).

FLEXPART output combined with source emission inventories may provide a more detailed analysis on the relationship between Arctic aerosol composition and sources. This analysis requires the following data processing steps (Fig. 2.9b). FLEXPART provides three-dimensional (latitude, longitude, and altitude) PES maps each six hours backward in time. First, the total residence time within the 15 days prior to sampling and within a certain vertical layer for each grid cell is obtained by adding up all PES maps backward in time. It is assumed that within this vertical layer, the so-called footprint layer, source emissions occur and mix instantaneously. Therefore, the lowest vertical level (0 - 400 m) is applied for most ground sources (e.g., Stohl et al., 2013), except for vegetation fires related to buoyant effects (e.g., Kondo et al., 2011), as discussed in Sect. 2.2.7.2. Figures 2.10a and b present typical examples of FLEXPART footprint partial column and total column PES maps, respectively. Second, so-called potential source inventories (PSIs) are generated, specifying geolocations of source sectors and source regions (see Sect. 2.2.7). Third, the prior obtained two-dimensional (latitude and longitude) PES map is folded with the two-dimensional PSI map. Finally, the total residence time of sampled air mass spent over a specific source within the 15 days prior to sampling and within the vertical footprint layer is obtained by adding up each grid cell of the PES-PSI-product.

2.2.7 *Potential source inventories*

Source contributions to Arctic aerosol composition are analyzed by combining FLEXPART air mass history with various footprint sources (see above). The potential source inventories (PSIs) are two-dimensional maps with horizontal grid spacing of 0.25°, specifying geolocation of source regions (see Sect.

---

[11] Inert tracer implies that no chemical and removal processes occur along transport.

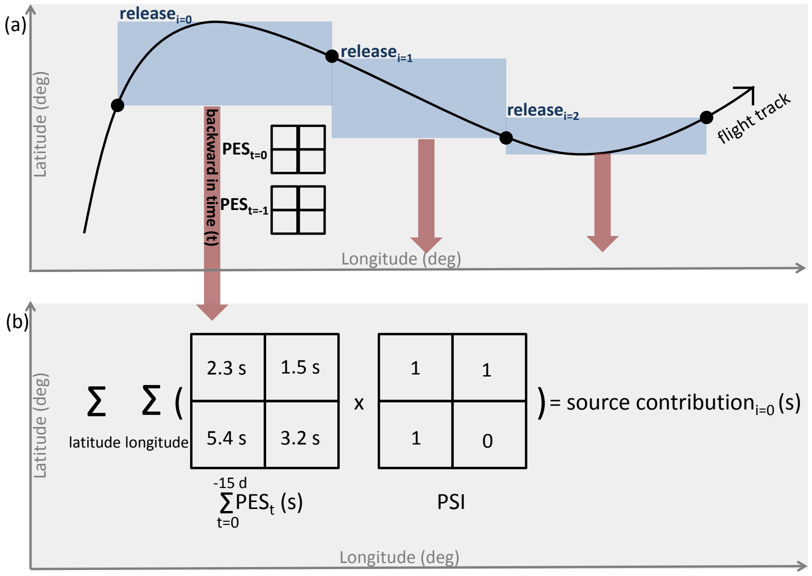

Figure 2.9: Scheme summarizing data processing steps to obtain source contributions to Arctic aerosol composition. (a) FLEXPART backward simulations. The vertical dimension is not presented. The black arrow represents the flight track. Black circles indicate 10-min sampling intervals (each indicated by index i) along the flight track. Blue boxes show particle release volumes. Red arrows and gridded potential emissions sensitivity (PES) maps represent the trace of particles backward in time (each indicated by index t). (b) Convolution of FLEXPART PES maps with potential emission inventories (PSIs) as an example for $i = 0$. FLEXPART PES maps (in unit of seconds) are added up backward in time (here, 15 days), indicated by the lower sigma sign with index t. The resulting PES map is folded with the PSI map (see Sect. 2.2.7). The obtained PES-PSI-products are added up with latitude and longitude, indicated by the two sigma signs. The final sum provides the source-specified contribution (in unit of seconds) to measurements at the release location.

2.2.7.1) and sectors (see Sects. 2.2.7.2 - 2.2.7.4). PSI maps classify (dimensionless) whether the specific source is present in the grid cell, or not, rather than providing quantitative source-specified emission data. This approach is convenient to assess the relation between sources and non-quantitative aerosol composition data by the ALABAMA. The following sections briefly describe the setup of various PSI maps by using data sets from satellite observations among others. The Arctic airborne measurements were conducted from 4 until 21 July 2014, whereas air mass history analysis presented here was done for 15 days prior to sampling.

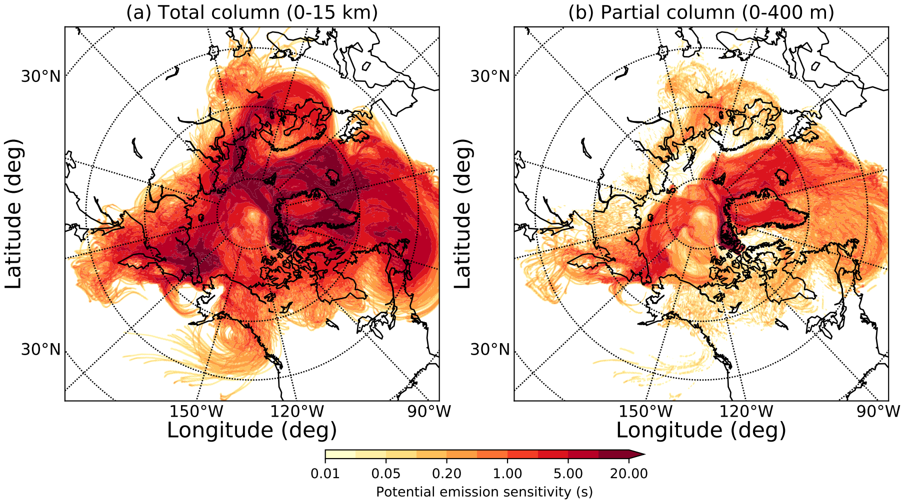

Figure 2.10: Example of FLEXPART 15-days integrated (a) total column and (b) partial column (0 - 400 m) potential emission sensitivity (PES) in unit of seconds, plotted on a polar stereographic map.

2.2.7.1 *Geographical source regions*

Geographical regions that contribute to Arctic aerosol in summer comprise primarily northern Eurasia, North America, East Asia, and the Arctic itself (see Sect. 1.2). Based on several Arctic studies (Stohl, 2006; Shindell et al., 2008; Bourgeois and Bey, 2011; Liu et al., 2015; Yang et al., 2018), main source regions are shown in Fig. 2.11. This study considers Europe and Siberia, likewise, Alaska, northern Canada (nCa), and southern North America (sNA) separately due to differences in vegetation fire occurrence (Fig. 2.12a), industrial sources (Fig. 2.12b), flaring spots (Fig. 2.12c), and population density (Fig. 2.12d). Large marine areas of the Pacific and Atlantic Oceans are included due to their vicinity to Arctic regions. Arctic regions are specified as located north of 73.5° N, based on the determination of the July 2014 polar dome location by Bozem et al. (2019).

2.2.7.2 *Vegetation fires*

The Visible Infrared Imaging Radiometer Suite (VIIRS) onboard the Suomi National Polar-Orbiting Partnership spacecraft can detect sub-pixel thermal anomalies by signals in mid- and thermal infrared spectral range (Schroeder et al., 2014; Schroeder and Giglio, 2018). Thermal anomalies typically include both active vegetation fires and industrial heat sources by fossil-fuel combustion etc. Data of the so-called near real-time VIIRS 375 m Active Fire product were downloaded online for 19 June until 21 July 2014 (NASA, 2018) and projected

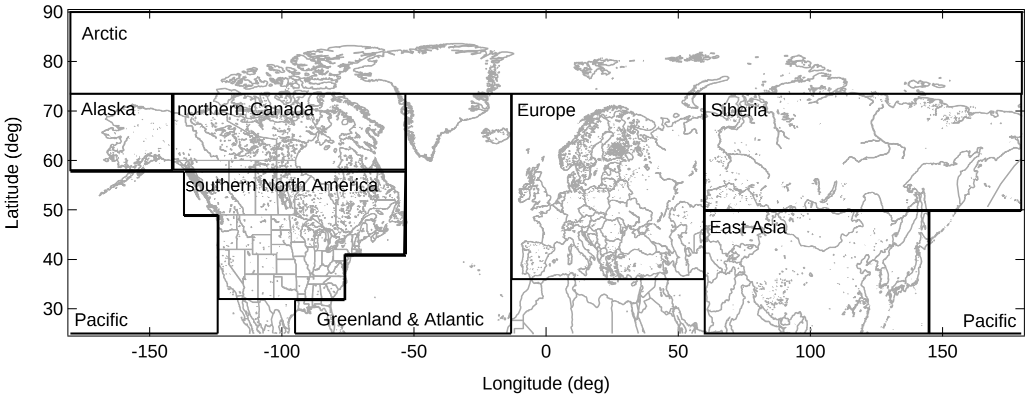

Figure 2.11: Map showing potential source inventories of geographical regions: Arctic, Alaska, northern Canada, southern North America, Pacific, Greenland & Atlantic, Europe, Siberia, and East Asia, referenced in FLEXPART air mass history analysis (see Sects. 4.2 and 4.4).

on potential source inventory (PSI) gridded maps by adding up observations in each grid cell. Thermal anomalies were identified by one or more observations per grid cell within the respective time.

The presence of vegetation fires can be distinguished from other thermal anomalies by the following approach. Anthropogenic heat sources, such as industry, flaring, and densely populated regions, are separately mapped (see Sect. 2.2.7.3) and subsequently excluded from the thermal anomaly PSI map. Residual heat sources in Fig. 2.12a thus present vegetation fires, accumulated for 19 June until 21 July 2014. This approach looks reasonable in comparison with Arndt et al. (2015), at least for boreal fires in northern Canada and Siberia. North American and north Asian biomass burning budgets were anomalously high in 2014 compared to 2001 - 2013 (Fig. 2.57 and Table 2.8 in Arndt et al., 2015). Particularly in summer 2014, large fires in the Great Slave Lake region and Siberia were evident (Fig. 2.40 in Arndt et al., 2015), confirming results in Fig. 2.12a. However, the main weakness of this approach is given by temporal variabilities of the data sets, as described in Sect. 2.2.7.3.

Vegetation fire injection heights are highly variable owing to a combination of fire type, fuel consumption, and prevailing meteorological conditions (e.g., Lavoué et al., 2000; Andreae and Merlet, 2001; Leung et al., 2007; Kondo et al., 2011; Val Martin et al., 2018). Several studies show injection heights for boreal fires in North America and Siberia primary between 1 km and 5 km (e.g., Lavoué et al., 2000; Stohl, 2006; Turquety et al., 2007; Leung et al., 2007; Val Martin et al., 2018). In view of having no better information, the footprint layer for vegetation fires is here defined between 1 km and 5 km.

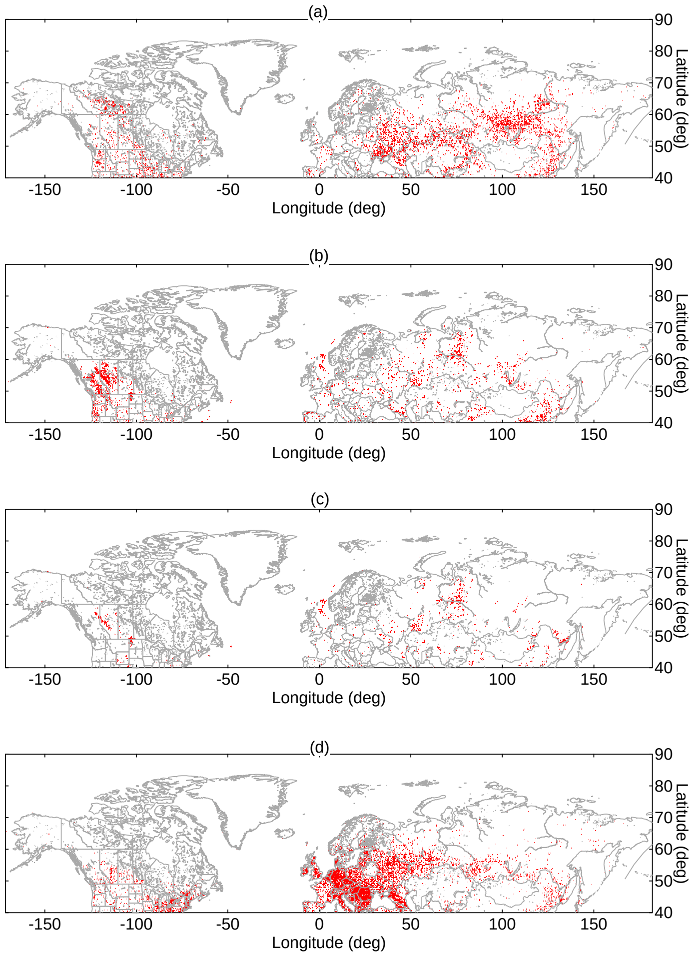

Figure 2.12: Map showing potential source inventories (PSIs) of sectors: (a) vegetation fires, (b) industry (including flaring), (c) flaring, and (d) population, referenced in FLEXPART air mass history analyses (see Sects. 4.2 and 4.5). Sub-figure (a) shows accumulated fires for 19 June until 21 July 2014; PSI vegetation fire maps that refer to each flight are given in Figs. A.16 and A.17. Red pixels indicate the presence of the respective source in the grid cell.

2.2.7.3 *Anthropogenic sources*

Industrial sources and flaring

The Nightfire product from VIIRS offers quantitative estimates of infrared source emission temperatures by taking advantage of absent solar reflectance in short-wave infrared spectral range during night (Elvidge et al., 2013, 2016). Emission temperatures typically exhibit bimodal distributions by a combination of gas flares dominating the upper mode (peaking in the 1600 - 2000 K range) and other industrial heat sources as well as vegetation fires dominating the lower mode (peaking in the 800 - 1200 K range; Elvidge et al., 2016; Liu et al., 2018). Thus, temperature distributions of vegetation fires and industrial

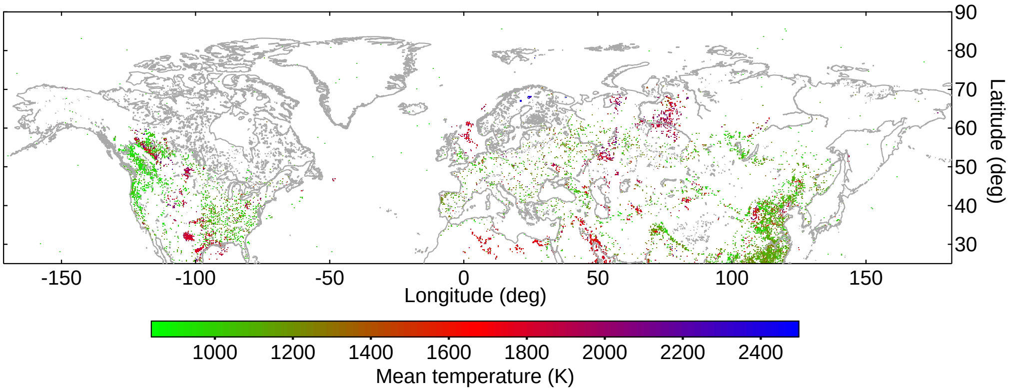

Figure 2.13: Map showing the mean infrared emission temperatures of industrial heat sources for November 2013 until January 2014.

sources can overlap, depending on the industry sector and the vegetation type. However, vegetation fires at mid- to northern latitudes exhibit a clear seasonality with minimum occurrence between November and January (e.g., Giglio et al., 2013). Consequently, this analysis took advantage of both emission temperatures and seasonality to differentiate between the presence of industrial hot spots and vegetation fires (Elvidge et al., 2013; Liu et al., 2018). VIIRS Nightfire data were thus downloaded for November 2013 until January 2014 and for latitudes north of 25 °N (NOAA, 2018a). Data points were projected on the PSI gridded map by averaging temperatures in each grid cell (Fig. 2.13). Industrial hot spots were identified by both pixel mean temperature larger than 840 K[12] as well as one or more observations per grid cell within the respective time, owing to source persistence (Fig. 2.12b).

Gas flares can be clearly detected by VIIRS Nightfire emission temperatures between 1600 K and 2000 K (Fig. 2.13) independent on season (Elvidge et al., 2016). Based on this temperature definition, VIIRS Nightfire provide the so-called *Flares only* product (NOAA, 2018b). Data between 30 March and 13 May 2014[13], were projected on PSI gridded map by adding up observations in each grid cell. Flares were identified by more than one observation per grid cell within the respective time, owing to source persistence (Fig. 2.12c).

Both approaches look reasonable by comparing Figs. 2.12b and c with Fig. 8 in Elvidge et al. (2016) and Fig. 8 in Liu et al. (2018). Oil/gas- and coal-related plants in northwestern Siberia (near Norilsk and Novy Urengoy), northern Eu-

---

[12] 840 K presents the lowest mean temperature for industrial sites, indicative for nonmetal-mineral producing plants (Liu et al., 2018).

[13] Data earlier in 2014 are not available and high latitude data later than May are not valuable due to 24 h solar irradiance.

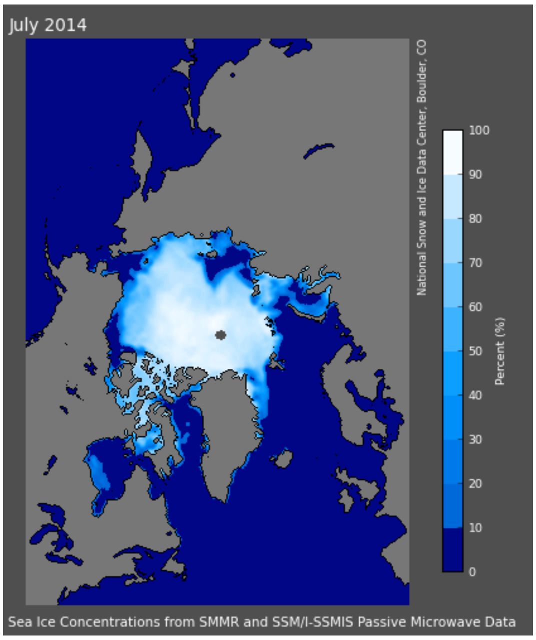

Figure 2.14: Polar stereographic map showing the July 2014 mean sea ice concentration from the National Snow and Ice Data Center (Cavalieri et al., 1996, updated yearly).

rope (North Sea, Norwegian Sea, and Nenets region) and Alaska (Prudhoe Bay) can be clearly identified (Figs. 2.12b and c). However, uncertainties remain by non-continuously operating industrial sources.

Population

Populated areas provide anthropogenic emissions from residential heating, transportation, cooking etc. The criteria for the PSI grid cell to be classified as populated is given by more than 1000 people live in a 0.25° x 0.25° area. Geolocational data on population are provided online (MaxMind, 2018). Densely populated regions in central Europe and coastal North American can be clearly identified, whereas Northern Canada, Alaska, and Siberia present sparsely populated regions (Fig. 2.12d).

2.2.7.4 *Arctic natural marine sources*

Arctic open water sources might have a large impact on aerosol properties in summertime Arctic regions (see Sect. 1.2.6). Sea ice coverage in July 2014 is thus assessed to obtain areas of open water in the Arctic. The Special Sensor Microwave Imager/Sounder (SSMIS) onboard the Defense Meteorological Satellite Program (DMSP) provides data on sea ice coverage, based on brightness temperature (Cavalieri et al., 1996, updated yearly). Data represent the fractional amount of sea ice covering a 25 x 25 km grid cell in a polar stereographic

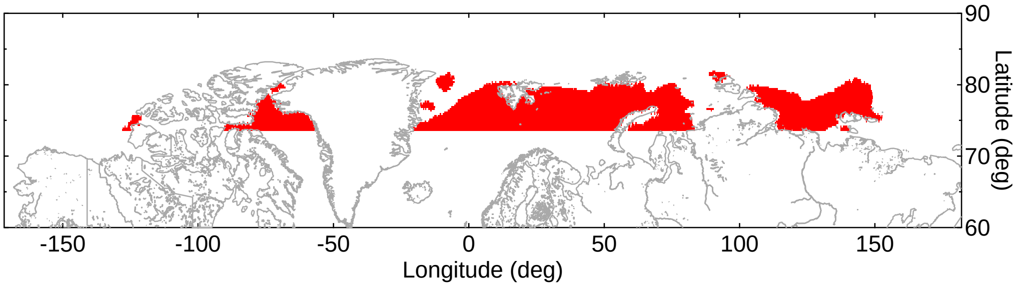

Figure 2.15: Map showing the potential source inventory (PSI) of July 2014 mean Arctic open water areas derived from Fig. 2.14.

projection. Figure 2.14 shows the mean July 2014 sea ice concentration. Polar stereographic coordinates were converted to geodetic latitude and longitude for polar regions (Snyder, 1982)[14]. The obtained data grid was synchronized with PSI gridded map by averaging concentrations in each grid cell. Arctic open water is defined by both sea ice concentrations less than 30 % and latitudes north of 73.5° N (see Sect. 2.2.7.1 and Fig. 2.15).

---

[14] Source code was taken from ftp://sidads.colorado.edu/pub/DATASETS/seaice/polar-stereo/tools/mapxy.for.

3

SINGLE PARTICLE CHEMICAL COMPOSITION - DATA ANALYSIS

The ALABAMA provides a multitude of single particle spectra during field and laboratory experiments. This section introduces the step-by-step data analysis, conducted in this study to obtain results on aerosol particle composition measured by the ALABAMA during the Arctic field experiment (see Ch. 4). The content of this chapter is partly adapted from Köllner et al. (2017).

3.1 PARTICLE CLASSIFICATION - ION MARKER METHOD

The software package Concise Retrieval of Information from Single Particles (CRISP)[1] is a comprehensive tool to process and analyze single particle mass spectra (Klimach, 2012). Raw spectra that provide signal intensities in mV as a function of ion flight time (t_{ToF}) are processed using CRISP by the following steps. First, by using CRISP-integrated wavelet transformation, CRISP performs the ion mass to charge ratio (m/z) calibration based on the proportionality of t_{ToF} to $\sqrt{m/z}$ (Klimach, 2012):

$$t_{\mathrm{ToF}} = a + b \cdot \sqrt{\frac{m}{z}}, \tag{12}$$

with calibration coefficients a and b, with b is being defined as follows:

$$b = \frac{1}{\sqrt{2 \cdot e}} \cdot \int \frac{1}{\sqrt{U(s_{\mathrm{ToF}})}} \cdot ds_{\mathrm{ToF}} \tag{13}$$

with ion flight path (s_{ToF}), elementary charge (e), and mass spectrometer high voltages (U). The calibration coefficient a considers the shot-to-shot variability of ion formation starting conditions (Brands et al., 2011; Klimach, 2012). Second, the area below the ion signal is determined by integrating the raw signal in mV over time, providing the so-called particle stick spectra with the ion peak area in mV·sample[2] (Klimach, 2012). Followed by this initial processing of raw spectra, single particle stick spectra are classified into various particle types.

Particle classification describes the assignment of each analyzed particle to

---

[1] CRISP was programmed in Igor Pro. (version 6.37; WaveMetrics, 2015).

[2] The oscilloscope sampling interval is set to 2 ns.

one out of a set particle types or groups. Typically tens to hundreds of thousands of single particle spectra are analyzed by the ALABAMA during field experiments. In turn, each particle spectrum can contain up to several dozen peaks of both negative and positive ions. To analyze and interpret this multidimensional data set, it is thus necessary to find an appropriate method to classify particles into a relatively small number of groups.

Several methods had been introduced in recent years to classify single particle mass spectra (e.g., Song et al., 1999; Hinz et al., 1999; Murphy et al., 2003; Gross et al., 2010; Klimach, 2012; Reitz et al., 2016; Sultana et al., 2017a; Christopoulos et al., 2018). However, automated clustering, based on fuzzy c-means algorithm (Bezdek et al., 1984; Hinz et al., 1999), has been primarily used for the ALABAMA data analysis (e.g., Roth et al., 2016; Schmidt et al., 2017) and is briefly described as follows. Single particle mass spectra are assigned to the nearest/similar cluster, using so-called distance functions based on, for example, Euclidean metric or Pearson correlation. The ion peak area values of the particle stick spectrum are then used to calculate the distance. Thus, the assignment of single particle spectra to particle clusters is influenced by dominant ion peaks, even though they do not necessarily reflect atmospheric composition, due to matrix effects and composition-dependent ionization efficiencies (see Sect. 2.1.1). Particles containing also smaller peaks are sorted into clusters that are derived from dominant ion peaks. Pre-scaling of the ion peak area by taking the square root can reduce relative differences (Rebotier and Prather, 2007), however, not to the extent that differences by ionization efficiencies etc. are fully compensated. Therefore, the so-called ion marker method is used in this study.

The ion marker method classifies particles based on the presence of pre-selected species that are of interest. This approach is not dependent on the absolute value of the ion peak areas within one spectrum, but only on the presence of a certain ion peak area above a defined threshold value. To the author's knowledge, the ion marker method was first introduced by Tolocka et al. (2004), later implemented in CRISP (Klimach, 2012), and partly applied for the ALABAMA particle classification in Roth et al. (2016). In principal, four analysis steps are required. First, a pre-selection of chemical compounds that are of interest for the study is necessary. In this study, prior fuzzy c-means clustering provided a brief overview of ions that were detected on average in Arctic summertime aerosol particles (not shown). In parallel, literature was reviewed based on the current knowledge and gaps of summertime Arctic aerosol (see Sect. 1.2). Second, ion markers of laboratory-generated particles of known composition are compared to ions from ambient particles analyzed during the field experiment

Table 2: Particle classification by marker species and associated ion markers applied in this study. References from SPMS laboratory and field studies are indicated by numbers that are defined below. The semicolon can be understood as the logical "and". This table is partly adapted from Köllner et al. (2017).

Marker species (abbreviation)	Ion markers	References (lab/field)	Comments
Trimethylamine (TMA)	m/z +59 ($(CH_3)_3N^+$); +58 ($C_3H_8N^+$)	1,2/3,4,5	
Sodium and/or chloride and/or nitrate (Na / Cl / Nitrate)	m/z +23 (Na^+); (at least two of the following ions) +46 (Na_2^+), +62 (Na_2O^+), +63 (Na_2OH^+); (at least one of the following isotopic patterns/ions) +81/83 (Na_2Cl^+), -35/37 (Cl^-), -93/95 ($NaCl_2^-$), -46 (NO_2^-), -62 (NO_3^-)	6,7,8/9,3	Isobaric interference with MSA at m/z -95
Elemental carbon (EC)	(at least six of the following ions) m/z +36, +48, ..., +144 (C_{3-12}^+) and/or (at least six of the following ions) m/z -36, -48, ..., -144 (C_{3-12}^-)	7,8/3,10	Except m/z -96 due to isobaric interference with SO_4^-
Ammonium (NH_4)	m/z +18 (NH_4^+)	10/3,7	
Sulfate (SO_4)	(at least one of the following ions) m/z -97 (HSO_4^-), -96 (SO_4^-)	10,2/3,7	

Continued on next page.

(see Sect. 3.1.1). Third, a threshold for the ion peak area needs to be determined to distinguish the ion signal from background noise (see Sect. 3.1.2). Finally, internal and external mixtures of several chemical compounds are identified by presenting particle types in the so-called decision tree (see Fig. 3.1.3).

3.1.1 *Ion markers*

Ambient particle mass spectra are interpreted based on comparison with spectra of laboratory-generated particles of known composition that have been accomplished under similar experimental conditions. In detail, mass spectra characteristics (i.e., ion markers) depend on operating condition of the abla-

Table 2: Continued.

Marker species (abbreviation)	Ion markers	References (lab/field)	Comments
Potassium (K)	m/z +39/41 (K^+)	7,2/3,10,11,12	isobaric interference with $C_3H_3^+$ at m/z +39 possible
Methanesulfonic acid (MSA)	m/z -95 ($CH_3O_3S^-$)	13/14	isobaric interference with PO_4^- excluded by absent PO_3^- at m/z -79
Low-molecular weight dicarboxylic acids (DCA)	(at least one of the following ions) m/z -89 ($C_2HO_4^-$), m/z -103 ($C_3H_3O_4^-$), m/z -117 ($C_4H_5O_4^-$)	13/15,16,17	representative: oxalic acid malonic acid succinic acid
Nitrate (NO_3)	(at least one of the following ions) m/z -46 (NO_2^-), -62 (NO_3^-)	10,13/3,7	

Given reference numbers are defined as follows: (1)Angelino et al. (2001),(2)this study in Sects. 3.1.1.1 and 3.1.1.2,(3)Roth et al. (2016),(4)Healy et al. (2015),(5)Rehbein et al. (2011),(6)Prather et al. (2013),(7)Schmidt et al. (2017),(8)Brands (2009),(9)Sierau et al. (2014),(10)Brands et al. (2011),(11)Hudson et al. (2004),(12)Pratt et al. (2011),(13)Silva and Prather (2000),(14)Gaston et al. (2010),(15)Lee et al. (2003),(16)Sullivan and Prather (2007),(17)Yang et al. (2009).

tion laser in the ionization region (i.e., wavelength, intensity, and beam homogeneity), in particular for organic compounds (e.g., Thomson et al., 1997; Suess and Prather, 1999; Silva and Prather, 2000; Angelino et al., 2001; Roth, 2009; Brands, 2009). For this study, ion markers were chosen based on laboratory studies by both the ALABAMA and other single particle mass spectrometers (SPMSs) using 266 nm laser wavelength (Table 2). Averaged laser intensities vary with studies between 10^8 W cm^{-2} and $3{\cdot}10^9$ W cm^{-2} (see Table 7 in Sect. B.1). However, the actual intensity that the particle is exposed to can still vary shot-by-shot, due to particle beam divergence combined with the Gaussian laser beam profile as well as laser beam inhomogeneities (e.g., Silva and Prather, 2000; Wenzel and Prather, 2004; Brands et al., 2011). Thus, uncertainties for mass spectral interpretation remain by varying laser intensities. At least, none of the studies operated the laser at intensities $> 10^{10}$ W cm^{-2}, at which molecules likely fragment to atomic ions (Reents and Schabel, 2001; Murphy et al., 2007).

The label of marker species is given by the known particle composition from laboratory-generated samples, rather than by the associated particle source (Table 2). Particle spectra showing carbon cluster ions are labeled as elemental carbon (EC). Essentially, the term EC refers to high-temperature residue, as measured by thermographic methods (e.g., Prather, 2012; Seinfeld and Pandis, 2016). Nonetheless, the term EC is widely used in the SPMS community for particles containing carbon cluster ions by linking the chemical structure to mass spectra analysis technique (e.g., Spencer et al., 2008; Prather, 2012; Corbin et al., 2012). In some cases, other terminology such as BC and soot can be found (e.g., Moffet and Prather, 2009; Roth et al., 2016; Schmidt et al., 2017). However, EC is preferred in this study by the following reasons. First, particle measurements by laser ablation/ionization do not provide optical properties of the particle, as it used to measure BC (Petzold et al., 2013; Bond et al., 2013). Second, soot is considered as being an internal mixture of elemental carbon, organic matter, and small amounts of other elements (e.g., Seinfeld and Pandis, 2016).

Particle spectra showing oxalic acid, malonic acid, and/or succinic acid are labeled as dicarboxylic acids (DCA). Silva and Prather (2000) reported the presence of deprotonated negative parent ions in mass spectra of organic acids (here, m/z -89, -103, and -117). Other organic acids of interest for Arctic aerosol composition, such as maleic acid, fumaric acid, or phthalic acid (Kawamura and Bikkina, 2016), were not significantly abundant in ambient particle spectra detected during the Arctic field experiment.

The following sections provide laboratory-generated particle mass spectra of trimethylamine, levoglucosan, and potassium sulfate by the ALABAMA to verify ion markers by other SPMS studies using 266 nm laser wavelength.

3.1.1.1 *Trimethylamine*

Particulate amines are of interest for this study due to the sparse knowledge of their sources and atmospheric abundance in Arctic regions (see Sect. 1.2.6). Prior fuzzy c-means clustering of the Arctic data set (not shown) indicated the presence of trimethylamine (TMA) by ion peaks at m/z +59 and +58 (Angelino et al., 2001). Besides TMA, other alkylamines and amino acids were not significantly abundant in Arctic ambient single particle spectra and/or could not be identified by isobaric interferences with other substances (see Sect. B.2). Potential reasons for this are discussed in Sect. 4.7. However, ion markers of

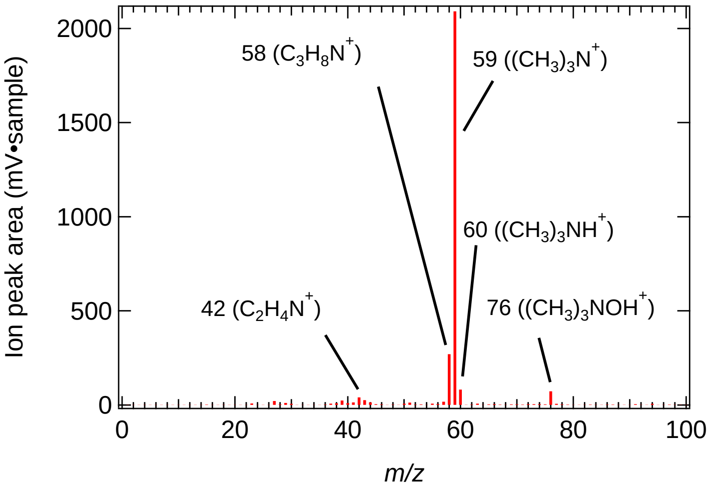

Figure 3.1: Trimethylamine (TMA) mean cation spectrum of 88 single particle spectra analyzed by the ALABAMA.

TMA measured by Angelino et al. (2001) were verified by ALABAMA laboratory measurements as follows.

A mixture of TMA dissolved in water and sulfuric acid was nebulized with an aerosol generation system. The resulting droplets passed through a diffusion dryer filled with silica gel to remove water. The particles further passed through a differential mobility analyzer (DMA) with the classifier set at the appropriate voltage to extract 300 nm particle size and were then guided into the ALABAMA. The ablation laser intensity was smaller for the TMA laboratory measurements ($\sim 5{\cdot}10^8\,\mathrm{W\,cm^{-2}}$) than for the Arctic field measurements ($\sim 2{\cdot}10^9\,\mathrm{W\,cm^{-2}}$) by degeneration of the laser optics (see Sect. B.1).

The mean mass spectrum in Fig. 3.1 is characterized by ion peaks at m/z +59 ($(CH_3)_3N^+$; molecular ion of TMA) and m/z +58 ($C_3H_8N^+$). This result confirms laboratory measurements by Angelino et al. (2001). Ion peaks at m/z +60 ($(CH_3)_3NH^+$) and m/z +76 ($(CH_3)_3NOH^+$) can be explained by protonation and oxidation of TMA, respectively (Angelino et al., 2001). The characteristic ion peaks of TMA (m/z +59 and m/z -58) were present in Arctic single particle mass spectra, despite the higher laser intensity during the Arctic field experiments compared to the TMA laboratory study.

3.1.1.2 *Levoglucosan and Potassium Sulfate*

Levoglucosan (or 1,6-anhydro-beta-glucopyranose; $C_6H_{10}O_5$) is a key organic tracer for vegetation fires (see Sect. 1.2.4). However, there is no consensus in SPMS literature about ion markers of levoglucosan. The averaged laboratory

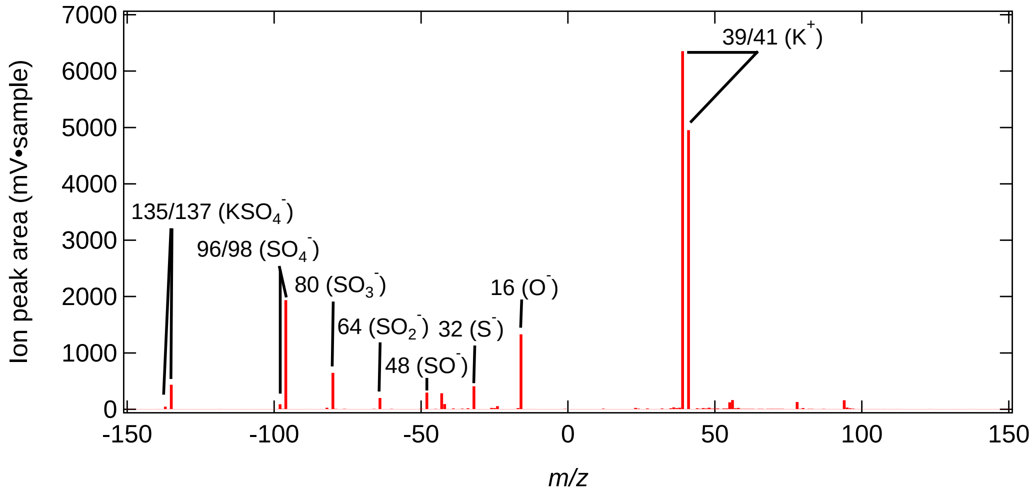

Figure 3.2: Potassium sulfate (KSO_4) mean bipolar spectrum of 69 single particle spectra analyzed by the ALABAMA. The isotopic ratio of potassium at m/z +41 and m/z +39 is too high, likely caused by saturation effects of the MCP.

mass spectrum by Silva et al. (1999) shows ion peaks at m/z -45, -59 and -71, while others also used m/z -73 to identify levoglucosan in ambient mass spectra (Moffet et al., 2008; Corbin et al., 2012). Consequently, ALABAMA laboratory measurements were conducted to identify mass spectra characteristics of levoglucosan.

Levoglucosan is poorly absorbing at 266 nm laser wavelength as found in this laboratory study. Therefore, the better absorbing material KSO_4 was mixed with levoglucosan. Both substances were suspended in purified water and nebulized with an aerosol generation system. Diffusion dryers filled with silica gel removed water from the particles and the resulting particles were introduced into the ALABAMA. Analogous to levoglucosan mixed with KSO_4, KSO_4 was separately analyzed to differentiate ion peaks originating from levoglucosan and KSO_4.

The mean mass spectrum of KSO_4 is characterized by molecular ion peaks at m/z -135/137 (Fig. 3.2). It further shows potassium peaks at m/z +39/41 as well as several fragments that contain sulfur and/or oxygen (m/z -96/98, -80, -64, -48, -21, and -16). In parallel, the mean mass spectrum of levoglucosan is obtained by subtracting the mean spectrum of KSO_4 from levoglucosan mixed with KSO_4 (Fig. 3.3). As a result, levoglucosan is characterized by fragments at m/z -71, -59, -45, confirming laboratory measurements by Silva et al. (1999). Additional fragments at m/z -58, -41, and -25 have been also reported by Silva et al. (1999), albeit not dominant in their study. However, in contrast to what was previously assumed (Köllner et al., 2017), these mass spectral characteris-

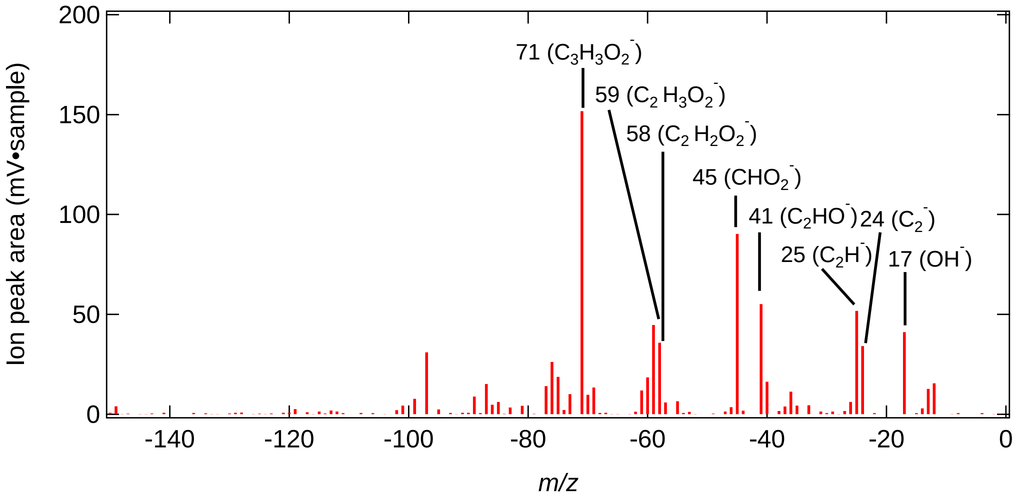

Figure 3.3: Mean anion spectrum of levoglucosan, obtained as the difference between the mean spectrum of levoglucosan with KSO_4 (average of 754 single particle spectra analyzed by the ALABAMA) and the pure KSO_4 mean spectrum (see Fig. 3.2).

tics are not unique for levoglucosan, by isobaric interferences with fragments of other oxygen-containing organic compounds (Table 3). It is thus difficult to clearly identify levoglucosan in ambient particle mass spectra. Due to those difficulties, levoglucosan is separately discussed in Ch. 4 and not added in Table 2.

3.1.2 *Ion peak area thresholds*

The ion peak area threshold is assessed to distinguish ion signals from background noise. The following criteria were used to determine this value. All ambient single mass spectra collected by the ALABAMA during the Arctic field experiment were used (Table 10 in Sect. C.3). Further, it was assumed that certain m/z values are not occupied by ions from ambient particles by laser ablation/ionization, such as m/z 2 - 11 and m/z 245 - 250 for both polarities. Finally, the threshold is defined at the 99 % - 100 % cumulative probability of ion peak areas of the non-occupied m/z values (Fig. 3.4). Together, the thresholds for positive and negative polarity are 10 mV·sample and 25 mV·sample, respectively.

Definitions of the threshold vary with literature (e.g., Tolocka et al., 2004; Moffet et al., 2008; Yao et al., 2011; Furutani et al., 2011; Roth et al., 2016). Exemplary, Tolocka et al. (2004) defined the threshold as having a signal-to-noise ratio of 4 above the average baseline level. Similar, Moffet et al. (2008)

Table 3: Organic compounds showing isobaric interferences with fragments of levoglucosan.

Compounds	Ion markers	References
Acetic acid	m/z-59	Brands et al. (2011)
Methylglyoxal	m/z-71,	Zauscher et al. (2013)*
	m/z-59	Zauscher et al. (2013)*
Acrylate	m/z-71	Zauscher et al. (2013)*
Polycyclic aromatic hydrocarbons	m/z-25	Silva and Prather (2000)
Polycyclic aromatic hydrocarbons	m/z-41	Silva and Prather (2000)
-cont. alkohol functional groups	m/z-41	Silva and Prather (2000)

*Zauscher et al. (2013, Supplement) further reported that most oxygen-containing organic standards show small ion peaks at m/z-45 and m/z-59.

set the threshold as being two times the detection threshold. Both studies did not report on the determination of the baseline and detection threshold. From the author's point of view, it is possible to derive a baseline by recording so-called empty mass spectra, provided when the ablation laser shoots with a fixed frequency and thus, does not trigger on particles. However, those empty mass spectra were not recorded during the Arctic field experiment[3]. Therefore, in this study, the non-occupied m/z values were used to determine the threshold. For comparison reasons, the thresholds 10 mV·sample and 25 mV·sample correspond to five to six times the standard deviation above the averaged ion peak areas of the non-occupied m/z values.

3.1.3 *Aerosol internal and external mixing state*

Particle classification proceeds further by creating decision tree(s) to identify internal and external aerosol particle mixtures. Chemical composition of a single aerosol particle is typically a complex interplay of signatures from both the particle source and atmospheric aging to the time of detection (see Sect. 1.2.2). Figure 3.5a schematically illustrates the internal and external mixing of substances, whereby Fig. 3.5b provides the associated decision tree.

The decision tree is structured as follows: upper/lower branches refer to pos-

---

[3] The author took note on this procedure for subsequent ALABAMA field measurements.

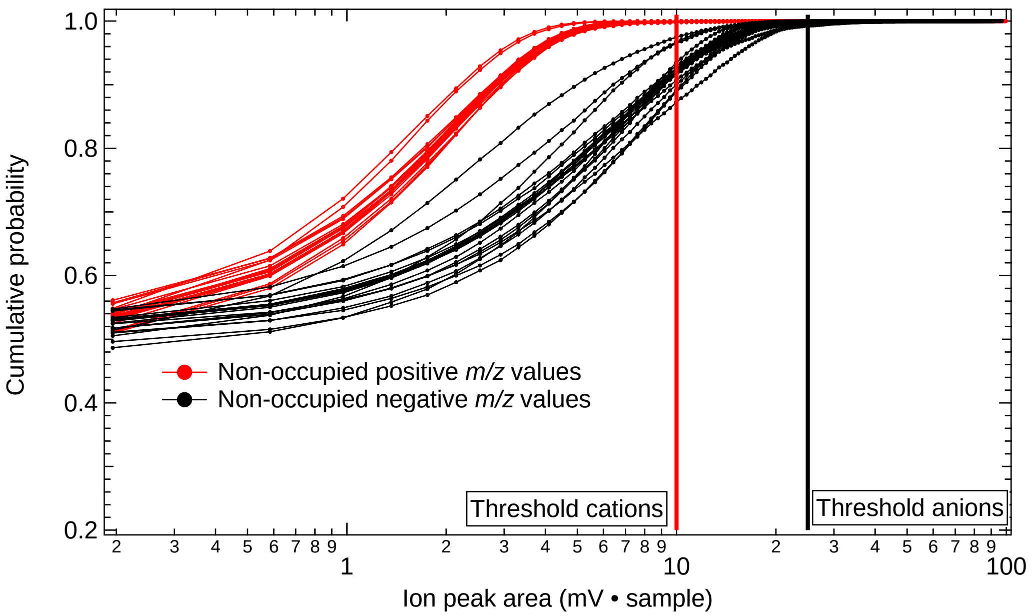

Figure 3.4: Cumulative probability distributions of the positive (red lines) and negative (black lines) ion peak areas at m/z 2 - 11 and m/z 245 - 250 (assumed non-occupied m/z values). The vertical lines depict the 99 % - 100 % thresholds.

itive/negative response for whether ion markers of the respective substance (here, indicated by colors and letters A to D) are above/below the ion peak area threshold. The label of the internally-mixed particle types is intentionally chosen according to ion markers that are present in the particle spectra (Fig. 3.5b). The absence of marker species in single particle spectra does not necessarily reflect particle composition, owing to composition-dependent ionization efficiencies, particle structural heterogeneity etc. (see Sect. 2.1.1). Exemplary for the labeling, substance A is partly internally mixed with substances B and C (Fig. 3.5a), providing the “A,B,C”-containing particle type (Fig. 3.5b). Further, substance D is externally mixed from other substances (Fig. 3.5a), providing the “D”-containing particle type (Fig. 3.5b).

3.2 SCALING THE ALABAMA PARTICLE FRACTION

Followed by the particle classification, the fraction of the ALABAMA particle types is calculated (Fig. 3.6a). Conceptually for the particle fraction, the counts of both all collected particles and particles of the specific type are binned into bins of simultaneously measured variables, such as altitude or CO mixing ratio (see horizontal axis in Fig. 3.6). Bin widths are chosen to guarantee an acceptable level of both statistical significance and resolution. For each bin, these counts are summed and divided by each other, providing the number fraction

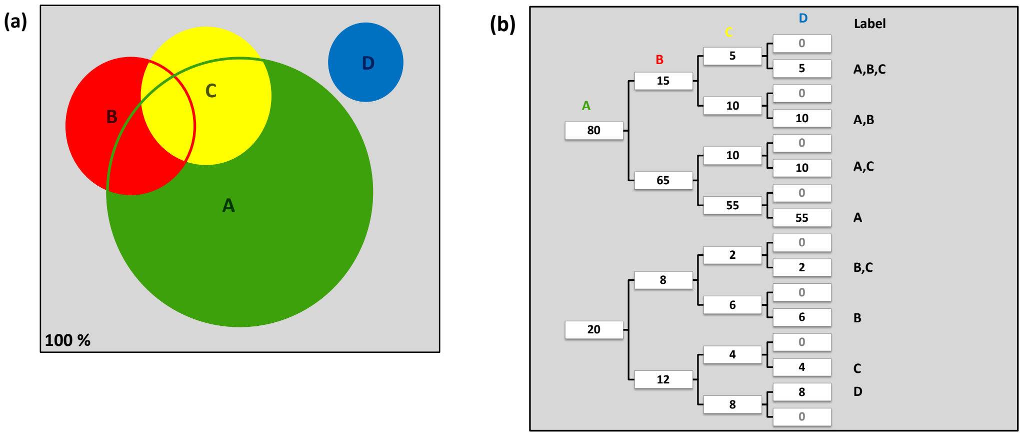

Figure 3.5: Schemes illustrating the external and internal particle mixing of different substances (A to D). (a) Diagram representing the relationship between different substances in individual particles. Different colors and associated letters present different substances. Circle areas are proportional to the number of particles including the substances. Overlapping of circles indicates internal mixing. The overall area is scaled to the overall number of particles (100 %). (b) Decision tree quantitatively (in percentage) presenting the associated diagram in (a). Upper/lower branches refer to the presence/absence of substances in particle mass spectra. The labels of the internally-mixed particle types are given on the right.

of the specific particle type (PF; see Fig. 3.6a). In some instances, there were not enough spectra in one bin. Thus, bins containing less than 20 spectra in total were excluded from the analysis. Together, the ALABAMA particle fraction (PF) refers to the relative contribution of the particle type with respect to all collected particles in comparison with simultaneously measured variables.

Further, the particle fraction is scaled to number concentrations, using measurements of a co-located quantitative reference instrument, hereafter the UHSAS onboard the Polar 6 (see Sect. 2.2.2). The UHSAS number concentration in a size range between 320 nm and 870 nm ($N_{>320}$; Fig. 3.6b) is used. Conceptually, scaled number concentrations of ALABAMA particle types are determined by multiplying the particle fraction with the averaged UHSAS number concentration in each bin ($PF \cdot N_{>320}$; Fig. 3.6c). The conversion of unscaled ALABAMA measurements into quantitative particle number concentrations allows to assign particle types to different sources (Sullivan and Prather, 2005). To note, quantitative number concentrations cannot be provided by the ALABAMA alone, mainly caused by the pressure-dependent CPI transmission efficiency (see Sect. 2.1.2) and lens alignment issues. The latter issue was caused by the bipod lens holding that was susceptible to vibrations (see Table 6 in Sect. A.3 and Sect. 2.1.4).

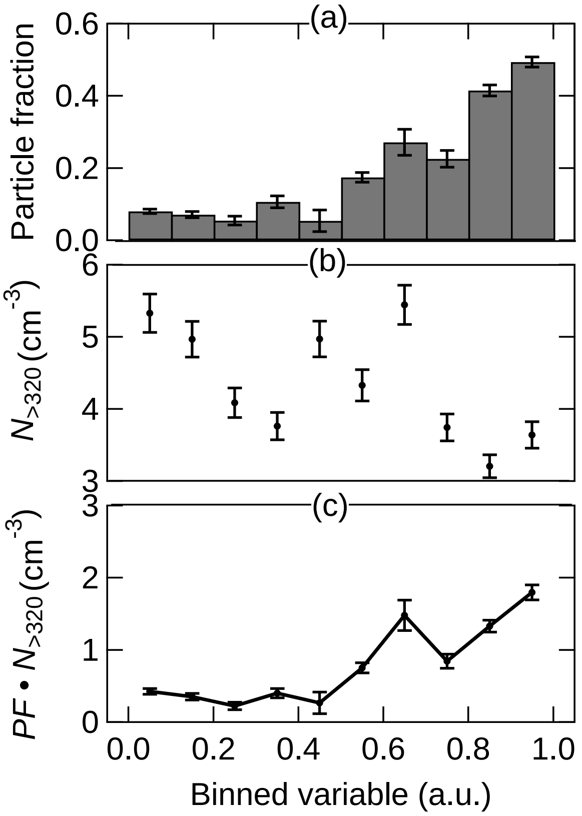

Figure 3.6: Example for the three-step scaling procedure. Variables that are simultaneously measured (such as altitude or CO mixing ratio) are binned and compared with (a) the ALABAMA number fraction of the specific particle type (PF), (b) the averaged UHSAS number concentration in a size range between 320 nm and 870 nm ($N_{>320}$), and (c) the scaled ALABAMA number concentration ($PF \cdot N_{>320}$).

This scaling procedure is similarly used in numerous SPMS field studies (e.g., Allen et al., 2000; Wenzel et al., 2003; Sodeman et al., 2005; Qin et al., 2006; Ault et al., 2009; Qin et al., 2012; Healy et al., 2012, 2013; Gunsch et al., 2018). Taking this number-based scaling method, some studies further calculated particle mass concentrations by assuming sphericity as well as by using averaged particle density and the measured particle size (e.g., Allen et al., 2000; Ault et al., 2009; Qin et al., 2012; Healy et al., 2012, 2013; Gunsch et al., 2018). The conversion determines the mass concentration of specific particle types, rather than of chemical species. There are several further mass quantification approaches for SPMS analyses introduced in recent years (e.g., Bhave et al., 2002; Qin et al., 2006; Shen et al., 2019). However, this study will not convert number to mass concentrations by reasons introduced in Sect. 2.1.1, such as matrix effects and incomplete particle ablation/ionization.

The scaling method assumes that the ALABAMA transmits, detects, and ablates/ionizes all particles with the same efficiency, namely the collection efficiency (CE). This assumption may introduce errors in the scaled number concentrations, as the detection efficiency (DE) and hit rate (HR) are observed to be dependent on several factors. The DE is size-dependent as explained in Sect. 2.1.3. However, a size-dependent scaling factor was not used in this study, owing to the low particle counting statistics per bin. As a result, the scaling method may lead to errors when determining the concentration of particles smaller than approximately 400 nm. Likewise, the HR is dependent on various particle characteristics, such as size, composition, and shape (see Sect. 2.1.4; Thomson et al., 1997; Kane et al., 2001; Moffet and Prather, 2009; Brands et al., 2011), caused by the laser ablation/ionization technique itself (i.e., actual laser intensity, particle beam divergence, ionization efficiencies etc.). The hit rate can thus vary during ambient measurements, which may cause a problem when interpreting the fraction of particle types as a function of simultaneously measured variables. Further details on the hit rate variability during the Arctic field experiment in July 2014 are given in Sect. B.3.

4

AEROSOL PARTICLE COMPOSITION IN THE SUMMERTIME ARCTIC

Parts of this chapter are based on the following publication: Köllner et al. (2017).

4.1 AIRBORNE ARCTIC FIELD EXPERIMENT NETCARE 2014

Motivated by the limited knowledge of summertime Arctic aerosol processes, an aircraft campaign took place from Resolute Bay, Nunavut (Canada) from 4 - 21 July 2014. The aircraft campaign named NETCARE 2014 was part of the "Network on Climate and Aerosols: Addressing Key Uncertainties in Remote Canadian Environments" (NETCARE) project. Resolute Bay is located at 74.71° N and 94.97° W, thus, within the influence region of the July 2014 polar dome, according to Bozem et al. (2019). Resolute Bay faces the Northwest Passage with the Lancaster Sound near Baffin Bay and Nares Strait (Fig. 4.1). The community includes approximately 200 residents as well as a number of researchers facilitated by the Polar Continental Shelf Program.

Eleven flights were conducted from Resolute Bay with the Polar 6 aircraft between 4 and 21 July 2014 (Fig. 4.2). As a result, the total sampling time was about 44 hours of which roughly half of the time has been spent each in the boundary layer (BL) and the free troposphere (FT). The analysis on boundary layer height is provided in Sect. 4.2. Flight tracks covered altitudes typically up to 3.5 km, while the flight on 8 July reached altitudes up to 6 km. The earliest and latest take-off and landing time was 15 UTC and 23 UTC[1], respectively, with the consequence that flights were performed only during daytime.

The measurements took place largely over remote areas characterized by open water (Lancaster Sound and polynyas north of Resolute Bay), sea ice, and Arctic vegetation (Fig. 4.2). The sharp transition between open water and sea ice was situated approximately 150 km south-east of Resolute Bay. The ice/water coverage in Fig. 4.2 was representative for the area from 4 to 12 July. The ice edge became less sharp with more fractured ice, along with higher wind speeds after 12 July.

---

[1] UTC minus 5 hours corresponds to local time.

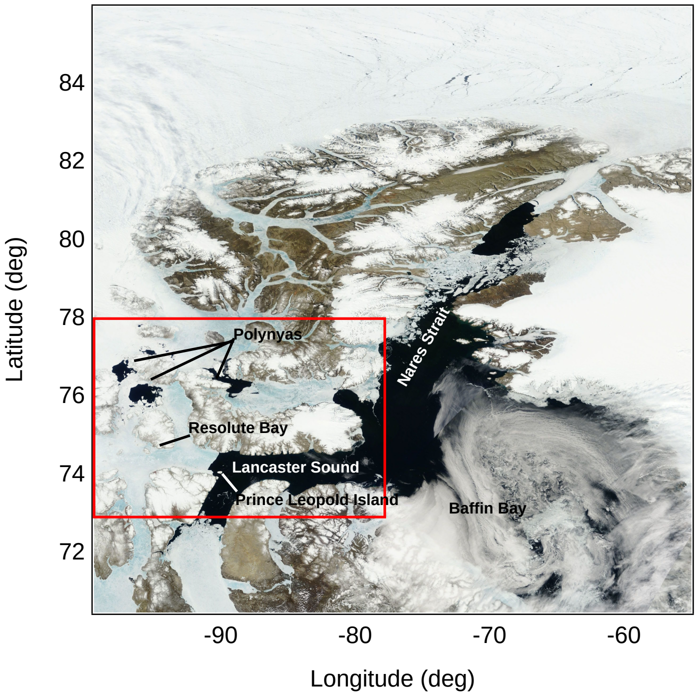

Figure 4.1: Satellite image (visible range from MODIS) from 4 July 2014 showing sea ice and open water conditions around Resolute Bay, in Lancaster Sound, Nares Strait, and Baffin Bay. The red box indicates the region expanded with flight tracks in Fig. 4.2. The satellite image is courtesy of NASA Worldview: https://worldview.earthdata.nasa.gov. The figure is adapted from Köllner et al. (2017).

Local anthropogenic pollution might have effected the measurements, but is primarily related to the sparse Arctic settlements with domestic activities, traffic, landfill and waste burning as well as local airports, and electric power generators (Aliabadi et al., 2015). The nearest neighboring communities are Arctic Bay and Grise Fjord with approximately 360 km distance to Resolute Bay. Further, the Canadian research vessel *Amundsen* reached the measurement region on 17 July. This was part of a coordinated ship-based measurement campaign within the NETCARE project (e.g., Abbatt et al., 2019). Parts of the flights from 19 to 21 July aimed to measure those shipping emissions (Aliabadi et al., 2016a). However, the ALABAMA was not successfully measuring the composition of particles emitted by the ship for two reasons. First, freshly emitted ship particles are typically smaller than the ALABAMA detectable size range. Second, sampling times within the fresh ship emissions were too short (some seconds) to obtain an acceptable level of particle counting statistics with the ALABAMA. Summarizing, the remoteness of the Resolute Bay region ideally allowed to study the pristine summertime Arctic atmosphere with access to open water regions.

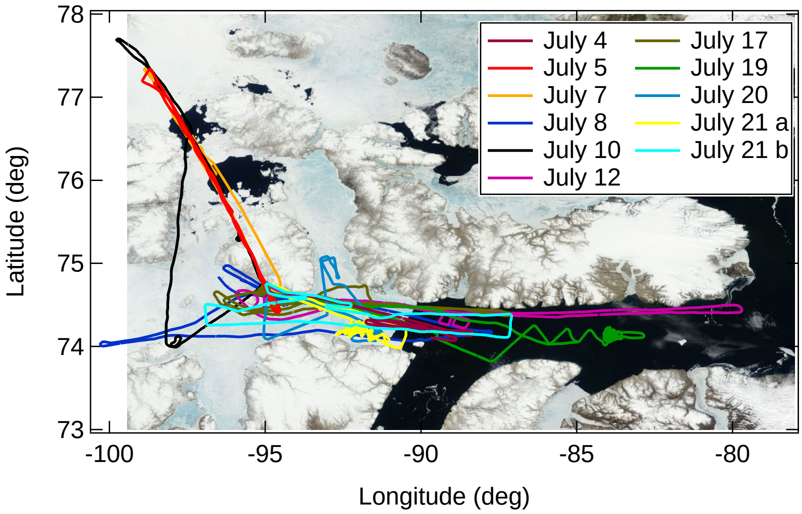

Figure 4.2: Satellite image (visible range from MODIS) from 4 July 2014 with a compilation of flight tracks conducted during 4 - 21 July 2014 (indicated with different colors). On July 21, two flights were performed indicated by a and b. The figure is adapted from Köllner et al. (2017).

This chapter will discuss the ALABAMA single particle composition measurements obtained during NETCARE 2014, to address the questions stated in Sect. 1.3. To note, the NETCARE program includes a suite of extensive Arctic field operations (i.e., ground-based, airborne, and ship-based) as well as Arctic aerosol and climate modeling activities. A detailed summary of the NETCARE results is given in Abbatt et al. (2019) and available online in the joint special issue of the journals Atmospheric Chemistry and Physics (ACP), Atmospheric Measurement Techniques (AMT), and Biogeoscience (BG): http://www.atmos-chem-phys.net/special_issue835.html.

4.2 METEOROLOGICAL OVERVIEW AND AIR MASS HISTORY

Meteorological conditions combined with air mass history play a major role when understanding Arctic aerosol composition influenced by local as well as distant sources and transport. The conditions changed over the course of the NETCARE 2014 campaign (compare Figs. 4.3a and b). As a result, the measurements were separated into two distinct regimes, according to the prevailing weather conditions and hence air mass history: the Arctic air mass period and the southern air mass period (Burkart et al., 2017).

In the following sections, meteorological conditions combined with particle and trace gas properties are illustrated with median and percentile values as

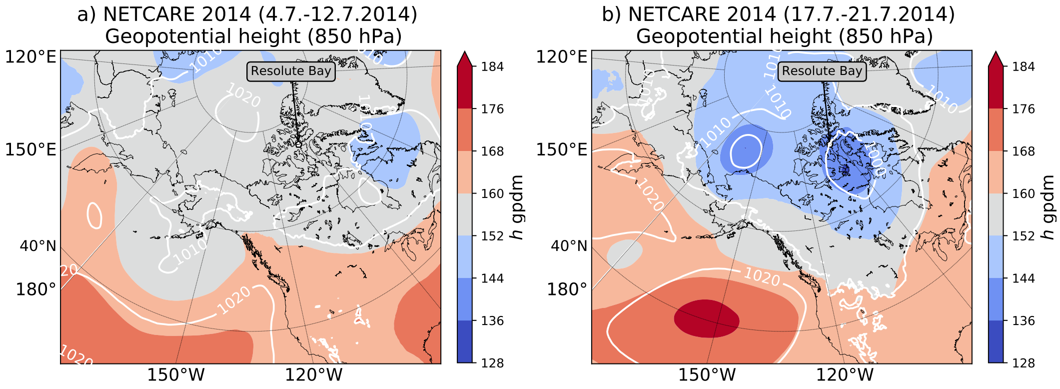

Figure 4.3: Mean geopotential height at 850 hPa indicated by colors in geopotential dekameter (gpdm) and sea level pressure represented by the white contour lines during (a) the Arctic and (b) the southern air mass periods, plotted on a polar stereographic map. The figure is courtesy of Bozem et al. (2019).

a function of sampling altitude (Figs. 4.4 and 4.9). These figures include all data measured during the respective time frame. Air mass history predicted by FLEXPART is summarized in Figs. 4.5, 4.7, 4.10, and 4.11 as a function of sampling altitude. In general for this chapter, contributions of different source regions and sectors are given as a fraction of the potential emission sensitivity within the lowest vertical level (0 - 400 m) of the model domain over a 15-days integrated backward simulation (so-called PES fraction), except for vegetation fires. For fires, the vertical layer between 1 km and 5 km was taken (see Sect. 2.2.7.2). Contributions of the different vertical model levels to sampling altitude are discussed in Sect. C.1.

4.2.1 *Arctic air mass period*

The measurement region was under the influence of a prevailing high-pressure system, leading to fairly constant meteorological conditions during 4 - 12 July (Fig. 4.3a). The period is referred to as Arctic air mass period as air mass history 15 days prior to sampling showed a dominant influence of air masses from within Arctic regions (Burkart et al., 2017).

Meteorological conditions were characterized by generally clear skies with a few low-level stratocumulus clouds (Leaitch et al., 2016), low wind speeds (Fig. 4.4c), and a stable stratified shallow boundary layer (Fig. 4.4a). Inferred from

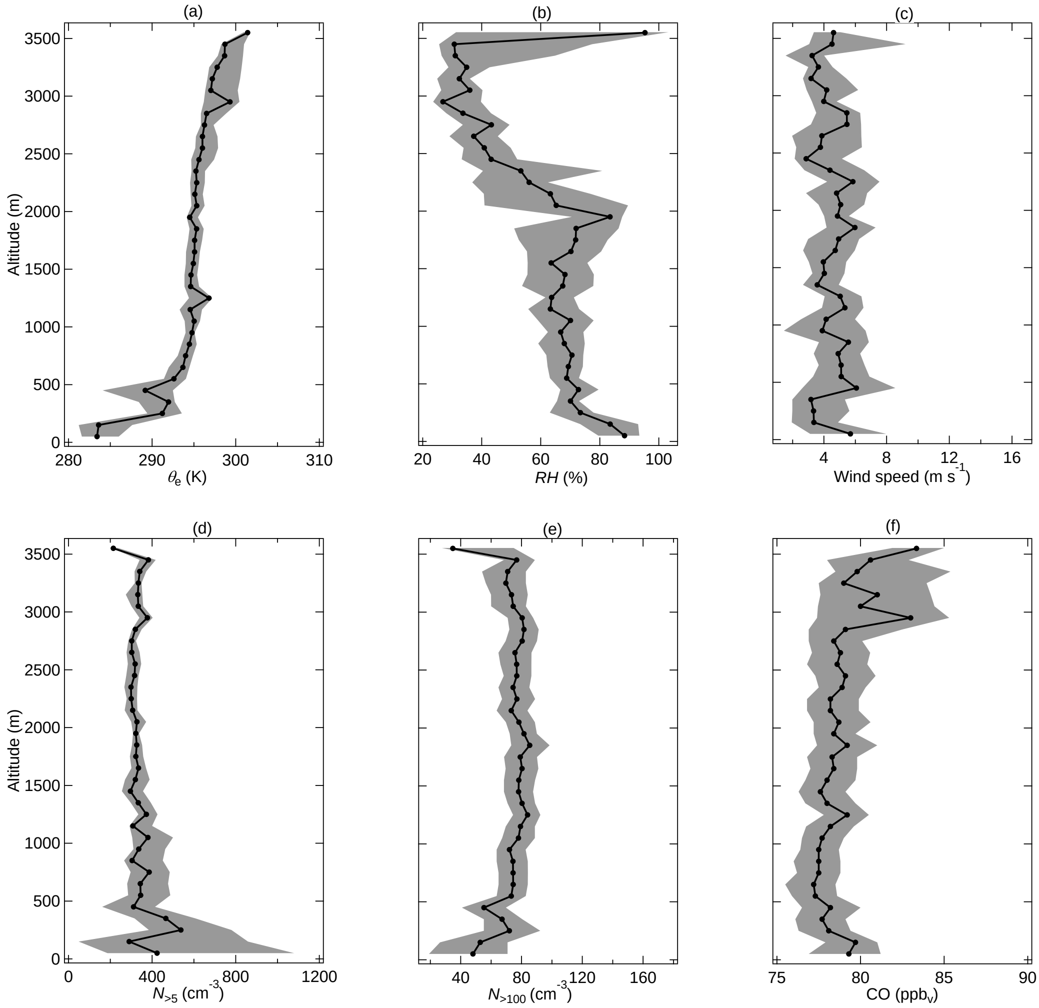

Figure 4.4: Vertically resolved median (black line) and interquartile range (gray shaded area) of pseudoequivalent potential temperature (θ_e), relative humidity (RH), wind speed, number concentrations of particles larger than 5 nm ($N_{>5}$) and larger than 100 nm ($N_{>100}$), and CO mixing ratio during the first period (see Table 1 for uncertainties).

the vertical profile of pseudoequivalent potential temperature $(\theta_e)^2$ in Fig. 4.4a, the local upper boundary layer (BL) height was on average between 250 m and 450 m, including a surface-based temperature inversion (not shown; see Burkart et al., 2017). To note, the free troposphere (FT) is referred to as the portion of the troposphere located above the BL. Aliabadi et al. (2016b) determined similar BL heights using the bulk Richardson number with the goal to analyze mixing and stability within the BL. The strong increase of θ_e with altitude in the BL reveals a stable stratification, which in turn should limit the potential

---

2 The pseudoequivalent potential temperature is conserved in both dry and saturated pseudo-adiabatic processes, and as such important when studying thermodynamic processes in the boundary layer if clouds and thus latent heat release are present (Wallace and Hobbs, 2006). For further details see Sect. C.2.

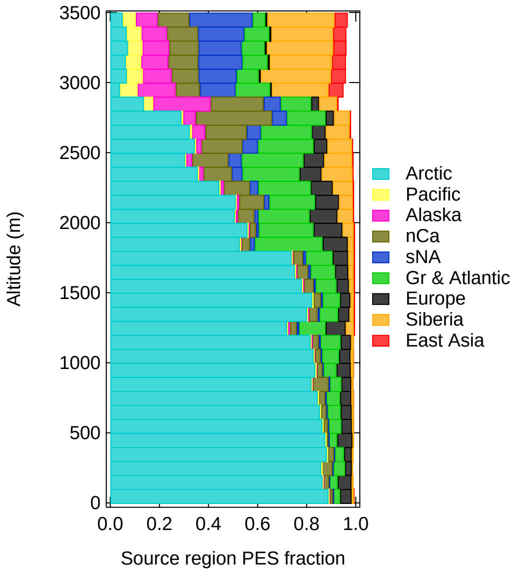

Figure 4.5: Vertically resolved cumulative contribution of source regions to sampling altitude during the Arctic air mass period. Further details on definitions of source regions are given in Sect. 2.2.7. The FLEXPART predicted contribution is expressed as a fraction of the potential emission sensitivity (PES) in the model domain lowest vertical level (0 - 400 m) over a 15-days backward simulation. Acronyms are defined as follows: nCa = northern Canada; sNA = southern North America; Gr = Greenland.

for turbulent mixing and vertical motion (Fig. 4.4a; e.g., Stull, 1997). Along with the stable stratification, the near-surface levels are largely isolated from aloft or at least show a different atmospheric composition (Fig. 4.4b and d-f). In detail, the conditions within the BL were very moist with RH larger than 70 % (Fig. 4.4b), reflecting the vicinity of open water areas and low-level clouds (Fig. 4.1). Within the BL compared to aloft, the total particle number concentration ($N_{>5}$) showed a larger variability with values up to 1100 cm^{-3} (Fig. 4.4d). In contrast, accumulation mode particles ($N_{>100}$) were less abundant in the BL compared to the FT (Fig. 4.4e). These results suggest an enhanced number of ultrafine particles in near-surface levels than aloft. Thus, new particle formation and subsequent growth of particles was promoted by a lowered condensation sink in the the pristine and clean Arctic BL during the Arctic air mass period (Burkart et al., 2017).

Air mass history during the first period reflects the concept of isentropic transport to Arctic regions (see Sect. 1.2.1), by both near-surface regions that are largely isolated from the rest of the atmosphere and regions aloft that are episodically influenced by air originating from southern latitudes (Fig. 4.5). Based on atmospheric distributions of CO and CO_2, Bozem et al. (2019) re-

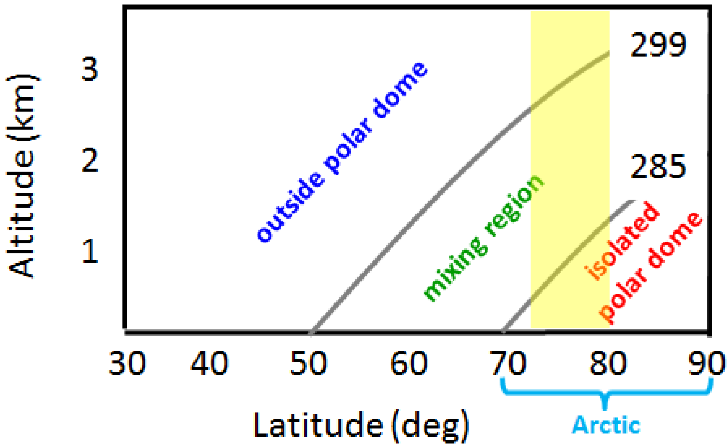

Figure 4.6: Schematic overview of polar dome vertical and spatial structure (on average) during the NETCARE 2014 campaign, according to Bozem et al. (2019). Gray lines represent isentropes and numbers show the associated potential temperatures (θ) in K. The term *Arctic* or *Arctic regions* used for FLEXPART air mass history analysis is based on the polar dome latitudinal boundary (see Sect. 2.2.7.1) and indicated with the curly blue bracket. The yellow box represents the measurement region around Resolute Bay.

ported the July 2014 polar dome to be located north of 73.5° N (see Sect. 2.2.7.1) with a twofold vertical structure. Potential temperatures (θ) below 285 K referred to as regions inside the isolated polar dome, while potential temperatures greater than approximately 299 K describe regions outside of the dome, the so-called extra-dome (Fig. 4.6). In addition, regions between 285 K and 299 K (θ) are characterized by a transition zone that potentially allows for mixing between dome and extra-dome air (Fig. 4.6). Potential temperatures of 285 K and 299 K correspond to 650 - 850 m and 2950 m altitude at the measurement site, respectively, inferred from θ vertical profiles in Fig. C.2. Thus, measurements within the local BL took place in the polar dome region, whereby measurements in the lower FT were performed primarily in the mixing region and outside the isolated dome (Fig. 4.6).

Air masses that had resided in the Arctic dominated regions inside the isolated polar dome (up to 90 % in Fig. 4.5). Particularly inside the polar dome region, a pronounced influence of air masses that had resided above Arctic open water is obvious in Fig. 4.7 (up to 20 %). Thus, air masses inside the polar dome region originated to a large degree from pristine Arctic regions with mainly natural aerosol sources affecting composition. This is also obvious when comparing measurements of $N_{>5}$ and $N_{>100}$ with potential temperature as the vertical coordinate (see Figs. C.3a and b, respectively). Regions within

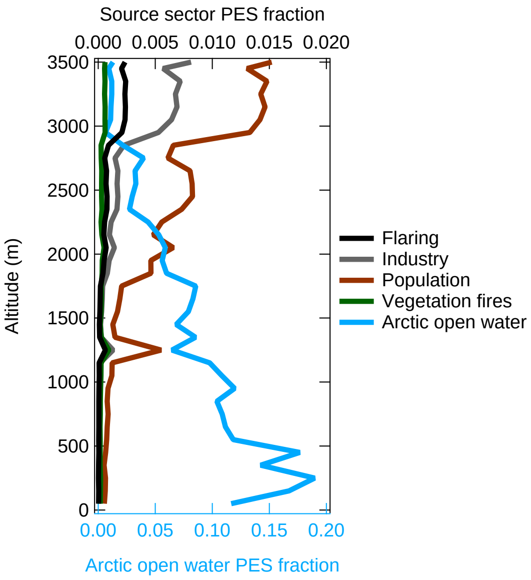

Figure 4.7: Vertically resolved cumulative contribution of source sectors to sampling altitude during the Arctic air mass period. Further details on source sectors are given in Sect. 2.2.7. The FLEXPART predicted contribution is expressed as a fraction of the potential emission sensitivity (PES) in the model domain lowest vertical level (0 - 400 m) over a 15-days backward simulation. The PES above vegetation fires refers to the 1 - 5 km vertical range. Bottom and top axes represent PES fractions of Arctic open water and other source sectors, respectively.

the isolated polar dome ($\theta < 285\,\mathrm{K}$) were characterized by an enhanced number of ultrafine particles (Burkart et al., 2017).

In the mixing region, influences of Arctic air masses were still pronounced (Fig. 4.5). However, contributions from southern latitude regions, i.e. Europe, Siberia, northern Canada, Greenland, and the Atlantic Ocean, were increasing with altitude (Fig. 4.5), as expected from the isentropic transport point of view (e.g., Klonecki et al., 2003). Figure 4.8 shows exemplary the transport pathway of air masses from Europe to the measurement region. Air masses that had resided over Europe in altitudes below 400 m ascended as they approached Arctic regions. The subsequent transport within the Arctic took place at levels above 400 m. Along with the increasing contribution of mid-latitude regions to air mass history, the influence of anthropogenic pollution, i.e. flaring, industry, and population was increasing with altitude (Fig. 4.7). Particularly, anthropogenic influences up to 3 km were accompanied with transport of air masses from Europe (compare Figs. 4.5 and 4.7). Consistent with enhanced influences of southern latitude aerosol sources, accumulation mode particles showed elevated concentrations in this mixing region, compared to below (see Fig. C.3b).

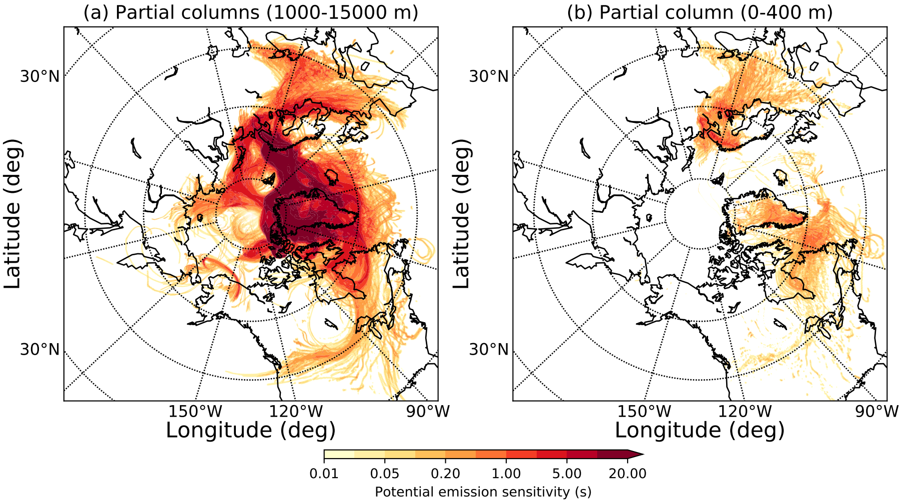

Figure 4.8: FLEXPART 15-days integrated (a) partial column 1 - 15 km and (b) partial column 0 - 400 m potential emission sensitivity (PES; for measurements on 12 July from 18:40 until 18:50 UTC) as an example of transport from European sources to the measurement region. Note that air mass transport into the Arctic took place mainly above 400 m.

Air mass history above the polar dome (>3 km) illustrates a sharp transition to a dominating influence of mid-latitude air masses (Fig. 4.5). Consistent with several modeling studies, contributions of regions south of 50 - 60° N (i.e., East Asia, Pacific, and southern North America) became significantly important only above 3 km, whereas sources in Europe and northern Canada frequently influenced measurements in lower altitudes (e.g., Bourgeois and Bey, 2011; Sobhani et al., 2018; Yang et al., 2018). Thus, anthropogenic pollution in altitudes above 3 km can be attributed to sources in East Asia and southern North America (compare Figs. 4.5 and 4.7). Consistent with this, CO mixing ratios were enhanced at altitudes above 3 km compared to below (Fig. 4.4f). In general during the Arctic air mass period, the contribution of vegetation fires was negligible small (Fig. 4.7).

4.2.2 *Southern air mass period*

Meteorological conditions changed after 12 July due to a low-pressure system that was initially centered to the west above the Beaufort Sea and finally passed through Resolute Bay on 15 July (not shown). Until 17 July, flying was impeded by the local weather situation with low visibility, fog, and precipitation along with the low-pressure system (Burkart et al., 2017). However, the measurement region came under the influence of an intense low-pressure

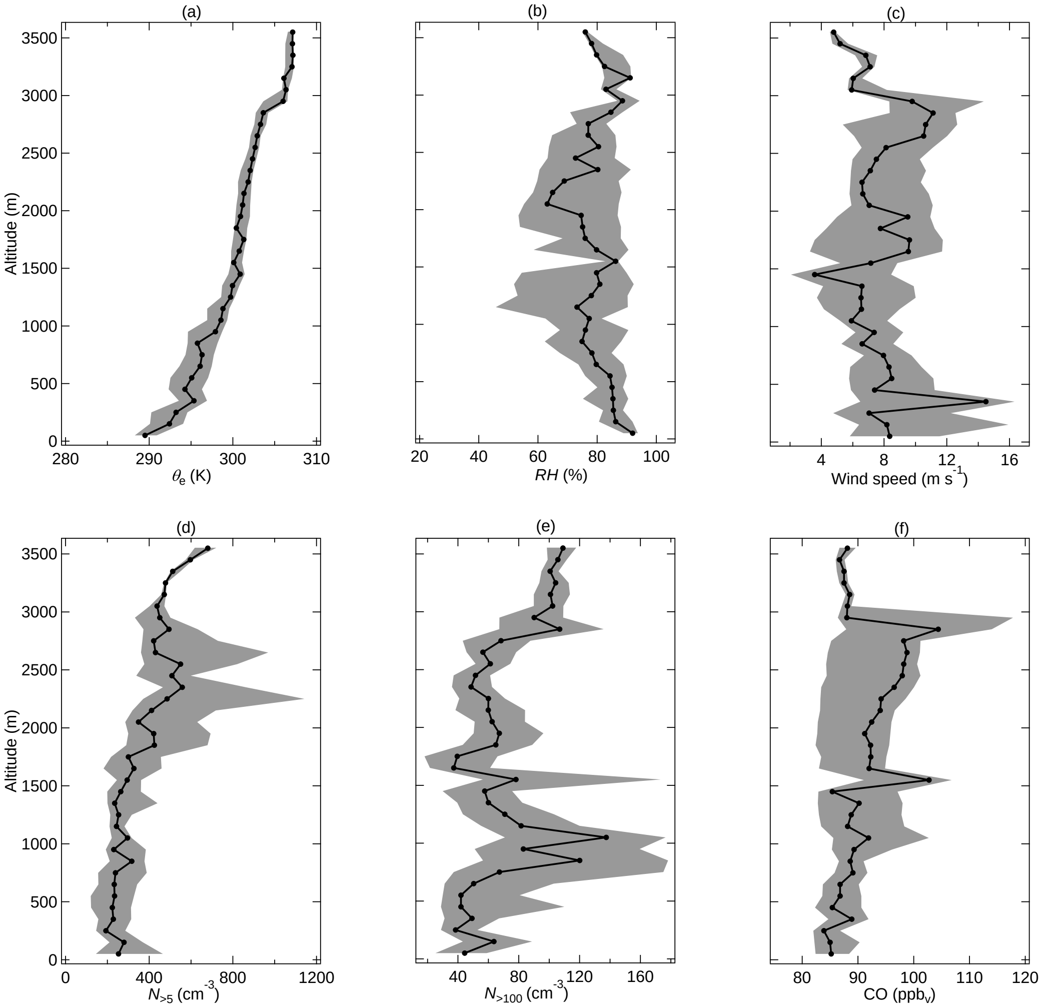

Figure 4.9: Vertically resolved median (black line) and interquartile range (gray shaded area) of pseudoequivalent potential temperature (θ_e), relative humidity (RH), wind speed, number concentrations of particles larger than 5 nm ($N_{>5}$) and larger than 100 nm ($N_{>100}$), and CO mixing ratio during the second period (see Table 1 for uncertainties).

system[3] located south of Resolute Bay (Fig. 4.3b) that led to fairly constant meteorological conditions during the period from 17 - 21 July. This period is referred to as southern air mass period, since air mass history shows the prevalence of air masses originating from southern latitudes.

Meteorological conditions were characterized by overcast sky, occasional precipitation, moist air throughout the lower troposphere (Fig. 4.9b), higher wind speeds (Fig. 4.9c), and warmer temperatures (Fig. 4.9a) compared to the Arctic air mass period. The BL was more difficult to identify compared to the prior period due to a less well defined temperature inversion. According to the

---

[3] Central pressure of the low-pressure system south of Resolute Bay was less than 990 hPa.

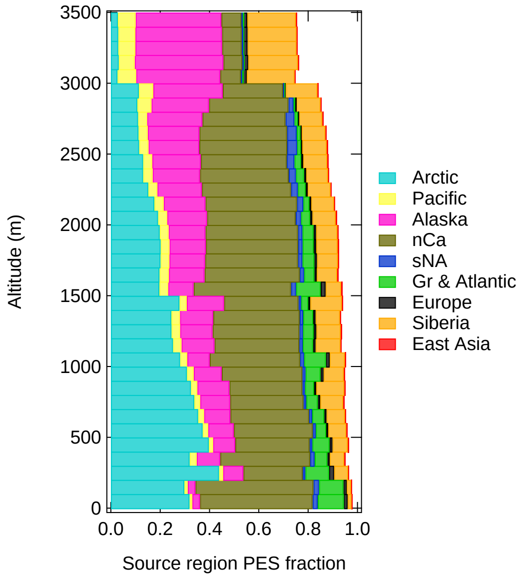

Figure 4.10: Vertically resolved cumulative contribution of source regions to sampling altitude during the the southern air mass period. Further details on definitions of source regions are given in Sect. 2.2.7. The FLEXPART predicted contribution is expressed as a fraction of the potential emission sensitivity (PES) in the model domain lowest vertical level (0 - 400 m) over a 15-days backward simulation. Acronyms are defined as follows: nCa = northern Canada; sNA = southern North America; Gr = Greenland.

detailed BL study by Aliabadi et al. (2016b), the BL height reached altitudes between approximately 200 m and 400 m. However, vertical mixing between the BL and FT was likely promoted caused by a combination of less intense temperature inversions, higher wind speeds, warmer temperatures, and a higher abundance of clouds compared to the first period (e.g., Stull, 1997; Fuelberg et al., 2010; Tjernström et al., 2012).

Air mass history suggests pronounced influences of southern latitude sources on Arctic composition (Figs. 4.10 and 4.11). First, the cumulative contribution of all regions outside the Arctic dominated air mass history within the lower troposphere with up to 97 % (Fig. 4.10). Along with this, northern Canada and Alaska exerted the largest influences, whereby the European influence was smaller than during the first period, consistent with the prevailing cyclonic activity south of Resolute Bay. Transport of air masses from northern Canada was accompanied with emissions from vegetation fires in the Great Slave Lake region (compare Figs. 4.12 and 2.12a).

Arctic atmospheric composition reflected the prevalence of southern latitude air masses that were influenced by vegetation fires and anthropogenic pollution.

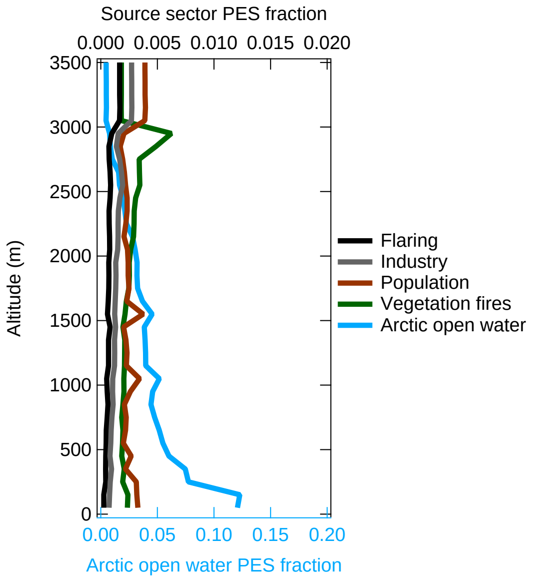

Figure 4.11: Vertically resolved cumulative contribution of source sectors to sampling altitude during the southern air mass period. Further details on source sectors are given in Sect. 2.2.7. The FLEXPART predicted contribution is expressed as a fraction of the potential emission sensitivity (PES) in the model domain lowest vertical level (0 - 400 m) over a 15-days backward simulation. The PES above vegetation fires refers to the 1 - 5 km vertical range. Bottom and top axes represent PES fractions of Arctic open water and other source sectors, respectively.

CO mixing ratios were generally higher than during the Arctic air mass period (Fig. 4.9f). Highest CO mixing ratios were measured at approximately 3 km when the vegetation fire influence was largest. In addition, distinct plumes[4] of enhanced CO mixing ratios and accumulation mode particles at approximately 1 km and 1.5 km (Figs. 4.9e and f) coincided with influences from populated areas in Europe (compare Figs. 4.10 and 4.11). Contributions from industrial and flaring activities were accompanied with transport of air masses from Alaska, Siberia, southern North America, and Europe (Figs. 4.10 and 4.11). Along with transport of accumulation mode particles, bursts of ultrafine particles from local new particle formation and subsequent growth were less abundant (compare Figs. 4.9d and e; see Burkart et al. (2017)). Finally, the contribution of air masses that had resided above Arctic open water was significantly lower during the southern air mass period (Fig. 4.11), compared to the Arctic air mass period.

Taken together, the NETCARE 2014 Arctic measurements took place in two distinct meteorological regimes. The first measurement period is referred to as the Arctic air mass period by a dominant influence of pristine Arctic air

---

[4] Frequent and distinct pollution episodes are referred to as plumes.

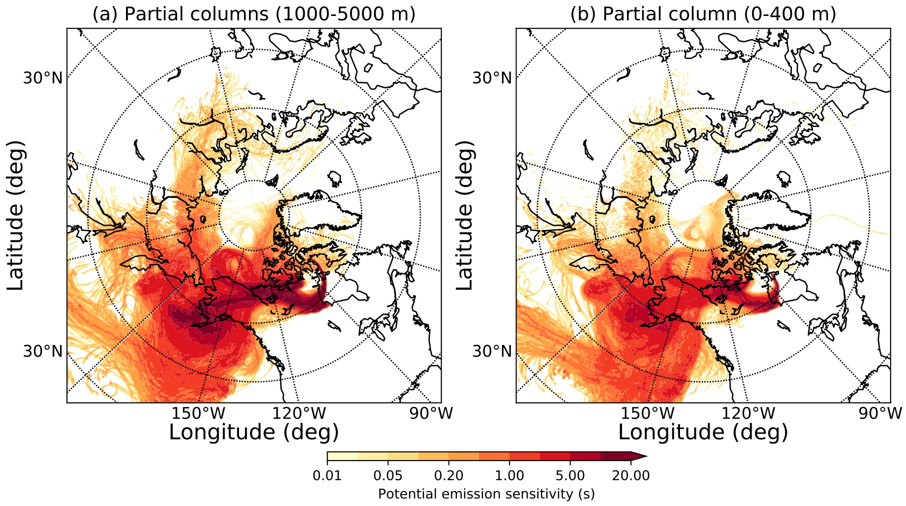

Figure 4.12: FLEXPART 15-days integrated (a) partial column 1 - 5 km and (b) partial column 0 - 400 m potential emission sensitivity (PES; for measurements on 19 July from 15:30 until 15:40 UTC) as an example of transport of emissions from vegetation fires in northern Canada (compare to Fig. 2.12a) to the measurement region.

masses within the stable stratified shallow Arctic boundary layer. The second, so-called southern air mass period, was characterized by a pronounced influence of outside Arctic regions on the summertime Arctic lower troposphere. This study thus allows to contrast the chemical composition of aerosol particles under primarily pristine and clean Arctic background conditions as well as under polluted conditions with signatures from vegetation fires and anthropogenic sources.

4.2.3 *Representativeness of the July 2014 measurement periods*

It is of relevance to assess the representativeness of both NETCARE 2014 periods with respect to climatological conditions, i.e. mean conditions between 1981 - 2010. Climatic anomalies were obtained by using re-analysis data prepared by NCEP/NCAR (Kalnay et al., 1996). Images in Fig. 4.13 were provided by the NOAA/ESRL Physical Sciences Division, Boulder Colorado, from their web site at http://www.esrl.noaa.gov/psd/data/composites/day/ (Kalnay et al., 1996).

The meteorological conditions with the high pressure influence during the Arctic air mass period were generally consistent with the climatology. First, 850 hPa geopotential heights were within +20 m of the climatology in the mea-

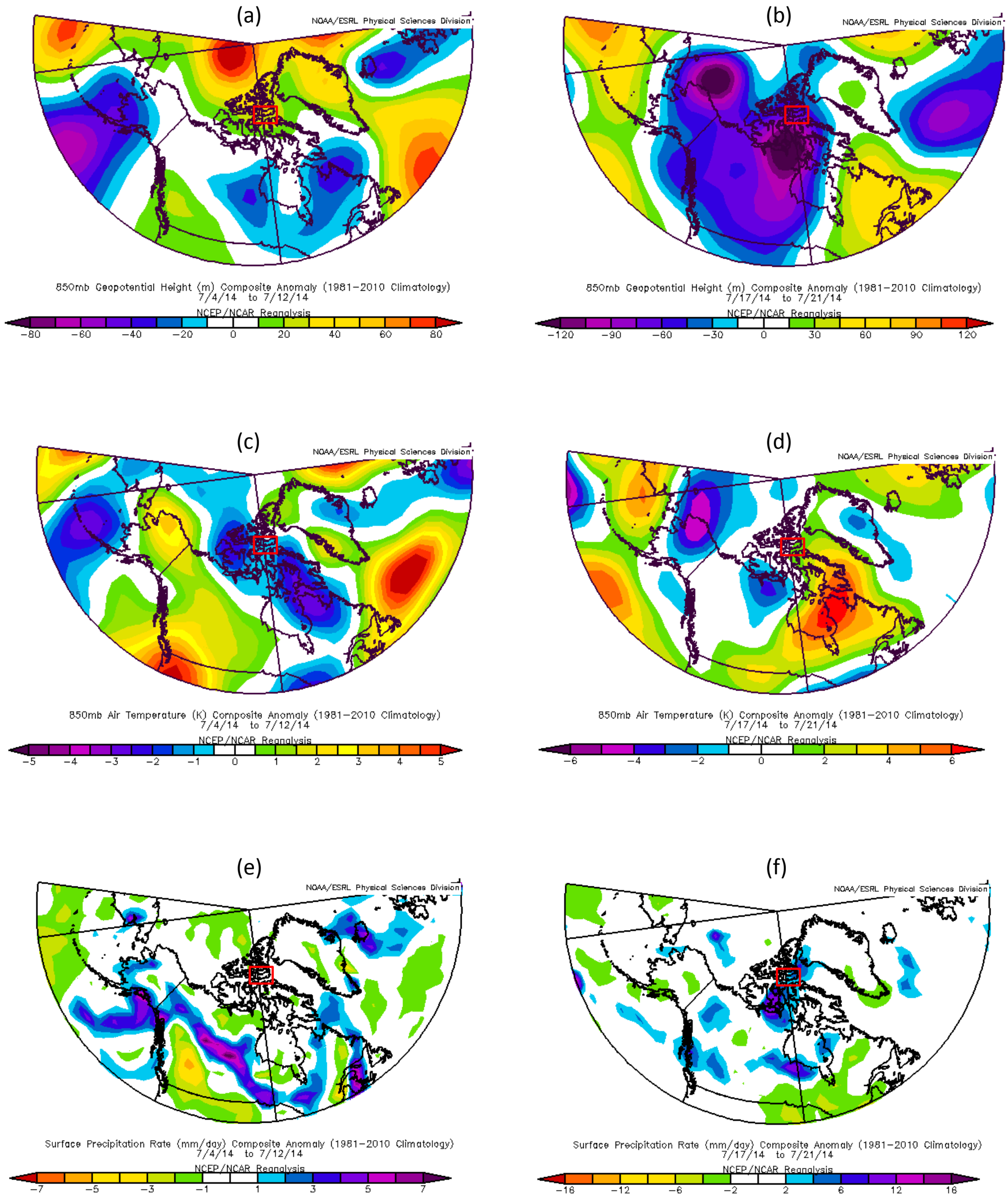

Figure 4.13: Anomaly from climatological mean (1981 - 2010) of 850 hPa geopotential height (a-b), 850 hPa air temperature (c-d), and 850 hPa precipitation rate (e-f) during the Arctic air mass period (left panel) and the southern air mass period (right panel). The measurement region is marked with a red box.

surement region (Fig. 4.13a). Second, air temperatures at 850 hPa were maximum 1 K lower than normal (Fig. 4.13c). Third, the precipitation anomaly was negligible small (Fig. 4.13e). Finally, local meteorological conditions, such as the shallow stable stratified BL and low wind speeds (see Sect. 4.2.1), represented typical features in the summertime Arctic atmosphere (e.g., Fuelberg et al., 2010; Tjernström et al., 2012).

In contrast to this, the southern air mass period with influences of the low-pressure system centered south of Resolute Bay were significantly anomalous compared to climatological mean. Geopotential height at 850 hPa shows a climatological departure down to -120 m close to the center of the low-pressure system (Fig. 4.13b). Further, warmer air than normal was advected into and more precipitation than normal fell in the measurement region (Figs. 4.13d and 4.13f). Air temperatures at 850 hPa deviated up to +6 K from the climatology in the region north-east of the Hudson Bay (Fig. 4.13d). Additionally, the vegetation fire activity in North America was anomalously high in summer 2014 compared to 2001 - 2013 (Arndt et al., 2015). Together, influences of vegetation fires on Arctic atmospheric composition were larger than on climatological average caused by a combination of anomalous meteorological conditions and intensive fires in northern Canada.

4.3 SINGLE PARTICLE CHEMICAL COMPOSITION - RESULTS

The ALABAMA chemically analyzed 10137 particles during the NETCARE 2014 study when sampling outside clouds (see details in Sect. C.3); 94 % of the spectra include size information; 78 % of the spectra have dual polarity (Fig. 4.14). Spectra with single negative polarity are not further analyzed in this study owing to their low counting statistics (< 300 spectra; see Table 10 in Sect. C.3). However, spectra with single positive polarity (19 %) are further analyzed (Fig. 4.14). Potential reasons for the lack of negative ions are discussed in Sect. C.4. Briefly, it might be that single-polarity spectra are produced in high relative humidity environments (Neubauer et al., 1998; Spencer et al., 2008), in particular in marine environments (Guasco et al., 2014).

Particle classification by the ion marker method introduced in Sect. 3.1 is illustrated with a decision tree in Fig. 4.14. Particle types are classified based on the presence of the following substances: elemental carbon (EC), sodium (Na), chloride (Cl), nitrate (NO_3), trimethylamine (TMA), dicarboxylic acids (DCA), potassium (K), ammonium (NH_4), methanesulfonic acid (MSA), and sulfate (SO_4) (see Table 2). Particle types that include less than 300 particles ($\sim 3\,\%$) are not further sub-classified by the low counting statistics (gray numbers in

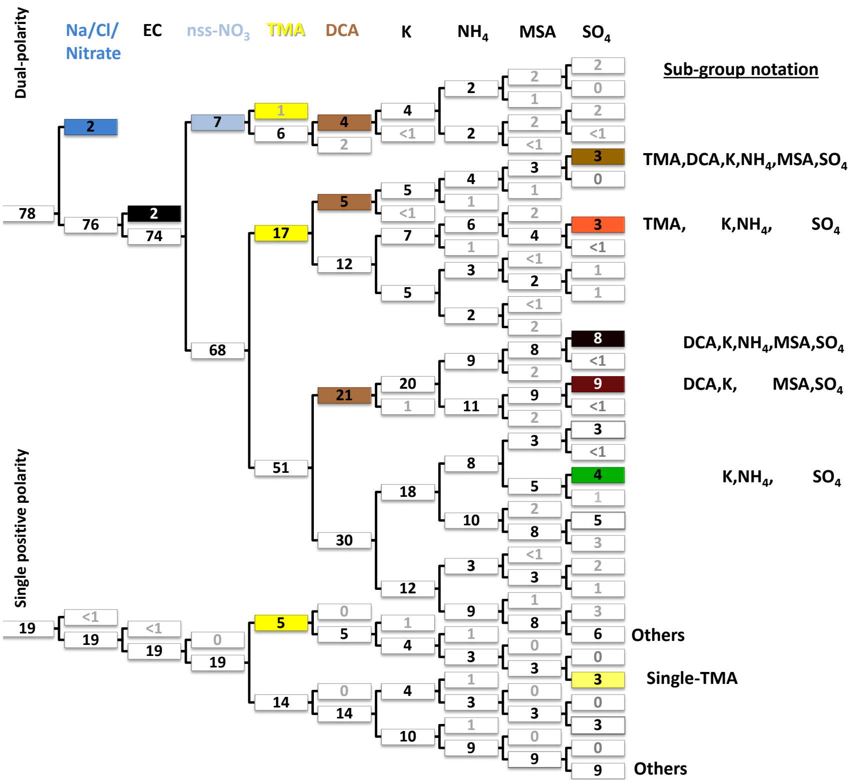

Figure 4.14: Classification of 10137 single particle spectra based on the ion marker method (see Sect. 3.1) and illustrated with the decision tree (see Sect. 3.1.3). Numbers are given as relative abundances in % normalized to 10137 particles. Classification includes the initial request on the existence of dual-polarity spectra. Selected main particle types indicated by colors contain: Na/Cl/Nitrate (dark blue), EC (black), non-sea-spray-(nss)-NO$_3$ (light blue), trimethylamine (TMA) (yellow), and dicarboxylic acids (DCA) (brown). Selected sub-types indicated by colors contain: "TMA,DCA,K,NH$_4$,MSA,SO$_4$" (light brown), "TMA,K,NH$_4$,SO$_4$" (orange), "DCA,K,NH$_4$,MSA,SO$_4$" (dark brown), "DCA,K,MSA,SO$_4$" (red-brown), "K,NH$_4$,SO$_4$" (green), and "Single-TMA" (light yellow). Particle sub-types with gray-shaded numbers were not further sub-classified. Particle types "Others" could not be classified into one of the particle types.

Fig. 4.14). For clarity reasons, the following analysis will only focus on five main particle types containing:

- Na/Cl/Nitrate
- EC
- Nitrate
- TMA
- DCA.

These types comprise an environmentally reasonable selection, as their characteristics contribute to a better understanding of aerosol processes in the summertime Arctic. Hence, the selection is based on the author's experience with

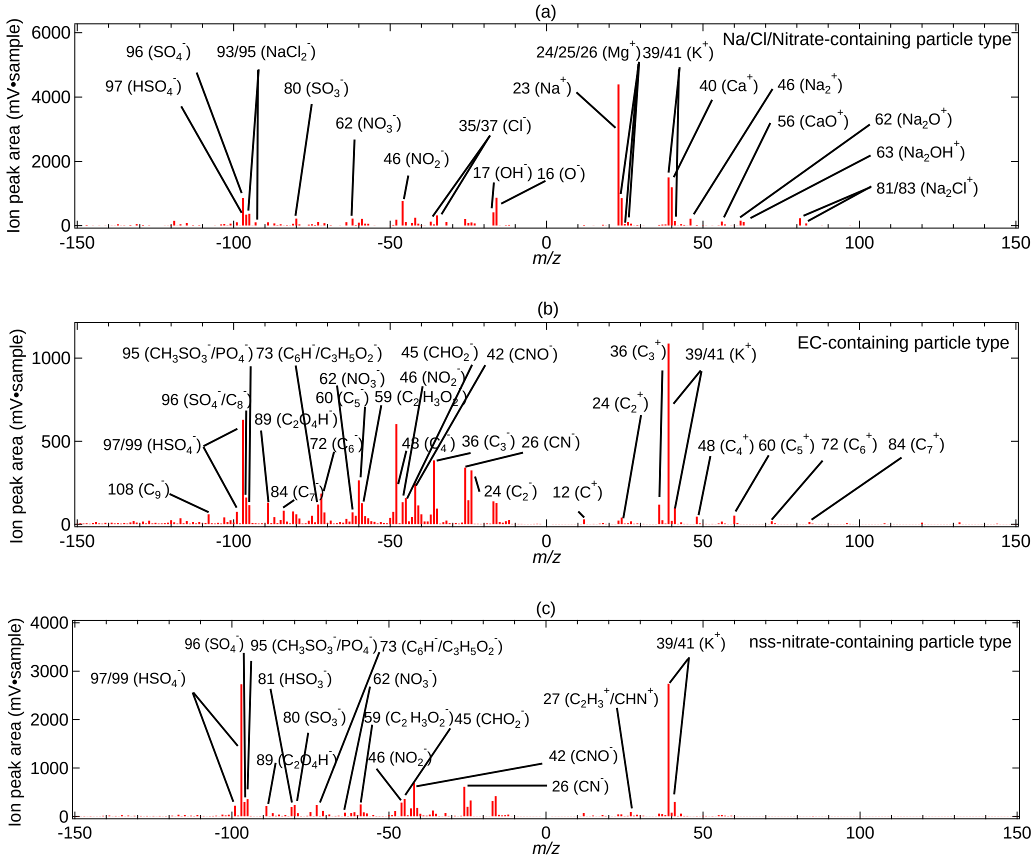

Figure 4.15: Bipolar mean spectra of the identified particle types: (a) Na/Cl/Nitrate-containing (195 particles ≙ 2 %), (b) EC-containing (188 particles ≙ 2 %), (c) nss-nitrate-containing (688 particles ≙ 7 %). **Continued on next page**.

the data set and the instrument. To note, EC- and Na/Cl/Nitrate-containing particles are excluded from other main types due to their low particle counting statistics. However, particle types other than EC and Na/Cl/Nitrate are not based on this hierarchical markering, which means that one particle can be assigned to several types if it includes several marker substances.

TMA- and DCA-containing particles are the most prominent types with relative contributions of 23 % and 31 % to the total number of analyzed particles, respectively (indicated by yellow and brown filling in Fig. 4.14). In contrast, particles containing Na/Cl/Nitrate, EC, and nitrate (externally mixed from Na and Cl) account for 2 %, 2 %, and 7 %, respectively. 15 % of all mass spectra analyzed by the ALABAMA could not be assigned to one of the ion marker species ("Others" in Fig. 4.14). The mean spectrum "Others" in Fig. C.6 primarily shows carbon cluster ions and fragments of hydrocarbons, both of which cannot be attributed to specific organic compounds. Generally, mean spectra

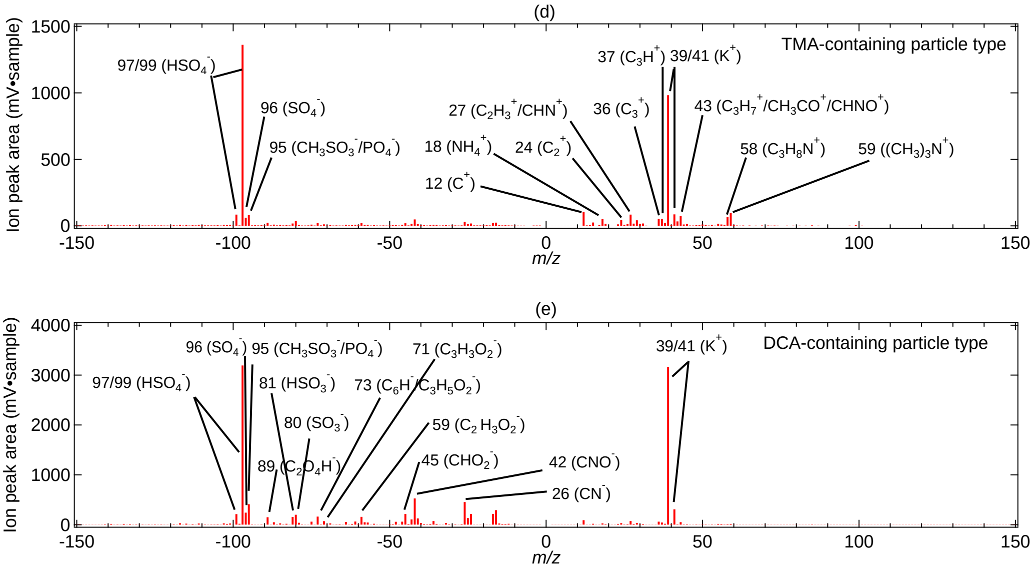

Figure 4.16: Continued: (d) TMA-containing (2325 particles $\widehat{=}$ 23 %) and (e) DCA-containing (3150 particles $\widehat{=}$ 31 %).

of the main particle types (Figs. 4.15 and 4.16) combined with additional ion signals (Table 4) provide an overview of the averaged chemical composition.

The internal mixing of particles that contain sodium, chloride, and/or nitrate (Na/Cl/Nitrate) suggests the presence of chemically aged sea spray particles (Figs. 4.15a and C.7; Table 4). First, substances such as sodium, chloride, magnesium, and calcium in particle mass spectra had been earlier related to the presence of inorganic sea salt (e.g., Prather et al., 2013). Second, MSA from DMS oxidation might also be internally mixed with sea spray particles. However, $NaCl_2^-$ and MSA have an isobaric interference at m/z-95 (Table 2). It is more likely that ion signals at m/z-95 are produced by $NaCl_2^-$ due to the presence of $NaCl_2^-$ isotopic pattern (m/z-93/95). Third, the internal mixing with sulfate and nitrate indicates that some particles have been exposed to chemical aging by reactions with nitric and sulfuric acids, respectively (e.g., Gard et al., 1998; Sierau et al., 2014; Gunsch et al., 2017). To note, nitrate was also present as an external mixture from sea spray particles, hereafter referred to as non-sea-spray (nss)-nitrate. Consistent with the chemical aging of sea spray particles, the internal mixing with DCA ($\sim$60 % of all sea spray particles), particularly oxalic acid (Table 4 and Fig. C.7), suggests the formation of SOA by aqueous-phase chemistry (see below; Kerminen et al., 1999; Sullivan and Prather, 2007; Laskin et al., 2012; Chi et al., 2015; Kawamura and Bikkina, 2016). To conclude, measurements of inorganic salts together with organics, nitrate, and sulfate infer the presence of sea spray particles that were exposed to chemical aging.

Table 4: Main particle types and their internal mixing with other substances derived from the mean spectra in Figs. 4.15 and 4.16. Additional ion signals of sulfate (m/z -97/99 (HSO$_4^-$), -96 (SO$_4^-$)) and potassium (m/z +39/41 (K$^+$)) were present in every mean spectrum and have therefore not been listed here. References from SPMS laboratory and field studies are indicated by numbers that are defined below. These references are used for the assignment of the additional ion signals to the corresponding substances.

Particle type denotation	Ion markers	Additional ion signals in mean spectrum	Corresponding substances
Na/Cl/ Nitrate -containing	m/z +23 (Na$^+$), +46 (Na$_2^+$),	m/z +24/25/26 (Mg$^+$),	magnesium[1,2]
	+62 (Na$_2$O$^+$), +63 (Na$_2$OH$^+$)	+40 (Ca$^+$), +56 (CaO$^+$)	calcium[1]
	+81/83 (Na$_2$Cl$^+$)	m/z -26 (CN$^-$), -42 (CNO$^-$),	nitrogen-cont. OM[1,2,3]
	m/z -35/37 (Cl$^-$),	-45 (CHO$_2^-$), -59 (C$_2$H$_3$O$_2^-$),	oxygen-cont. OM[3,4,5]
	-46 (NO$_2^-$), -62(NO$_3^-$),	-71 (C$_3$H$_3$O$_2^-$), -73 (C$_3$H$_5$O$_2^-$)	
	-93/95 (NaCl$_2^-$)	-89 (C$_2$HO$_4^-$)	oxalic acid[9]
EC -containing	m/z +12, +24,..., +84 (C$_{1-7}^+$)	m/z -26 (CN$^-$), -42 (CNO$^-$),	nitrogen-cont. OM[6]
	m/z -12, -24,..., -96 (C$_{1-8}^-$)	-45 (CHO$_2^-$), -59 (C$_2$H$_3$O$_2^-$),	oxygen-cont. OM[8]
		-73 (C$_3$H$_5$O$_2^-$),	
		-89 (C$_2$HO$_4^-$),	oxalic acid[9]
		-95 (CH$_3$O$_3$S$^-$),	MSA[9]
		-46 (NO$_2^-$), -62(NO$_3^-$)	nitrate[9]
nss-nitrate -containing	m/z -46 (NO$_2^-$), -62(NO$_3^-$)	m/z -26 (CN$^-$), -42 (CNO$^-$),	nitrogen-cont. OM[6]
		-45 (CHO$_2^-$), -59 (C$_2$H$_3$O$_2^-$),	oxygen-cont. OM[8]
		-73 (C$_3$H$_5$O$_2^-$),	
		-89 (C$_2$HO$_4^-$)	oxalic acid[9]

Continued on next page.

However, several pieces of evidence suggest the incorporation of organic matter (OM) from primary emissions with sea spray particles in the Arctic summer (Fig. C.7 and Table 4). Arctic and mid-latitude field studies reported the contribution of the sea surface carbon pool to organic matter that is enriched in sea spray particles (Blanchard and Woodcock, 1980; Russell et al., 2010; Hawkins and Russell, 2010; Quinn et al., 2014; Frossard et al., 2014; Wilson et al., 2015). It is further known from SPMS laboratory studies that organic nitrogen fragments (CN$^-$ and CNO$^-$; Table 4 and Fig. C.7) present in inorganic salts to be linked with biologically active waters (e.g., Prather et al., 2013; Guasco et al., 2014). Consistent with this, nitrogen- and oxygen-containing OM together with calcium, sodium, and phosphate can be associated with biological species measured by SPMSs (Pratt et al., 2009a; Schmidt et al., 2017). Together, both primary and secondary organic matter were likely internally mixed with sea

Table 4: Continued.

Particle type denotation	Ion markers	Additional ion signals in mean spectrum	Corresponding substances
TMA -containing	m/z +59 ($(CH_3)_3N^+$), +58 ($C_3H_8N^+$)	m/z +18 (NH_4^+), +12, ..., +36 (C_{1-3}^+), +27 ($C_2H_3^+/CHN^+$) , +37 (C_3H^+), +43 ($C_3H_7^+/CH_3CO^+/$ $CHNO^+$) m/z -95 ($CH_3O_3S^-$)	ammonium[9] carbon cluster ions[9] hydrocarbons[7] oxidized organics[7] MSA[9]
DCA -containing	m/z -89 ($C_2HO_4^-$), -103 ($C_3H_3O_4^-$), -117 ($C_4H_5O_4^-$)	m/z +27 ($C_2H_3^+/CHN^+$), m/z -26 (CN^-), -42 (CNO^-), -45 (CHO_2^-), -59 ($C_2H_3O_2^-$), -73 ($C_3H_5O_2^-$)	hydrocarbons[7] nitrogen-cont. OM[6] oxygen-cont. OM[8]

Given reference numbers are defined as follows: (1) Prather et al. (2013), (2) Guasco et al. (2014), (3) Pratt et al. (2009a), (4) Schmidt et al. (2017), (5) Trimborn et al. (2002), (6) Silva et al. (1999), (7) Schmidt (2015), (8) Zauscher et al. (2013), (9) see Table 2.

spray particles measured during the NETCARE 2014 campaign.

The averaged chemical composition of EC- and nss-nitrate-containing types provide evidence for the internal mixing with secondary substances such as sulfate, MSA, and oxygen-containing OM (Figs. 4.15b-c and Table 4). In addition, 20 % of the EC particles are internally mixed with nitrate. More than 50 % of the nss-nitrate- and EC-containing particle spectra include ion signals of dicarboxylic acids, particularly oxalic acid at m/z -89 (for nss-nitrate see Fig. 4.14). Further, oxygen-containing OM can likely be assigned to fragments of glyoxylic acid (m/z -73), methylglyoxal (m/z -71), and acetic acid (m/z -59) (Table 3; Silva and Prather, 2000; Zauscher et al., 2013). However, it cannot be excluded that negative ion signals at m/z -71, -59, and -45 are produced by fragments of levoglucosan due to isobaric interferences (see Sect. 3.1.1.2). Interestingly, nss-nitrate was more abundant (12 %) during the second measurement period than during the Arctic air mass period (5 %), consistent with the pronounced influence of southern latitude sources. A detailed discussion on sources of EC and nss-nitrate in the summertime Arctic is given in the following sections.

TMA, DCA, and other marker species provide a complex interplay of particle internal and external mixtures as shown in Fig. 4.14. The mixing state is therefore considered by the following six sub-types that contain (Fig. 4.14):

- TMA,DCA,K,NH_4,MSA,SO_4

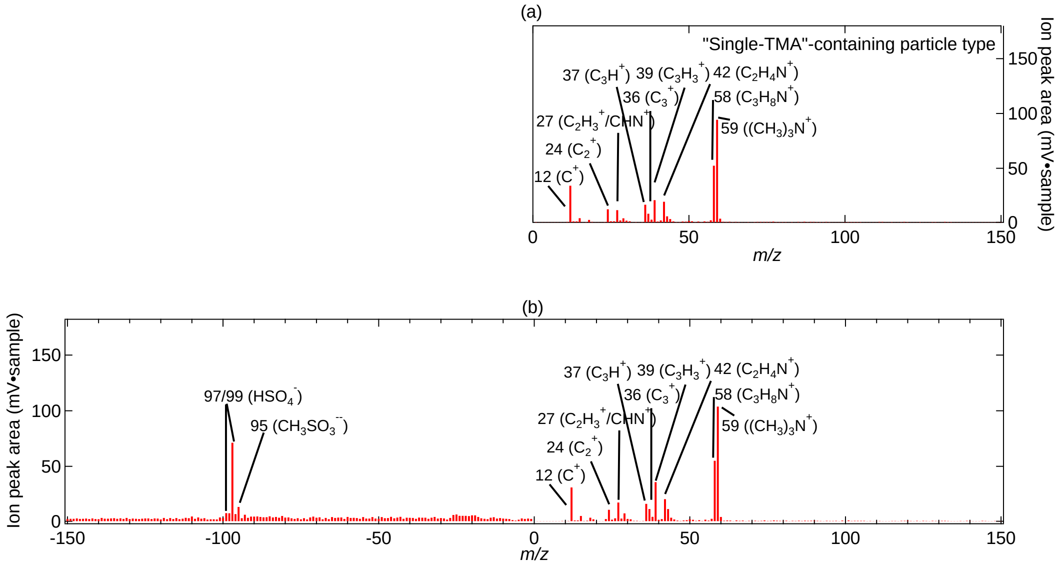

Figure 4.17: Mean Spectra of the "Single-TMA" particle sub-type (a) from single-polarity mass spectrum (3 %, light yellow in Fig. 4.14) and (b) from its analogous particle type with dual polarity (2 %, not colored in Fig. 4.14).

- TMA,K,NH_4,SO_4
- DCA,K,NH_4,MSA,SO_4
- DCA,K,MSA,SO_4
- K,NH_4,SO_4
- Single-TMA.

The selection is based on the following criteria. Sub-groups need to have minimum fractional abundance of 3 %. Similar to the main types, these sub-groups comprise an environmentally reasonable selection. The mean spectra of the sub-types can be found in Figs. C.8 and 4.17.

Particulate TMA was largely externally mixed from EC, sea spray, and nss-nitrate (Fig. 4.14). In parallel, TMA-containing particles showed an internal mixture with DCA, potassium, ammonium, and other organics (Figs. 4.14 and 4.16d). In detail for organics, 90 % of the TMA spectra contained at least one of the following positive ion signals: m/z +12, ..., +36, m/z +27, and m/z +43, indicative for fragments of hydrocarbons and oxidized organics (Fig. 4.16d and Table 4). Furthermore, the mean spectrum of TMA illustrates the internal mixing with sulfate and MSA, suggesting the presence of aminium salts (Murphy et al., 2007; Barsanti et al., 2009; Smith et al., 2010). The formation of particulate TMA was thus likely accompanied by acid-base reactions including TMA, sulfuric acid, and/or methanesulfonic acid (Facchini et al., 2008). This result demonstrates that amines, beside ammonia, may take part in the neutralization of acidic aerosol particles. Importantly, 23 % of the TMA-containing spectra lacked negative ions (Fig. 4.14). Consequently, it is not possible to infer whether “Single-TMA” particles were internally mixed with sulfate and/or MSA (Fig. 4.17a). Nevertheless, the analogous particle type with dual polarity (Fig. 4.17b; not colored in Fig. 4.14) indicates the concurrent presence of sulfate and/or MSA and thus the existence of aminium salts.

Particulate DCA summarizes the presence of oxalic, malonic, and/or succininc acid (see Table 2), with oxalic acid as most abundant (86 %), followed by succinic acid with 41 % and malonic acid with 38 % (not shown). In addition, 67 % of the DCA spectra show the concurrent presence of methylglyoxal and glyoxylic acid at m/z -71 and -73, respectively (Fig. 4.16e and Table 4). In contrast to what was previously assumed (Köllner et al., 2017), these ion markers are not unique for levoglucosan (see Sect. 3.1.1.2). The internal mixture of DCA with methylglyoxal and glyoxylic acid suggests the formation of aqueous-phase SOA. Briefly, methylglyoxal and glyoxylic acid are produced by the oxidation of biogenic and anthropogenic organic precursor gases, such as isoprene and toulene (e.g., Lim et al., 2005; Seinfeld and Pandis, 2016). Laboratory and modeling studies further reported that both intermediate oxidation products can subsequently participate in heterogeneous aqueous-phase photochemical reactions to form oxalic acid (e.g., Warneck, 2003; Lim et al., 2005; Carlton et al., 2006; Sorooshian et al., 2006; Ervens et al., 2011). In parallel to oxalic acid, higher homologues such as succinic and malonic acid can be similarly formed by aqueous-phase oxidation (e.g., Altieri et al., 2008; Tan et al., 2010; Ervens et al., 2011). It is also possible that succinic, malonic acid, and finally oxalic acid were formed via photochemical oxidation of precursor fatty acids from marine-biogenic sources (e.g., oleic acid; Bikkina et al., 2014; Kawamura and Bikkina, 2016). Taken together, the formation pathways of DCA in the atmosphere are complex owing to numerous precursor gases, intermediate oxidation products, and also primary sources (Kawamura and Bikkina, 2016). However, the internal mixing of dicarboxylic acids with glyoxylic acid and methylglyoxal provides evidence for the formation of aqueous-phase SOA, rather than for DCA from primary sources.

First conclusions on aging and formation of the different particle types were drawn based on their averaged chemical composition and mixing. The following sections provide a detailed discussion on aerosol sources and formation processes.

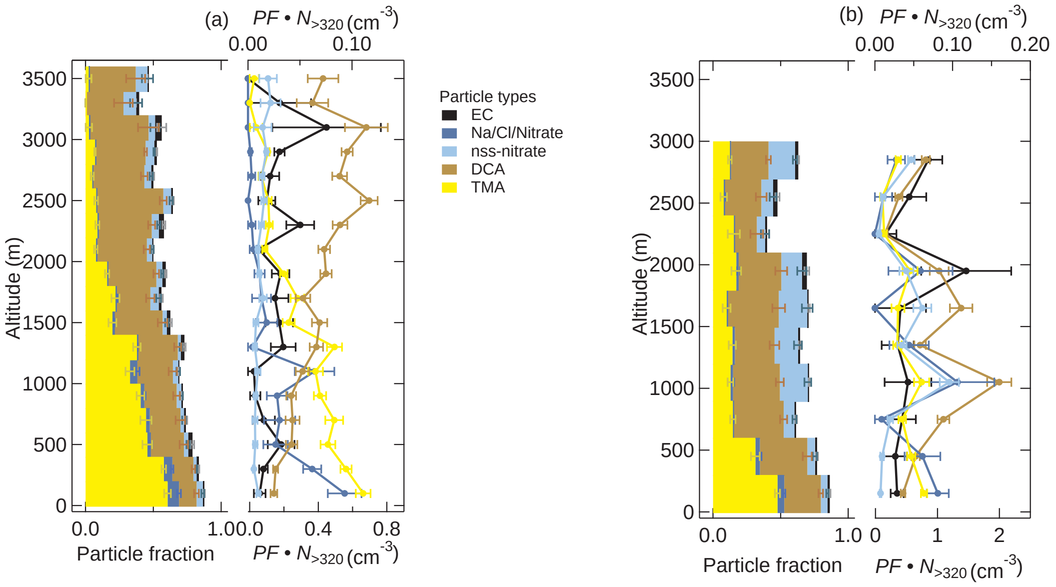

Figure 4.18: Vertically resolved aerosol composition of the identified main particle types by the ALABAMA during the Arctic (a) and southern (b) air mass periods. Figures (a) and (b) represent each: (left) the cumulative particle fraction (PF) and (right) the scaled number concentration ($PF \cdot N_{>320}$) with top axis referring to EC-containing (black) and Na/Cl/Nitrate-containing (dark blue) particles and bottom axis referring to nss-nitrate-containing (light blue), DCA-containing (brown), and TMA-containing (yellow) particles. Uncertainty analyses are given in Sect. C.7.

4.4 ARCTIC REGIONAL AND TRANSPORT INFLUENCES ON AEROSOL PARTICLE COMPOSITION

This section addresses influences of long-range transport and Arctic regional processes on the vertical structure of summertime Arctic single particle composition. The ALABAMA analysis showed different particle composition between the Arctic BL and the lower FT (Fig. 4.18), reflecting the stable stratification in the lowest 400 m (see Sect. 4.2). TMA- and Na/Cl/Nitrate-containing particles were largely abundant in the BL, whereas DCA-, EC-, and nss-nitrate-containing particles were enhanced in the lower FT (Fig. 4.18). These results suggest that both aerosol processes within the Arctic and during transport from southern latitude sources exerted influences on the vertical structure of summertime Arctic aerosol composition. The ALABAMA particle types are thus discussed in relationship to geographical source regions. Further, data on particle size and degree of oxidative aging are used to identify aerosol processes. To note, the following figures are based on the method introduced in Sect. 3.2 and are structured as given in Fig. 3.6. For clarity reasons, the averaged $N_{>320}$ is presented separately in Sect. C.6.

Several observations indicate a surface source of TMA within the polar dome region. The fraction and number concentration of TMA-containing particles increased with decreasing altitude, having the highest abundance within the BL (Fig. 4.18). Further, the comparison between HR-ToF-AMS estimated oxygen-to-carbon (O/C) and hydrogen-to-carbon (H/C) ratios and particle composition by the ALABAMA allows to analyze the degree of particle oxidative aging (Jimenez et al., 2009; Heald et al., 2010; Ng et al., 2011; Willis et al., 2017). This analysis had only been done for the first period due to the low counting statistics of the ALABAMA data distributed over O/C and H/C values during the second period. Figures 4.19a and b demonstrate that particulate TMA was largely present when less oxygenated organics were measured by the HR-ToF-AMS (up to 75 % in the upper left corner). This result suggests that a dominant fraction of TMA particles had not been subject to extensive oxidative aging. Consistent with this observation, the size distribution of TMA particles was shifted towards smaller diameters compared to other particle types (Fig. 4.20a).

To gain further insights into source regions of TMA, FLEXPART predicted air mass history in relationship with ALABAMA particle composition was analyzed. Particularly during the Arctic air mass period, the presence of particulate TMA was highest when time spent within the polar dome 15 days prior to sampling was highest (Fig. 4.21a). In parallel, the presence of TMA-containing particles was anti-correlated with the residence time in regions outside the polar dome, i.e. northern Canada (Fig. 4.21c), Europe (Fig. 4.21e), and East Asia (Fig. 4.21g). Thus, particulate TMA dominated the ALABAMA particle composition when the summertime Arctic atmosphere was largely isolated from distant sources. Together, air mass history combined with particle properties and a stable stratified BL suggests that a large fraction of TMA-containing particles originated from surface sources within the polar dome.

Those indications were less pronounced during the southern air mass period. TMA-containing particles were more evenly distributed across the size distribution (Fig. 4.20b), compared to the Arctic air mass period. Likewise, air mass history shows no significant trend if TMA particles were influenced by Arctic regional or transport processes (Figs. 4.21b, d, and f). Given that contributions of southern latitude regions dominated air mass history throughout the lower troposphere (Fig. 4.10), conclusions on the influence of regional Arctic processes are difficult to draw. However, the fraction and number concentration of particulate TMA peaked in the BL even during the second period (Fig. 4.18b). The following section will provide further details on source sector attributions

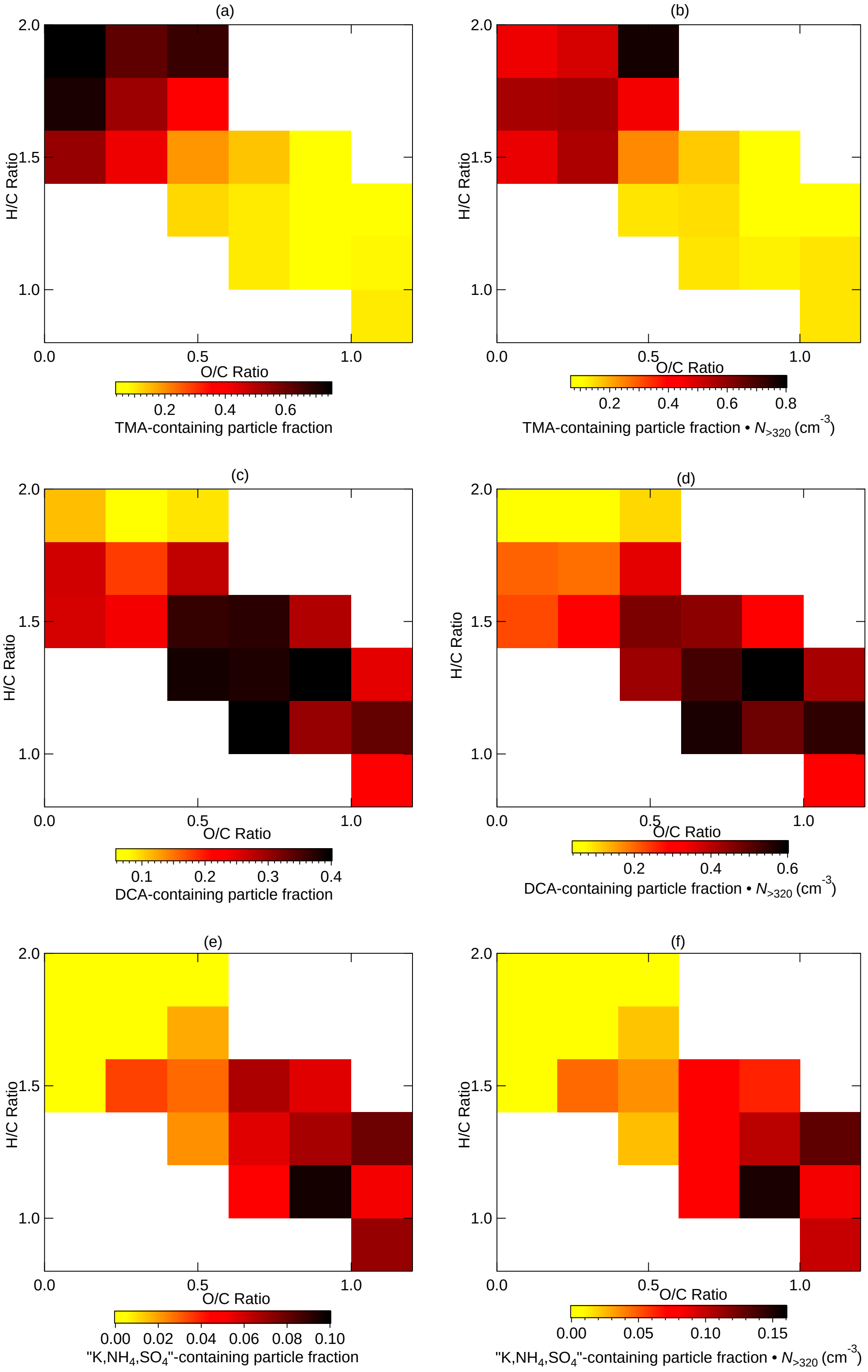

Figure 4.19: Comparison between the HR-ToF-AMS estimated oxygen-to-carbon (O/C) and hydrogen-to-carbon (H/C) ratios colored by (a-b) TMA-, (c-d) DCA-, and (e-f) "K,NH$_4$,SO$_4$"-containing particles measured by the ALABAMA with (left panel) the particle fraction and (right panel) the scaled number concentration ($PF \cdot N_{>320}$). Uncertainty analyses are given in Sect. C.7.

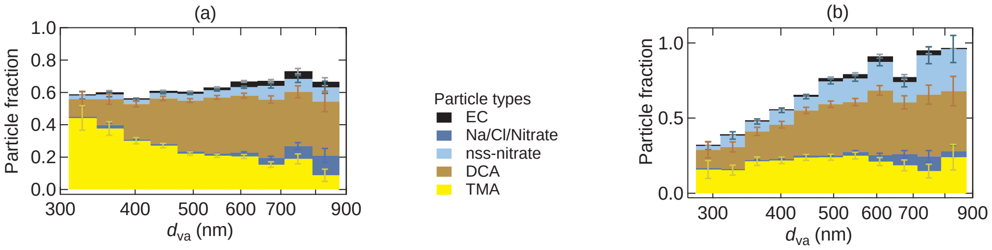

Figure 4.20: Size-resolved aerosol composition of the identified main particle types by the ALABAMA during the Arctic (a) and southern (b) air mass periods. Both figures represent the cumulative particle fraction of: EC-containing (black), nss-nitrate-containing (light blue), DCA-containing (brown), Na/Cl/Nitrate-containing (dark blue), and TMA-containing (yellow) particles. Uncertainty analysis is given in Sect. C.7.

during both periods.

In contrast to Arctic regional sources of TMA when present in the BL, the abundance in the lower FT might be related to transport processes. The fraction of TMA particles in the FT was dominated by the sub-type "TMA,K,NH_4,SO_4" (Fig. 4.22). Those particles were larger compared to the "Single-TMA" sub-type (Fig. 4.23), indicating that "TMA,K,NH_4,SO_4"-containing particles were longer exposed to chemical aging. In addition, the presence of "TMA,K,NH_4,SO_4"-containing particles was not correlating with the residence time over Arctic regions (Fig. 4.24). It is thus likely that this small fraction of TMA-containing particles was related to aerosol transport into Arctic regions. Taken together, the abundance of particulate TMA in the summertime Arctic was driven by both regional Arctic and transport-related processes, whereby the former process dominated the abundance of TMA particles in the summertime Arctic.

Along with aerosol processes within Arctic regions, Na/Cl/Nitrate-containing particles can be attributed to primary sea-to-air emissions within the Arctic. This particle type primarily existed at lowest altitudes (Fig. 4.18). Furthermore, air mass history during the Arctic air mass period shows that they were largely abundant when the residence time over Arctic regions prior to sampling was high (Fig. 4.21a). Similar to TMA-containing particles, air mass history during the southern air mass period presents no significant trend regarding the origin of Na/Cl/Nitrate-containing particles. However, the size distribution in Fig. 4.20 strengthens the hypothesis that particles resulted from primary marine emissions (see Sect. 4.3), since Na/Cl/Nitrate-containing particles were mainly larger than 600 nm.

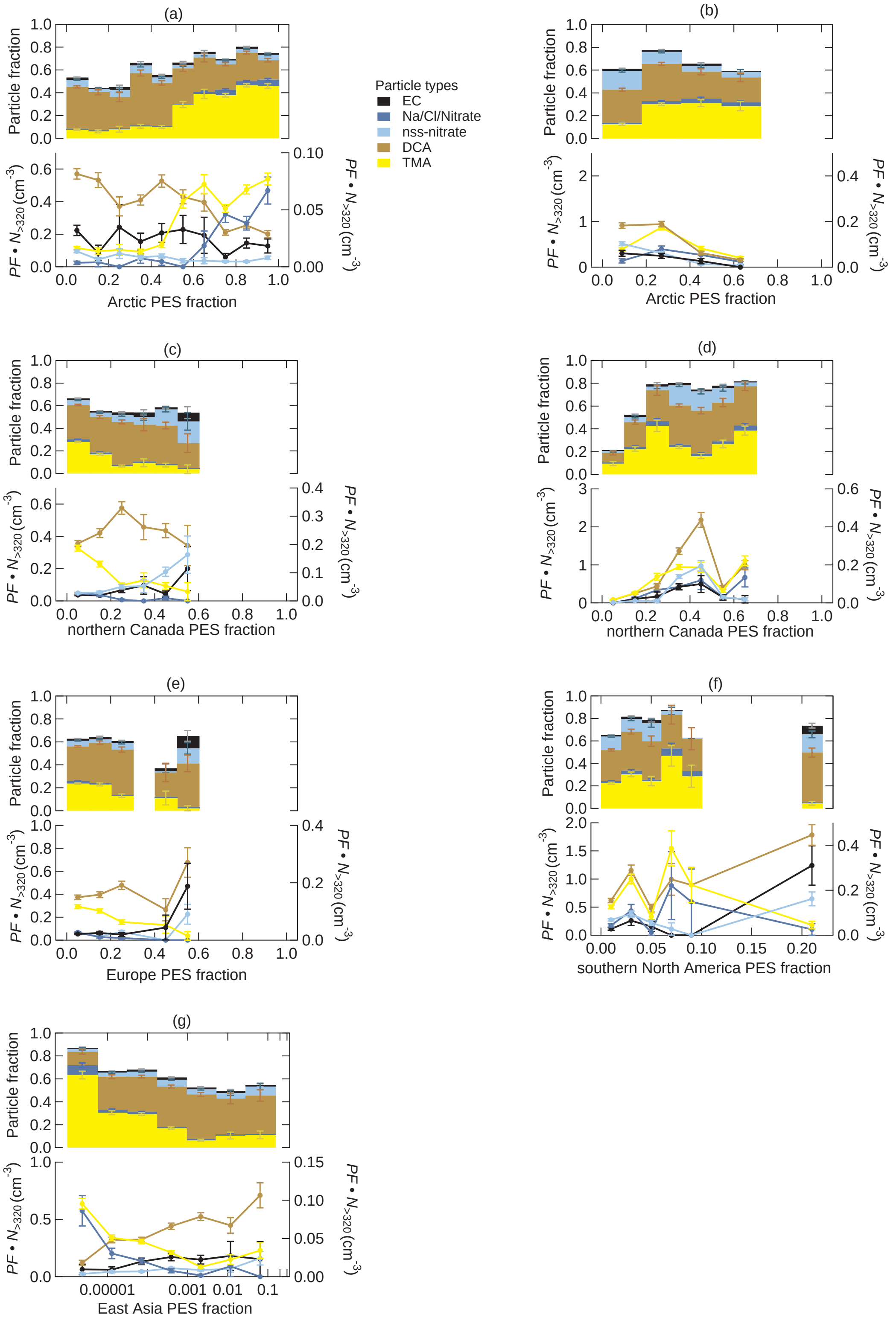

Figure 4.21: Comparison between aerosol composition of the identified main particle types by the ALABAMA and FLEXPART predicted air mass residence time over the Arctic (a-b), northern Canada (c-d), Europe (e), southern North America (f), and East Asia (g) during the Arctic (left panel) and southern (right panel) air mass periods. Figures represent each: (top) the cumulative particle fraction (PF) and (bottom) the scaled number concentration ($PF \cdot N_{>320}$) with right axis referring to EC-containing (black) and Na/Cl/Nitrate-containing (dark blue) particles and left axis referring to nss-nitrate-containing (light blue), DCA-containing (brown), and TMA-containing (yellow) particles. Uncertainty analyses are given in Sect. C.7.

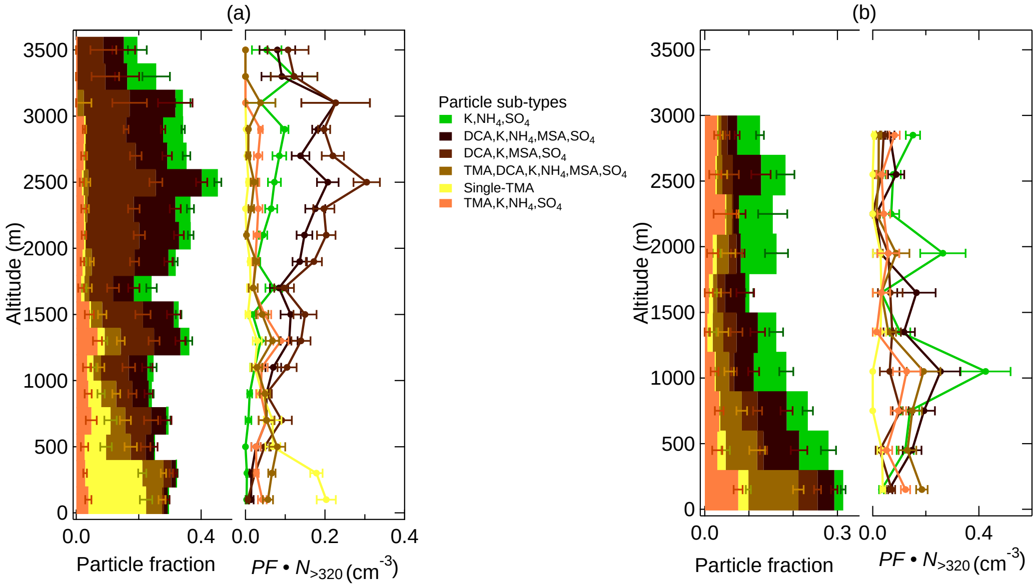

Figure 4.22: Vertically resolved aerosol composition of the identified particle sub-types by the ALABAMA during the Arctic (a) and southern (b) air mass periods. Figures (a) and (b) represent each: (left) the cumulative particle fraction (PF) and (right) the scaled number concentration ($PF \cdot N_{>320}$). Uncertainty analyses are given in Sect. C.7.

DCA-containing particles likely originated from both Arctic regional sources and transport of lower latitude emissions, depending on the internal mixing state. In detail, when DCA particles were internally mixed with TMA (“TMA,DCA,K,NH_4,MSA,SO_4”-containing sub-type), their fraction and number concentration increased with decreasing altitude (Fig. 4.22). In parallel, the presence of this particle type was coincident with a larger residence time over the Arctic during the first period (Fig. 4.24a). The vertical structure together with air mass history thus suggests the importance of regional sources on the abundance of dicarboxylic acids in the Arctic summer.

In contrast to Arctic regional sources, particulate DCA that was internally mixed with sulfate, MSA, ammonium, and potassium (“DCA,K,NH_4,MSA,SO_4”- and “DCA,K,MSA,SO_4”-containing sub-types) can likely be attributed to aerosol that was transported to Arctic regions. Both particle sub-types were largely present in the FT and had a negligible small abundance in the stable stratified BL (Fig. 4.22). Further, the fraction and number concentration of DCA-containing particles coincided with air masses that were more oxidative aged compared to TMA (compare Figs. 4.19c-d with 4.19a-b). Consistent with this result, the size of “DCA,K,NH_4,MSA,SO_4”- and “DCA,K,MSA,SO_4”-containing particles was larger compared to other types (Fig. 4.23). Finally, air mass his-

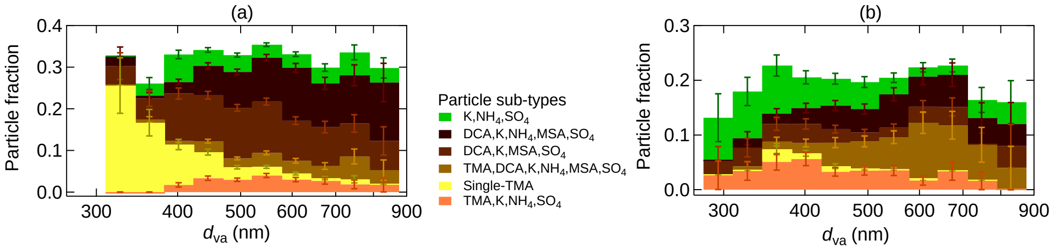

Figure 4.23: Size-resolved aerosol composition of the identified particle sub-types by the ALABAMA during the Arctic (a) and southern (b) air mass periods. Figures (a) and (b) represent the cumulative particle fraction. Uncertainty analysis is given in Sect. C.7.

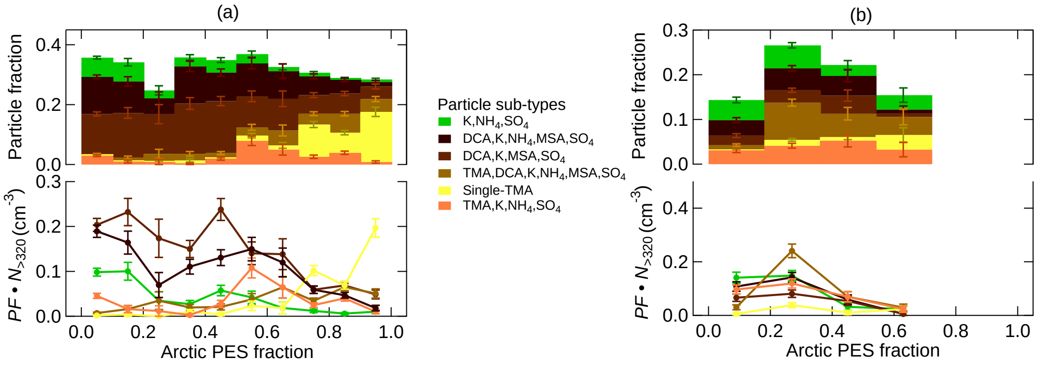

Figure 4.24: Comparison between FLEXPART predicted air mass residence time over the Arctic and aerosol composition of the identified particle sub-types by the ALABAMA during the Arctic (a) and southern (b) air mass periods. Figures (a) and (b) represent each: (top) the cumulative particle fraction (PF) and (bottom) the scaled number concentration ($PF \cdot N_{>320}$). Uncertainty analyses are given in Sect. C.7.

tory shows that the abundance of these particles correlated with time spent outside Arctic regions (Fig. 4.24). However, no significant trend with a distinct source region outside the Arctic was found (not shown), as expected from the variety of biogenic and anthropogenic precursor gases (see Sect. 4.3).

Besides the presence of DCA in the Arctic FT, aerosol transport from lower latitudes further influenced Arctic particle composition by particles that contained nss-nitrate and EC. Both particle types were more pronounced in the FT compared to the BL (Fig. 4.18). Comparing both periods, the fraction and number concentration of nss-nitrate-containing particles were larger during the southern air mass period, reflecting the pronounced influence of vegetation fires during this time (see Sect. 4.5). Consistently, particles containing nss-nitrate were predominantly present when the residence time over northern Canada was

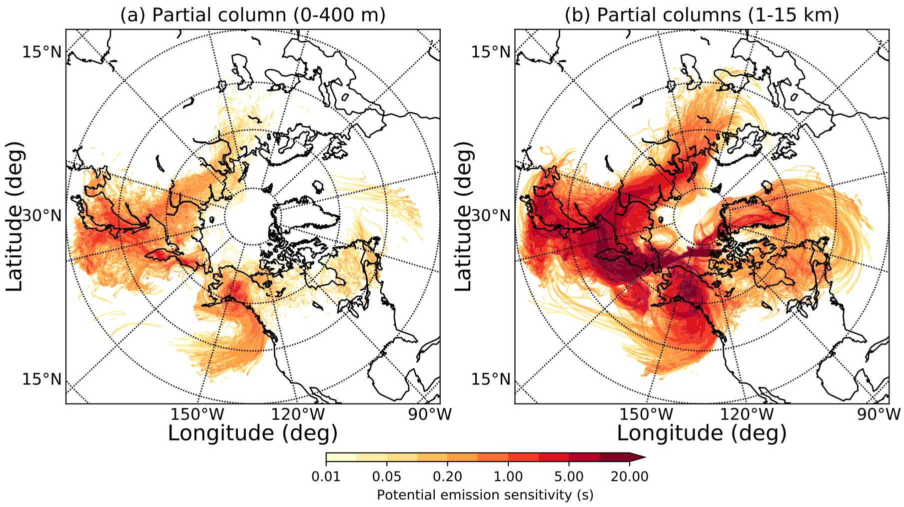

Figure 4.25: FLEXPART 15-days integrated (a) partial column 0 - 400 m and (b) partial column 1 - 15 km potential emission sensitivity (PES; for measurements on 5 July from 19:00 until 19:10 UTC) as an example of transport from sources in East Asia (particularly Japan) to the measurement region.

high (Fig. 4.21d). However, also during the Arctic air mass period, the abundance of nss-nitrate-containing particles can be assigned to aerosol transport from lower latitudes. Contributions from Europe and East Asia were significant during this time (Figs. 4.21e and g, respectively). Figure 4.25a presents an example of the FLEXPART predicted transport pathway from East Asia (particularly Japan) to the Arctic. The subsequent advection to Arctic regions took place mainly in altitudes above 1 km (Fig. 4.25b), as expected from the isentropic point of view (e.g., Klonecki et al., 2003). Aerosol transport from sources in northern Canada, Europe, and southern North America, however, contributed to the presence of EC (Figs. 4.21c, e, and f, respectively). Finally, nss-nitrate- and EC-containing particles were larger in diameter compared to TMA-containing particles (Fig. 4.20), consistent with pronounced influences of aerosol processing during long-range transport (see Sect. 1.2.2).

Particles containing only potassium, ammonium, and sulfate (“K,NH_4,SO_4”-containing sub-type) can also be associated with chemically aged aerosol that was transported to Arctic regions. The particle sub-type was largely present in the FT (Fig. 4.22) and the abundance correlated with time spent outside the Arctic (Fig. 4.24). Although the size distribution shows no clear trend (Fig. 4.23), the presence of “K,NH_4,SO_4”-containing particles coincided with air masses that were largely oxidative aged (Figs. 4.19e-f).

Taken together, aerosol particle composition measured by the ALABAMA in the summertime Arctic lower troposphere was driven by combination of processes occurring along transport and within Arctic regions. The typical composition during NETCARE 2014 in the stable stratified shallow BL was characterized by particulate TMA, sodium, and chloride from regional Arctic sources. In contrast, chemically aged particles containing EC, nss-nitrate, and DCA dominated air masses aloft, along with long-transport from mid-latitude sources. However, it was further shown that DCA particles when present in the Arctic BL and internally mixed with TMA originated from sources within Arctic regions. Likewise, particulate TMA when present in the FT can be attributed to long-range transport of aerosol from sources outside the Arctic. The following section presents a detailed analysis of the influences from specific aerosol sources within and outside the Arctic on aerosol particle composition.

4.5 MARINE, ANTHROPOGENIC, AND VEGETATION FIRE INFLUENCES ON AEROSOL PARTICLE COMPOSITION

This section contributes to our understanding of aerosol sources affecting particle composition in the Arctic summer. FLEXPART predicted air mass history, together with potential source inventories (PSIs; see Sect. 2.2.7), is used to provide a comprehensive source apportionment analysis of Arctic aerosol. To note, further details on contributions from certain source sectors are given in Sect. C.8.

Several pieces of evidence suggest the existence of marine-biogenic sources of particulate TMA within the Arctic summer. The MSA-to-sulfate ratio measured by the HR-ToF-AMS is generally used to asses the relative contributions of marine-biogenic and anthropogenic sources to total particulate sulfate (Kerminen et al., 1999). Important for this study is the earlier finding that the higher the ratio is, the stronger is the marine influence on particle composition (Kerminen et al., 1999; Willis et al., 2017). During both measurement periods, the fraction and number concentration of TMA-containing particles increased with increasing MSA-to-sulfate ratio (Figs. 4.26a-b). Consistent with this, the presence of particle sub-types that include an internal mixing of TMA with MSA, sulfate, and/or DCA ("TMA,DCA,K,NH_4,MSA,SO_4" and "Single-TMA"; see Fig. 4.17b) coincided with high MSA-to-sulfate ratios (Figs. 4.27a-b). Likewise, particulate TMA was predominantly abundant when the residence time over Arctic open water regions was high (Fig. 4.28a-b). Regarding the TMA sub-types, the presence of particles containing TMA, MSA, sulfate, and/or DCA coincided with time spent over Arctic open water regions (Fig. 4.29). Particularly during the Arctic air mass period, TMA particles were predomi-

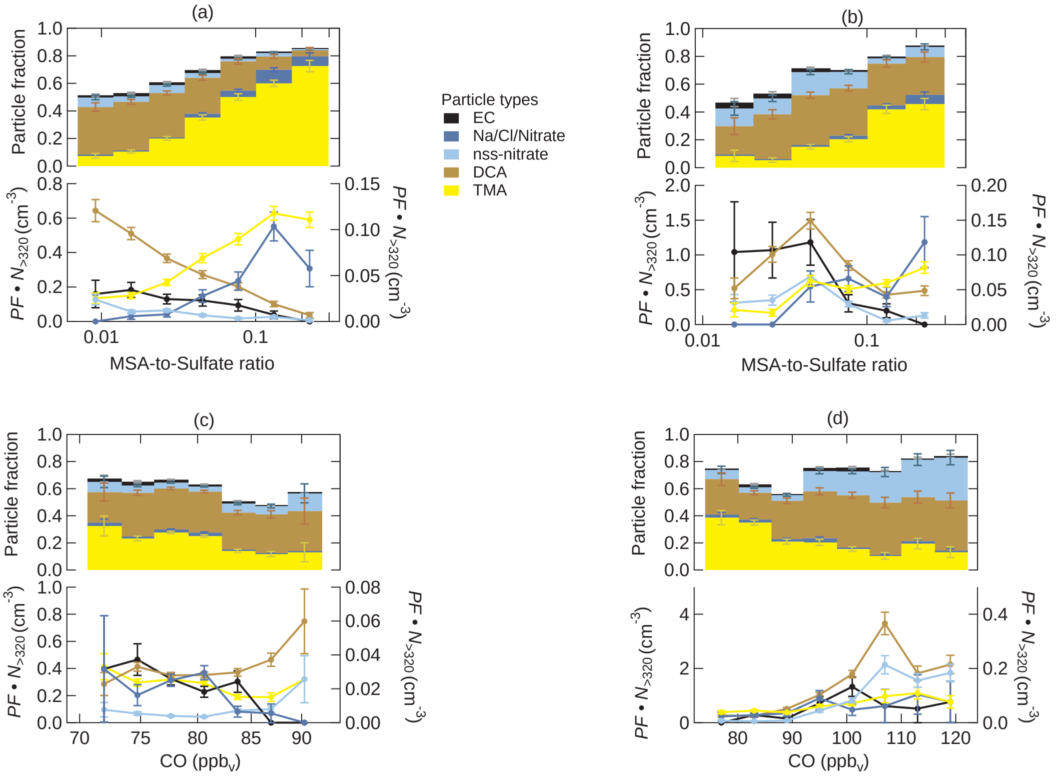

Figure 4.26: Comparison between aerosol composition of the identified main particle types by the ALABAMA and MSA-to-sulfate ratio measured by the HR-ToF-AMS (a-b) as well as CO mixing ratios (c-d) during the Arctic (left panel) and southern (right panel) air mass periods. Figures represent each: (top) the cumulative particle fraction (PF) and (bottom) the scaled number concentration ($PF \cdot N_{>320}$) with right axis referring to EC-containing (black) and Na/Cl/Nitrate-containing (dark blue) particles and left axis referring to nss-nitrate-containing (light blue), DCA-containing (brown), and TMA-containing (yellow) particles. Uncertainty analyses are given in Sect. C.7.

nantly abundant when the air resided for more than 8 days prior to sampling over Arctic open water areas and was as such largely isolated from distant anthropogenic sources (Fig. 4.28a). Together, regional marine-biogenic emissions contributed the abundance of particulate TMA internally mixed with MSA, sulfate, and/or DCA in the summertime marine Arctic BL. Along with marine influences, Na/Cl/Nitrate-containing particles were also largely abundant when the residence time over Arctic open water regions was high (Figs. 4.28a-b). As a result, air mass history together with findings in Sects. 4.3 and 4.4 demonstrates that Na/Cl/Nitrate-containing particles in the summertime Arctic BL were related to locally emitted sea spray particles.

Besides the marine-biogenic source of TMA, it is evident that the abundance of

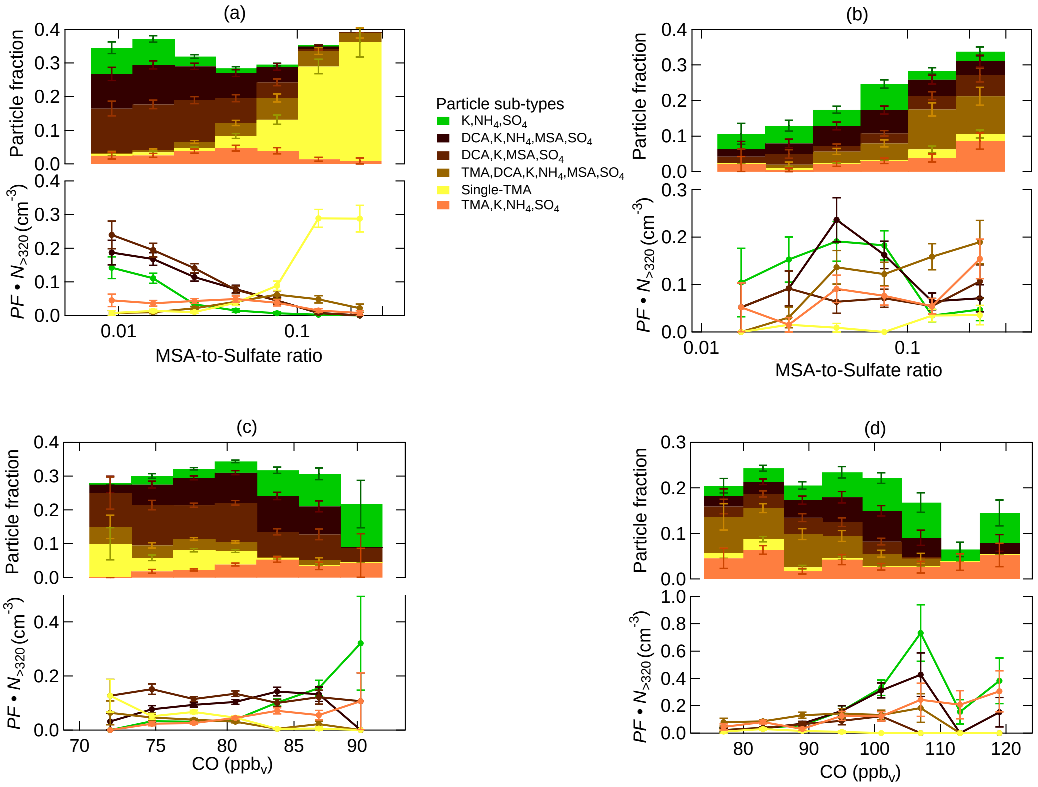

Figure 4.27: Comparison between aerosol composition of the identified particle sub-types by the ALABAMA and MSA-to-sulfate ratio measured by the HR-ToF-AMS (a-b) as well as CO mixing ratios (c-d) during the Arctic (left panel) and southern (right panel) air mass periods. Figures represent each: (top) the cumulative particle fraction (PF) and (bottom) the scaled number concentration ($PF \cdot N_{>320}$). Uncertainty analyses are given in Sect. C.7.

TMA in the Arctic FT might be associated with combustion processes. CO is here used as a conservative tracer of combustion-related emissions. The TMA particle sub-type "TMA,K,NH_4,SO_4" in the FT was linked to transport of aerosol to Arctic regions (see Sect. 4.4). Consistent with this, the comparison with CO mixing ratios demonstrates that this particle sub-type was largely present in higher CO environments (Figs. 4.27c-d). However, by comparing this particle type with air mass history, neither anthropogenic sources nor vegetation fires can clearly be assigned to "TMA,K,NH_4,SO_4"-containing particles (see Fig. C.17). Taken together, several observations provide evidence that two sources contributed to the presence of particulate TMA in the summertime Arctic: inner-Arctic marine-biogenic sources and long-transport of chemically aged aerosol in the Arctic FT from combustion-related sources. Similar to "TMA,K,NH_4,SO_4"-containing particles, the particle sub-type "K,NH_4,SO_4" cannot be attributed to a distinct source sector (Figs. 4.29 and C.17). Interestingly, the presence of this particle sub-type increased with CO mixing ratios

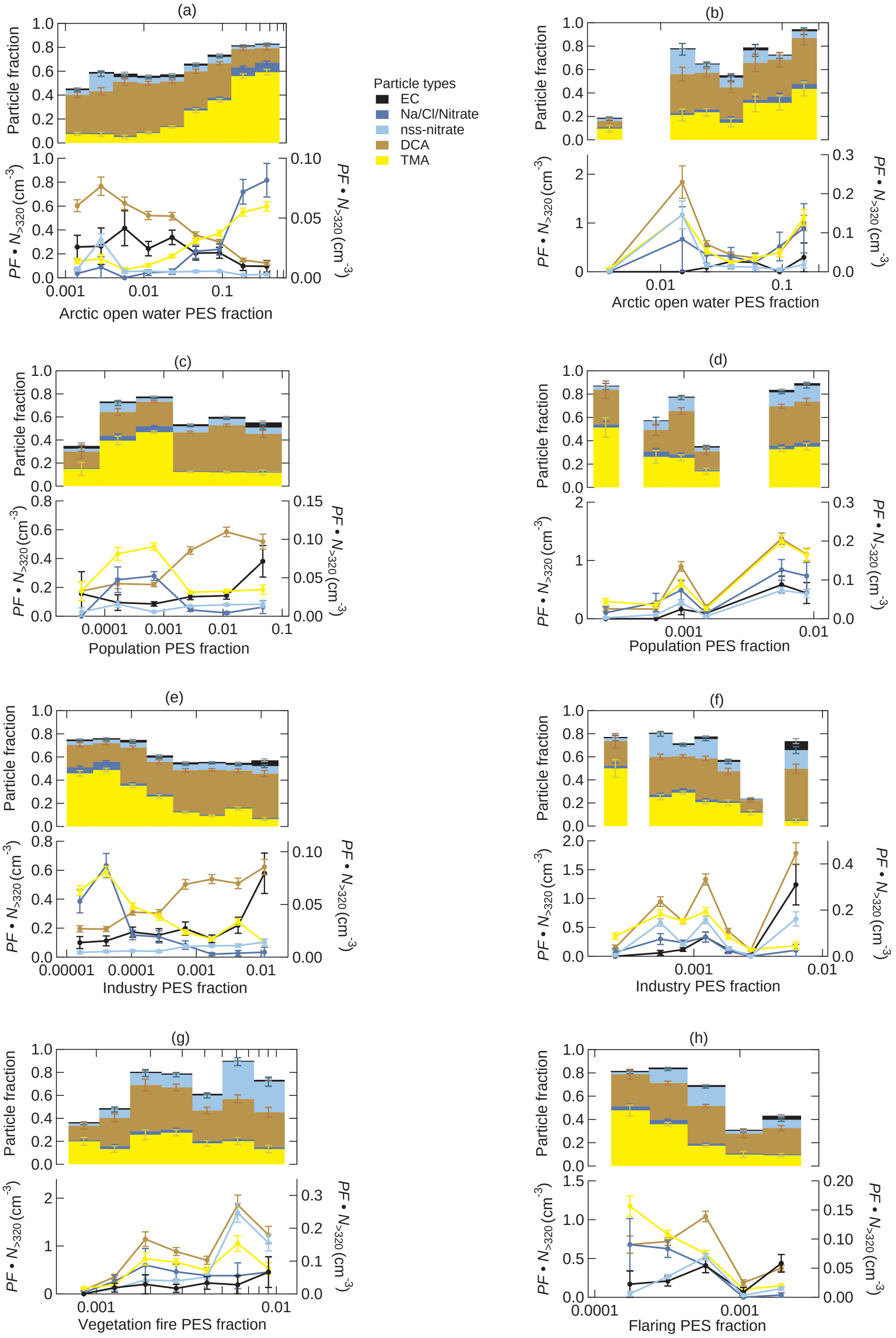

Figure 4.28: Comparison between aerosol composition of the identified main particle types by the ALABAMA and FLEXPART predicted air mass residence time over Arctic open water areas (a-b), populated areas (c-d), industrial areas (e-f), vegetation fires (g), and over areas associated with flaring emissions (h) during the Arctic (a, c, and e) and southern (b, d, and f-h) air mass periods. Figures represent each: (top) the cumulative particle fraction (PF) and (bottom) the scaled number concentration ($PF \cdot N_{>320}$) with right axis referring to EC-containing (black) and Na/Cl/Nitrate-containing (dark blue) particles and left axis referring to nss-nitrate-containing (light blue), DCA-containing (brown), and TMA-containing (yellow) particles. Uncertainty analyses are given in Sect. C.7.

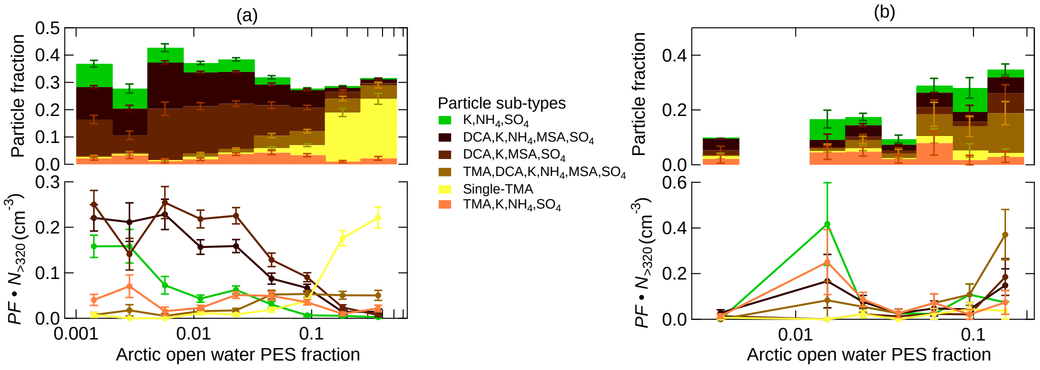

Figure 4.29: Comparison between FLEXPART predicted air mass residence time over Arctic open water areas and aerosol composition of the identified particle sub-types by the ALABAMA during the Arctic (a) and southern (b) air mass periods. Figures (a) and (b) represent each: (top) the cumulative particle fraction (PF) and (bottom) the scaled number concentration ($PF \cdot N_{>320}$). Uncertainty analyses are given in Sect. C.7.

(Figs. 4.27c-d). Thus, particles containing potassium, ammonium, and sulfate might be associated with combustion-related emissions, followed by chemical aging along transport to Arctic regions.

Along with DCA-containing particles in the summertime Arctic, the vertical abundance was influenced by both marine inner-Arctic sources (see above) as well as sources from lower latitudes, depending on the internal mixing state. By comparing the DCA sub-types that were externally mixed from TMA (“DCA,K,NH_4,MSA,SO_4”- and “DCA,K,MSA,SO_4”-containing sub-types) with air mass history, no significant trends were found (see Fig. C.17). In addition, both sub-types show no significant correlation with CO mixing ratio (Figs. 4.27c-d). This is consistent with the variety of DCA precursor gases from terrestrial vegetation, oceans, and anthropogenic activity (e.g., Kawamura and Bikkina, 2016). To summarize, particulate DCA that was externally mixed from TMA can be related to chemically aged aerosol particles that were transported to Arctic regions. However, the occurrence cannot finally be associated with distinct sources.

Anthropogenic and/or vegetation fire emissions contributed largely to the abundance of EC- and nss-nitrate-containing particles in the summertime Arctic FT. The fraction and number concentration of nss-nitrate particles increased with increasing CO mixing ratios (Figs. 4.26c-d). Likewise, air mass history shows that nss-nitrate was largely abundant when time spent over populated areas as well as over vegetation fires was high, particularly during the second period

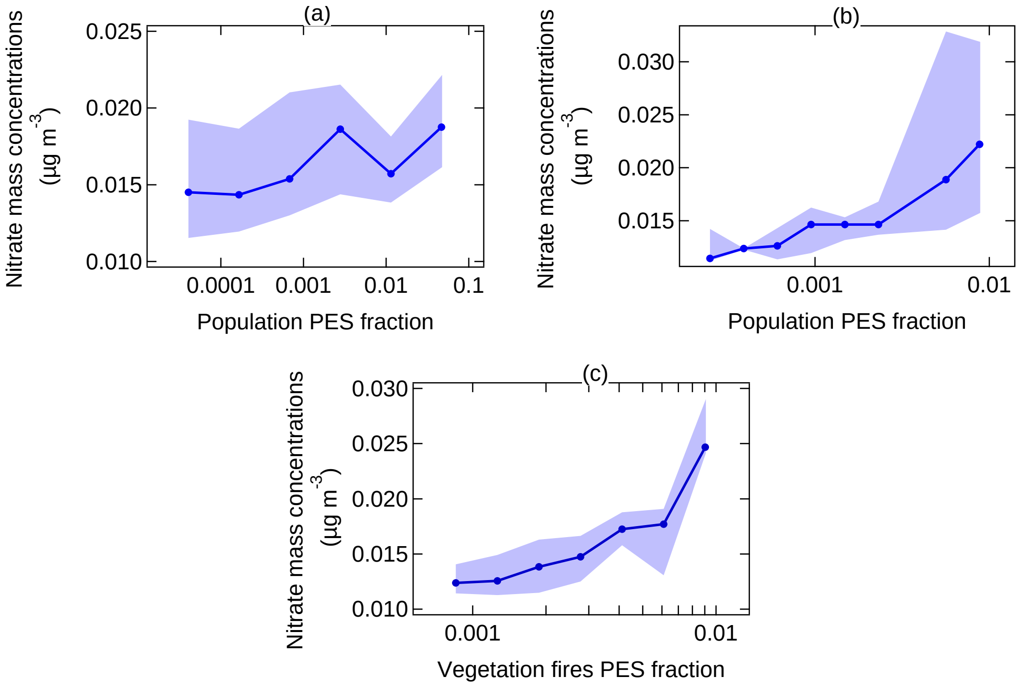

Figure 4.30: Median (blue line) and interquartile ranges (blue shaded area) of the nitrate mass concentrations measured by the HR-ToF-AMS compared to the FLEXPART predicted air mass residence time over populated areas during the Arctic (a) and southern (b) air mass periods as well as over vegetation fires during the southern air mass period (c). Uncertainties are given in Table 1.

(Figs. 4.28d and g, respectively). Thus, the advection of vegetation fire emissions from northern Canada to Arctic regions was accompanied with elevated concentrations of nss-nitrate. Consistent with these results, nitrate mass concentrations measured by the HR-ToF-AMS also increased with influences from vegetation fires and population (Fig. 4.30). Similar to nitrate, enhanced sulfate and ammonium concentrations measured by the HR-ToF-AMS coincided with time spent over vegetation fires in southern latitudes (Fig. C.18).

In parallel, air mass history illustrates that elevated concentrations of EC particles occurred when the residence time over populated and/or industrial areas in Europe and southern North America was high (compare Figs. 4.28c-f with Figs. 4.21e-f). Complementary, the quantitative analysis of refractory black carbon (rBC) by the SP2 shows qualitatively similar trends for the Arctic air mass period (Fig. 4.31). However, the rBC mass concentrations were generally low during the NETCARE 2014 campaign (Schulz et al., 2019), reflecting the largely isolated nature of the summertime Arctic from the rest of the atmosphere. SP2 data from the second period were not considered, as the instrument measured only during three out of the five flights. However, the

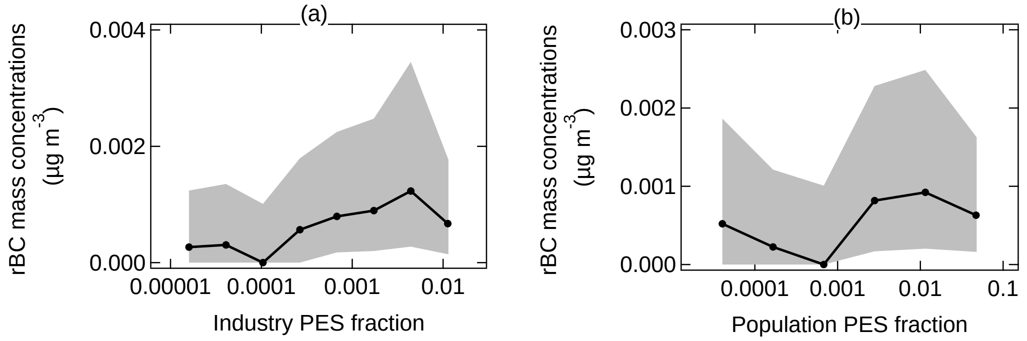

Figure 4.31: Median (black line) and interquartile ranges (black shaded area) of the refractory black carbon (rBC) mass concentration measured by the SP2 compared to the FLEXPART predicted air mass residence time over industrial areas (a) and populated areas (b) during the Arctic air mass period. Uncertainties are given in Table 1.

ALABAMA shows that during the second period the presence of EC particles in the Arctic can partly be associated with flaring emissions in southern North America (compare Figs. 4.28h and 4.21f). Interestingly, Fig. 4.32 illustrates that long-range transport from southern North America to Arctic regions was accompanied with emissions from oil production industry in Alberta, Canada (compare with Fig. 2.12c).

Along with vegetation fires, levoglucosan is a key organic tracer of biomass combustion (Simoneit et al., 1999). However, the identification of levoglucosan by SPMS technique is challenging due to isobaric interferences with several other oxidized organics (see Sect. 3.1.1.2 and Zauscher et al., 2013). During the NETCARE 2014 campaign, 17 % of all analyzed particle mass spectra show ion markers, indicative for the presence of levoglucosan, namely m/z-45, -59, and/or -71 (see Fig. 3.3 and Köllner et al., 2017). However, the presented particle type shows no clear trend with the residence time over vegetation fires, as evident by comparing the particle fraction with FLEXPART predicted air mass history (Fig. C.19). Thus, in contrast to what was previously assumed (Köllner et al., 2017), particle mass spectra with ion signals at m/z-45, -59, and/or -71 cannot be clearly assigned to biomass burning origin.

Taken together, aerosol particle composition in the summertime Arctic lower troposphere was driven by a combination of anthropogenic, vegetation fire, and marine emissions. Regional marine-biogenic emissions influenced the particle composition in the Arctic BL, given by the presence of particles containing TMA, MSA, sulfate, and/or DCA. In contrast, long-range transport of anthropogenic emissions from East Asia, Europe, and southern North America

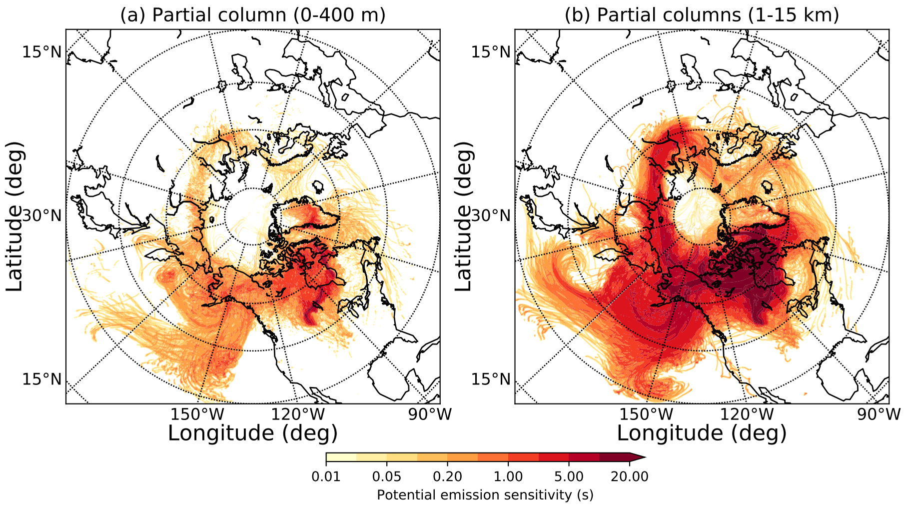

Figure 4.32: FLEXPART 15-days integrated (a) partial column 0 - 400 m and (b) partial column 1 - 15 km potential emission sensitivity (PES; for measurements on 21 July from 18:30 until 18:40 UTC) as an example of transport from oil field emissions in Alberta (Canada) to the measurement region.

provided an enhancement of nss-nitrate and EC particles in the summertime Arctic FT. In addition, intensive vegetation fires combined with the prevailing cyclonic activity largely contributed to the abundance of nss-nitrate-containing particles during the southern air mass period.

4.6 SECONDARY MARINE INFLUENCES ON ORGANIC AEROSOL COMPOSITION

The clean and pristine Arctic background conditions during the first period provide the unique opportunity to study the presence of secondary organic aerosol (SOA) from marine-biogenic precursor gases. Measurements by the HR-ToF-AMS combined with air mass history suggests that marine processes dominated the presence of organic matter (OM) in low SO_4 environments (Fig. 4.33; Willis et al., 2017). The organics-to-sulfate ratio peaked when the residence time over Arctic open water region was highest (Fig. 4.33). Complementary measurements by the ALABAMA of particle mixing state allow now to analyze the contribution of secondary and primary processes on marine organics in the Arctic summer.

When the organics-to-sulfate ratio was highest, ALABAMA analysis suggests organic matter to be attributed with sea spray, TMA, and DCA particles (Fig. 4.34a). The incorporation of OM in sea spray particles was discussed in Sect.

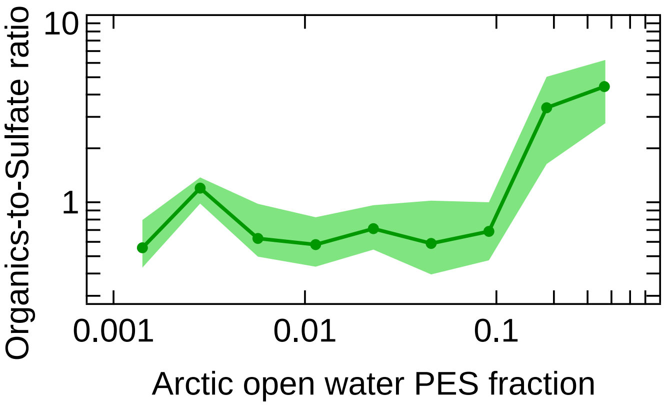

Figure 4.33: FLEXPART predicted residence time over Arctic open water areas compared with median (green line) and interquartile ranges (green shaded area) of the organics-to-sulfate ratio measured by the HR-ToF-AMS. Uncertainties are given in Table 1.

4.3. Briefly, both primary and secondary organic species internally mixed with sea spray particles likely contributed to the organic fraction within the marine Arctic BL. However, the external mixing of sea spray particles from particulate TMA and DCA suggests a role of SOA formation by gaseous emissions from the marine-biogenic environment (Figs. 4.34 and 4.14). Several pieces of evidence strengthen this hypothesis.

The "Single-TMA" sub-type represented a fraction of TMA particles that was externally mixed from any tracer indicating primary aerosol processes, similar to potassium (see Fig. 4.17). Consistent with SOA formation, the size distribution of "Single-TMA" was shifted toward smaller diameters, compared to sea spray particles (compare Figs. 4.20a and 4.23a). Interestingly, this subtype accounted for the dominant fraction of TMA particles in the BL (see Fig. 4.22a). Likewise, these particles were predominantly abundant when the organics-to-sulfate and MSA-to-sulfate ratios were high (Figs. 4.34b and 4.27a, respectively). The mean spectrum of the analogous particle type with dual polarity suggests the presence of aminium salts by TMA, MSA, and/or sulfate (see Fig. 4.17b). Thus, followed by the release of gaseous TMA emissions from Arctic marine biology, an uptake of TMA by acidic particles and subsequent acid-base reactions likely occurred forming aminium salts (e.g., Van Neste et al., 1987; Gibb et al., 1999; Facchini et al., 2008; Ge et al., 2011a; Healy et al., 2015). It is further possible that gas-to-particle partitioning of TMA was enhanced in the vicinity of clouds and fog through dissolution in droplets and subsequent acid-base reactions (e.g., Rehbein et al., 2011).

Particulate DCA internally mixed with TMA ("TMA,DCA,K,NH_4,MSA,SO_4"-

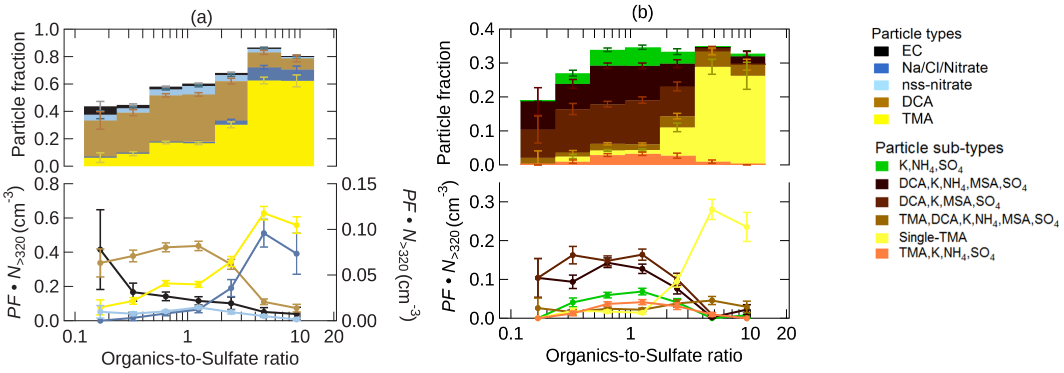

Figure 4.34: Comparison between organics-to-sulfate ratio measured by the HR-ToF-AMS and aerosol composition of the identified main particle types (a) and sub-types (b) by the ALABAMA during the Arctic air mass period. Both figures represent: (top) the cumulative particle fraction (PF) and (bottom) the scaled number concentration ($PF \cdot N_{>320}$). The right axis in (a) refers to EC-containing (black) and Na/Cl/Nitrate-containing (dark blue) particles and the left axis in (a) refers to nss-nitrate-containing (light blue), DCA-containing (brown), and TMA-containing (yellow) particles. Uncertainty analyses are given in Sect. C.7.

containing sub-type) might also result from SOA formation by marine-biogenic precursor gases, such as isoprene and/or fatty acids (see Sect. 4.3 and Kawamura and Bikkina, 2016) owing to several reasons. First, it was shown in Sect. 4.5 that this particle sub-type can be attributed to marine-biogenic sources (see Fig. 4.29a). Second, this sub-type was externally mixed from sea spray particles (see Fig. 4.14). Third, analogous to “Single-TMA” particles, this particle type was abundant when organics-to-sulfate ratio was high (Fig. 4.34b).

Taken together, the characteristics of TMA- and DCA-containing particles in the marine Arctic BL suggest that gaseous emissions from inner-Arctic marine-biogenic sources act as a precursor gases to form secondary organic aerosol.

4.7 DISCUSSION AND COMPARISON WITH LITERATURE

This section will discuss how findings of this study contribute to our current understanding of summertime Arctic aerosol particle composition and related processes (see Sect. 1.2). So far, single particle composition measurements in the Arctic summer are confined to ship- and ground-based studies by Sierau et al. (2014) and Gunsch et al. (2017). Thus, this is the first study providing vertically resolved single particle chemical composition measurements in the Arctic summer. The findings are further compared to results from modeling and experimental studies conducted in the field of Arctic aerosol research.

One interesting finding of this study is that northward transport and related processes contributed significantly to aerosol particle composition in the summertime Arctic lower troposphere, although wet scavenging along transport constitutes the main aerosol removal process in summer (e.g., Croft et al., 2016a). In detail, the presence of EC-containing particles was related to long-range transport of anthropogenic emissions from Europe and southern North America. This result is consistent with recent modeling studies, demonstrating the importance of anthropogenic BC sources in northern Eurasia and North America (e.g., Huang et al., 2010; Bourgeois and Bey, 2011; Sobhani et al., 2018). However, contributions from sources in South Asia cannot be confirmed by this study, which might be related to maximum sampling altitude up to 3.5 km that is less sensitive to Asian pollution sources (e.g., Bourgeois and Bey, 2011; Sharma et al., 2013; Sobhani et al., 2018). Further, distant sources in southern North America can affect the abundance of EC-containing particles in the Arctic summer. Particularly, regions in western Canada (Alberta) that are known to operate numerous oil producing facilities influenced aerosol particle composition in the Arctic summer, consistent with recent work by Stohl et al. (2013) and Evangeliou et al. (2018).

Arctic SPMS studies by Sierau et al. (2014) and Gunsch et al. (2017) reported particle types similar to the EC-containing type (denoted as “ECOC+K+sulfate” type 1a/b and soot type, respectively). Sierau et al. (2014) attributed this particle type to distant combustion-related sources of continental origin, consistent with the current results. In contrast, Gunsch et al. (2017) assigned a large fraction of soot particles to regional Arctic emissions from nearby oil fields at Prudhoe Bay. However, along with the remoteness of Resolute Bay, this study cannot confirm the presence of EC particles to be associated with nearby anthropogenic sources such as shipping and flaring. However, it is likely that ALABAMA measurements presented in this study missed a large portion of fresh EC particles that are predominantly smaller than 100 nm.

Along with northward aerosol transport, anthropogenic and vegetation fire emissions in regions outside the Arctic dominated the abundance of nss-nitrate in the Arctic summer. This result is consistent with previous observational and modeling studies, demonstrating the increase of nitrate concentrations in response to transport from lower latitude sources (Kuhn et al., 2010; Chang et al., 2011), mainly from vegetation fires (Brock et al., 2011; Breider et al., 2014). Interestingly, the current analysis shows no significant evidence of influences from vegetation fires on the abundance of EC particles, contrary to earlier findings (e.g., Hirdman et al., 2010; Bourgeois and Bey, 2011; Stohl et al., 2013; Breider et al., 2014; Sobhani et al., 2018). This result might be explained by the following reasons. It is known from previous field studies that chemically aged BC particles from vegetation fires are thickly coated with organics and inorganics (e.g., Paris et al., 2009; Singh et al., 2010; Kondo et al., 2011; Brock et al., 2011). In addition, a laboratory study by Silva et al. (1999) reported the vast majority of biomass burning particles to include potassium. Given that potassium is known to produce matrix effects, owing to its low ionization efficiency (e.g., Silva and Prather, 2000), positive ion signals, other than K^+, in biomass burning particle spectra are likely suppressed by the presence of potassium. Further, Moffet and Prather (2009) reported negative ion mass spectra of aged soot to be dominated by nitrate and sulfate signals. Together, it is likely that signals of carbon cluster ions, indicative for the presence of EC/soot, are suppressed by other substances that are abundant in biomass burning particles. This result is consistent with previous SPMS measurements during field experiments at southern latitudes characterizing biomass burning aerosol (e.g., Pratt et al., 2011; Zauscher et al., 2013; Gunsch et al., 2018). In detail, mean mass spectra of aged biomass burning particles are generally characterized by the concurrent presence of potassium, sulfate, nitrate, organic acids, and nitrogen-containing organics, confirming findings in this study (see Fig. 4.15c).

Our results further suggest that organic matter in the Arctic marine boundary layer is a result of both primary emissions and secondary processes, confirming recent modeling and experimental studies (Fu et al., 2013b; Leaitch et al., 2018; Croft et al., 2019; Tremblay et al., 2019). Primary marine organics were identified by the internal mixing with sodium, chloride, magnesium, and calcium, indicative for the occurrence of sea salt. This finding reflects the work of other studies in Arctic regions, linking the occurrence of organic-rich sea spray particles with the sea surface carbon pool (e.g., Hawkins and Russell, 2010; Russell et al., 2010; Fu et al., 2013b; Frossard et al., 2014; Wilson et al., 2015). Beside these primary marine OM, it had been recently reported the importance of SOA from precursor gases emitted by marine inner-Arctic sources (e.g., Croft et al., 2019). The work by Croft et al. (2019) is supported by findings of the current study, which provides evidence that a larger population of organic matter was externally mixed from sea spray particles. SOA is represented in the ALABAMA data mainly as TMA and DCA, besides other organic signals that could not be identified.

The presence of dicarboxylic acids from biogenic organic precursors, such as isoprene, monoterpenes, or fatty acids, is known from previous Arctic ground-based and shipborne measurements in summer (e.g., Fu et al., 2009a; Kawamura et al., 2012; Hansen et al., 2014). However, it was further illustrated that gas-phase TMA released by Arctic marine biota contributed to SOA, likely via acid-base reactions to form aminium salts. This result is consistent with numerous chamber studies and lower latitude observations. However, this is the first study demonstrating the incorporation of amines in Arctic aerosol from inner-Arctic marine-biogenic sources. Interestingly, a recent study in Antarctica by Dall'Osto et al. (2019) showed, analogous to this work, significant contributions of secondary particulate TMA from marine-biogenic emissions.

As evident from literature, marine biology releases a variety of alkylamines, such as monomethylamine, dimethylamine, trimethylamine, and diethylamine (e.g., Van Neste et al., 1987; Schade and Crutzen, 1995; Gibb et al., 1999; Ge et al., 2011a; van Pinxteren et al., 2019). However, beside TMA, other alkylamines were not significantly abundant in Arctic ambient single particle spectra and/or could not be identified by isobaric interferences with other substances (see Sect. B.2). The dominant abundance of TMA in Arctic single particle mass spectra might by explained by the following reasons. The highest emission rates from the ocean were measured for TMA, rather than for mono- or dimethylamine (Schade and Crutzen, 1995; Ge et al., 2011a). In addition, the ocean can act as a net sink of dimethylamine (e.g., Van Neste et al., 1987; van Pinxteren et al., 2019). Finally, TMA is known to be the most abundant amine in the atmosphere (Ge et al., 2011a; Healy et al., 2015). In addition to marine inner-Arctic sources, it was shown that particulate TMA in the Arctic summer is linked to long-range transport of combustion-related emissions, albeit to a lesser extent. Possible sources, referring to Ge et al. (2011a), might be given by anthropogenic activities, such as waste incineration, vehicle exhaust, and residential heating as well as biomass burning.

Along with natural aerosol sources, several studies reported on mineral dust from high-latitude sources influencing summertime Arctic surface concentrations (e.g., Breider et al., 2014; Sierau et al., 2014; Sobhani et al., 2018). This cannot be confirmed by ALABAMA aerosol composition measurements. Only a negligible small fraction of the analyzed particles can be assigned to dust particles (not shown) by ion markers indicative for silicon, iron, and aluminum (e.g., Schmidt et al., 2017). However, this result need not necessarily reflects atmospheric composition, as the ALABAMA upper size cut-off during the NETCARE 2014 study was primarily confined to submicron particle size, rather than to supermicron size, where typically dust occurs.

This study raises the question of the representativeness of earlier results from ground-based and shipborne observations of aerosol particle composition in the summertime Arctic lower troposphere. Particularly, the vertical distribution of DCA-containing particles demonstrated that a large portion of organic acids had been transported to Arctic regions, rather than formed in the Arctic. This result is in line with findings of an Arctic airborne study by Schmale et al. (2011), indicating low-volatility highly oxygenated aerosol in pollution plumes from lower latitudes. So far, direct observations of dicarboxylic acids in Arctic regions were confined to measurements in the BL (Kawamura et al., 2012; Leaitch et al., 2018), suggesting summer minimum concentrations due to a combination of diminished transport of precursors and more efficient aerosol wet removal compared to other seasons. Along with results of the NETCARE 2014 observations, it can be assumed that those previous studies likely missed a considerable fraction of DCA in the Arctic summer. Taken together, this study provided new insights into the understanding of marine-biogenic and transport-related processes controlling the vertical structure of summertime Arctic aerosol composition.

5

CONCLUSIONS AND OUTLOOK

Motivated by the limited knowledge of summertime Arctic aerosol, this study aimed for a better understanding of sources and formation processes impacting the vertical structure of aerosol particle chemical composition. Aircraft-based measurements were performed using the single particle aerosol mass spectrometer ALABAMA ($300\,\mathrm{nm} < d_{\mathrm{va}} < 900\,\mathrm{nm}$) in the summertime Canadian Arctic lower troposphere. These measurements add to a very few airborne observations focusing on summertime Arctic aerosol composition. The following part will summarize the main findings of this study with respect to the questions stated in Sect. 1.3. It will also provide ideas on future directions in the field of Arctic aerosol research, based on limitations of this study.

Vertically resolved single particle composition

The study has shown that the vertical structure of single particle composition in the summertime Arctic lower troposphere was driven by a combination of aerosol processes occurring along northward transport and within Arctic regions. Particle composition in the isolated stable stratified boundary layer was characterized by the abundance of particulate trimethylamine (TMA), sodium, chloride, dicarboxylic acids (DCA), and other organics from regional Arctic sources. In contrast, particle composition aloft was characterized by the presence of nitrate, elemental carbon (EC), DCA, and TMA from mid-latitude sources.

Sea spray aerosol from primary sea-to-air emissions

Several pieces of evidence suggest the importance of regional marine influences on the aerosol particle composition in the Arctic summer. Primary sea-to-air emissions contributed to the presence of nitrogen- and oxygen-containing organic matter that was incorporated in sea salt particles, including sodium, chloride, magnesium, and calcium. Sea spray particles with sizes larger than 600 nm were predominantly abundant in the Arctic marine boundary layer. With support from air mass history analysis, it was observed that the presence of sea spray particles correlated with the residence time over Arctic open water areas.

Secondary particulate trimethylamine from Arctic marine sources

Marine-biogenic emissions of precursor gases resulted in a secondary aerosol formation by TMA together with DCA, other unidentified organics, MSA, and/or sulfate. The maximum fraction of TMA-containing particles occurred in the boundary layer where less oxygenated organics were measured by a concurrently operated HR-ToF-AMS. The presence of TMA-containing particles correlated, similar to sea spray particles, with time spent over Arctic open water regions. However, particulate TMA was externally mixed from sea spray particles and smaller in diameter, suggesting a role of marine-derived secondary organic aerosol formation occurring alongside with primary sea-to-air emissions. Beside these inner-Arctic marine sources, this study further identified mid-latitude combustion emissions and subsequent transport as a minor source of TMA in the Arctic. Taken together, these findings provide new insights into the strong biogenic influence on summertime Arctic aerosol, which is likely to increase when sea ice retreats. This work further provides the first comprehensive analysis on amines from Arctic marine sources participating in secondary aerosol formation.

Dicarboxylic acids from mid-latitude and Arctic marine sources

Observations further illustrated that the vertical abundance of particulate DCA in the Arctic summer was influenced by both aerosol transport from mid-latitude sources and Arctic marine-biogenic sources, depending on particle mixing state. When particulate DCA was internally mixed with TMA and present in the Arctic boundary layer, DCA were likely formed by the release of precursor gases from marine biology followed by photochemical processing. However, the vast majority of DCA particles were externally mixed from TMA and abundant in the Arctic free troposphere. Long-range transport of aerosol and precursors from distant sources along with photochemical aging thus influenced the abundance of DCA particles in the summertime Arctic free troposphere. Taken together, these findings add to our understanding of Arctic aerosol from previous work, because previous studies made use of ground-based and shipborne datasets. Combined with the largely stable stratified nature of the Arctic lower troposphere, previous datasets might be less sensitive to organic acids from long-range transport and related processes. The current findings thus emphasize the importance of measuring vertically resolved aerosol composition in the Arctic.

Nitrate and elemental carbon from mid-latitude sources

Along with aerosol transport into Arctic regions, a combination of both vegetation fires in Canada and anthropogenic sources in Europe, North America, and East Asia contributed to the presence of particles containing nitrate and/or EC in the summertime Arctic lower troposphere. First, non-sea-spray (nss)-nitrate-containing particles were largely present in high CO environments. Second, the presence of particles containing EC and/or nitrate correlated with time spent over populated and industrial areas in Europe, East Asia, and southern North America. In particular, EC emissions from oil production industry, including flaring, in Alberta (Canada) were detected. In addition, elevated concentrations of nss-nitrate occurred when the residence time over vegetation fires in northern Canada was high. Third, particles sizes of both types were larger compared to TMA-containing particles, suggesting a role of chemical aging during transport. Together, these results indicate the important role of mid-latitude aerosol sources on summertime Arctic particle composition in the lower free troposphere. Particularly, contributions from biomass burning emissions on summertime Arctic aerosol are likely to increase under future climate predictions (e.g., Randerson et al., 2006; de Groot et al., 2013; Marelle et al., 2018; Evangeliou et al., 2019).

To conclude, this study contributes to our fundamental understanding on Arctic marine and mid-latitude sources as well formation processes of summertime Arctic aerosol composition. The observations illustrated the importance of measuring the aerosol particle mixing state, in order to elucidate the relative role of primary and secondary processes as well as of various aerosol sources. However, several important questions remain, partly owing to limitations of the current study. Being limited by the spatial and temporal range of the NETCARE 2014 measurements, it is difficult to asses the representativeness of the findings on a broader Arctic picture. Future widespread and long-term measurements would help to extend the results to other Arctic regions and seasons. Lagrangian flight experiments would help to better constrain the relative role of aerosol processing, including wet removal and photochemical aging, on summertime Arctic particle composition. Based on limitations in sampling altitude, future Arctic airborne measurements in the mid to upper troposphere are necessary to further characterize the impact of mid-latitude pollution sources on summertime Arctic aerosol properties. This research has further raised questions on the contribution of amines to particle nucleation and growth as well as within cloud processing in the summertime Arctic. Therefore, Arctic field observations of nucleation and Aitken mode particle composition (by using Atmospheric-Pressure-interface–Time-of-Flight Mass Spectrometers (APi-ToF-MS) and Thermal Desorption Chemical Ionization Mass Spectrometry (TDCIMS)) combined with precursor gases (by using for example Gas Chromatography-Mass Spectrometry (GC-MS)) are needed to improve our understanding of particle formation and growth. In addition, aerosol measurements coupled with a counterflow virtual impactor are required to better understand the interaction between amines and other marine-derived species with summertime Arctic clouds. This has been realized in a follow-up study in 2017 (ACLOUD). Future field studies should also deploy instrumentation to quantify amine concentrations in sea water and in the Arctic atmosphere in gas as well as particle phase. Finally, it is of relevance to further characterize organic compounds in Arctic aerosol along with their sources, formation processes, and impact on clouds.

A

SUPPLEMENTARY INFORMATION FOR CHAPTER 2

A.1 UPSTREAM FLOW RATE AND INLET ORIFICE DIAMETER: DEPENDENCE ON LENS PRESSURE

The ALABAMA upstream volumetric flow rate (f_{upstream}) as a function of the pressure inside the aerodynamic lens (p_{lens}) was measured (Fig. A.1) using a thermal mass flowmeter (TSI Incorporated, 2003). The flowmeter displayed the flow at standard conditions (294.2 K and 1013 hPa; TSI Incorporated, 2003), referred in this section as STP. The equivalent CPI orifice diameter (d_{CPI}) as a function of p_{lens} (Fig. A.1) was calculated as follows:

$$d_{\text{CPI}} = \frac{d_{\text{nozzle}}}{\sqrt{\frac{f_{\text{lens}}}{f_{\text{upstream}}}}}, \tag{14}$$

with the diameter of the last lens aperture (d_{nozzle}) (3 mm; Liu et al. (2007)), and the volumetric flow rate inside the lens (f_{lens}) that is defined as follows:

$$f_{\text{lens}} = \frac{f_{\text{upstream}} \cdot p_{\text{upstream}}}{p_{\text{lens}}}. \tag{15}$$

The f_{upstream} (in $\text{cm}^3\,\text{s}^{-1}$) was further used to derive particle number concentrations (N_{coinc} and N_0 in cm^{-3}) from particle counts measured by the ALABAMA (C_{coinc} and C_0 in s^{-1}) as follows:

$$N = \frac{C}{f_{\text{upstream}}}. \tag{16}$$

A.2 UNCERTAINTY ANALYSES

Inlet transmission and detection efficiency

The absolute uncertainty of the detection efficiency (σ_{DE}^{abs}) and the absolute uncertainty of the inlet transmission efficiency ($\sigma_{TE_{\text{Inlet}}}^{\text{abs}}$) are calculated based on Poisson statistics and Gaussian propagation of uncertainties:

$$\sigma_{TE_{\text{Inlet}}}^{\text{abs}} = \frac{N_0}{N_{\text{reference}}}\sqrt{\left(\sigma_0^{\text{rel}}\right)^2 + \left(\sigma_{\text{reference}}^{\text{rel}_1}\right)^2 + \left(\sigma_{\text{reference}}^{\text{rel}_2}\right)^2 + \left(\sigma_{\text{CPI}}^{\text{rel}}\right)^2}, \tag{17a}$$

$$\sigma_{\text{DE}}^{\text{abs}} = \frac{N_{\text{coinc}}}{N_{\text{reference}}}\sqrt{\left(\sigma_{\text{coinc}}^{\text{rel}}\right)^2 + \left(\sigma_{\text{reference}}^{\text{rel}_1}\right)^2 + \left(\sigma_{\text{reference}}^{\text{rel}_2}\right)^2 + \left(\sigma_{\text{CPI}}^{\text{rel}}\right)^2}, \tag{17b}$$

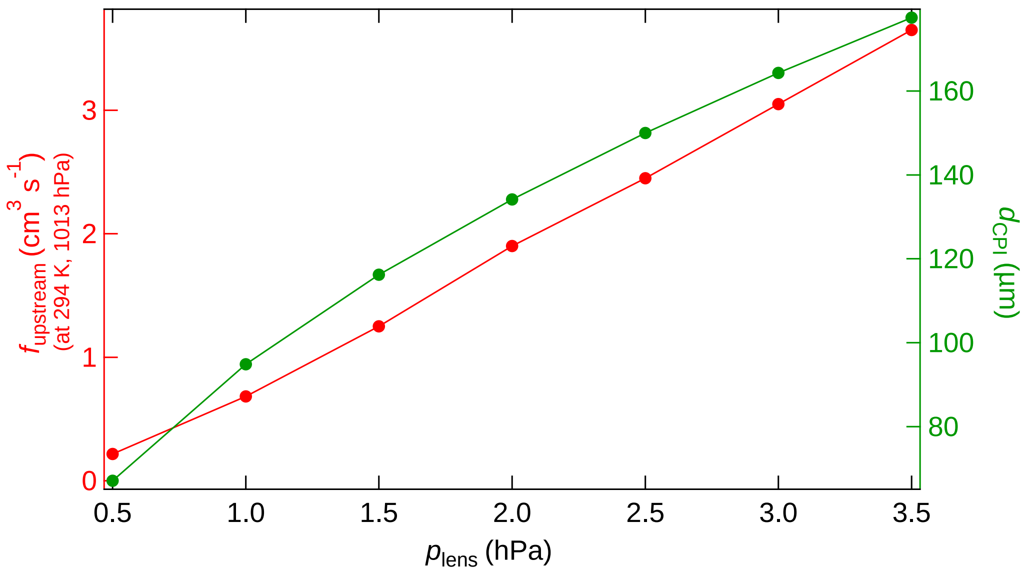

Figure A.1: Upstream flow rate (f_{upstream} in red) and equivalent CPI orifice diameter (d_{CPI} in green) as a function of lens pressure (p_{lens}). Uncertainty analyses are given in Sect. A.2.

with the relative statistical uncertainty of the particle counts detected by both ALABAMA optical detection stages ($\sigma^{\text{rel}}_{\text{coinc}}$) and the relative statistical uncertainty of the particle counts detected by the ALABAMA first optical detection stage (σ^{rel}_{0}) that are defined as follows:

$$\sigma^{\text{rel}}_{0} = \frac{1}{\sqrt{C_0}}, \tag{18a}$$

$$\sigma^{\text{rel}}_{\text{coinc}} = \frac{1}{\sqrt{C_{\text{coinc}}}}, \tag{18b}$$

with the particle counts detected by the ALABAMA first optical detection stage (C_0) and the particle counts detected by both ALABAMA optical detection stages within a pre-defined time interval (C_{coinc}). The relative statistical uncertainty of the particle counts detected by the reference instrument ($\sigma^{\text{rel}_1}_{\text{reference}}$) is defined as follows:

$$\sigma^{\text{rel}_1}_{\text{reference}} = \frac{1}{\sqrt{C_{\text{reference}}}}, \tag{19}$$

with the particle counts detected by the reference instrument ($C_{\text{reference}}$). The reference instruments reproducibilities ($\sigma^{\text{rel}_2}_{\text{reference}}$) are 3 % and 2 % for the OPC (GRIMM Aerosol Technik, 2008) and the CPC (GRIMM Aerosol Technik, 2003), respectively. For the Arctic field experiment, the UHSAS was used as reference instrument with $\sigma^{\text{rel}_2}_{\text{reference}}$ is 5 % by the instrument counting efficiency of 95 % (see Table 1; Cai et al., 2008; Schulz et al., 2019). Equations 17a and

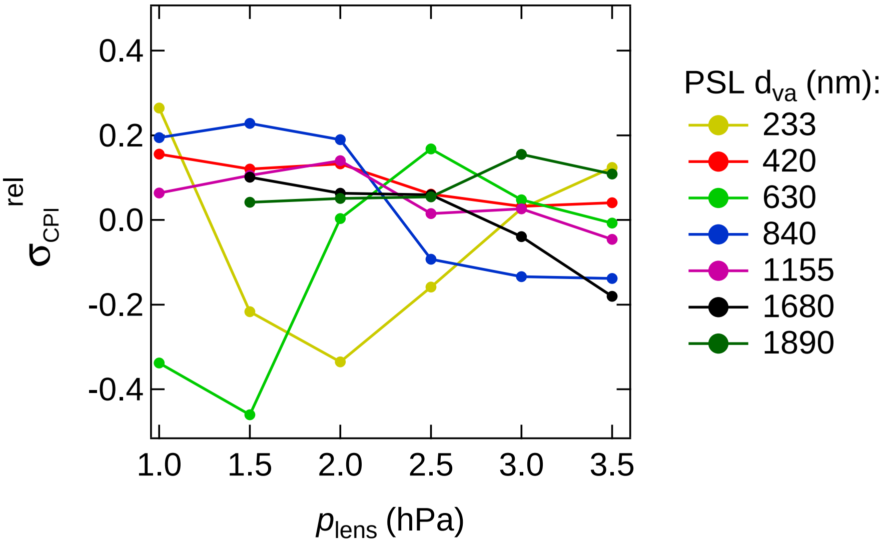

Figure A.2: Reproducibility of the CPI transmission efficiency ($\sigma_{\mathrm{CPI}}^{\mathrm{rel}}$) as a function of lens pressure (p_{lens}) and particle size (d_{va}).

b further include the reproducibility of the CPI transmission efficiency ($\sigma_{\mathrm{CPI}}^{\mathrm{rel}}$), which is defined as follows:

$$\sigma_{\mathrm{CPI}}^{\mathrm{rel}} = \frac{\left| \left(\frac{N_{\mathrm{coinc}}}{N_{\mathrm{reference}}}\right)_{\mathrm{pinch}} - \left(\frac{N_{\mathrm{coinc}}}{N_{\mathrm{reference}}}\right)_{\mathrm{relax}} \right|}{\left(\frac{N_{\mathrm{coinc}}}{N_{\mathrm{reference}}}\right)_{\mathrm{pinch}}}. \tag{20}$$

To obtain $\sigma_{\mathrm{CPI}}^{\mathrm{rel}}$, measurements with variable p_{lens} described in Sect. A.3 were repeated, starting at highest/lowest p_{lens} and subsequent stepwise pinching/relaxing of the O-ring, respectively. This method accounts for CPI hysteresis effects and general reproducibility. Results in Fig. A.2 were used to determine the average value $\sigma_{\mathrm{CPI}}^{\mathrm{rel}}$ of 0.12 ± 0.10. Reasons for the variable CPI transmission efficiency at constant lens pressure and particle size remain unclear. It is likely that the O-ring folding varies between the process of pinching and relaxing.

Systematic uncertainties of parameters considering the particle detection by the ALABAMA include the flowmeter accuracy of 2 % (TSI Incorporated, 2003) and the flowmeter offset that was not reported. However, the flow offset by the TSI flowmeter is typically between $0.01\,\mathrm{l\,min^{-1}}$ and $0.03\,\mathrm{l\,min^{-1}}$. Systematic uncertainties of parameters considering the particle detection by the reference instruments OPC and CPC include the flow accuracy of 5 % and 3 % (GRIMM Aerosol Technik, 2008, 2003), respectively. Systematic uncertainties are generally not considered for the depicted uncertainty bars.

Table 5: Uncertainty of the modal diameter ($\mathrm{d_{va}}$) of manufactured PSL particles. In case, the uncertainty was not reported, it was assumed to be 10 nm, indicated by the asterisk.

($\mathrm{d_{va}}$ ± uncertainty) nm	Manufacturer	Catalog no
*201 ± 10	Sigma Aldrich	95581-10ML-F
233 ± 3	Polysciences, Inc.	64013
252 ± 6	Duke Scientific Corporation	3240A
315 ± 6	Duke Scientific Corporation	3300A
420 ± 5	Polysciences, Inc.	64017
*518 ± 10	Sigma Aldrich	95585-10ML-F
*578 ± 10		
630 ± 8	Polysciences, Inc.	64021
840 ± 9	Duke Scientific Corporation	64025
1155 ± 18	Duke Scientific Corporation	4011A
1680 ± 19	Duke Scientific Corporation	4016A
1890 ± 23	Duke Scientific Corporation	4018A
2100 ± 23	Duke Scientific Corporation	4011A

Particle beam divergence

The absolute uncertainty of the qualitative measure of particle beam divergence ($\sigma^{\mathrm{abs}}_{BD_{\mathrm{qualit}}}$) is calculated based on Poisson statistics and Gaussian propagation of uncertainties:

$$\sigma^{\mathrm{abs}}_{BD_{\mathrm{qualit}}} = \frac{N_0}{N_{\mathrm{coinc}}}\sqrt{\left(\sigma^{\mathrm{rel}}_{0}\right)^2 + \left(\sigma^{\mathrm{rel}}_{\mathrm{coinc}}\right)^2}. \tag{21}$$

Upstream pressure

Upstream pressure in Fig. 2.3 is derived from a pressure sensor built in the OPC. The OPC manual does not provide details on the sensor type. However, pictures of the sensor indicate that the manufacturer is Honeywell. The relative uncertainty is specified with ± 2.0 % (Honeywell, 2019).

Lens pressure

The lens pressure inside the ALABAMA is measured by an analog pressure sensor from Analog Microelectronics GmbH (type: AMS 4711). The relative uncertainty is specified maximum with ± 2.5 % (Analog Microelectronics, 2015).

PSL particle size

Manufacturers provide the uncertainty of the modal geometric diameter of PSL particles. This value is multiplied by 1.05 to derive the uncertainty of the modal $\mathrm{d_{va}}$ value (Table 5).

Hit rate

The absolute uncertainty of the hit rate ($\sigma_{HR}^{\mathrm{abs}}$) is calculated using binomial statistics:

$$\sigma_{HR}^{\mathrm{abs}} = \frac{\sqrt{N_{\mathrm{hits}}(1 - HR)}}{N_{\mathrm{shots}}}, \tag{22}$$

with the number of particles that are successfully ionized by the ablation laser and that create a mass spectrum (N_{hits}), the number of laser shots (N_{shots}), and the hit rate (HR).

Collection efficiency

The absolute uncertainty of the collection efficiency ($\sigma_{CE}^{\mathrm{abs}}$) is calculated using Gaussian propagation of uncertainties:

$$\sigma_{CE}^{\mathrm{abs}} = \sqrt{(HR \cdot \sigma_{DE}^{\mathrm{abs}})^2 \cdot (DE \cdot \sigma_{HR}^{\mathrm{abs}})^2}. \tag{23}$$

Particle velocity

The absolute uncertainty of the particle velocity ($\sigma_{V_p}^{\mathrm{abs}}$) is calculated using Gaussian propagation of uncertainties:

$$\sigma_{V_p}^{\mathrm{abs}} = \frac{0.07\,\mathrm{m} \cdot 25\,\mathrm{MHz}}{upcount^2} \cdot \sigma_{upcount}^{\mathrm{abs}}, \tag{24}$$

with the absolute uncertainty of the upcount value ($\sigma_{upcount}^{\mathrm{abs}}$), given by the half bin width of the *upcount* bar in the histograms (Figs. A.9 and A.11).

Table 6: ALABAMA modifications relevant for the experiments conducted within this study. The Arctic field experiment NETCARE 2014 was conducted in July 2014 (Sects. 2.1.4-2.1.5 and Ch. 4). Laboratory measurements in Sect. 2.1.2 were conducted between October and December 2015. Laboratory measurements in Sects. 2.1.3, 2.1.4, A.3, and A.6 were conducted from September to October 2017.

Time	Prior setup	New setup
09/14	bipod holding of the lens	tripod holding of the lens (Fig. A.3)
→	20 mm distance between lens bottom and skimmer top	$<$ 20 mm distance between lens bottom and skimmer top
09/14	skimmer orifice diameter 0.3	skimmer orifice diameter 0.35 mm
05/17	O-ring material Nitril/NBR	O-ring material silicon
05/17	O-ring inner diameter 0.8 mm	O-ring inner diameter 0.5 mm

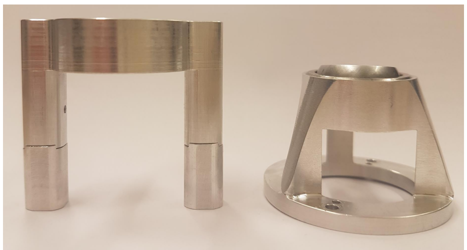

Figure A.3: Bipod (left) and tripod (right) holding of the aerodynamic lens.

A.3 DETECTION EFFICIENCY: DEPENDENCE ON LENS PRESSURE

The ALABAMA detection efficiency (see Eq. 6) is additionally influenced by the aerodynamic lens pressure (e.g., Liu et al., 2007). Section 2.1.3 introduced the ALABAMA detection efficiency as a function of particle size at constant lens pressure of 3.5 hPa. Along the same experiment, measurements of *DE* at varying lens pressure between 0.5 and 3.5 hPa were conducted, by varying the CPI orifice diameter. To the author's knowledge, this is the first study to investigate the influence of the lens pressure on the ALABAMA detection efficiency.

Figure A.4 shows the detection efficiency as a function of lens pressure and particle size at upstream pressure of approximately 1013 hPa. The increase of the ALABAMA *DE* with lens pressure can be associated with the performance of the aerodynamic lens (see Sect. 2.1.3). Briefly, Zhang et al. (2002) recommended a particle Stokes number less than 1 to obtain both a reasonable

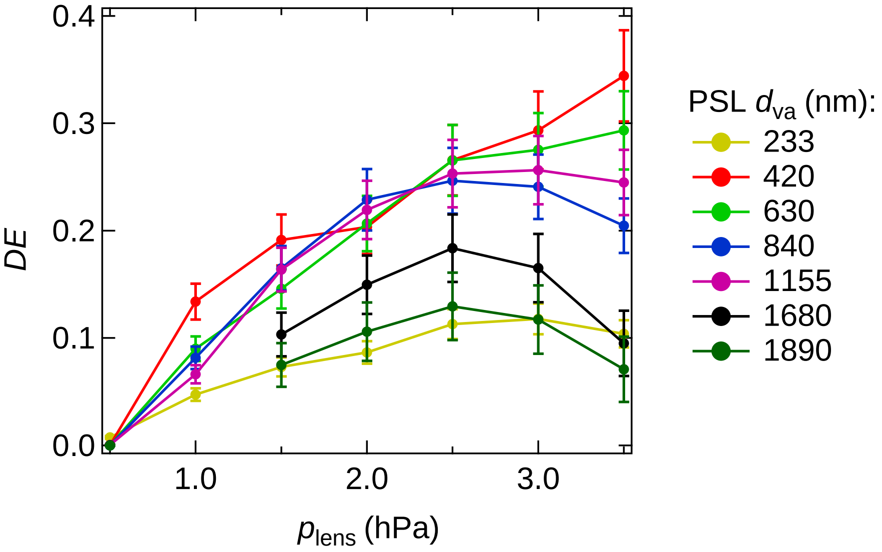

Figure A.4: Detection efficiency (DE) as a function of both lens pressure (p_{lens}) and particle size (d_{va}). Uncertainty analyses are given in Sect. A.2.

particle beam collimation and small impaction losses. The Stokes number in the free molecular regime is roughly $\propto p_g^{-1}$ (here, p_{lens}) and $\propto d_p$ (Zhang et al., 2002) if other gas and particle properties as well as lens characteristic dimensions are kept constant. Thus, a higher lens pressure favors the transmission of larger particles.

In contrast, measurements in Fig. A.4 show a decreasing DE for particles larger than 800 nm and a lens pressure higher than 2.5 hPa. This trend might be caused by a combined effect of a shifted particle beam symmetry axis (Brands et al., 2011) and a varying particle beam divergence with particle size and lens pressure (Zhang et al., 2002, 2004). The beam axis shift as a function of particles size can likely be attributed to lens manufacturing tolerances and assembling of the multiple lens apertures (Schreiner et al., 1999; Murphy, 2006). Measurements at variable lens positions (lens scan) controlled by micrometer screws would be necessary (Klimach, 2012; Clemen et al., 2019) to quantitatively determine both beam properties (particle beam divergence and axis shift). However, the aerodynamic lens was kept at a fixed position for each particle size and lens pressure, since micrometer screws are not yet implemented in the ALABAMA setup. Another measure, albeit qualitative, of the particle beam divergence (BD_{qualit}) is given by comparing N_0 and N_{coinc}:

$$BD_{\mathrm{qualit}} = \frac{N_0}{N_{\mathrm{coinc}}}. \tag{25}$$

Figure A.5 shows two features. First, the beam divergence was minimal for particles between 400 nm and 800 nm. Second, a higher lens pressure tended

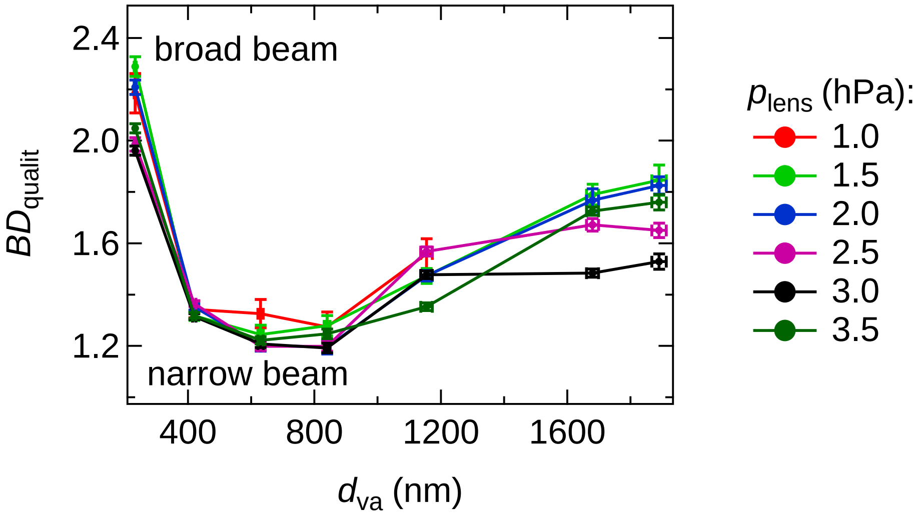

Figure A.5: Qualitative measure of particle beam divergence (BD_{qualit}) as a function of both particle size (d_{va}) and lens pressure (p_{lens}). Uncertainty analyses are given in Sect. A.2.

to result in a less divergent particle beam. Both qualitative results confirm the experimental and modeling results by Klimach (2012) and Zhang et al. (2002, 2004), respectively. Thus, it is likely that an increasing beam divergence for particles larger than 800 nm and lens pressure larger than 2.5 hPa caused a decreasing detection efficiency. Taken together, the experimental setup in this study is just partly applicable to characterize the ALABAMA detection efficiency as a function of lens pressure. Measurements with scanning lens positions controlled by micrometer screws would significantly help to understand the role of particle beam divergence and axis shift with varying lens pressure and particle size on the detection efficiency.

A.4 VARIABILITY OF THE PARTICLE HIT RATE

The ALABAMA data acquisition software directly displays the hit rate based on Eq. 8 as moving average over the last 100 ablation laser shots (see black line in Fig. A.6), to monitor the instrument performance during operation. It turned out that the hit rate moving average is fluctuating, although hit rate-influencing parameters are kept constant. Those hit rate variabilities are inconvenient for aligning the ablation laser. This section briefly discusses the underlying process.

The variability of the hit rate moving average results from the laser shot counting statistics that is given by the Binomial distribution. The concept of the hit

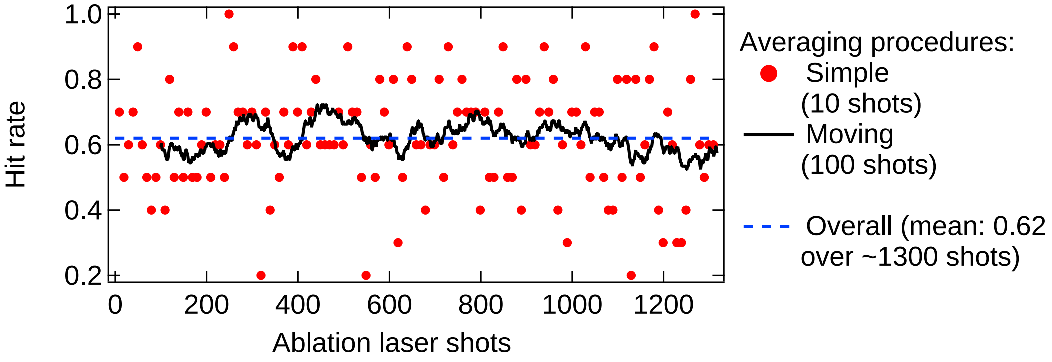

Figure A.6: Two averaging methods for ALABAMA hit rate calculation (see Eq. 8): simple average (red dots) of the number of recorded mass spectra (N_{hits}) over 10 ablation laser shots (N_{shots}) and moving average (black line) of the number of recorded mass spectra (N_{hits}) over 100 shots (N_{shots}). The moving average is used in the ALABAMA data acquisition software. The blue dashed line indicates the averaged ALABAMA hit rate over roughly 1300 shots with 0.62 ± 0.17 (mean $\pm 1\sigma_{\text{measured}}$). The data set is from an arbitrary ALABAMA experiment, at which crucial hit rat-influencing parameters were kept constant.

rate can be described by a Bernoulli experiment. Only two mutually exclusive events can happen: either a mass spectrum is created by laser ablation/ionization ("Hit") or not ("non-Hit"). Here, the occurrence of "Hit" is noted as 1 and of "non-Hit" as 0. The Binomial probability distribution results from a chain of such Bernoulli experiments (e.g., Schönwiese, 2000). It is shown that the hit rate simple average of a real ALABAMA experiment (with $\mathrm{N} = 10$ trials; see Fig. A.6) is to a good approximation binomially distributed (Fig. A.7). The relative standard deviations of the measured hit rate ($\sigma_{\text{measured}} = 0.17$) and of the Binomial probability distribution (σ_{binomial}[1] $= 0.15$) differ by approximately 10 %. The observed variability of the hit rate is thus determined by the statistical distribution of the hit rate. Therefore, the online hit rate display is only of limited use for the alignment of the ablation laser.

---

[1] The relative standard deviation of the Binomial distribution is calculated as follows: $\sigma_{\text{binomial}} = \frac{\sqrt{\mathrm{N \cdot p \cdot q}}}{N}$.

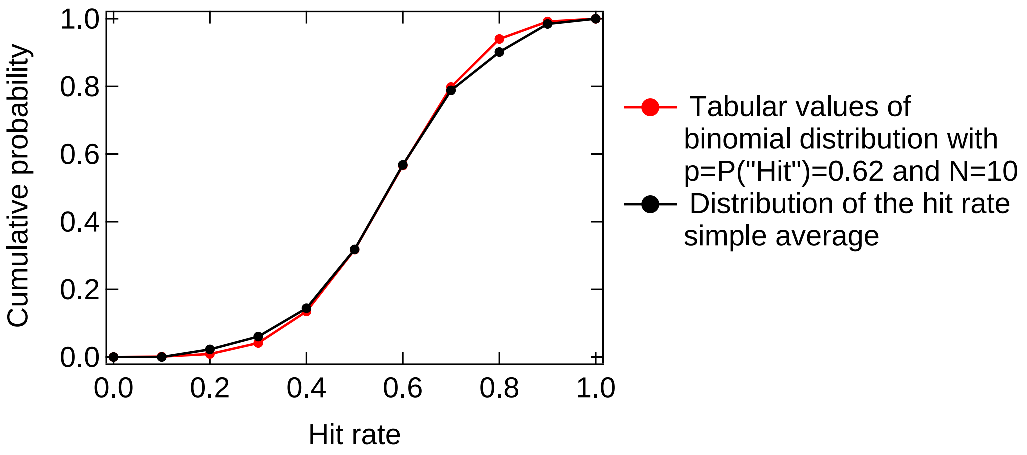

Figure A.7: The red line represents the cumulative Binomial probability distribution of tabular values with probability $p = 0.62$ and $q = 0.38$ as well as with 10 trials (N). The black line represents the cumulative distribution of ALABAMA hit rate measurements in 10 trials (Fig. A.6).

A.5 SIZE OF COLLECTED PARTICLES DURING THE ARCTIC FIELD EXPERIMENT

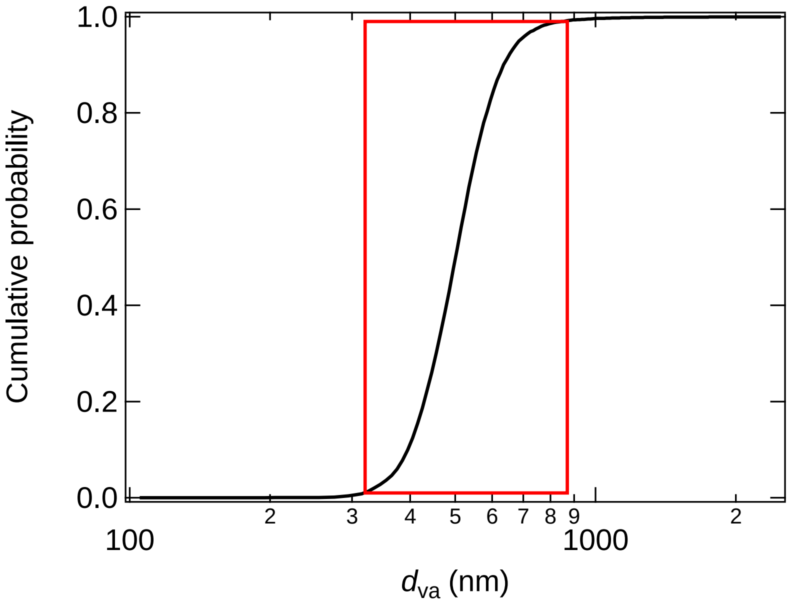

Figure A.8: Cumulative probability distribution of the vacuum-aerodynamic diameter (d_{va}) of collected particles during the Arctic field experiment. The red box indicates the presence of 98 % of all collected particles, providing the size range between 320 nm and 870 nm (d_{va}).

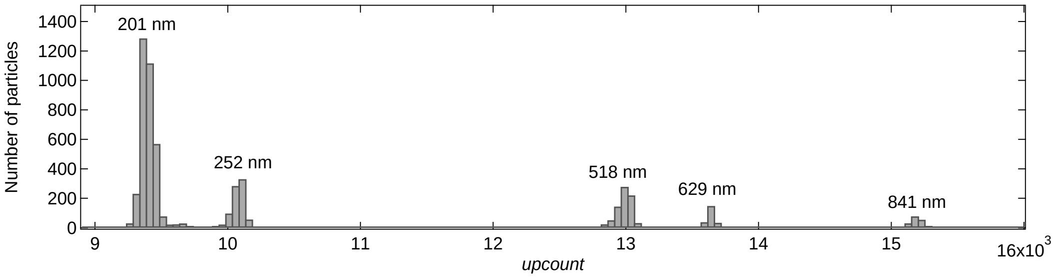

Figure A.9: Histogram of *upcount* values for various PSL particle d_{va} in nm at 3.2 hPa lens pressure during the Arctic field experiment in July 2014 (NETCARE 2014).

Figure A.8 shows the size range of all particles collected[2] during the Arctic field experiment in July 2014. The 1 % and 99 % percentiles are given by 320 nm and 870 nm d_{va}.

A.6 PARTICLE SIZING: DEPENDENCE ON LENS PRESSURE

The particle velocity depends on aerodynamic lens pressure (e.g., Roth, 2014). The ALABAMA can be operated at different lens pressure, so that typically one size calibration is conducted during each field experiment. However, this section introduces an approach to derive fit coefficients, according to Eq. 10, as a function of p_{lens}. Along the same laboratory experiment explained in Sect. A.3, measurements of the *upcount* value for various PSL d_{va} and p_{lens} were conducted (Fig. A.10). The modal values of the *upcount* histograms (Fig. A.11) together with Eq. 9 provide the particle velocity. According to Eq. 10, the pressure-dependent global fit provides the fit coefficients, V_0 and V_{g1}, as a function of p_{lens}, where k is assumed to be independent on p_{lens}[3] (Fig. A.10). The fit calculates the effective k with (303.8 ± 5.0) nm. It turned out that V_0, in contrast to V_{g1}, is in good approximation a linear function of p_{lens} (Figs. A.12 and A.13, respectively). The size calibration in July 2014 (see Fig. 2.7) shows different values and thus different fit coefficients compared to the September/October 2017 laboratory measurements (this section) caused by a modified ALABAMA lens holding, as described in Table 6.

Within the scope of this PhD project, the ALABAMA was involved in another field experiment, so-called BALTIC'15 campaign, that was performed in

---

[2] To note, collected particles are all particles that were successfully detected and ablated/ionized.

[3] When considering size calibration data for each lens pressure separately (not shown), it turned out that the fit coefficient k is constant within its uncertainties and thus independent on lens pressure.

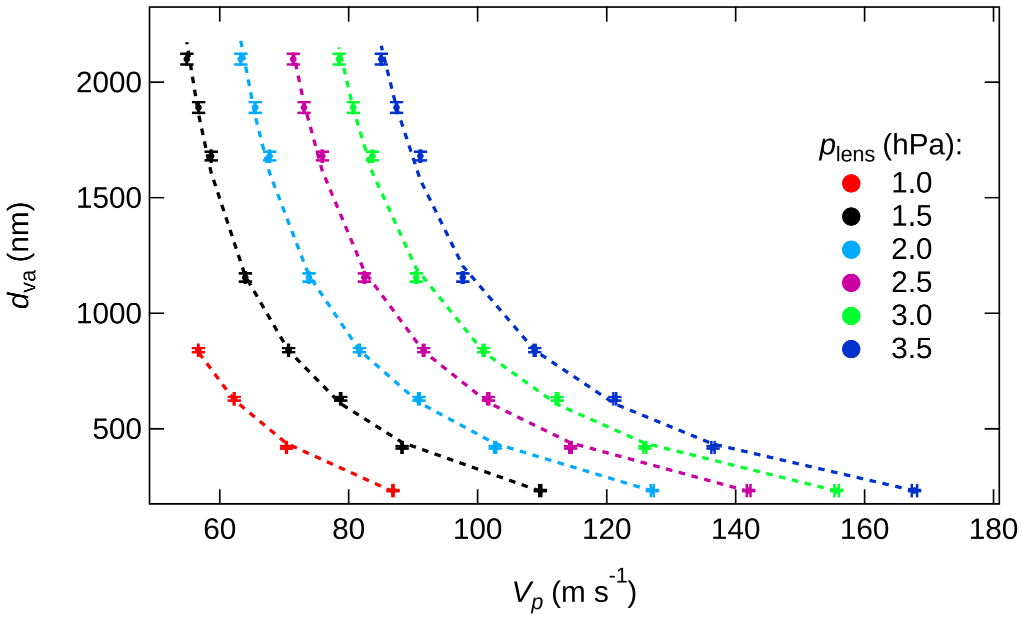

Figure A.10: Vacuum-aerodynamic diameter (d_{va}) as a function of both particle velocity (V_p) and lens pressure (p_{lens}). Uncertainty analyses are given in Sect. A.2. A global fit was conducted (dashed lines) according to Eq. 10 resulting in V_0 and V_{g1}, both of which depending on p_{lens} (Figs. A.12 and A.13, respectively), as well as an effective value of k with (303.8 ± 5.0) nm. Fit functions (dashed lines) consider only the uncertainty of d_{va} and not that of V_p by negligible small values. Fit residuals can be found in Fig. A.15. At 1 hPa lens pressure, particles larger than 840 nm were too slow to be detected within the maximum pre-defined coincidence time interval.

August 2015 in the Baltic Sea region. The publication from Zanatta et al. (2019) includes BALTIC’15 ALABAMA data of particle composition and size. Particle size data are based on Figs. A.12 and A.13 at 1.9 hPa lens pressure, whereby V_{g1} was determined by linear interpolation between 1.5 and 2.0 hPa lens pressure. The following fit coefficients were used: $V_0 = 48.0\,\text{m}\,\text{s}^{-1}$, $V_{g1} = 151.3\,\text{m}\,\text{s}^{-1}$, and $k = 303.8$ nm.

In general for this study, fit functions were performed using the program Igor Pro (version 6.37; WaveMetrics, 2015). Fitting algorithms are based on total least-squares method. Relative fit residuals in Figs. A.14 and A.15 are calculated as follows:

$$\text{Fit residual} = \frac{\text{“Expected from fit”} - \text{“Observed”}}{\text{“Expected from fit”}}. \qquad (26)$$

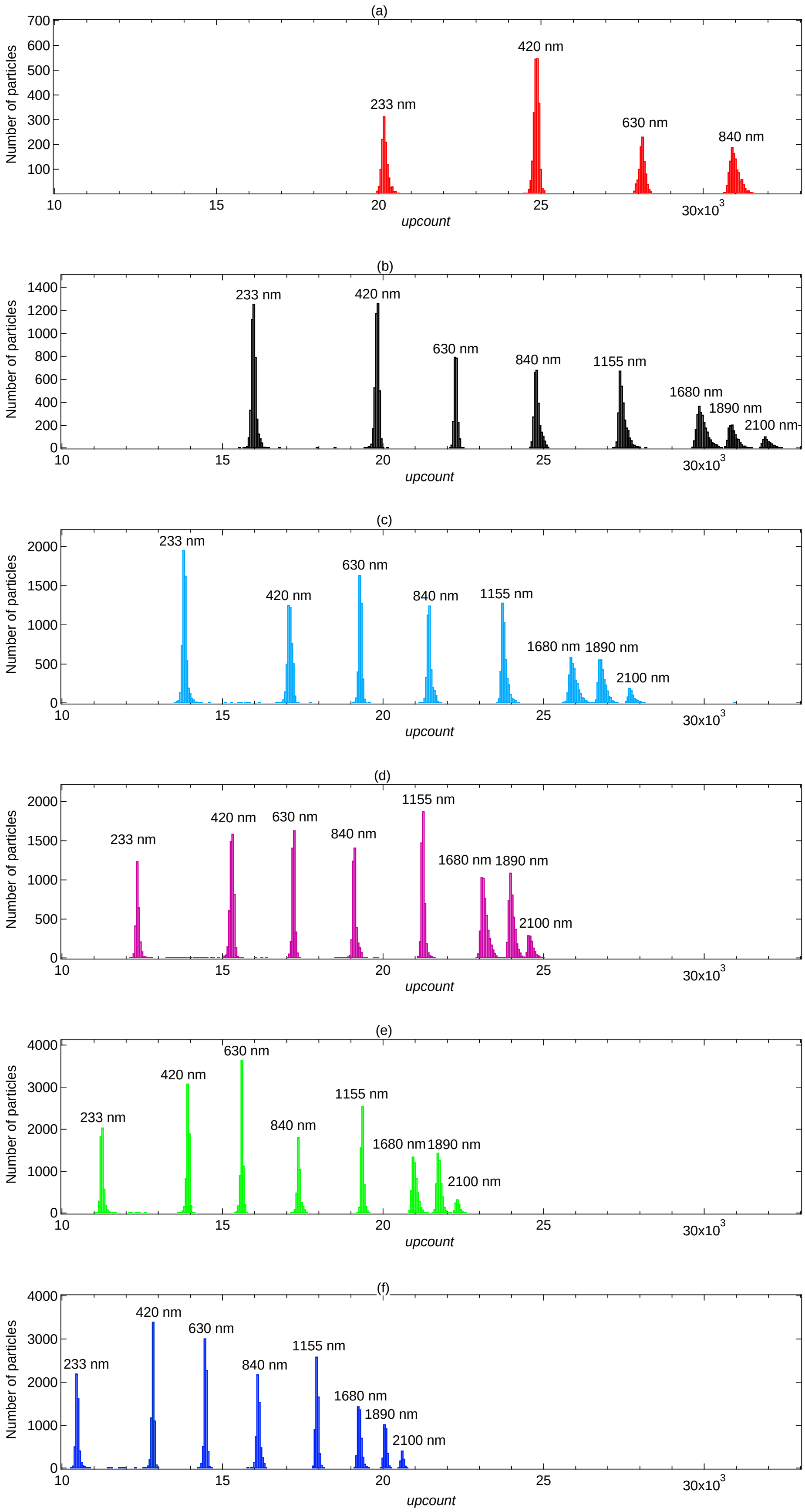

Figure A.11: Histograms of *upcount* values for various PSL particle sizes (d_{va}) in nm at (a) 1 hPa, (b) 1.5 hPa, (c) 2 hPa, (d) 2.5 hPa, (e) 3 hPa, and (f) 3.5 hPa lens pressure.

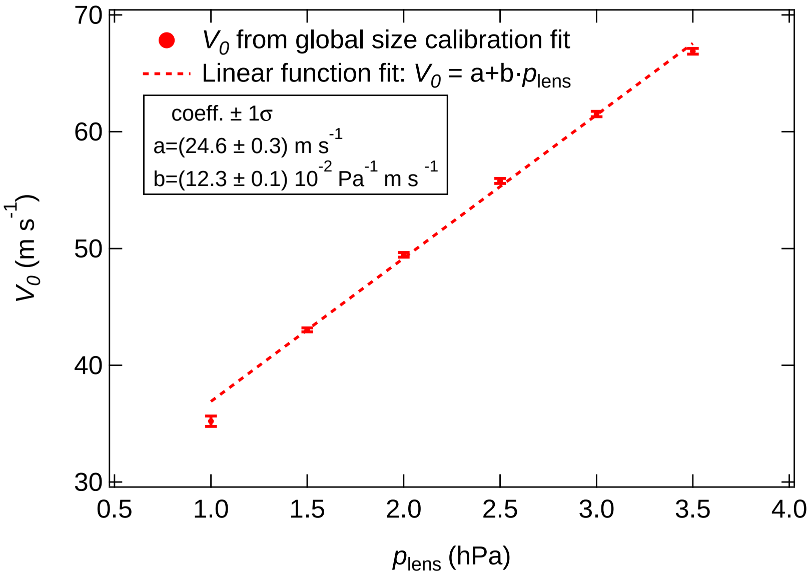

Figure A.12: Particle velocity before the gas expansion (V_0) as a function of lens pressure (p_{lens}) derived from the pressure-dependent global fit in Fig. A.10. The uncertainty of V_0 results from the global fit. Uncertainty of p_{lens} is discussed in Sect. A.2. The linear fit (dashed line), with R^2 of 0.95, considers only the uncertainty of V_0 and not that of p_{lens} by negligible small values. The text box presents the associated fit coefficients.

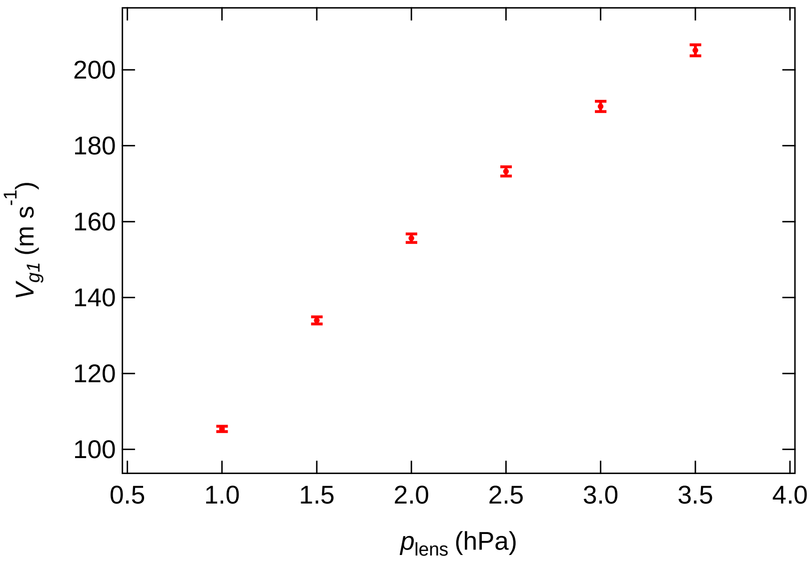

Figure A.13: Gas velocity after the gas expansion (V_{g1}) as a function of lens pressure (p_{lens}) derived from the pressure-dependent global fit in Fig. A.10. The uncertainty of V_{g1} results from the global fit. Uncertainty of p_{lens} is discussed in Sect. A.2.

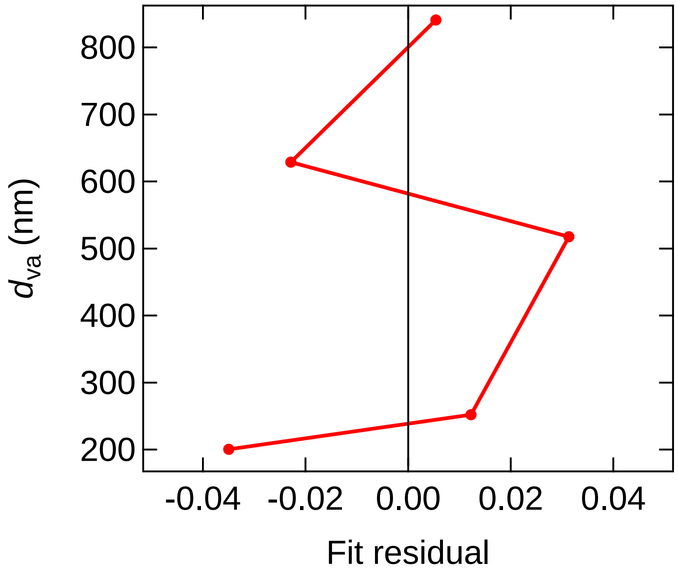

Figure A.14: Particle size (d_{va}) relative fit residuals associated with the size calibration fit in Fig. 2.7 during the Arctic field experiment in July 2014 (NETCARE 2014).

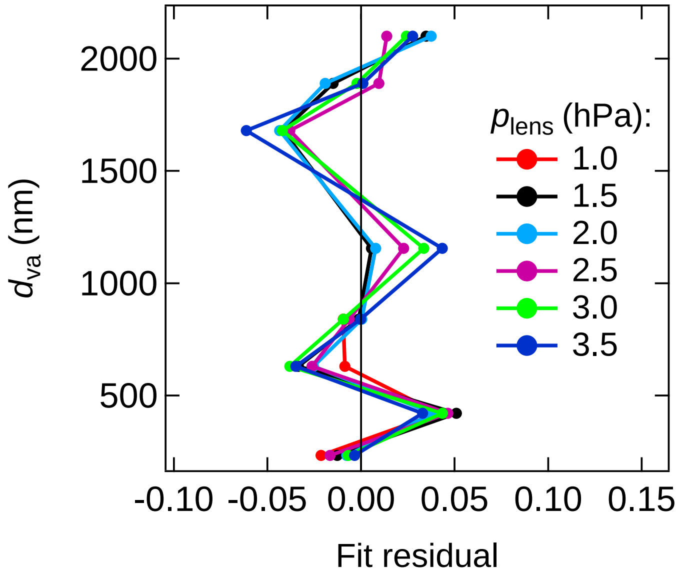

Figure A.15: Particle size (d_{va}) relative fit residuals associated with the global size calibration fit in Fig. A.10 as a function of lens pressure (p_{lens}).

A.7 POTENTIAL SOURCE INVENTORIES

Figures A.16 and A.17 show PSI vegetation fire maps that refer to each flight during the Arctic field experiment.

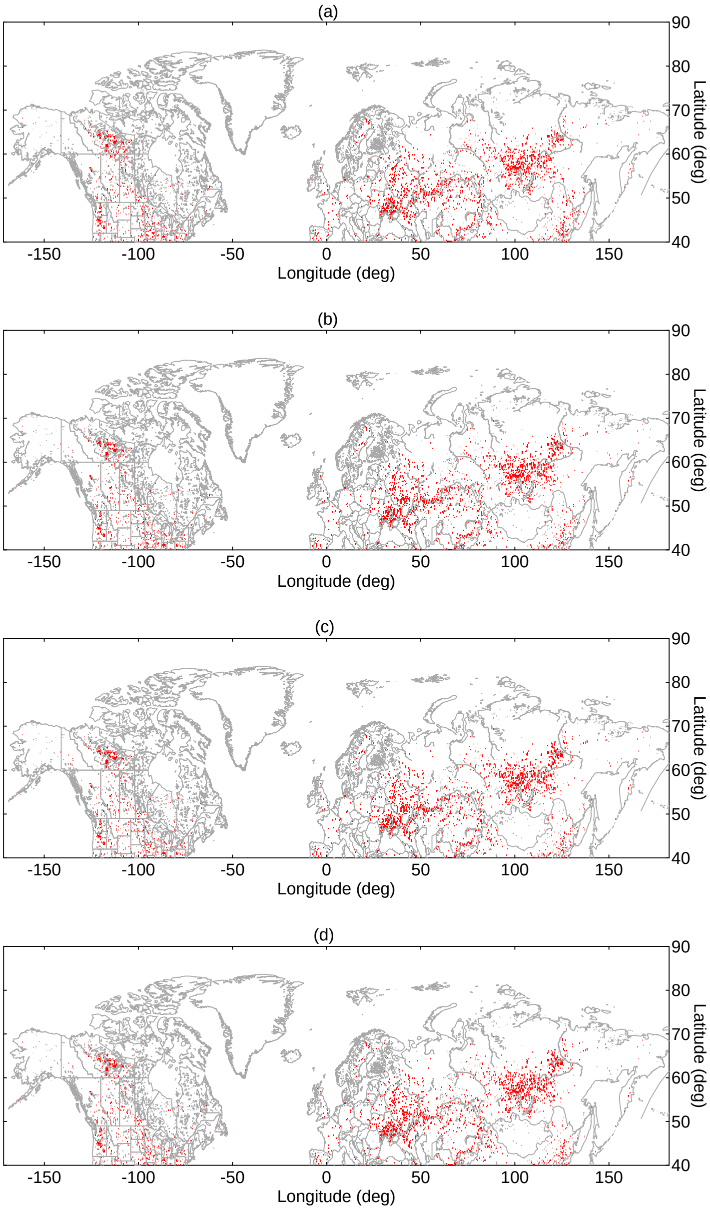

Figure A.16: Map showing potential source inventories of vegetation fires used for the FLEXPART air mass history analyses of measurements at (a) 17 July, (b) 19 July, (c) 20 July, and (d) 21 July 2014. Red pixels indicate the presence of vegetation fires in the grid cell.

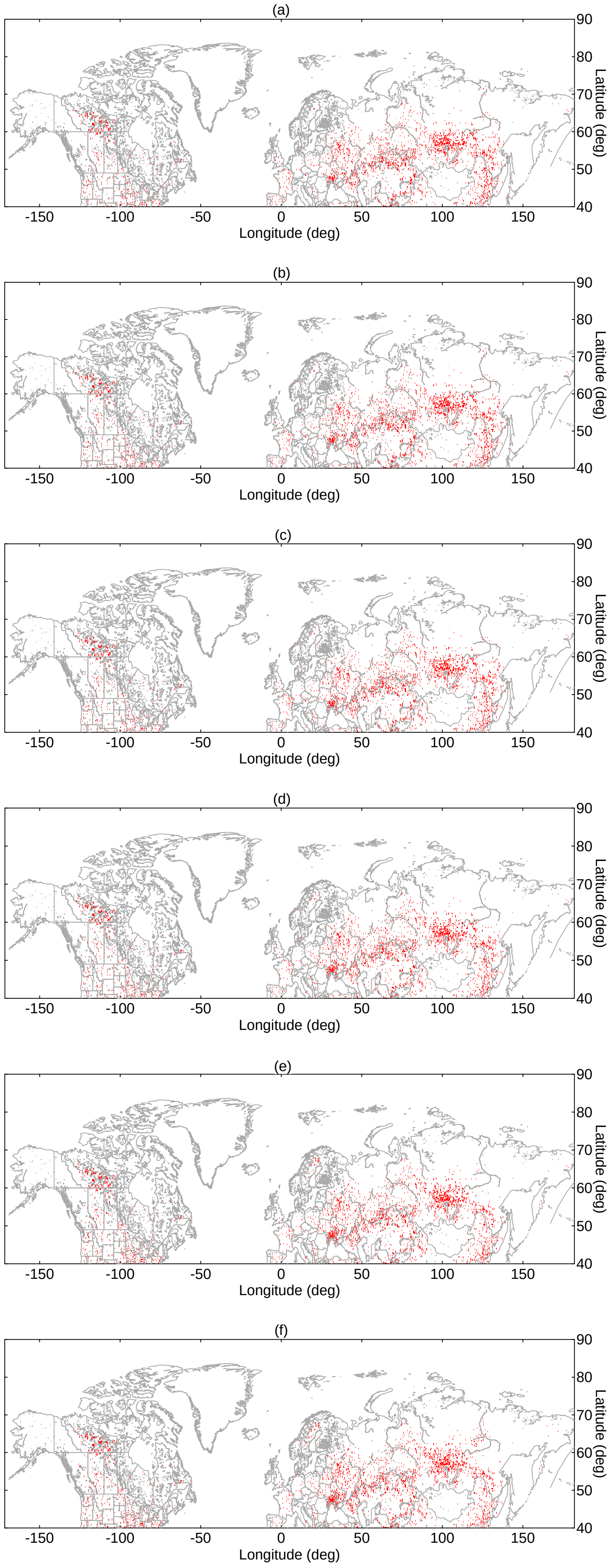

Figure A.17: Map showing potential source inventories of vegetation fires used for the FLEXPART air mass history analyses of measurements at (a) 4 July, (b) 5 July, (c) 7 July, (d) 8 July, (e) 10 July, and (f) 12 July 2014. Red pixels indicate the presence of vegetation fires in the grid cell.

B

SUPPLEMENTARY INFORMATION FOR CHAPTER 3

B.1 LASER INTENSITIES

The energy per pulse of the ALABAMA ablation laser was measured using an energymeter (EnergyMax-USB J-25MUV-193, Coherent Europe B.V.) at the exit window of the laser beam. The laser intensity was further calculated by using the pulse length of 6 ns (Quantel, 2008), the laser spot diameter in the ionization region of (200 ± 50) µm (Roth, 2014), and the measured laser energy per pulse.

Table 7: Laser intensity or energy per pulse given for different studies that were used as ion marker references (see Table 2). Values with asterisk are explained below. In some cases, operating conditions of the laser were not reported.

Studies	Laser intensity or energy per pulse
Angelino et al. (2001)	-
Prather et al. (2013)	1.2 - 1.5 mJ per pulse
Schmidt et al. (2017)	-
Brands et al. (2011)	$2.6{\cdot}10^9\ \mathrm{W\,cm^{-2}}$
Silva and Prather (2000)	10^8 - $10^9\ \mathrm{W\,cm^{-2}}$
Brands (2009)	sodium chloride: $2.6{\cdot}10^9\ \mathrm{W\,cm^{-2}}$
	elemental carbon: $3.1{\cdot}10^8\ \mathrm{W\,cm^{-2}}$
Lab study in Sect. 2.1.4	*$3.7{\cdot}10^9\ \mathrm{W\,cm^{-2}}$
Arctic experiment NETCARE 2014	*1.6 - $2.1{\cdot}10^9\ \mathrm{W\,cm^{-2}}$
TMA lab study	*$5.3{\cdot}10^8\ \mathrm{W\,cm^{-2}}$
Levoglucosan+KSO_4 lab study	*$3.2{\cdot}10^9\ \mathrm{W\,cm^{-2}}$

*Values with asterisk describe ALABAMA laser intensities that were calculated using laser energies per pulse of 7 mJ, 3 mJ to 4 mJ, 1 mJ, and 6 mJ measured during the laboratory study in Sect. 2.1.4 , the Arctic field experiment (NETCARE 2014) in Ch. 4, the TMA laboratory study in Sect. 3.1.1.1, and the levoglucosan+KSO_4 laboratory study in Sect. 3.1.1.2, respectively.

B.2 OTHER ALKYLAMINES AND AMINO ACIDS

Laboratory studies by Silva and Prather (2000), Angelino et al. (2001), and Schmidt et al. (2017) reported ion markers of several alkylamines and amino acids (Tables 8 and 9). In addition, ambient particle mass spectra by Healy et al. (2015) showed the presence of several alkylamines at different European sites.

For the Arctic field experiment, none of the alkylamine ion markers listed in Table 8 significantly exceeded the positive ion peak area threshold (10 mV·sample; see Sect. 3.1.2), except dimethylamine at m/z +46 (Fig. B.1). However, dimethylamine and Na_2^+ have an isobaric interference at m/z +46. By comparing ion peak area values at m/z +23 (Na^+) and m/z +46, two different regimes are obvious (Fig. B.2). First, ion signals at m/z +46 can likely be assigned to the presence of Na_2^+, if the ion peak area of Na^+ (m/z +23) was larger than approximately 200 mV·sample, by correlating high ion peak area values at m/z +23 (Na^+) and m/z +46 (Na_2^+) (upper red box in Fig. B.2). The second regime is given by low ion peak area values at m/z +23 (< 200 mV·sample) and non-correlating ion peak area values at m/z +46, indicating the presence of dimethylamine. However, less than 5 % of all analyzed spectra during the Arctic field experiment are confined in the second regime. By this low number of spectra, a further detailed analysis on dimethylamine abundance, sources, and formation is not provided in this study.

Table 8: Marker species of different alkylamines (other than TMA) as well as associated ion markers and references. This table is partly adapted from Köllner et al. (2017).

Ion markers	Marker species (abbreviation)	References
m/z +46	dimethylamine	Healy et al. (2015)
m/z +74	diethylamine (DEA)	Angelino et al. (2001)
m/z +86	DEA, triethylamine (TEA), and/or dipropylamine (DPA)	see above
m/z +101	TEA	see above
m/z +102	DPA	see above
m/z +114	DPA and/or tripropylamine (TPA)	see above
m/z +143	TPA	see above

In some spectra, ion markers of different amino acids at m/z +40, +56, and +63 exceeded the positive ion peak area threshold (Table 9 and Fig. B.1). However, these ion markers were concurrently present in less than 2 % of all analyzed spectra in the Arctic. In addition, those ion markers have isobaric interferences with Ca^+ (m/z +40), CaO^+ (m/z +56), and Na_2OH^+ (m/z +63), impeding the assignment to amino acids. Together, beside TMA, other alkylamines and/or amino acids were not significantly abundant in Arctic ambient single particle spectra and/or could not be identified by isobaric interferences with other substances.

Table 9: Marker species of different amino acids as well as associated ion markers and references. This table is partly adapted from Köllner et al. (2017).

Ion markers	Marker species (abbreviation)	References
m/z +40	Alanine, cysteine, glutamic acid, leucine, and/or proline	Schmidt et al. (2017)
m/z +56	Alanine, cysteine, glutamic acid, leucine, and/or proline	see above
m/z +63	Alanine, cysteine, glutamic acid, leucine, and/or proline	see above
m/z +76	Glycine	Silva and Prather (2000)
m/z +86	Leucine	Schmidt et al. (2017)
m/z +111	Proline	see above
m/z +130	Tryptophan	see above
m/z +132	Leucine	see above

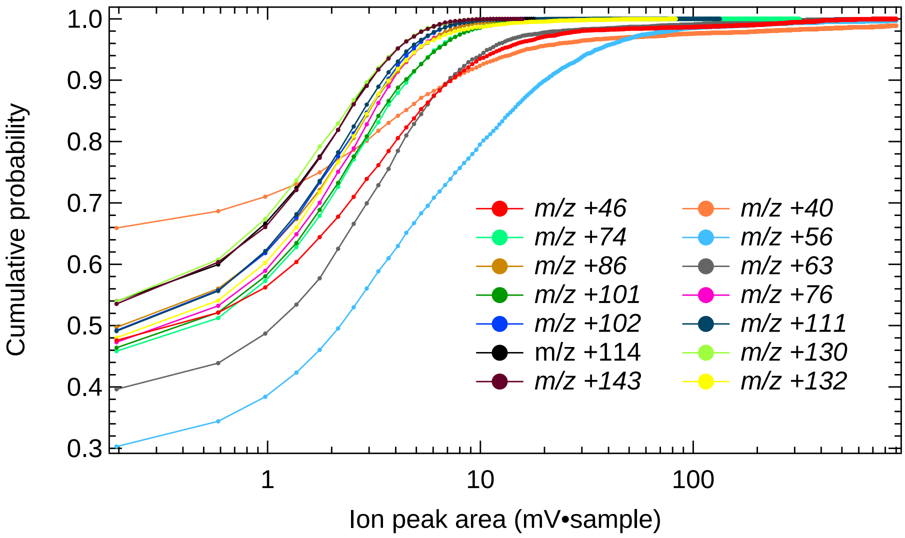

Figure B.1: Cumulative probability distributions of ion peak area values from different alkylamines and amino acids marker ions (Tables 8 and 9).

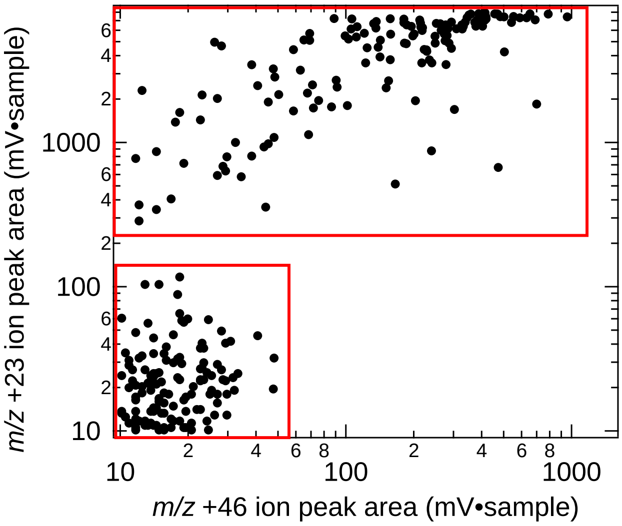

Figure B.2: Comparison of ion peak area values at m/z +23 and m/z +46. Red boxes indicate two different regimes.

B.3 HIT RATE VARIABILITY DURING THE ARCTIC FIELD EXPERIMENT

The following approach estimates the NETCARE 2014 hit rate (HR) variability that is caused by several instrumental issues as explained in Sect. 3.2. Figure B.3 presents the distribution of the averaged hit rate measured during the

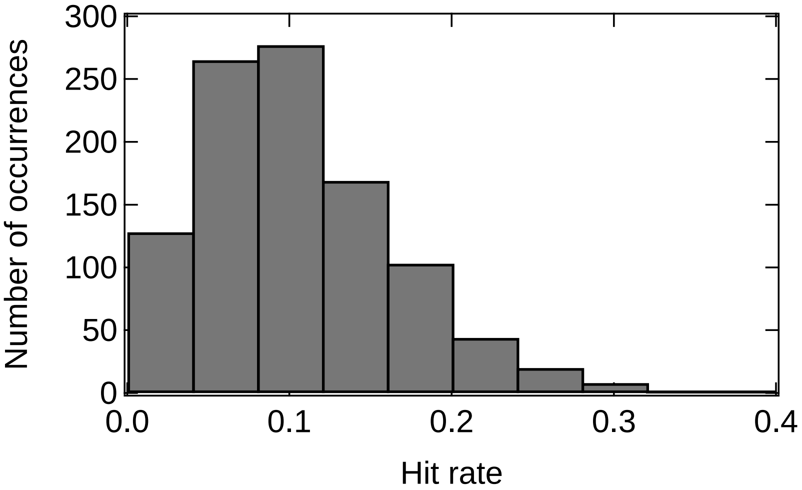

Figure B.3: Histogram of hit rate values with each value includes $N = 100$ trials (here, laser shots), measured during the Arctic field experiment (NETCARE 2014) outside clouds. The averaged hit rate value is 0.1 ($p = 0.1$).

Arctic field experiment outside clouds[1]. By assuming that the measured distribution cannot solely be explained by binomial distributed numbers, it needs to be described by a combination of both binomial distributed numbers and the variability caused by instrumental issues. Combined with the Gaussian propagation of uncertainties, the relative standard deviation of the measured hit rate distribution ($\sigma_{\mathrm{measured}}$) can thus be estimated as follows:

$$\sigma^2_{\mathrm{measured}} = \sigma^2_{\mathrm{binomial}} + \sigma^2_{\mathrm{others}}, \tag{27}$$

with $\sigma_{\mathrm{measured}} = 0.06$, the relative standard deviation related to instrumental issues that influence the hit rate (σ_{others}), and the relative standard deviation of the Binomial probability distribution ($\sigma_{\mathrm{binomial}}$), which is calculated as follows:

$$\sigma_{\mathrm{binomial}} = \frac{\sqrt{N \cdot p \cdot q}}{N}, \tag{28}$$

with trials N is 100, probability of success p is 0.1, and probability of failure q is 0.9. The resulting $\sigma_{\mathrm{binomial}}$ is 0.03. Based on $\sigma_{\mathrm{binomial}}$ and Eq. 27, the σ_{others} is 0.05. Together, since the averaged ALABAMA hit rate of 0.1 can vary by 0.05 due to instrumental issues, it is assumed for the analyses in Sects. 4.4-4.6 that the particle fraction needs to vary by more than a factor of 2 to be significant.

---

[1] The inlet used for particle sampling (see Sect. 2.2.1) is not suitable for in-cloud measurements. Therefore, aerosol particles analyzed inside clouds were discarded by the method introduced in Sect. C.3.

C

SUPPLEMENTARY INFORMATION FOR CHAPTER 4

C.1 AIR MASS HISTORY AND POLAR DOME VERTICAL BOUNDARIES

The lowest vertical model level (0 - 400 m) contributed with 20 % to 30 % to Arctic near-surface composition (Fig. C.1). The remaining 70 % to 80 % were given by contributions from air masses aloft. The contribution of the lowest 400 m gradually decreased with increasing sampling altitude. Contributions of upper tropospheric/lower stratospheric air masses (> 5 km) increased with increasing sampling altitude, while influences on composition within the polar dome were small (up to 12 %), consistent with a study by Stohl (2006).

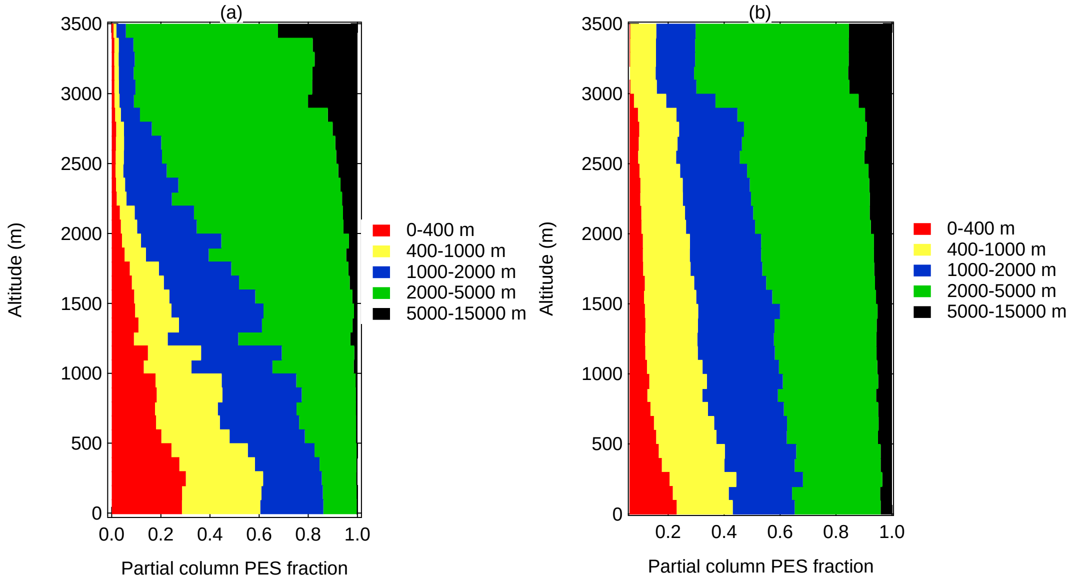

Figure C.1: Vertically resolved cumulative contribution of FLEXPART vertical columns to sampling altitude during the Arctic (a) and the southern (b) air mass periods. The FLEXPART predicted contribution is expressed as a fraction of the potential emission sensitivity (PES) in the model domain over a 15-days backward simulation.

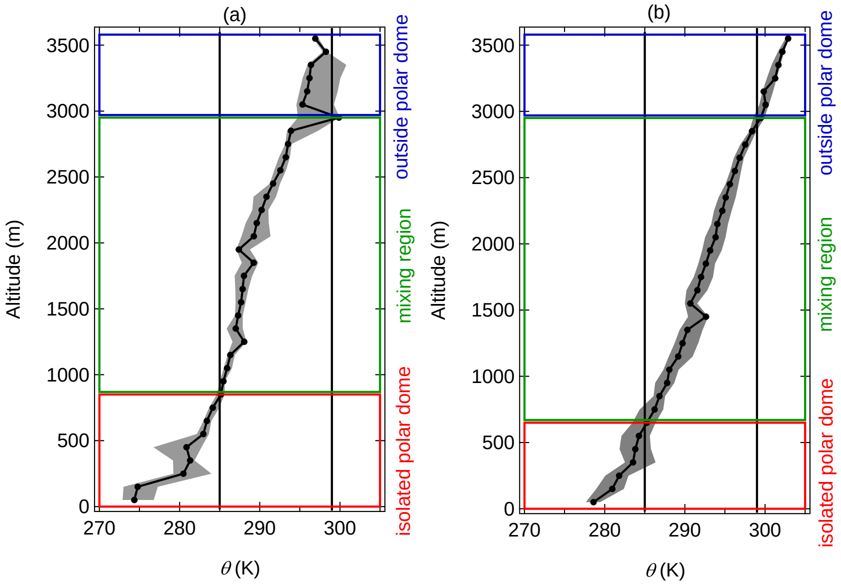

Figure C.2: Vertically resolved median (black line) and interquartile ranges (gray shaded area) of the potential temperature (θ) during the Arctic (a) and the southern (b) air mass periods. Vertical black lines represent θ values from Bozem et al. (2019), determining vertical boundaries of the isolated polar dome (red box), the mixing region (green box), and the outside polar dome region (blue box).

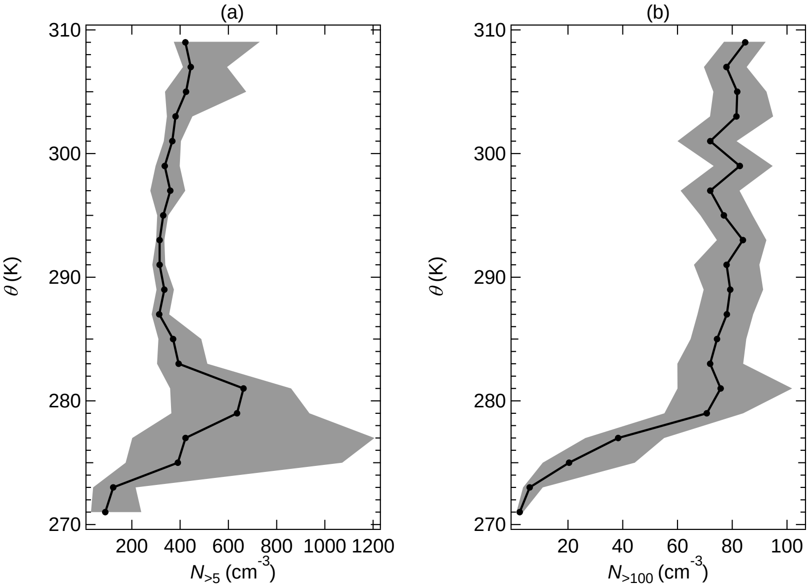

Figure C.3: Median (black line) and interquartile ranges (gray shaded area) of number concentrations of particles larger than 5 nm ($N_{>5}$) and larger than 100 nm ($N_{>100}$) compared to potential temperature as the vertical coordinate during the Arctic air mass period.

C.2 PSEUDOEQUIVALENT POTENTIAL TEMPERATURE AND RELATIVE HUMIDITY

The pseudoequivalent potential temperature (θ_e) of an air parcel that is lifted in the atmosphere is defined as follows. After all water vapor has condensed, released its latent heat, and fallen out (i.e., pseudo-adiabatic lifting), the air parcel is compressed dry adiabatically to standard pressure of 1000 hPa. The temperature at this point is called θ_e (AMS Glossary, 2018; Wallace and Hobbs, 2006) that can be calculated by summing up the terms of internal energy, potential energy, and latent heat (Kraus, 2004):

$$\theta_\mathrm{e} \approx T + \frac{g \cdot h}{c_\mathrm{p}} + \frac{L_\mathrm{v} \cdot q_\mathrm{v}}{c_\mathrm{p}}, \tag{29}$$

with temperature (T), gravity (g) = $9.81\,\mathrm{m\,s^{-2}}$, altitude (h), specific heat capacity of air for constant pressure (c_p) = $1003\,\mathrm{J\,kg^{-1}\,K^{-1}}$, latent heat of condensation at 273 K and 1013 hPa (L_v) = $2.5{\cdot}10^6\,\mathrm{J\,kg^{-1}}$ (Wallace and Hobbs, 2006), and specific humidty (q_v). The specific humidity is defined as the ratio between the mass of water vapor and the mass of moist air in the same volume. In good approximation q_v is given be the following equation:

$$q_\mathrm{v} = 0.622 \frac{e_\mathrm{v}}{p_\mathrm{air}}, \tag{30}$$

with the atmospheric pressure (p_air) and the water vapor pressure (e_v). Here, q_v is derived from the H_2O mixing ratio by volume ($\mathrm{VMR_{H2O}}$) in ppm$_v$ measured by the LI-7200 CO_2/H_2O analyzer:

$$\mathrm{VMR_{H20}} = \frac{e_\mathrm{v}}{p_\mathrm{air}} \cdot 10^6. \tag{31}$$

$\mathrm{VMR_{H2O}}$ and p_air are further used to calculate the relative humidity (RH) as follows:

$$RH = \frac{e_\mathrm{v}}{e_\mathrm{v}^*} \cdot 100, \tag{32}$$

with the saturation vapor pressure (e_v^*) calculated using the Murray equation:

$$e_\mathrm{v}^* = 6.1078 \cdot \exp \frac{a \cdot (T - 273.16\,K)}{T - b}, \tag{33}$$

with empirically derived constants $a = 17.2693882$ and $b = 35.86$ K (Kraus, 2004).

C.3 NUMBER OF ANALYZED PARTICLES DURING NETCARE 2014

Table 10 summarizes the total number of particles analyzed during the NETCARE 2014 measurements. Briefly, the inlet used for particle sampling was not

Table 10: Number of chemically analyzed particles (mass spectra produced) by the ALABAMA within approximately 44 hours of sampling during the NETCARE 2014 campaign. The asterisk indicates that the selection is based on analyzed particles outside clouds.

Selection	Number of spectra
Analyzed particles	17091
Analyzed particles outside clouds	10137
* with size information	9574
* with dual polarity	7894
* with single positive polarity	1945
* with single negative polarity	298

suitable for measurements inside clouds. Therefore, aerosol particles sampled inside clouds were excluded from the further analysis by using the cloud droplet concentration, which was measured by an under-wing Forward Scattering Spectrometer (Leaitch et al., 2016). In-cloud sampling was defined by measuring cloud droplet number concentration larger than $0.01\,\mathrm{cm}^{-3}$.

C.4 MISSING NEGATIVE MASS SPECTRA

ALABAMA measurements during the NETCARE 2014 campaign show that 19 % of the analyzed spectra outside clouds have single positive polarity (see Table 10). Single-polarity spectra produced by laser ablation/ionization had been earlier reported by several field studies (e.g., Bein et al., 2005; Sodeman et al., 2005; Pratt and Prather, 2010; Roth, 2014). The lack of negative mass spectra can be explained by several possibilities. First, instrumental issues can inhibit the formation of negative ions. In detail, negative high-voltages in the mass spectrometer might not have been tuned properly. High-voltages can also automatically switch off, if the pressure inside the mass spectrometer exceeds $5{\cdot}10^{-6}$ hPa. However, for the Arctic measurements, the pressure has been always lower than this critical pressure value. Second, particle chemical composition can also explain the lack of negative mass spectra by certain particle types that do not produce negative ions. Third, the water content of a particle can negatively affect the formation of negative ions during the laser ablation/ionization process. Several laboratory and field studies (particularly in marine environments) reported a humidity effect on the anion signal intensity (Neubauer et al., 1998; Spencer et al., 2008; Guasco et al., 2014). However,

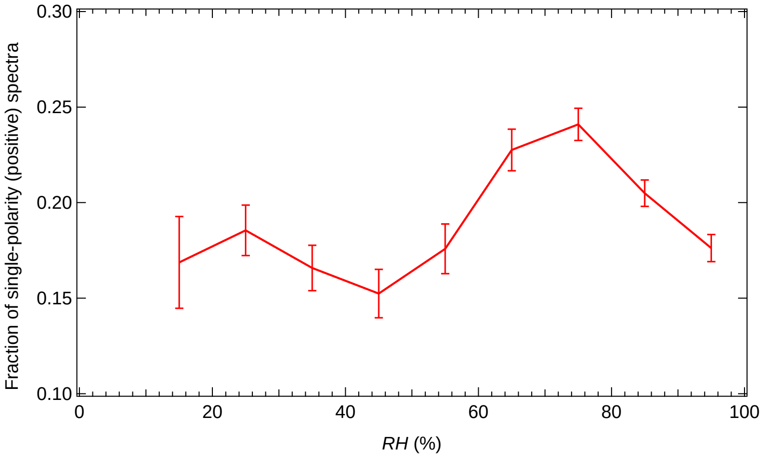

Figure C.4: Relative humidity (RH) compared to the fraction of particle mass spectra that have single positive polarity. Spectra are defined as single positive polarity when none of the anion peaks exceeds the threshold of 25 mV·sample (see Sect. 3.1.2). Uncertainty analyses are given in Sect. C.7

the underlying process remains unclear.

The ALABAMA measurements in the Arctic can partly confirm these earlier results (Fig. C.4). The fraction of single positive polarity spectra increased with increasing RH, whereby at RH larger than 80 % the fraction decreased again. Neubauer et al. (1998) did not report measurements at RH larger than 80 %. Particle composition may further play a role for the humidity dependence (Neubauer et al., 1998). In high relative humidity environments, chloride and nitrate negative ion signals could still be clearly identified, whereas sulfate and MSA negative ion signals were suppressed, according to Neubauer et al. (1998). ALABAMA measurements showed that particles containing chloride and/or nitrate can still be detected in high RH environments (Fig. C.5). Taken together, reasons for the lack of negative ion mass spectra cannot be fully clarified. The analysis presented in Ch. 4 includes particle spectra that have both dual-polarity and single positive polarity.

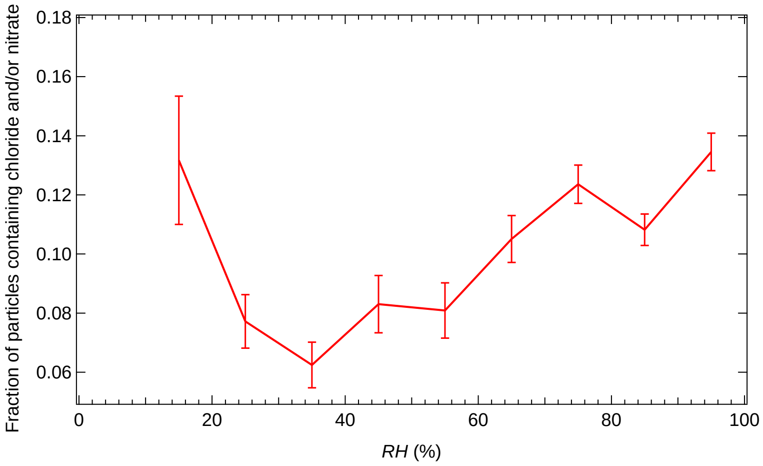

Figure C.5: Relative humidity (*RH*) compared to the fraction of particles that contain chloride (m/z-35/37; see Table 2) and/or nitrate (m/z-46 or m/z-62; see Table 2). Uncertainty analysis is given in Sect. C.7.

C.5 ADDITIONAL MEAN SPECTRA

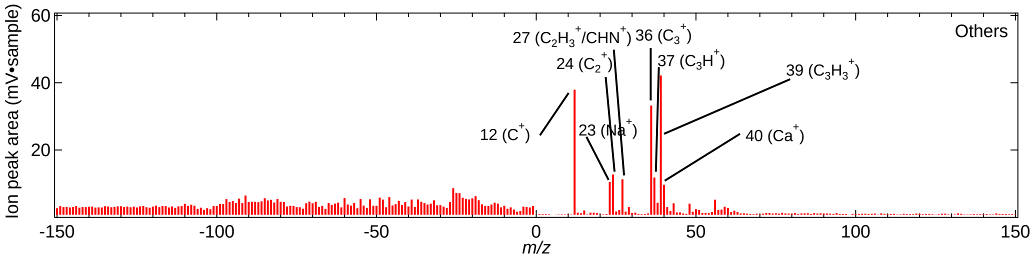

Figure C.6: Bipolar mean spectrum of the remaining 1486 particles (15 % of all mass spectra analyzed by the ALABAMA) that could not be classified into one of the particle types. These particles are therefore summarized as "Others".

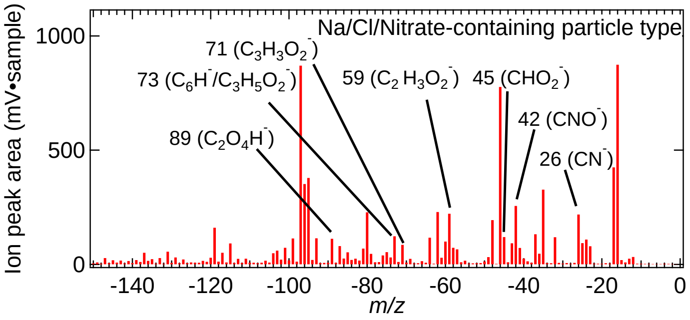

Figure C.7: Expanded mean anion spectrum of the Na/Cl/Nitrate-containing particles. Only peaks associated with organic matter are highlighted.

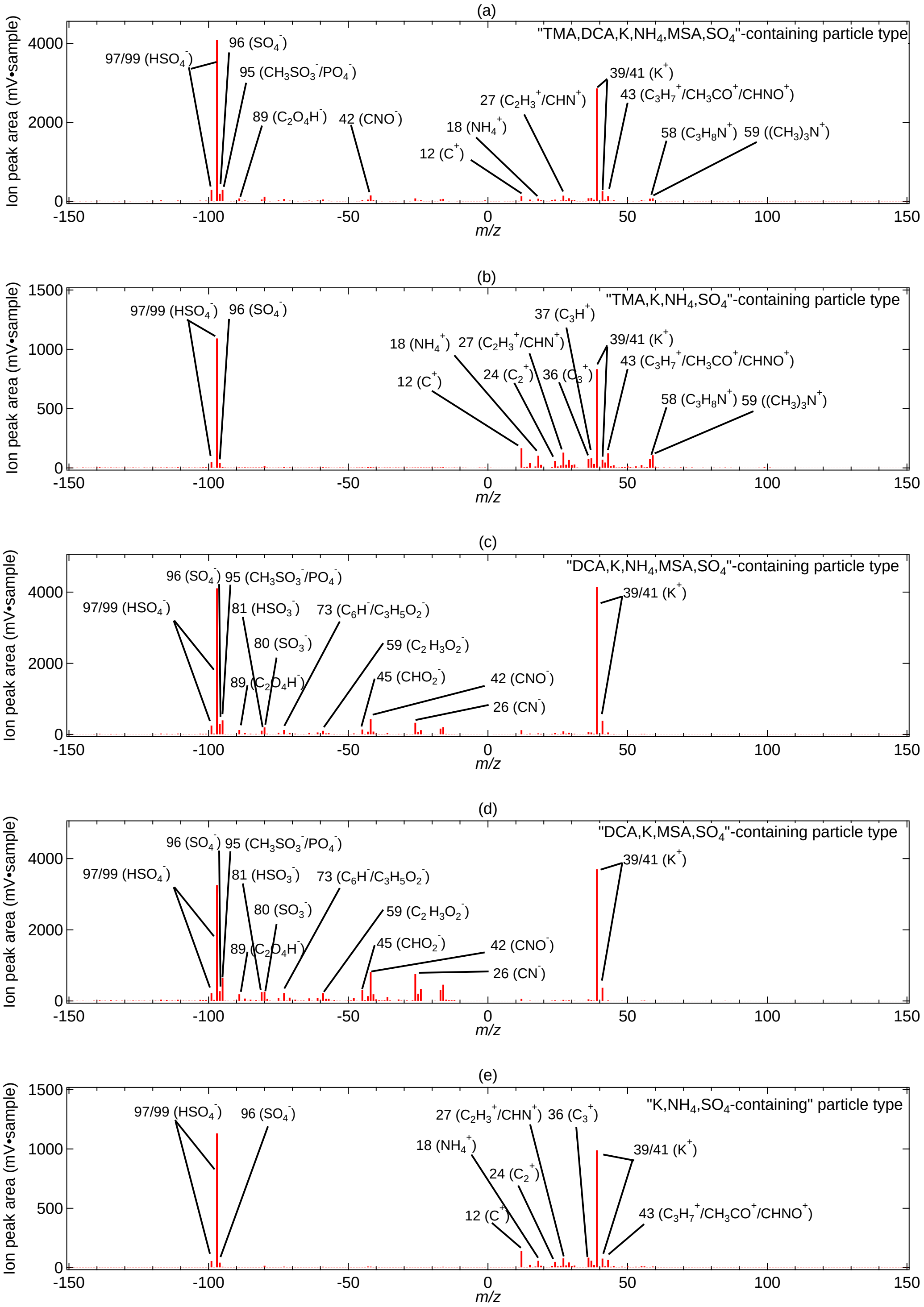

Figure C.8: Bipolar mean spectra of the identified particle sub-types: (a) “TMA,DCA,K,NH_4,MSA,SO_4”-containing (327 particles ≙ 3 %), (b) “TMA,K,NH_4,SO_4”-containing (326 particles ≙ 3 %), (c) “DCA,K,NH_4,MSA,SO_4”-containing (772 particles ≙ 8 %), (d) “DCA,K,MSA,SO_4”-containing (327 particles ≙ 9 %), and (e)“K,NH_4,SO_4”-containing (407 particles ≙ 4 %).

C.6 COMPARISON BETWEEN $N_{>320}$ AND VARIOUS PARAMETERS

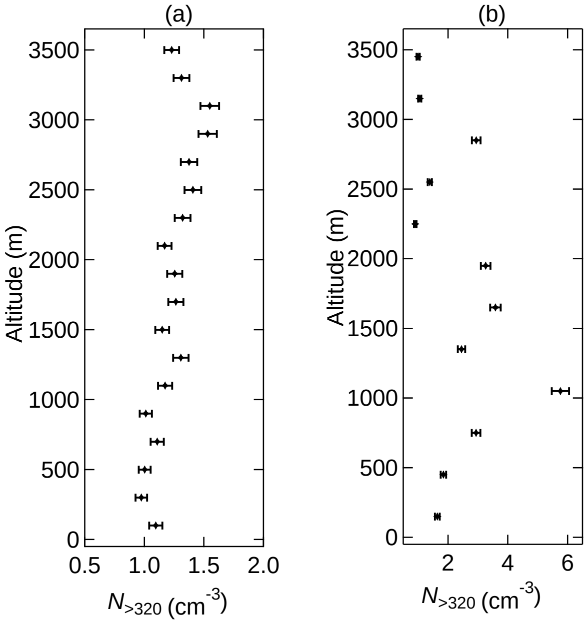

Figure C.9: Vertically resolved averaged UHSAS number concentration in a size range between 320 and 870 nm ($N_{>320}$) during the Arctic (a) and the southern (b) air mass periods. Uncertainty analysis is given in Sect. C.7.

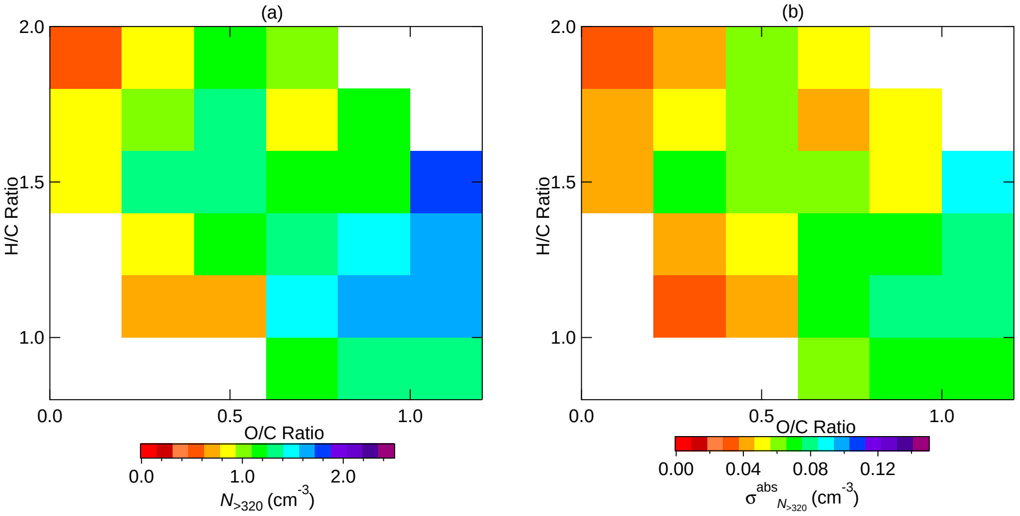

Figure C.10: Comparison between the HR-ToF-AMS estimated oxygen-to-carbon (O/C) and hydrogen-to-carbon (H/C) ratios colored by (a) the averaged UHSAS number concentration in a size range between 320 and 870 nm ($N_{>320}$) and (b) the absolute uncertainty of $N_{>320}$ ($\sigma^{\text{abs}}_{N>320}$). Uncertainty analysis is given in Sect. C.7.

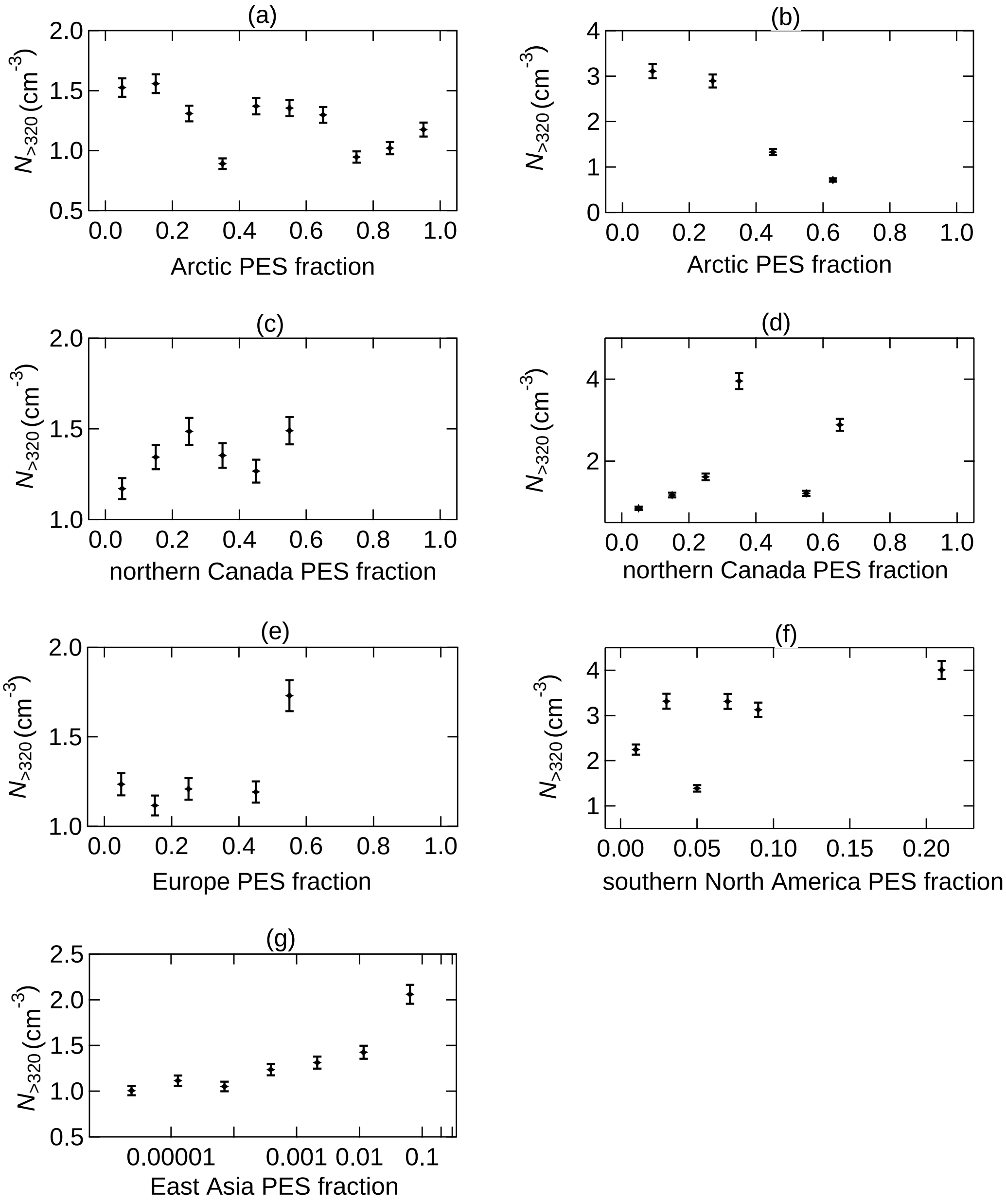

Figure C.11: Comparison between averaged UHSAS number concentration in a size range between 320 and 870 nm ($N_{>320}$) and FLEXPART predicted air mass residence time over the Arctic (a-b), northern Canada (c-d), Europe (e), southern North America (f), and East Asia (g) during the Arctic (left panel) and the southern (right panel) air mass periods. Uncertainty analysis is given in Sect. C.7.

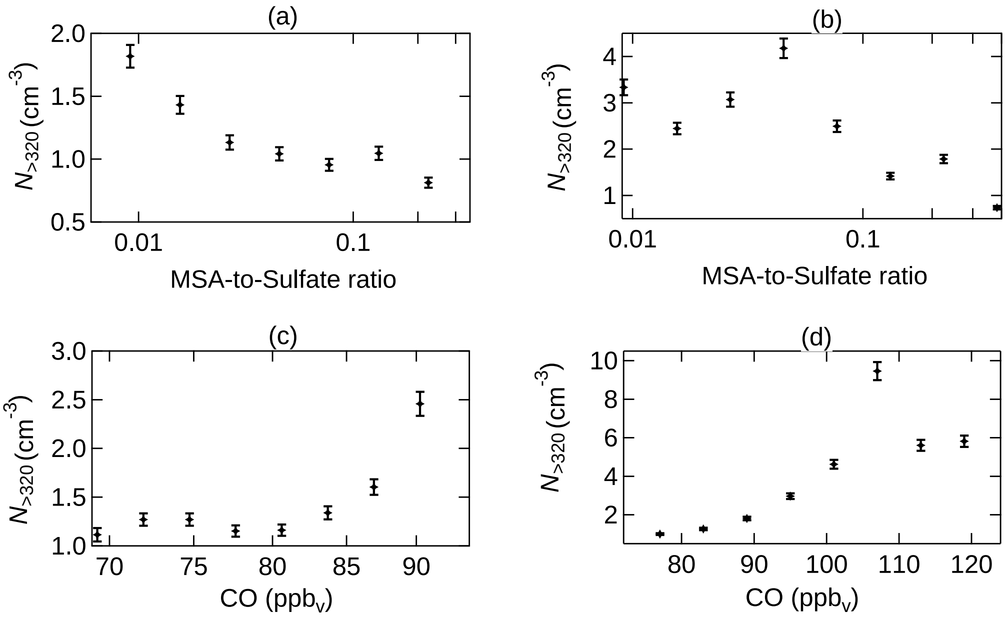

Figure C.12: Comparison between averaged UHSAS number concentration in a size range between 320 and 870 nm ($N_{>320}$) and MSA-to-sulfate ratio measured by the HR-ToF-AMS (a-b) and CO mixing ratios (c-d) during the Arctic (left panel) and the southern (right panel) air mass periods. Uncertainty analysis is given in Sect. C.7.

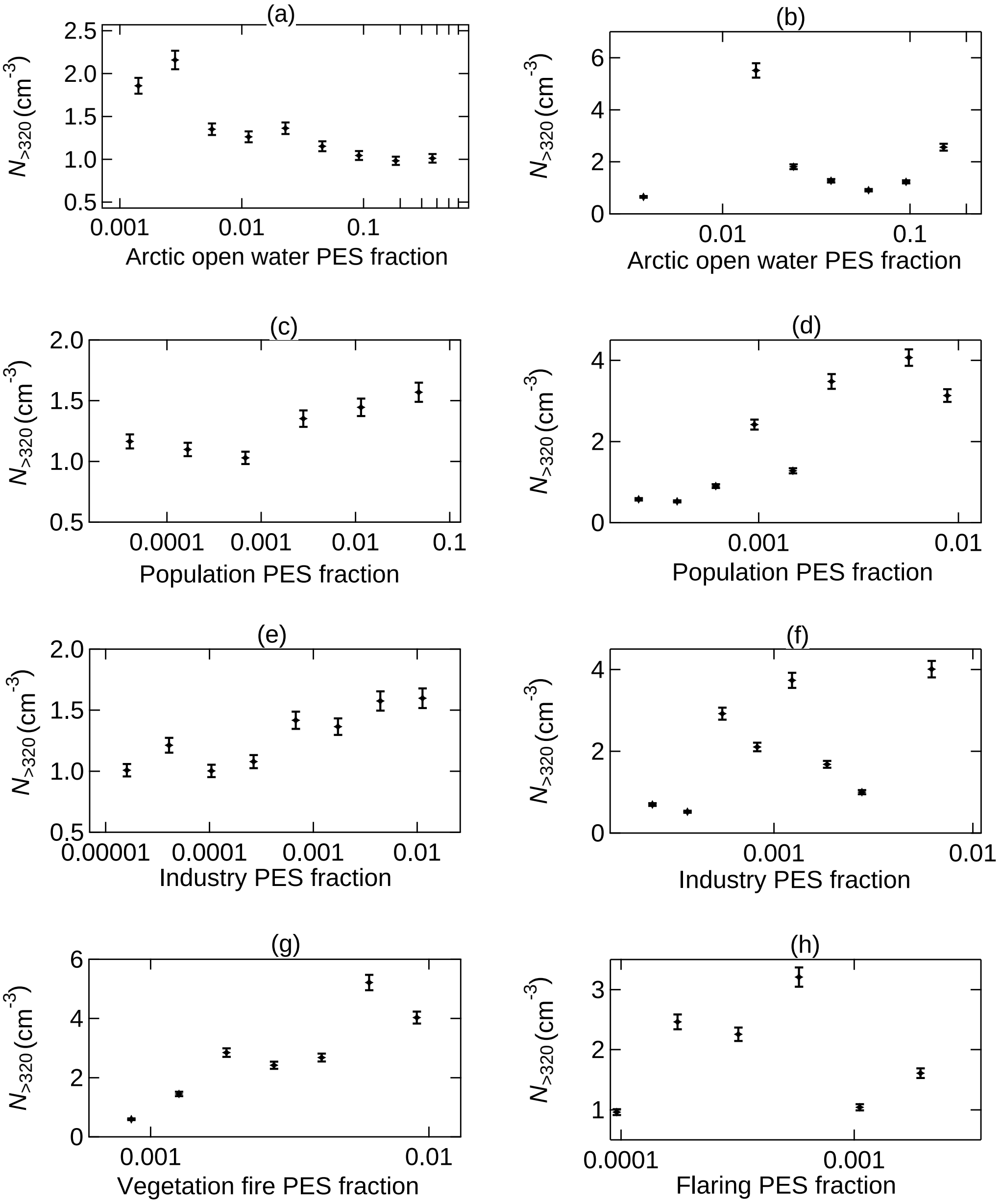

Figure C.13: Comparison between averaged UHSAS number concentration in a size range between 320 and 870 nm ($N_{>320}$) and FLEXPART predicted air mass residence time over Arctic open water areas (a-b), populated areas (c-d), industrial areas (e-f), vegetation fires (g), and over areas associated with flaring emissions (h) during the Arctic (a, c, and e) and the southern (b, d, and f-h) air mass periods. Uncertainty analysis is given in Sect. C.7.

C.7 UNCERTAINTY ANALYSES

UHSAS number concentration ($N_{>320}$)

The absolute uncertainty of the averaged UHSAS number concentration for each bin ($\sigma^{\mathrm{abs}}_{N_{>320}}$) is calculated based on Poisson statistics and Gaussian propagation of uncertainties:

$$\sigma^{\mathrm{abs}}_{N_{>320}} = N_{>320}\sqrt{\left(\sigma^{\mathrm{rel}}_{\mathrm{UHSAS}}\right)^2 + \left(\sigma^{\mathrm{rel_1}}_{\mathrm{UHSAS}}\right)^2}, \tag{34}$$

with the relative statistical uncertainty of the particles counts detected by the UHSAS ($\sigma^{\mathrm{rel}}_{\mathrm{UHSAS}}$) that is defined as follows:

$$\sigma^{\mathrm{rel}}_{\mathrm{UHSAS}} = \frac{1}{\sqrt{C_{>320}}}, \tag{35}$$

with the counts of particles greater than 320 nm in diameter ($C_{>320}$). The $\sigma^{\mathrm{rel_1}}_{\mathrm{UHSAS}}$ is 5 % derived from the UHSAS collection efficiency of 95 % (see Table 1).

ALABAMA particle fraction (PF)

The absolute uncertainty of the ALABAMA particle fraction for each bin ($\sigma^{\mathrm{abs}}_{PF}$) is calculated using binomial statistics:

$$\sigma^{\mathrm{abs}}_{PF} = \frac{\sqrt{N_{\mathrm{hits}} \cdot PF \cdot (1 - PF)}}{N_{\mathrm{hits}}}, \tag{36}$$

with the number of particles that are successfully ionized by the ablation laser and that create a mass spectrum (N_{hits}) and the fraction of the specific particle type (PF).

ALABAMA scaled number concentration ($PF \cdot N_{>320}$)

The absolute uncertainty of the ALABAMA scaled number concentration for each bin ($\sigma^{\mathrm{abs}}_{PF \cdot N_{>320}}$) is calculated using Gaussian propagation of uncertainties:

$$\sigma^{\mathrm{abs}}_{PF \cdot N_{>320}} = \sqrt{\left(PF \cdot \sigma^{\mathrm{abs}}_{N_{>320}}\right)^2 + \left(N_{>320} \cdot \sigma^{\mathrm{abs}}_{PF}\right)^2}. \tag{37}$$

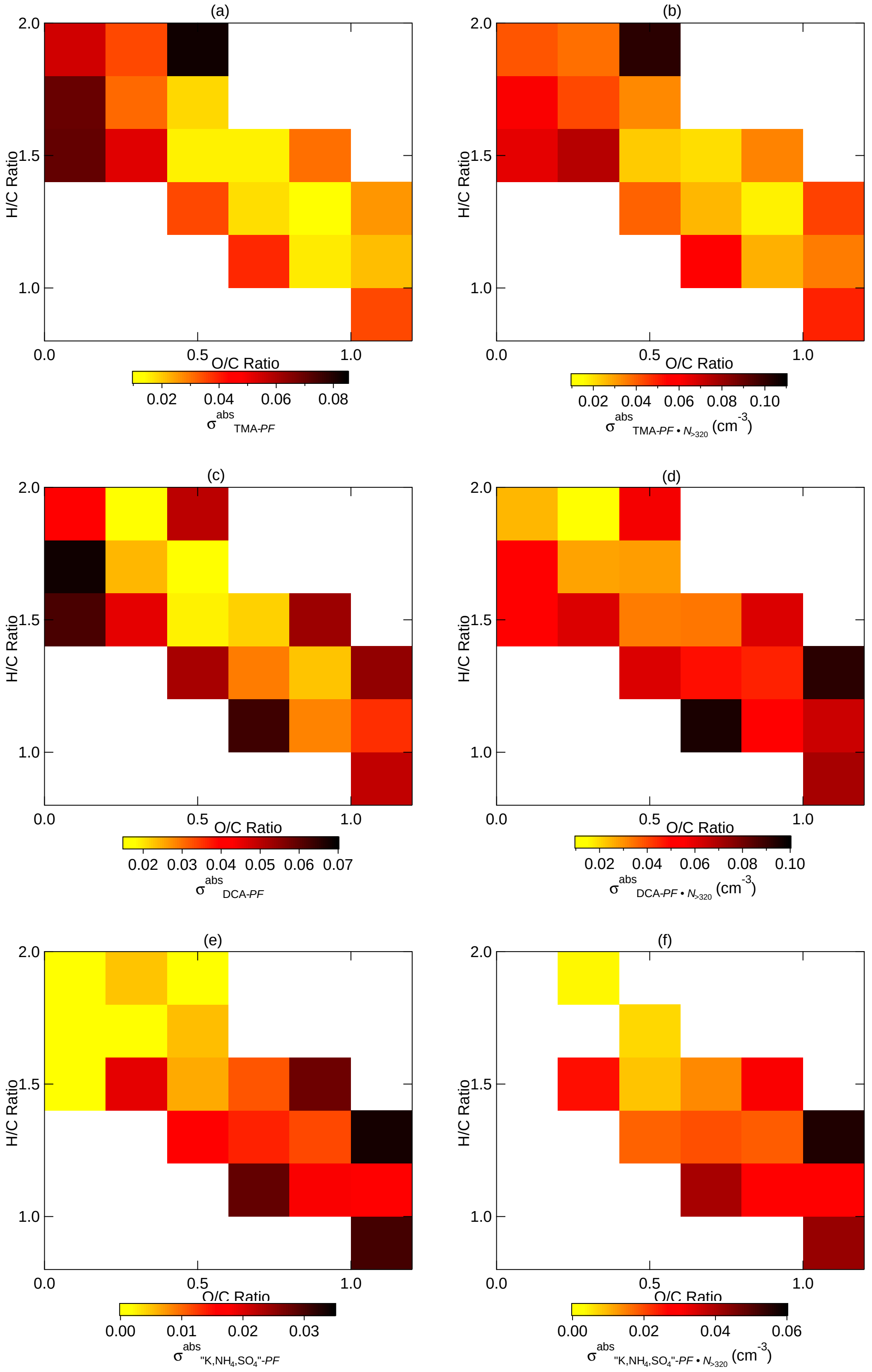

Figure C.14: Comparison between the HR-ToF-AMS estimated oxygen-to-carbon (O/C) and hydrogen-to-carbon (H/C) ratios colored by (a-b) TMA-, (c-d) DCA-, and (e-f) "K,NH_4,SO_4"-containing particles measured by the ALABAMA with (left panel) the absolute uncertainty of the particle fraction (σ_{PF}^{abs}) and (right panel) the scaled number concentration ($\sigma_{PF \cdot N_{>320}}^{\text{abs}}$).

C.8 PRE-PROCESSING OF SOURCE SECTOR CONTRIBUTIONS

By comparing PES fractions of different source sectors during the NETCARE 2014 measurements, two types of plumes are obvious (Figs. C.15 and C.16): plumes with definite contributions from one source sector separated from other sectors (Figs. C.15c, e, and f) and plumes with mixed contributions from different source sectors (mixed plumes; Figs. C.15a, b, and d as well as C.16d). However, a combination of both plume types is given in Figs. C.16a-c and e-j. In such cases, mixed plumes were excluded from the further analysis, in order to provide a distinct source attribution. This had only been done if data statistics were still sufficient after selection. In detail, certain thresholds were set for selection (indicated with black boxes in Figs. C.16a-c and e-j), differentiating mixed plumes from plumes of distinct source attribution. As a result for the southern air mass period, contributions from vegetation fires are separated from anthropogenic sources (Figs. C.16g-i); contributions from populated areas are separated from vegetation fires and other anthropogenic sources (Figs. C.16a-b and g); and contributions from Arctic open water areas are separated from other sectors (Figs. C.16c, e-f, and j).

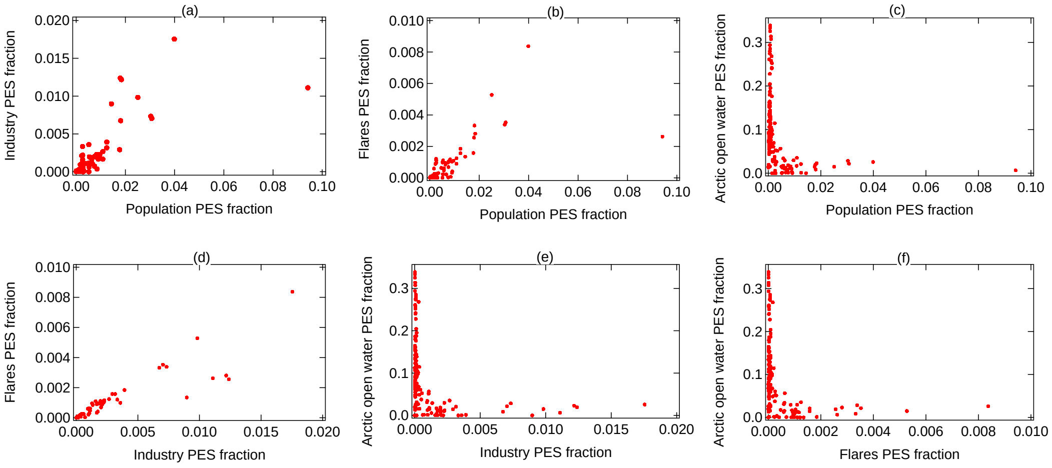

Figure C.15: Comparison between different source sectors during the Arctic air mass period.

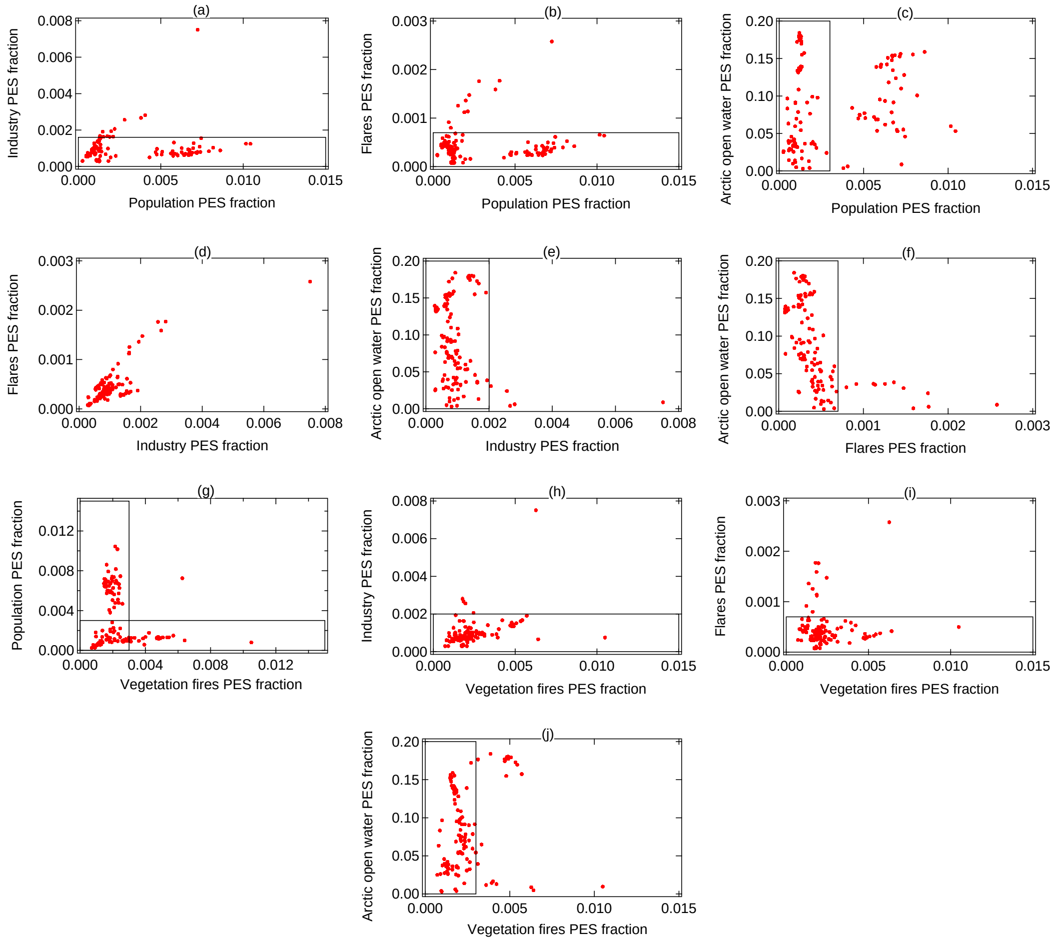

Figure C.16: Comparison between different source sectors during the southern air mass period. Black boxes represent thresholds to differentiate between different sectors.

C.9 ADDITIONAL FIGURES FOR AIR MASS HISTORY

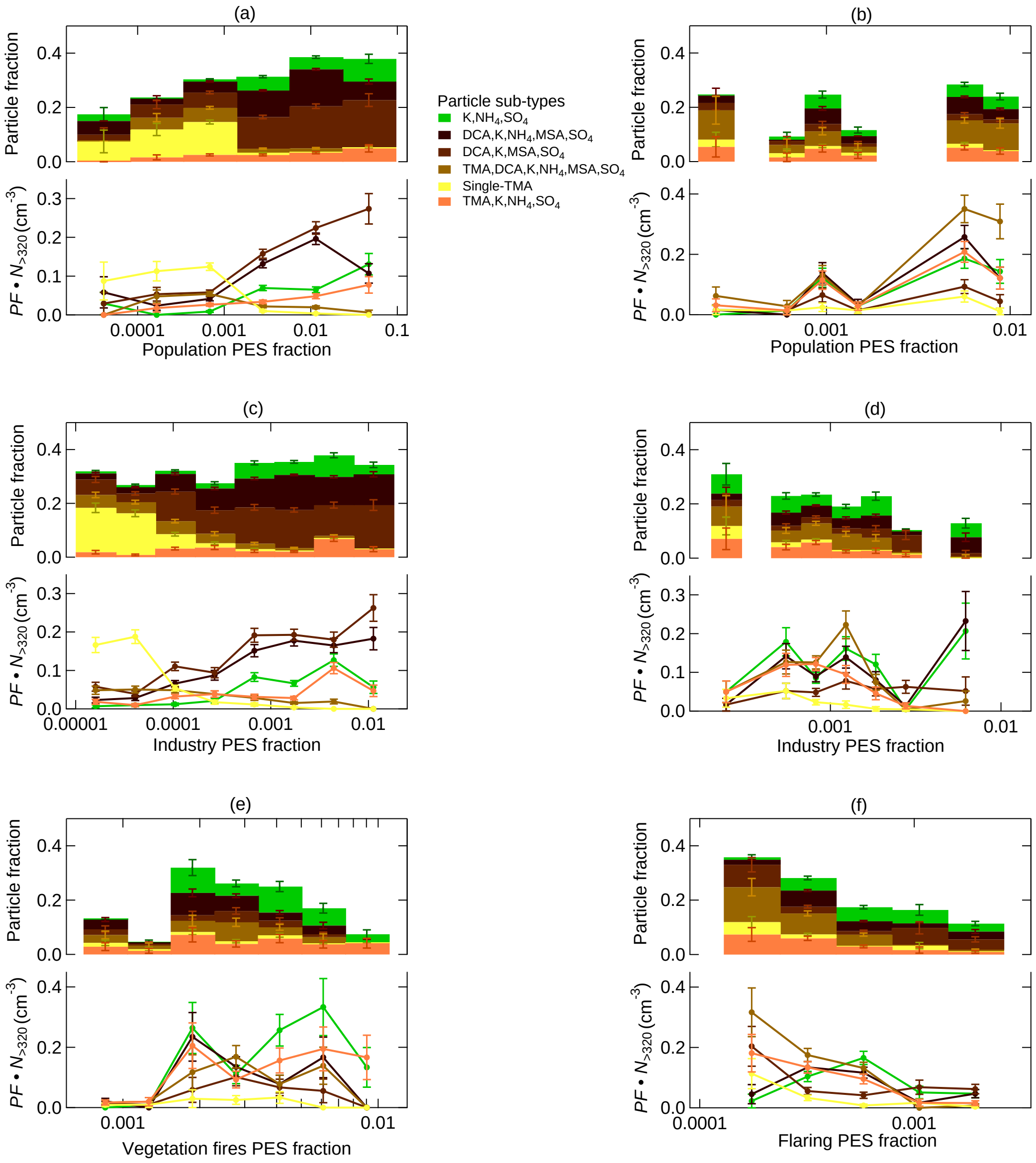

Figure C.17: Comparison between aerosol composition of the identified particle sub-types by the ALABAMA and FLEXPART predicted air mass residence time over populated areas (a-b), industrial areas (c-d), vegetation fires (e), and over areas associated with flaring emissions (f) during the Arctic (a and c) and the southern (b and d-f) air mass periods. Figures represent each: (top) the cumulative particle fraction (PF) and (bottom) the scaled number concentration ($PF \cdot N_{>320}$). Uncertainty analyses are given in Sect. C.7.

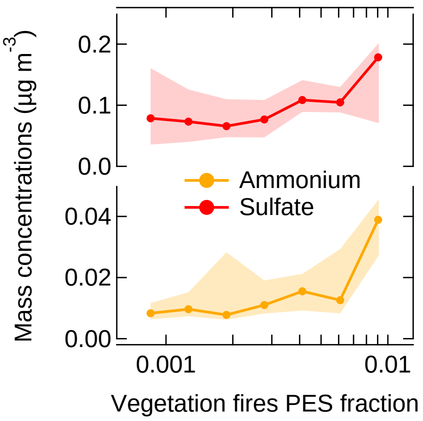

Figure C.18: Median (solid line) and interquartile ranges (shaded area) of the sulfate (red, top panel) and ammonium (orange, bottom panel) mass concentrations measured by the HR-ToF-AMS compared to the FLEXPART predicted air mass residence time over vegetation fires during the southern air mass period. Uncertainties are given in Table 1.

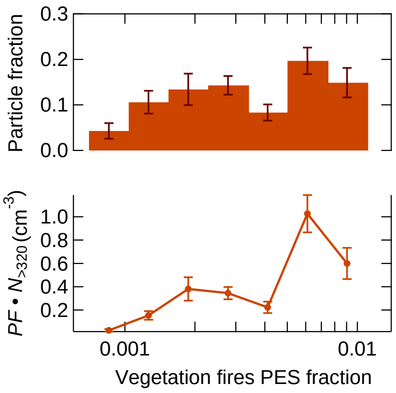

Figure C.19: Comparison between FLEXPART predicted air mass residence time over vegetation fires and the ALABAMA particle type indicative for the presence of levoglucosan (for details see Köllner et al., 2017) during the southern air mass period. The figure represents (top) the particle fraction (PF) and (bottom) the scaled number concentration ($PF \cdot N_{>320}$). Uncertainty analyses are given in Sect. C.7.

BIBLIOGRAPHY

AMAP (2010). “Assessment 2007: Oil and Gas Activities in the Arctic - Effects and Potential Effects.” *Arctic Monitoring and Assessment Programme (AMAP), Oslo, Norway* 2, pp. vii + 277.

AMS Glossary (2018). Last access: 24.05.2019. URL: http://glossary.ametsoc.org/wiki/Pseudoequivalent_potential_temperature.

Abbatt, J. P. D. et al. (2019). “Overview paper: New insights into aerosol and climate in the Arctic.” *Atmos. Chem. Phys.* 19.4, pp. 2527–2560. DOI: 10.5194/acp-19-2527-2019.

Acosta Navarro, J. C., V. Varma, I. Riipinen, Ø. Seland, A. Kirkevåg, H. Struthers, T. Iversen, H.-C. Hansson, and A. M. L. Ekman (2016). “Amplification of Arctic warming by past air pollution reductions in Europe.” *Nature Geoscience* 9, pp. 277–281. URL: http://dx.doi.org/10.1038/ngeo2673.

Aero-Laser GmbH (2013). *Ultra-Fast Carbon-Monoxide Analyser AL5002-Manual-Version 1.24.* Aero-Laser GmbH.

Akagi, S. K., R. J. Yokelson, C. Wiedinmyer, M. J. Alvarado, J. S. Reid, T. Karl, J. D. Crounse, and P. O. Wennberg (2011). “Emission factors for open and domestic biomass burning for use in atmospheric models.” *Atmos. Chem. Phys.* 11.9, pp. 4039–4072. DOI: 10.5194/acp-11-4039-2011.

Aliabadi, A. A., R. M. Staebler, and S. Sharma (2015). “Air quality monitoring in communities of the Canadian Arctic during the high shipping season with a focus on local and marine pollution.” *Atmos. Chem. Phys.* 15.5, pp. 2651–2673. DOI: 10.5194/acp-15-2651-2015.

Aliabadi, A. A. et al. (2016a). “Ship emissions measurement in the Arctic by plume intercepts of the Canadian Coast Guard icebreaker *Amundsen* from the *Polar 6* aircraft platform.” *Atmos. Chem. Phys.* 16.12, pp. 7899–7916. DOI: 10.5194/acp-16-7899-2016.

Aliabadi, A. A., R. Staebler, M. Liu, and A. Herber (2016b). “Characterization and Parametrization of Reynolds Stress and Turbulent Heat Flux in the Stably-Stratified Lower Arctic Troposphere Using Aircraft Measurements.” *Bound.-Lay. Meteorol.* Pp. 1–28. DOI: 10.1007/s10546-016-0164-7.

Allen, J. O., D. P. Fergenson, E. E. Gard, L. S. Hughes, B. D. Morrical, M. J. Kleeman, D. S. Gross, M. E. Gälli, K. A. Prather, and G. R. Cass (2000). "Particle Detection Efficiencies of Aerosol Time of Flight Mass Spectrometers under Ambient Sampling Conditions." *Environ. Sci. Technol.* 34.1, pp. 211–217. DOI: 10.1021/es9904179.

Almeida, J. et al. (2013). "Molecular understanding of sulphuric acid-amine particle nucleation in the atmosphere." *Nature* 502, pp. 359–363. DOI: 10.1038/nature12663.

Altieri, K., S. Seitzinger, A. Carlton, B. Turpin, G. Klein, and A. Marshall (2008). "Oligomers formed through in-cloud methylglyoxal reactions: Chemical composition, properties, and mechanisms investigated by ultra-high resolution FT-ICR mass spectrometry." *Atmos. Environ.* 42.7, pp. 1476 –1490. URL: https://doi.org/10.1016/j.atmosenv.2007.11.015.

Analog Microelectronics (2015). *AMS 4711 - Miniaturized pressure transmitter with 0 .. 5 V output.* Tech. rep. Analog Microelectronics GmbH.

Andreae, M. O. (1983). "Soot Carbon and Excess Fine Potassium: Long-Range Transport of Combustion-Derived Aerosols." *Science* 220.4602, pp. 1148–1151. DOI: 10.1126/science.220.4602.1148.

Andreae, M. O. and P. Merlet (2001). "Emission of trace gases and aerosols from biomass burning." *Global Biogeochem. Cy.* 15.4, pp. 955–966. DOI: 10.1029/2000GB001382.

Angelino, S., D. T. Suess, and K. A. Prather (2001). "Formation of Aerosol Particles from Reactions of Secondary and Tertiary Alkylamines: Characterization by Aerosol Time-of-Flight Mass Spectrometry." *Environ. Sci. Technol.* 35(15), pp. 3130–3138. DOI: 10.1021/es0015444.

Arndt, D. S. et al. (2015). "Bulletin of the American Meteorological Society." State of the Climate. Journal Article. Chap. State of the Climate in 2014. URL: https://repository.library.noaa.gov/view/noaa/17469.

Asmi, E., V. Kondratyev, D. Brus, T. Laurila, H. Lihavainen, J. Backman, V. Vakkari, M. Aurela, J. Hatakka, Y. Viisanen, T. Uttal, V. Ivakhov, and A. Makshtas (2016). "Aerosol size distribution seasonal characteristics measured in Tiksi, Russian Arctic." *Atmos. Chem. Phys.* 16.3, pp. 1271–1287. DOI: 10.5194/acp-16-1271-2016.

Ault, A. P., M. J. Moore, H. Furutani, and K. A. Prather (2009). "Impact of Emissions from the Los Angeles Port Region on San Diego Air Quality during Regional Transport Events.” *Environ. Sci. Technol.* 43.10, pp. 3500–3506. DOI: 10.1021/es8018918.

Aventech (2018). Last access: 25.05.2018. URL: www.aventech.com/products/aimms20.html.

Bahreini, R., E. J. Dunlea, B. M. Matthew, C. Simons, K. S. Docherty, P. F. DeCarlo, J. L. Jimenez, C. A. Brock, and A. M. Middlebrook (2008). “Design and Operation of a Pressure-Controlled Inlet for Airborne Sampling with an Aerodynamic Aerosol Lens.” *Aerosol Sci. Technol.* 42.6, pp. 465–471. DOI: 10.1080/02786820802178514.

Barrie, L. A. (1986). “Arctic air pollution: An overview of current knowledge.” *Atmos. Environ.* 20.4, pp. 643–663. DOI: 10.1016/0004-6981(86)90180-0.

Barrie, L. A. and M. J. Barrie (1990). “Chemical components of lower tropospheric aerosols in the high arctic: Six years of observations.” *J. Atmos. Chem.* 11.3, pp. 211–226. DOI: 10.1007/BF00118349.

Barsanti, K. C., P. H. McMurry, and J. N. Smith (2009). “The potential contribution of organic salts to new particle growth.” *Atmos. Chem. Phys.* 9.9, pp. 2949–2957. DOI: 10.5194/acp-9-2949-2009.

Behrenfeld, M. J., Y. Hu, R. T. O’Malley, E. S. Boss, C. A. Hostetler, D. A. Siegel, J. L. Sarmiento, J. Schulien, J. W. Hair, X. Lu, S. Rodier, and A. J. Scarino (2016). “Annual boom-bust cycles of polar phytoplankton biomass revealed by space-based lidar.” *Nature Geoscience* 10, pp. 118–122. URL: https://doi.org/10.1038/ngeo2861.

Bein, K. J., Y. Zhao, A. S. Wexler, and M. V. Johnston (2005). “Speciation of size-resolved individual ultrafine particles in Pittsburgh, Pennsylvania.” *J. Geophys. Res.-Atmos.* 110.D7. DOI: 10.1029/2004JD004708.

Bezdek, J. C., R. Ehrlich, and W. Full (1984). “FCM: The fuzzy c-means clustering algorithm.” *Computers and Geosciences* 10.2, pp. 191 –203. URL: https://doi.org/10.1016/0098-3004(84)90020-7.

Bhatt, U. S., D. A. Walker, M. K. Raynolds, J. C. Comiso, H. E. Epstein, G. Jia, R. Gens, J. E. Pinzon, C. J. Tucker, C. E. Tweedie, and P. J. Webber (2010). “Circumpolar Arctic Tundra Vegetation Change Is Linked to Sea Ice Decline.” *Earth Interactions* 14.8, pp. 1–20. DOI: 10.1175/2010EI315.1.

Bhave, P. V., J. O. Allen, B. D. Morrical, D. P. Fergenson, G. R. Cass, and K. A. Prather (2002). “A Field-Based Approach for Determining ATOFMS Instrument

Sensitivities to Ammonium and Nitrate." *Environ. Sci. Technol.* 36.22, pp. 4868–4879. DOI: 10.1021/es015823i.

Bikkina, S., K. Kawamura, Y. Miyazaki, and P. Fu (2014). "High abundances of oxalic, azelaic, and glyoxylic acids and methylglyoxal in the open ocean with high biological activity: Implication for secondary OA formation from isoprene." *Geophys. Res. Lett.* 41.10, pp. 3649–3657. DOI: 10.1002/2014GL059913.

Blanchard, D. C. and A. H. Woodcock (1980). "THE PRODUCTION, CONCENTRATION, AND VERTICAL DISTRIBUTION OF THE SEA-SALT AEROSOL." *Ann. NY Acad. Sci.* 338.1, pp. 330–347. DOI: 10.1111/j.1749-6632.1980.tb17130.x.

Bond, T. C. et al. (2013). "Bounding the role of black carbon in the climate system: A scientific assessment." *J. Geophys. Res.-Atmos.* 118.11, pp. 5380–5552. DOI: 10.1002/jgrd.50171.

Boucher, O., D. Randall, P. Artaxo, C. Bretherton, G. Feingold, P. Forster, V.-M Kerminen, Y. Kondo, H. Liao, U. Lohmann, P. Rasch, S. Satheesh, S. Sherwood, B. Stevens, and X. Zhang (2013). "Climate Change 2013: The Physical Science Basis. Contribution of Working Group I to the Fifth Assessment Report of the Intergovernmental Panel on Climate Change." Ed. by T. Stocker, D. Qin, G.-K. Plattner, M. Tignor, S. Allen, J. Boschung, A. Nauels, Y. Xia, V. Bex, and P. Midgley. Cambridge University Press. Chap. Clouds and Aerosols, pp. 571–658. DOI: DOI:10.1017/CBO9781107415324.016.

Boucher, O. (2015). "Atmospheric Aerosols: Properties and Climate Impacts." Springer, Dordrecht. Chap. Aerosol Modelling, pp. 51–81.

Bourgeois, Q. and I. Bey (2011). "Pollution transport efficiency toward the Arctic: Sensitivity to aerosol scavenging and source regions." *J. Geophys. Res.-Atmos.* 116.D8. DOI: 10.1029/2010JD015096.

Bozem, H., P. Hoor, D. Kunkel, F. Köllner, J. Schneider, A. Herber, H. Schulz, W. R. Leaitch, A. A. Aliabadi, M. D. Willis, J. Burkart, and J. P. D. Abbatt (2019). "Characterization of Transport Regimes and the Polar Dome during Arctic Spring and Summer using in-situ Aircraft Measurements." *Atmos. Chem. Phys. Discuss.* 2019, pp. 1–36. DOI: 10.5194/acp-2019-70.

Brands, M., M. Kamphus, T. Böttger, J. Schneider, F. Drewnick, A. Roth, J. Curtius, C. Voigt, A. Borbon, M. Beekmann, A. Bourdon, T. Perrin, and S. Borrmann (2011). "Characterization of a Newly Developed Aircraft-Based Laser Ablation Aerosol Mass Spectrometer (ALABAMA) and First Field Deployment in Urban

Pollution Plumes over Paris During MEGAPOLI 2009." *Aerosol Sci. Technol.* 45.1, pp. 46–64. DOI: 10.1080/02786826.2010.517813.

Brands, M. (2009). "Aufbau und Charakterisierung eines fugzeuggetragenen Einzelpartikel-Massenspektrometers." PhD thesis. Johannes-Gutenberg Universität Mainz.

Breider, T. J., L. J. Mickley, D. J. Jacob, Q. Wang, J. A. Fisher, R. Y.-W. Chang, and B. Alexander (2014). "Annual distributions and sources of Arctic aerosol components, aerosol optical depth, and aerosol absorption." *J. Geophys. Res.-Atmos.* 119.7, pp. 4107–4124. DOI: 10.1002/2013JD020996.

Breider, T. J., L. J. Mickley, D. J. Jacob, C. Ge, J. Wang, M. Payer Sulprizio, B. Croft, D. A. Ridley, J. R. McConnell, S. Sharma, L. Husain, V. A. Dutkiewicz, K. Eleftheriadis, H. Skov, and P. K. Hopke (2017). "Multidecadal trends in aerosol radiative forcing over the Arctic: Contribution of changes in anthropogenic aerosol to Arctic warming since 1980." *J. Geophys. Res.-Atmos.* 122.6, pp. 3573–3594. DOI: 10.1002/2016JD025321.

Brock, C. A. et al. (2011). "Characteristics, sources, and transport of aerosols measured in spring 2008 during the aerosol, radiation, and cloud processes affecting Arctic Climate (ARCPAC) Project." *Atmos. Chem. Phys.* 11.6, pp. 2423–2453. DOI: 10.5194/acp-11-2423-2011.

Browse, J., K. S. Carslaw, S. R. Arnold, K. Pringle, and O. Boucher (2012). "The scavenging processes controlling the seasonal cycle in Arctic sulphate and black carbon aerosol." *Atmos. Chem. Phys.* 12.15, pp. 6775–6798. DOI: 10.5194/acp-12-6775-2012.

Browse, J., K. S. Carslaw, G. W. Mann, C. E. Birch, S. R. Arnold, and C. Leck (2014). "The complex response of Arctic aerosol to sea-ice retreat." *Atmos. Chem. Phys.* 14.14, pp. 7543–7557. DOI: 10.5194/acp-14-7543-2014.

Bullard, J. E., M. Baddock, T. Bradwell, J. Crusius, E. Darlington, D. Gaiero, S. Gassó, G. Gisladottir, R. Hodgkins, R. McCulloch, C. McKenna-Neuman, T. Mockford, H. Stewart, and T. Thorsteinsson (2016). "High-latitude dust in the Earth system." *Rev. Geophys.* 54.2, pp. 447–485. DOI: 10.1002/2016RG000518.

Bundke, U., M. Berg, N. Houben, A. Ibrahim, M. Fiebig, F. Tettich, C. Klaus, H. Franke, and A. Petzold (2015). "The IAGOS-CORE aerosol package: instrument design, operation and performance for continuous measurement aboard in-service aircraft." *Tellus B* 67.1. 28339. DOI: 10.3402/tellusb.v67.28339.

Burkart, J., M. D. Willis, H. Bozem, J. L. Thomas, K. Law, P. Hoor, A. A. Aliabadi, F. Köllner, J. Schneider, A. Herber, J. P. D. Abbatt, and W. R. Leaitch (2017).

"Summertime observations of elevated levels of ultrafine particles in the high Arctic marine boundary layer." *Atmos. Chem. Phys.* 17.8, pp. 5515–5535. DOI: 10.5194/acp-17-5515-2017.

Cai, Y., A. Zelenyuk, and D. Imre (2006). "A High Resolution Study of the Effect of Morphology On the Mass Spectra of Single PSL Particles with Na-containing Layers and Nodules." *Aerosol Sci. Technol.* 40.12, pp. 1111–1122. DOI: 10.1080/02786820601001677.

Cai, Y., D. C. Montague, W. Mooiweer-Bryan, and T. Deshler (2008). "Performance characteristics of the ultra high sensitivity aerosol spectrometer for particles between 55 and 800 nm: Laboratory and field studies." *J. Aerosol Sci.* 39.9, pp. 759 –769. URL: https://doi.org/10.1016/j.jaerosci.2008.04.007.

Carlson, T. N. (1981). "Speculations on the movement of polluted air to the Arctic." *Atmos. Environ.* 15.8. Arctic Air Chemistry Proceedings of the Second Symposium, pp. 1473 –1477. URL: https://doi.org/10.1016/0004-6981(81)90354-1.

Carlton, A. G., B. J. Turpin, H.-J. Lim, K. E. Altieri, and S. Seitzinger (2006). "Link between isoprene and secondary organic aerosol (SOA): Pyruvic acid oxidation yields low volatility organic acids in clouds." *Geophys. Res. Lett.* 33.6. DOI: 10.1029/2005GL025374.

Cavalieri, D. J., C. L. Parkinson, P. Gloersen, and H. J. Zwally (1996, updated yearly). *Sea Ice Concentrations from Nimbus-7 SMMR and DMSP SSM/I-SSMIS Passive Microwave Data, Version 1, NSIDC-0051.* Boulder, Colorado USA. NASA National Snow and Ice Data Center Distributed Active Archive Center. Last access: 08.06.2018. DOI: https://doi.org/10.5067/8GQ8LZQVL0VL.

Chang, R. Y.-W., C. Leck, M. Graus, M. Müller, J. Paatero, J. F. Burkhart, A. Stohl, L. H. Orr, K. Hayden, S.-M. Li, A. Hansel, M. Tjernström, W. R. Leaitch, and J. P. D. Abbatt (2011). "Aerosol composition and sources in the central Arctic Ocean during ASCOS." *Atmos. Chem. Phys.* 11.20, pp. 10619–10636. DOI: 10.5194/acp-11-10619-2011.

Chapin, F. S. et al. (2005). "Role of Land-Surface Changes in Arctic Summer Warming." *Science* 310.5748, pp. 657–660. DOI: 10.1126/science.1117368.

Chapman, W. L. and J. E. Walsh (1993). "Recent Variations of Sea Ice and Air Temperature in High Latitudes." *B. Am. Meteorol. Soc.* 74.1, pp. 33–47. DOI: 10.1175/1520-0477(1993)074<0033:RVOSIA>2.0.CO;2.

Chi, J. W., W. J. Li, D. Z. Zhang, J. C. Zhang, Y. T. Lin, X. J. Shen, J. Y. Sun, J. M. Chen, X. Y. Zhang, Y. M. Zhang, and W. X. Wang (2015). "Sea salt aerosols as a reactive surface for inorganic and organic acidic gases in the Arctic troposphere." *Atmos. Chem. Phys.* 15.19, pp. 11341–11353. DOI: 10.5194/acp-15-11341-2015.

Christopoulos, C. D., S. Garimella, M. A. Zawadowicz, O. Möhler, and D. J. Cziczo (2018). "A machine learning approach to aerosol classification for single-particle mass spectrometry." *Atmos. Meas. Tech.* 11.10, pp. 5687–5699. DOI: 10.5194/amt-11-5687-2018.

Clemen, H.-C. (2020). "Massenspektrometrische Analyse über Zusammensetzung und Prozessierungsverhalten von Eiskristallresiduen aus Mischphasenwolken und atmosphärisch relevanter Eiskeime, bei simultaner Weiterentwicklung des Einzelpartikel-Laserablationsmassenspektrometers ALABAMA zur Optimierung der Detektions- und Ablationseffizienz von Aerosolpartikeln." PhD thesis. in prep., Johannes Gutenberg-Universität Mainz.

Clemen, H.-C. et al. (2019). "Further development of the single-particle laser ablation mass spectrometer ALABAMA to enhance the collection efficiency of ice nucleating particles." *in prep. for Atmos. Meas. Tech.*

Collins, D. B. et al. (2017). "Frequent ultrafine particle formation and growth in Canadian Arctic marine and coastal environments." *Atmos. Chem. Phys.* 17.21, pp. 13119–13138. DOI: 10.5194/acp-17-13119-2017.

Corbett, J. J., D. A. Lack, J. J. Winebrake, S. Harder, J. A. Silberman, and M. Gold (2010). "Arctic shipping emissions inventories and future scenarios." *Atmos. Chem. Phys.* 10.19, pp. 9689–9704. DOI: 10.5194/acp-10-9689-2010.

Corbin, J., P. Rehbein, G. Evans, and J. Abbatt (2012). "Combustion particles as ice nuclei in an urban environment: Evidence from single-particle mass spectrometry." *Atmos. Environ.* 51, pp. 286–292. URL: https://doi.org/10.1016/j.atmosenv.2012.01.007.

Creamean, J. M., M. Maahn, G. de Boer, A. McComiskey, A. J. Sedlacek, and Y. Feng (2018). "The influence of local oil exploration and regional wildfires on summer 2015 aerosol over the North Slope of Alaska." *Atmos. Chem. Phys.* 18.2, pp. 555–570. DOI: 10.5194/acp-18-555-2018.

Croft, B., G. R. Wentworth, R. V. Martin, W. R. Leaitch, J. G. Murphy, B. N. Murphy, J. K. Kodros, J. P. D. Abbatt, and J. R. a. Pierce (2016a). "Contribution of Arctic seabird-colony ammonia to atmospheric particles and cloud-albedo radiative effect." *Nat. Commun.* 7.13444. DOI: 10.1038/ncomms13444.

Croft, B., R. V. Martin, W. R. Leaitch, P. Tunved, T. J. Breider, S. D. D'Andrea, and J. R. Pierce (2016b). "Processes controlling the annual cycle of Arctic aerosol number and size distributions.” *Atmos. Chem. Phys.* 16.6, pp. 3665–3682. DOI: 10.5194/acp-16-3665-2016.

Croft, B. et al. (2019). “Arctic marine secondary organic aerosol contributes significantly to summertime particle size distributions in the Canadian Arctic Archipelago.” *Atmos. Chem. Phys.* 2019.5, pp. 2787–2812. DOI: 10.5194/acp-19-2787-2019.

Cubison, M. J. et al. (2011). “Effects of aging on organic aerosol from open biomass burning smoke in aircraft and laboratory studies.” *Atmos. Chem. Phys.* 11.23, pp. 12049–12064. DOI: 10.5194/acp-11-12049-2011.

Curry, J. A., J. L. Schramm, and E. E. Ebert (1995). “Sea Ice-Albedo Climate Feedback Mechanism.” *J. Climate* 8.2, pp. 240–247. DOI: 10.1175/1520-0442(1995)008<0240:SIACFM>2.0.CO;2.

Dahlkötter, F., M. Gysel, D. Sauer, A. Minikin, R. Baumann, P. Seifert, A. Ansmann, M. Fromm, C. Voigt, and B. Weinzierl (2014). “The Pagami Creek smoke plume after long-range transport to the upper troposphere over Europe - aerosol properties and black carbon mixing state.” *Atmos. Chem. Phys.* 14.12, pp. 6111–6137. DOI: 10.5194/acp-14-6111-2014.

Dall’Osto, M., D. C. S. Beddows, P. Tunved, R. Krejci, J. Ström, H.-C. Hansson, Y. J. Yoon, K.-T. Park, S. Becagli, R. Udisti, T. Onasch, C. D. O’Dowd, R. Simó, and R. M. Harrison (2017). “Arctic sea ice melt leads to atmospheric new particle formation.” *Scientific Reports* 7.3318. DOI: 10.1038/s41598-017-03328-1.

Dall‘Osto, M., D. Ceburnis, C. Monahan, D. R. Worsnop, J. Bialek, M. Kulmala, T. Kurtén, M. Ehn, J. Wenger, J. Sodeau, R. Healy, and C. O’Dowd (2012). “Nitrogenated and aliphatic organic vapors as possible drivers for marine secondary organic aerosol growth.” *J. Geophys. Res.-Atmos.* 117.D12311. DOI: 10.1029/2012JD017522.

Dall’Osto, M., R. L. Airs, R. Beale, C. Cree, M. F. Fitzsimons, D. Beddows, R. M. Harrison, D. Ceburnis, C. O’Dowd, M. Rinaldi, M. Paglione, A. Nenes, S. Decesari, and R. Simó (2019). “Simultaneous Detection of Alkylamines in the Surface Ocean and Atmosphere of the Antarctic Sympagic Environment.” *ACS Earth Space Chem.* 3.5, pp. 854–862. DOI: 10.1021/acsearthspacechem.9b00028.

Dawson, M. L., M. E. Varner, V. Perraud, M. J. Ezell, R. B. Gerber, and B. J. Finlayson-Pitts (2012). “Simplified mechanism for new particle formation from methanesulfonic acid, amines, and water via experiments and ab initio calculations.” *P. Natl. Acad. Sci.* 109.46, pp. 18719–18724. DOI: 10.1073/pnas.1211878109.

De Groot, W. J., M. D. Flannigan, and A. S. Cantin (2013). “Climate change impacts on future boreal fire regimes.” *Forest Ecology and Management* 294, pp. 35–44. URL: https://doi.org/10.1016/j.foreco.2012.09.027.

DeCarlo, P. F., I. M. Ulbrich, J. Crounse, B. de Foy, E. J. Dunlea, A. C. Aiken, D. Knapp, A. J. Weinheimer, T. Campos, P. O. Wennberg, and J. L. Jimenez (2010). “Investigation of the sources and processing of organic aerosol over the Central Mexican Plateau from aircraft measurements during MILAGRO.” *Atmos. Chem. Phys.* 10.12, pp. 5257–5280. DOI: 10.5194/acp-10-5257-2010.

DeCarlo, P. F., J. G. Slowik, D. R. Worsnop, P. Davidovits, and J. L. Jimenez (2004). “Particle Morphology and Density Characterization by Combined Mobility and Aerodynamic Diameter Measurements. Part 1: Theory.” *Aerosol Sci. Technol.* 38.12, pp. 1185–1205. DOI: 10.1080/027868290903907.

DeCarlo, P. F., J. R. Kimmel, A. Trimborn, M. J. Northway, J. T. Jayne, A. C. Aiken, M. Gonin, K. Fuhrer, T. Horvath, K. S. Docherty, D. R. Worsnop, and J. L. Jimenez (2006). “Field-Deployable, High-Resolution, Time-of-Flight Aerosol Mass Spectrometer.” *Anal. Chem.* 78.24, pp. 8281–8289. DOI: 10.1021/ac061249n.

Dreiling, V. and B. Friederich (1997). “Spatial distribution of the arctic haze aerosol size distribution in western and eastern Arctic.” *Atmos. Res.* 44.1. Arctic Haze, pp. 133 –152. URL: https://doi.org/10.1016/S0169-8095(96)00035-X.

Drewnick, F. (2000). “Entwicklung und Charakterisierung eines Laser-massenspektrometrischen Verfahrens: Ein Beitrag zur Aerosolanalytik.” PhD thesis. Universität Hohenheim.

Eckhardt, S., O. Hermansen, H. Grythe, M. Fiebig, K. Stebel, M. Cassiani, A. Baecklund, and A. Stohl (2013). “The influence of cruise ship emissions on air pollution in Svalbard - a harbinger of a more polluted Arctic?” *Atmos. Chem. Phys.* 13.16, pp. 8401–8409. DOI: 10.5194/acp-13-8401-2013.

Elvidge, C. D., M. Zhizhin, F.-C. Hsu, and K. E. Baugh (2013). “VIIRS Nightfire: Satellite Pyrometry at Night.” *Remote Sensing* 5.9, pp. 4423–4449. DOI: 10.3390/rs5094423.

Elvidge, C. D., M. Zhizhin, K. Baugh, F.-C. Hsu, and T. Ghosh (2016). “Methods for Global Survey of Natural Gas Flaring from Visible Infrared Imaging Radiometer Suite Data.” *Energies* 9.1. DOI: 10.3390/en9010014.

Engvall, A.-C., R. Krejci, J. Ström, R. Treffeisen, R. Scheele, O. Hermansen, and J. Paatero (2008). “Changes in aerosol properties during spring-summer period in the Arctic troposphere." *Atmos. Chem. Phys.* 8.3, pp. 445–462. DOI: 10.5194/acp-8-445-2008.

Erupe, M. E., A. A. Viggiano, and S.-H. Lee (2011). "The effect of trimethylamine on atmospheric nucleation involving H_2SO_4." *Atmos. Chem. Phys.* 11.10, pp. 4767–4775. DOI: 10.5194/acp-11-4767-2011.

Ervens, B., B. J. Turpin, and R. J. Weber (2011). "Secondary organic aerosol formation in cloud droplets and aqueous particles (aqSOA): a review of laboratory, field and model studies." *Atmos. Chem. Phys.* 11.21, pp. 11069–11102. DOI: 10.5194/acp-11-11069-2011.

Evangeliou, N., R. L. Thompson, S. Eckhardt, and A. Stohl (2018). "Top-down estimates of black carbon emissions at high latitudes using an atmospheric transport model and a Bayesian inversion framework." *Atmos. Chem. Phys.* 18.20, pp. 15307–15327. DOI: 10.5194/acp-18-15307-2018.

Evangeliou, N., A. Kylling, S. Eckhardt, V. Myroniuk, K. Stebel, R. Paugam, S. Zibtsev, and A. Stohl (2019). "Open fires in Greenland in summer 2017: transport, deposition and radiative effects of BC, OC and BrC emissions." *Atmos. Chem. Phys.* 19.2, pp. 1393–1411. DOI: 10.5194/acp-19-1393-2019.

Facchini, M. C., S. Decesari, M. Rinaldi, C. Carbone, E. Finessi, M. Mircea, S. Fuzzi, F. Moretti, E. Tagliavini, D. Ceburnis, and C. D. O'Dowd (2008). "Important Source of Marine Secondary Organic Aerosol from Biogenic Amines." *Environ. Sci. Technol.* 42.24, pp. 9116–9121. DOI: 10.1021/es8018385.

Fan, S.-M. (2013). "Modeling of observed mineral dust aerosols in the arctic and the impact on winter season low-level clouds." *J. Geophys. Res.-Atmos.* 118.19, pp. 11,161–11,174. DOI: 10.1002/jgrd.50842.

Ferrero, L. et al. (2016). "Vertical profiles of aerosol and black carbon in the Arctic: a seasonal phenomenology along 2 years (2011–2012) of field campaigns." *Atmos. Chem. Phys.* 16.19, pp. 12601–12629. DOI: 10.5194/acp-16-12601-2016.

Fiebig, M., A. Stohl, M. Wendisch, S. Eckhardt, and A. Petzold (2003). "Dependence of solar radiative forcing of forest fire aerosol on ageing and state of mixture." *Atmos. Chem. Phys.* 3.3, pp. 881–891. DOI: 10.5194/acp-3-881-2003.

Fisher, J. A. et al. (2011). "Sources, distribution, and acidity of sulfate-ammonium aerosol in the Arctic in winter-spring." *Atmos. Environ.* 45.39, pp. 7301 –7318. URL: https://doi.org/10.1016/j.atmosenv.2011.08.030.

Flanner, M. G., K. M. Shell, M. Barlage, D. K. Perovich, and M. A. Tschudi (2011). “Radiative forcing and albedo feedback from the Northern Hemisphere cryosphere between 1979 and 2008.” *Nature Geoscience* 4, pp. 151–155. URL: https://doi.org/10.1038/ngeo1062.

Flanner, M. G. (2013). “Arctic climate sensitivity to local black carbon.” *J. Geophys. Res.-Atmos.* 118.4, pp. 1840–1851. DOI: 10.1002/jgrd.50176.

Freud, E., R. Krejci, P. Tunved, R. Leaitch, Q. T. Nguyen, A. Massling, H. Skov, and L. Barrie (2017). “Pan-Arctic aerosol number size distributions: seasonality and transport patterns.” *Atmos. Chem. Phys.* 17.13, pp. 8101–8128. DOI: 10.5194/acp-17-8101-2017.

Frossard, A. A., L. M. Russell, S. M. Burrows, S. M. Elliott, T. S. Bates, and P. K. Quinn (2014). “Sources and composition of submicron organic mass in marine aerosol particles.” *J. Geophys. Res.-Atmos.* 119.22. 2014JD021913, pp. 12,977–13,003. DOI: 10.1002/2014JD021913.

Froyd, K. D., S. M. Murphy, D. M. Murphy, J. A. de Gouw, N. C. Eddingsaas, and P. O. Wennberg (2010). “Contribution of isoprene-derived organosulfates to free tropospheric aerosol mass.” *P. Natl. Acad. Sci.* 107.50, pp. 21360–21365. DOI: 10.1073/pnas.1012561107.

Fu, P. Q., K. Kawamura, J. Chen, B. Charrière, and R. Sempéré (2013a). “Organic molecular composition of marine aerosols over the Arctic Ocean in summer: contributions of primary emission and secondary aerosol formation.” *Biogeosciences* 10.2, pp. 653–667. DOI: 10.5194/bg-10-653-2013.

Fu, P., K. Kawamura, J. Chen, and L. A. Barrie (2009a). “Isoprene, Monoterpene, and Sesquiterpene Oxidation Products in the High Arctic Aerosols during Late Winter to Early Summer.” *Environ. Sci. Technol.* 43.11, pp. 4022–4028. DOI: 10.1021/es803669a.

Fu, P., K. Kawamura, and L. A. Barrie (2009b). “Photochemical and Other Sources of Organic Compounds in the Canadian High Arctic Aerosol Pollution during Winter-Spring.” *Environ. Sci. Technol.* 43.2, pp. 286–292. DOI: 10.1021/es803046q.

Fu, P., K. Kawamura, K. Usukura, and K. Miura (2013b). “Dicarboxylic acids, ketocarboxylic acids and glyoxal in the marine aerosols collected during a round-the-world cruise.” *Mar. Chem.* 148, pp. 22 –32. URL: https://doi.org/10.1016/j.marchem.2012.11.002.

Fu, P., K. Kawamura, J. Chen, M. Qin, L. Ren, Y. Sun, Z. Wang, L. A. Barrie, E. Tachibana, A. Ding, and Y. Yamashita (2015). “Fluorescent water-soluble organic aerosols in the High Arctic atmosphere.” *Scientific Reports* 5.9845. Article. URL: http://dx.doi.org/10.1038/srep09845.

Fuelberg, H. E., D. L. Harrigan, and W. Sessions (2010). “A meteorological overview of the ARCTAS 2008 mission.” *Atmos. Chem. Phys.* 10.2, pp. 817–842. DOI: 10.5194/acp-10-817-2010.

Furutani, H., J. Jung, K. Miura, A. Takami, S. Kato, Y. Kajii, and M. Uematsu (2011). “Single-particle chemical characterization and source apportionment of iron-containing atmospheric aerosols in Asian outflow.” *J. Geophys. Res.-Atmos.* 116.D18. DOI: 10.1029/2011JD015867.

Fyfe, J. C., K. von Salzen, N. P. Gillett, V. K. Arora, G. M. Flato, and J. R. McConnell (2013). “One hundred years of Arctic surface temperature variation due to anthropogenic influence.” *Scientific Reports* 3.2645. URL: http://dx.doi.org/10.1038/srep02645.

GRIMM Aerosol Technik (2003). *User Manuel- Condensation Particle Counter*. Second. GRIMM Aerosol Technik.

GRIMM Aerosol Technik (2008). *Handbuch Version Rev-A Aerosolspektrometer SERIE 1.129 SKY-OPC*. GRIMM Aerosol Technik.

Gao, R. S., J. P. Schwarz, K. K. Kelly, D. W. Fahey, L. A. Watts, T. L. Thompson, J. R. Spackman, J. G. Slowik, E. S. Cross, J.-H. Han, P. Davidovits, T. B. Onasch, and D. R. Worsnop (2007). “A Novel Method for Estimating Light-Scattering Properties of Soot Aerosols Using a Modified Single-Particle Soot Photometer.” *Aerosol Sci. Technol.* 41.2, pp. 125–135. DOI: 10.1080/02786820601118398.

Gard, E. E., M. J. Kleeman, D. S. Gross, L. S. Hughes, J. O. Allen, B. D. Morrical, D. P. Fergenson, T. Dienes, M. E. Gälli, R. J. Johnson, G. R. Cass, and K. A. Prather (1998). “Direct Observation of Heterogeneous Chemistry in the Atmosphere.” *Science* 279.5354, pp. 1184–1187. DOI: 10.1126/science.279.5354.1184.

Garrett, T. J. and C. Zhao (2006). “Increased Arctic cloud longwave emissivity associated with pollution from mid-latitudes.” *Nature* 440, pp. 787–789. URL: https://doi.org/10.1038/nature04636.

Garrett, T., C. Zhao, and P. Novelli (2010). “Assessing the relative contributions of transport efficiency and scavenging to seasonal variability in Arctic aerosol.” *Tellus B* 62.3, pp. 190–196. DOI: 10.1111/j.1600-0889.2010.00453.x.

Gaston, C. J., K. A. Pratt, X. Qin, and K. A. Prather (2010). "Real-Time Detection and Mixing State of Methanesulfonate in Single Particles at an Inland Urban Locaion during a Phytoplankton Bloom." *Environ. Sci. Technol.* 44(5), pp. 1566–1572. DOI: 10.1021/es902069d.

Gautier, D. L., K. J. Bird, R. R. Charpentier, A. Grantz, D. W. Houseknecht, T. R. Klett, T. E. Moore, J. K. Pitman, C. J. Schenk, J. H. Schuenemeyer, K. Sørensen, M. E. Tennyson, Z. C. Valin, and C. J. Wandrey (2009). "Assessment of Undiscovered Oil and Gas in the Arctic." *Science* 324.5931, pp. 1175–1179. DOI: 10.1126/science.1169467.

Ge, X., A. S. Wexler, and S. L. Clegg (2011a). "Atmospheric amines - Part I. A review." *Atmos. Environ.* 45.3, pp. 524 –546. URL: http://dx.doi.org/10.1016/j.atmosenv.2010.10.012.

Ge, X., A. S. Wexler, and S. L. Clegg (2011b). "Atmospheric amines - Part II. Thermodynamic properties and gas/particle partitioning." *Atmos. Environ.* 45.3, pp. 561 –577. URL: http://dx.doi.org/10.1016/j.atmosenv.2010.10.013.

Giamarelou, M., K. Eleftheriadis, S. Nyeki, P. Tunved, K. Torseth, and G. Biskos (2016). "Indirect evidence of the composition of nucleation mode atmospheric particles in the high Arctic." *J. Geophys. Res.-Atmos.* 121.2. 2015JD023646, pp. 965–975. DOI: 10.1002/2015JD023646.

Gibb, S. W., R. F. C. Mantoura, and P. S. Liss (1999). "Ocean-atmosphere exchange and atmospheric speciation of ammonia and methylamines in the region of the NW Arabian Sea." *Global Biogeochem. Cy.* 13.1, pp. 161–178. DOI: 10.1029/98GB00743.

Giglio, L., J. T. Randerson, and G. R. van der Werf (2013). "Analysis of daily, monthly, and annual burned area using the fourth-generation global fire emissions database (GFED4)." *J. Geophys. Res.-Biogeo.* 118.1, pp. 317–328. DOI: 10.1002/jgrg.20042.

Gilgen, A., W. T. K. Huang, L. Ickes, D. Neubauer, and U. Lohmann (2018). "How important are future marine and shipping aerosol emissions in a warming Arctic summer and autumn?" *Atmos. Chem. Phys.* 18.14, pp. 10521–10555. DOI: 10.5194/acp-18-10521-2018.

Glasoe, W. A., K. Volz, B. Panta, N. Freshour, R. Bachman, D. R. Hanson, P. H. McMurry, and C. Jen (2015). "Sulfuric acid nucleation: An experimental study of the effect of seven bases." *J. Geophys. Res.-Atmos.* 120.5. 2014JD022730, pp. 1933–1950. DOI: 10.1002/2014JD022730.

Granier, C., U. Niemeier, J. H. Jungclaus, L. Emmons, P. Hess, J.-F. Lamarque, S. Walters, and G. P. Brasseur (2006). "Ozone pollution from future ship traffic in the Arctic northern passages." *Geophys. Res. Lett.* 33.13. DOI: 10.1029/2006GL026180.

Greenaway, K. (1950). "Experiences with Arctic flying weather." *Canadian Branch Royal. Met. Soc.* 1.9. URL: http://cmosarchives.ca/RMS/r0109.pdf.

Groot Zwaaftink, C. D., H. Grythe, H. Skov, and A. Stohl (2016). "Substantial contribution of northern high-latitude sources to mineral dust in the Arctic." *J. Geophys. Res.-Atmos.* 121.22, pp. 13,678–13,697. DOI: 10.1002/2016JD025482.

Gross, D. S., M. E. Gälli, P. J. Silva, and K. A. Prather (2000). "Relative Sensitivity Factors for Alkali Metal and Ammonium Cations in Single-Particle Aerosol Time-of-Flight Mass Spectra." *Anal. Chem.* 72.2, pp. 416–422. DOI: 10.1021/ac990434g.

Gross, D. S. et al. (2010). "Environmental chemistry through intelligent atmospheric data analysis." *Environmental Modelling and Software* 25.6, pp. 760 –769. URL: https://doi.org/10.1016/j.envsoft.2009.12.001.

Guasco, T. L., L. A. Cuadra-Rodriguez, B. E. Pedler, A. P. Ault, D. B. Collins, D. Zhao, M. J. Kim, M. J. Ruppel, S. C. Wilson, R. S. Pomeroy, V. H. Grassian, F. Azam, T. H. Bertram, and K. A. Prather (2014). "Transition Metal Associations with Primary Biological Particles in Sea Spray Aerosol Generated in a Wave Channel." *Environ. Sci. Technol.* 48.2, pp. 1324–1333. DOI: 10.1021/es403203d.

Guazzotti, S. A., D. T. Suess, K. R. Coffee, P. K. Quinn, T. S. Bates, A. Wisthaler, A. Hansel, W. P. Ball, R. R. Dickerson, C. Neusüß, P. J. Crutzen, and K. A. Prather (2003). "Characterization of carbonaceous aerosols outflow from India and Arabia: Biomass/biofuel burning and fossil fuel combustion." *J. Geophys. Res.-Atmos.* 108.D15. DOI: 10.1029/2002JD003277.

Gunsch, M. J., R. M. Kirpes, K. R. Kolesar, T. E. Barrett, S. China, R. J. Sheesley, A. Laskin, A. Wiedensohler, T. Tuch, and K. A. Pratt (2017). "Contributions of transported Prudhoe Bay oil field emissions to the aerosol population in Utqiaġvik, Alaska." *Atmos. Chem. Phys.* 17.17, pp. 10879–10892. DOI: 10.5194/acp-17-10879-2017.

Gunsch, M. J., N. W. May, M. Wen, C. L. H. Bottenus, D. J. Gardner, T. M. VanReken, S. B. Bertman, P. K. Hopke, A. P. Ault, and K. A. Pratt (2018). "Ubiquitous influence of wildfire emissions and secondary organic aerosol on summertime atmospheric aerosol in the forested Great Lakes region." *Atmos. Chem. Phys.* 18.5, pp. 3701–3715. DOI: 10.5194/acp-18-3701-2018.

Hallquist, M. et al. (2009). “The formation, properties and impact of secondary organic aerosol: current and emerging issues.” *Atmos. Chem. Phys.* 9.14, pp. 5155–5236. DOI: 10.5194/acp-9-5155-2009.

Hamacher-Barth, E., C. Leck, and K. Jansson (2016). “Size-resolved morphological properties of the high Arctic summer aerosol during ASCOS-2008.” *Atmos. Chem. Phys.* 16.10, pp. 6577–6593. DOI: 10.5194/acp-16-6577-2016.

Hansen, A. M. K., K. Kristensen, Q. T. Nguyen, A. Zare, F. Cozzi, J. K. Nøjgaard, H. Skov, J. Brandt, J. H. Christensen, J. Ström, P. Tunved, R. Krejci, and M. Glasius (2014). “Organosulfates and organic acids in Arctic aerosols: speciation, annual variation and concentration levels.” *Atmos. Chem. Phys.* 14.15, pp. 7807–7823. DOI: 10.5194/acp-14-7807-2014.

Hao, L. Q., A. Kortelainen, S. Romakkaniemi, H. Portin, A. Jaatinen, A. Leskinen, M. Komppula, P. Miettinen, D. Sueper, A. Pajunoja, J. N. Smith, K. E. J. Lehtinen, D. R. Worsnop, A. Laaksonen, and A. Virtanen (2014). “Atmospheric submicron aerosol composition and particulate organic nitrate formation in a boreal forestland-urban mixed region.” *Atmos. Chem. Phys.* 14.24, pp. 13483–13495. DOI: 10.5194/acp-14-13483-2014.

Hawkins, L. N. and L. M. Russell (2010). “Polysaccharides, Proteins, and Phytoplankton Fragments: Four Chemically Distinct Types of Marine Primary Organic Aerosol Classified by Single Particle Spectromicroscopy.” *Advances in Meteorology* 2010.612132. DOI: 10.1155/2010/612132.

Heald, C. L., J. H. Kroll, J. L. Jimenez, K. S. Docherty, P. F. DeCarlo, A. C. Aiken, Q. Chen, S. T. Martin, D. K. Farmer, and P. Artaxo (2010). “A simplified description of the evolution of organic aerosol composition in the atmosphere.” *Geophys. Res. Lett.* 37.L08803. DOI: 10.1029/2010GL042737.

Healy, R. M., J. Sciare, L. Poulain, K. Kamili, M. Merkel, T. Müller, A. Wiedensohler, S. Eckhardt, A. Stohl, R. Sarda-Estève, E. McGillicuddy, I. P. O’Connor, J. R. Sodeau, and J. C. Wenger (2012). “Sources and mixing state of size-resolved elemental carbon particles in a European megacity: Paris.” *Atmos. Chem. Phys.* 12.4, pp. 1681–1700. DOI: 10.5194/acp-12-1681-2012.

Healy, R. M., J. Sciare, L. Poulain, M. Crippa, A. Wiedensohler, A. S. H. Prévôt, U. Baltensperger, R. Sarda-Estève, M. L. McGuire, C.-H. Jeong, E. McGillicuddy, I. P. O’Connor, J. R. Sodeau, G. J. Evans, and J. C. Wenger (2013). “Quantitative determination of carbonaceous particle mixing state in Paris using single-particle mass spectrometer and aerosol mass spectrometer measurements.” *Atmos. Chem. Phys.* 13.18, pp. 9479–9496. DOI: 10.5194/acp-13-9479-2013.

Healy, R. M., G. J. Evans, M. Murphy, B. Sierau, J. Arndt, E. McGillicuddy, I. P. O'Connor, J. R. Sodeau, and J. C. Wenger (2015). "Single-particle speciation of alkylamines in ambient aerosol at five European sites." *Anal. Bioanal. Chem.* 407.20, pp. 5899–5909. DOI: 10.1007/s00216-014-8092-1.

Hecobian, A. et al. (2011). "Comparison of chemical characteristics of 495 biomass burning plumes intercepted by the NASA DC-8 aircraft during the ARCTAS/CARB-2008 field campaign." *Atmos. Chem. Phys.* 11.24, pp. 13325–13337. DOI: 10.5194/acp-11-13325-2011.

Heintzenberg, J., P. Tunved, M. Galí, and C. Leck (2017). "New particle formation in the Svalbard region 2006–2015." *Atmos. Chem. Phys.* 17.10, pp. 6153–6175. DOI: 10.5194/acp-17-6153-2017.

Heintzenberg, J. (1980). "Particle size distribution and optical properties of Arctic haze." *Tellus* 32.3, pp. 251–260. DOI: 10.3402/tellusa.v32i3.10580.

Hennigan, C. J., A. P. Sullivan, J. L. Collett, and A. L. Robinson (2010). "Levoglucosan stability in biomass burning particles exposed to hydroxyl radicals." *Geophys. Res. Lett.* 37.L09806. DOI: 10.1029/2010GL043088.

Herber, A. B., K. Dethloff, C. Haas, D. Steinhage, J. W. Strapp, J. Bottenheim, T. McElroy, and T. Yamanouchi (2008). "POLAR 5 - a new research aircraft for improved access to the Arctic." *ISAR-1, Drastic Change under the Global Warming, Extended Abstract.*

Hinds, W. C. (1999). *Aerosol technology: properties, behavior, and measurement of airborne particles.* Wiley-Interscience. Wiley. ISBN: 9780471194101.

Hinz, K. P., M. Greweling, F. Drews, and B. Spengler (1999). "Data processing in on-line laser mass spectrometry of inorganic, organic, or biological airborne particles." *J. Am. Soc. Mass Spectrom.* 10.7, pp. 648–660. DOI: 10.1016/S1044-0305(99)00028-8.

Hirdman, D., H. Sodemann, S. Eckhardt, J. F. Burkhart, A. Jefferson, T. Mefford, P. K. Quinn, S. Sharma, J. Ström, and A. Stohl (2010). "Source identification of short-lived air pollutants in the Arctic using statistical analysis of measurement data and particle dispersion model output." *Atmos. Chem. Phys.* 10.2, pp. 669–693. DOI: 10.5194/acp-10-669-2010.

Hoffmann, D., A. Tilgner, Y. Iinuma, and H. Herrmann (2010). "Atmospheric Stability of Levoglucosan: A Detailed Laboratory and Modeling Study." *Environ. Sci. Technol.* 44.2, pp. 694–699. DOI: 10.1021/es902476f.

Hoffmann, T. and J. Warnke (2007). “Volatile Organic Compounds in the Atmosphere.” Ed. by R. Koppmann. Blackwell Publishing Ltd. Chap. Chapter 9: Organic Aerosols, pp. 342–387.

Holland, M. M. and C. M. Bitz (2003). “Polar amplification of climate change in coupled models.” *Climate Dyn.* 21.3, pp. 221–232. DOI: 10.1007/s00382-003-0332-6.

Honeywell (2019). Last access: February 2019. URL: https://sensing.honeywell.com/de-de/index.php?ci_id=159835&la_id=1&N=161488.

Hoppel, W. A., G. M. Frick, J. W. Fitzgerald, and B. J. Wattle (1994). “A Cloud Chamber Study of the Effect That Nonprecipitating Water Clouds Have on the Aerosol Size Distribution.” *Aerosol Sci. Technol.* 20.1, pp. 1–30. DOI: 10.1080/02786829408959660.

Hu, Q.-H., Z.-Q. Xie, X.-M. Wang, H. Kang, and P. Zhang (2013). “Levoglucosan indicates high levels of biomass burning aerosols over oceans from the Arctic to Antarctic.” *Scientific Reports* 3.3119. DOI: 10.1038/srep03119.

Huang, L., S. L. Gong, C. Q. Jia, and D. Lavoué (2010). “Relative contributions of anthropogenic emissions to black carbon aerosol in the Arctic.” *J. Geophys. Res.-A* 115.D19. DOI: 10.1029/2009JD013592.

Huang, Z., J. Huang, T. Hayasaka, S. Wang, T. Zhou, and H. Jin (2015). “Short-cut transport path for Asian dust directly to the Arctic: a case study.” *Environ. Res. Lett.* 10.11, p. 114018. URL: http://stacks.iop.org/1748-9326/10/i=11/a=114018.

Hudson, P. K., D. M. Murphy, D. J. Cziczo, D. S. Thomson, J. A. de Gouw, C. Warneke, J. Holloway, H.-J. Jost, and G. Hübler (2004). “Biomass-burning particle measurements: Characteristic composition and chemical processing.” *J. Geophys. Res.* 109.D23S27. DOI: 10.1029/2003JD004398.

Huffman, J. A., J. T. Jayne, F. Drewnick, A. C. Aiken, T. Onasch, D. R. Worsnop, and J. L. Jimenez (2005). “Design, Modeling, Optimization, and Experimental Tests of a Particle Beam Width Probe for the Aerodyne Aerosol Mass Spectrometer.” *Aerosol Sci. Technol.* 39.12, pp. 1143–1163. DOI: 10.1080/02786820500423782.

IPCC, (2014). *Climate Change 2014: Synthesis Report. Contribution of Working Groups I, II and III to the Fifth Assessment Report of the Intergovernmental Panel on Climate Change [Core Writing Team, R.K. Pachauri and L.A. Meyer (eds.)]. IPCC, Geneva, Switzerland, 151 pp.*

Igel, A. L., A. M. L. Ekman, C. Leck, M. Tjernström, J. Savre, and J. Sedlar (2017). "The free troposphere as a potential source of arctic boundary layer aerosol particles." *Geophys. Res. Lett.* 44.13. 2017GL073808, pp. 7053–7060. DOI: 10.1002/2017GL073808.

Iversen, T. (1984). "On the atmospheric transport of pollution to the Arctic." *Geophys. Res. Lett.* 11.5, pp. 457–460. DOI: 10.1029/GL011i005p00457.

Iziomon, M. G., U. Lohmann, and P. K. Quinn (2006). "Summertime pollution events in the Arctic and potential implications." *J. Geophys. Res.-Atmos.* 111.D12206. DOI: 10.1029/2005JD006223.

Jayne, J. T., D. C. Leard, X. Zhang, P. Davidovits, K. A. Smith, C. E. Kolb, and D. R. Worsnop (2000). "Development of an Aerosol Mass Spectrometer for Size and Composition Analysis of Submicron Particles." *Aerosol Sci. Technol.* 33.1-2, pp. 49–70. DOI: 10.1080/027868200410840.

Jen, C. N., P. H. McMurry, and D. R. Hanson (2014). "Stabilization of sulfuric acid dimers by ammonia, methylamine, dimethylamine, and trimethylamine." *J. Geophys. Res.-Atmos.* 119.12. 2014JD021592, pp. 7502–7514. DOI: 10.1002/2014JD021592.

Jen, C. N., R. Bachman, J. Zhao, P. H. McMurry, and D. R. Hanson (2016). "Diamine-sulfuric acid reactions are a potent source of new particle formation." *Geophys. Res. Lett.* 2015GL066958. DOI: 10.1002/2015GL066958.

Jiao, C. and M. G. Flanner (2016). "Changing black carbon transport to the Arctic from present day to the end of 21st century." *J. Geophys. Res.-Atmos.* 121.9, pp. 4734–4750. DOI: 10.1002/2015JD023964.

Jimenez, J. L. et al. (2009). "Evolution of Organic Aerosols in the Atmosphere." *Science* 326.5959, pp. 1525–1529. DOI: 10.1126/science.1180353.

Johnson, M. T. and T. G. Bell (2008). "Coupling between dimethylsulfide emissions and the oceanatmosphere exchange of ammonia." *Environ. Chem.* 5.4, pp. 259–267. URL: https://doi.org/10.1071/EN08030.

Kalnay, E. et al. (1996). "The NCEP/NCAR 40-Year Reanalysis Project." *B. Am. Meteorol. Soc.* 77.3, pp. 437–472. DOI: 10.1175/1520-0477(1996)077<0437:TNYRP>2.0.CO;2.

Kamphus, M., M. Ettner-Mahl, M. Brands, J. Curtius, F. Drewnick, and S. Borrmann (2008). "Comparison of Two Aerodynamic Lenses as an Inlet for a Single Particle Laser Ablation Mass Spectrometer." *Aerosol Sci. Technol.* 42.11, pp. 970–980. DOI: 10.1080/02786820802372158.

Kane, D. B., B. Oktem, and M. V. Johnston (2001). "Nanoparticle Detection by Aerosol Mass Spectrometry." *Aerosol Sci. Technol.* 34.6, pp. 520–527. DOI: 10.1080/02786820117085.

Karl, M., C. Leck, E. Coz, and J. Heintzenberg (2013). "Marine nanogels as a source of atmospheric nanoparticles in the high Arctic." *Geophys. Res. Lett.* 40.14, pp. 3738–3743. DOI: 10.1002/grl.50661.

Kawamura, K., K. Ono, E. Tachibana, B. Charriére, and R. Sempéré (2012). "Distributions of low molecular weight dicarboxylic acids, ketoacids and α-dicarbonyls in the marine aerosols collected over the Arctic Ocean during late summer." *Biogeosciences* 9.11, pp. 4725–4737. DOI: 10.5194/bg-9-4725-2012.

Kawamura, K. and S. Bikkina (2016). "A review of dicarboxylic acids and related compounds in atmospheric aerosols: Molecular distributions, sources and transformation." *Atmos. Res.* 170, pp. 140 –160. URL: https://doi.org/10.1016/j.atmosres.2015.11.018.

Kawamura, K., H. Kasukabe, and L. A. Barrie (1996). "Source and reaction pathways of dicarboxylic acids, ketoacids and dicarbonyls in arctic aerosols: One year of observations." *Atmos. Environ.* 30.10, pp. 1709 –1722. URL: http://dx.doi.org/10.1016/1352-2310(95)00395-9.

Kawamura, K., H. Kasukabe, and L. A. Barrie (2010). "Secondary formation of water-soluble organic acids and α-dicarbonyls and their contributions to total carbon and water-soluble organic carbon: Photochemical aging of organic aerosols in the Arctic spring." *J. Geophys. Res.-Atmos.* 115.D21306. DOI: 10.1029/2010JD014299.

Kay, J. E. and A. Gettelman (2009). "Cloud influence on and response to seasonal Arctic sea ice loss." *J. Geophys. Res.-Atmos.* 114.D18204. DOI: 10.1029/2009JD011773.

Kerminen, V.-M., K. Teinilä, R. Hillamo, and T. Mäkelä (1999). "Size-segregated chemistry of particulate dicarboxylic acids in the Arctic atmosphere." *Atmos. Environ.* 33.13, pp. 2089 –2100. URL: https://doi.org/10.1016/S1352-2310(98)00350-1.

Kerminen, V.-M., X. Chen, V. Vakkari, T. Petäjä, M. Kulmala, and F. Bianchi (2018). "Atmospheric new particle formation and growth: review of field observations.” *Environ. Res. Lett.* 13.103003. URL: http://stacks.iop.org/1748-9326/13/i=10/a=103003.

Khon, V. C. and I. I. Mokhov (2010). “Arctic climate changes and possible conditions of Arctic navigation in the 21st century.” *Izv. Atmos. Ocean. Phys.* 46.1, pp. 14–20. DOI: 10.1134/S0001433810010032.

Kiendler-Scharr, A. et al. (2016). “Ubiquity of organic nitrates from nighttime chemistry in the European submicron aerosol.” *Geophys. Res. Lett.* 43.14, pp. 7735–7744. DOI: 10.1002/2016GL069239.

Kim, M. J., G. A. Novak, M. C. Zoerb, M. Yang, B. W. Blomquist, B. J. Huebert, C. D. Cappa, and T. H. Bertram (2017). “Air-Sea exchange of biogenic volatile organic compounds and the impact on aerosol particle size distributions.” *Geophys. Res. Lett.* 44.8, pp. 3887–3896. DOI: 10.1002/2017GL072975.

Kirpes, R. M., A. L. Bondy, D. Bonanno, R. C. Moffet, B. Wang, A. Laskin, A. P. Ault, and K. A. Pratt (2018). “Secondary sulfate is internally mixed with sea spray aerosol and organic aerosol in the winter Arctic.” *Atmos. Chem. Phys.* 18.6, pp. 3937–3949. DOI: 10.5194/acp-18-3937-2018.

Klimach, T. (2012). “Chemische Zusammensetzung der Aerosole: Design und Datenauswertung eines Einzelpartikel-Laserablationsmassenspektrometers.” PhD thesis. Johannes-Gutenberg Universität Mainz.

Klonecki, A., P. Hess, L. Emmons, L. Smith, J. Orlando, and D. Blake (2003). “Seasonal changes in the transport of pollutants into the Arctic troposphere-model study.” *J. Geophys. Res.-Atmos.* 108.D4. 8367. DOI: 10.1029/2002JD002199.

Kluschat, B. (2016). “Untersuchung des Polar Dome anhand von flugzeuggestützen in-situ Spurengasmessungen.” MA thesis. Johannes-Gutenberg Universität Mainz.

Kolesar, K. R., J. Cellini, P. K. Peterson, A. Jefferson, T. Tuch, W. Birmili, A. Wiedensohler, and K. A. Pratt (2017). “Effect of Prudhoe Bay emissions on atmospheric aerosol growth events observed in Utqiaġvik (Barrow), Alaska.” *Atmos. Environ.* 152, pp. 146 –155. URL: https://doi.org/10.1016/j.atmosenv.2016.12.019.

Köllner, F., J. Schneider, M. D. Willis, T. Klimach, F. Helleis, H. Bozem, D. Kunkel, P. Hoor, J. Burkart, W. R. Leaitch, A. A. Aliabadi, J. P. D. Abbatt, A. B. Herber, and S. Borrmann (2017). “Particulate trimethylamine in the summertime Canadian high Arctic lower troposphere.” *Atmos. Chem. Phys.* 17.22, pp. 13747–13766. DOI: 10.5194/acp-17-13747-2017.

Kondo, Y. et al. (2011). “Emissions of black carbon, organic, and inorganic aerosols from biomass burning in North America and Asia in 2008.” *J. Geophys. Res.-Atmos.* 116.D8. DOI: 10.1029/2010JD015152.

Kramshøj, M., I. Vedel-Petersen, M. Schollert, Å. Rinnan, J. Nymand, H. Ro-Poulsen, and R. Rinnan (2016). “Large increases in Arctic biogenic volatile emissions are a direct effect of warming.” *Nature Geoscience* 9, pp. 349–352. URL: http://dx.doi.org/10.1038/ngeo2692.

Kraus, H. (2004). *Die Atmosphäre der Erde: Eine Einführung in die Meteorologie.* Springer-Verlag Berlin Heidelberg New York.

Kroll, J. H. and J. H. Seinfeld (2008). “Chemistry of secondary organic aerosol: Formation and evolution of low-volatility organics in the atmosphere.” *Atmos. Environ.* 42, pp. 3593–3624. DOI: 10.1016/j.atmosenv.2008.01.003.

Kuhn, T., R. Damoah, A. Bacak, and J. J. Sloan (2010). “Characterising aerosol transport into the Canadian High Arctic using aerosol mass spectrometry and Lagrangian modelling.” *Atmos. Chem. Phys.* 10.21, pp. 10489–10502. DOI: 10.5194/acp-10-10489-2010.

Kupiszewski, P., C. Leck, M. Tjernström, S. Sjogren, J. Sedlar, M. Graus, M. Müller, B. Brooks, E. Swietlicki, S. Norris, and A. Hansel (2013). “Vertical profiling of aerosol particles and trace gases over the central Arctic Ocean during summer.” *Atmos. Chem. Phys.* 13.24, pp. 12405–12431. DOI: 10.5194/acp-13-12405-2013.

Kürten, A., A. Bergen, M. Heinritzi, M. Leiminger, V. Lorenz, F. Piel, M. Simon, R. Sitals, A. C. Wagner, and J. Curtius (2016). “Observation of new particle formation and measurement of sulfuric acid, ammonia, amines and highly oxidized organic molecules at a rural site in central Germany.” *Atmos. Chem. Phys.* 16.19, pp. 12793–12813. DOI: 10.5194/acp-16-12793-2016.

Laborde, M., P. Mertes, P. Zieger, J. Dommen, U. Baltensperger, and M. Gysel (2012). “Sensitivity of the Single Particle Soot Photometer to different black carbon types.” *Atmos. Meas. Tech.* 5.5, pp. 1031–1043. DOI: 10.5194/amt-5-1031-2012.

Lana, A., T. G. Bell, R. Simó, S. M. Vallina, J. Ballabrera-Poy, A. J. Kettle, J. Dachs, L. Bopp, E. S. Saltzman, J. Stefels, J. E. Johnson, and P. S. Liss (2011). “An updated climatology of surface dimethlysulfide concentrations and emission fluxes in the global ocean.” *Global Biogeochem. Cy.* 25.1. DOI: 10.1029/2010GB003850.

Lange, R., M. Dall’Osto, H. Skov, J. Nøjgaard, I. Nielsen, D. Beddows, R. Simo, R. Harrison, and A. Massling (2018). “Characterization of distinct Arctic aerosol accumulation modes and their sources." *Atmos. Environ.* 183, pp. 1–10. URL: https://doi.org/10.1016/j.atmosenv.2018.03.060.

Laskin, A., R. C. Moffet, M. K. Gilles, J. D. Fast, R. A. Zaveri, B. Wang, P. Nigge, and J. Shutthanandan (2012). "Tropospheric chemistry of internally mixed sea salt and organic particles: Surprising reactivity of NaCl with weak organic acids." *J. Geophys. Res.-Atmos.* 117.D15. DOI: 10.1029/2012JD017743.

Lathem, T. L., A. J. Beyersdorf, K. L. Thornhill, E. L. Winstead, M. J. Cubison, A. Hecobian, J. L. Jimenez, R. J. Weber, B. E. Anderson, and A. Nenes (2013). "Analysis of CCN activity of Arctic aerosol and Canadian biomass burning during summer 2008." *Atmos. Chem. Phys.* 13.5, pp. 2735–2756. DOI: 10.5194/acp-13-2735-2013.

Lavoué, D., C. Liousse, H. Cachier, B. J. Stocks, and J. G. Goldammer (2000). "Modeling of carbonaceous particles emitted by boreal and temperate wildfires at northern latitudes." *J. Geophys. Res.-Atmos* 105.D22, pp. 26871–26890. DOI: 10.1029/2000JD900180.

Law, K. S. and A. Stohl (2007). "Arctic Air Pollution: Origins and Impacts." *Science* 315.5818, pp. 1537–1540. DOI: 10.1126/science.1137695.

Leaitch, W. R., S. Sharma, L. Huang, D. Toom-Sauntry, A. Chivulescu, A. M. Macdonald, K. von Salzen, J. R. Pierce, A. K. Bertram, J. C. Schroder, N. C. Shantz, R. Y.-W. Chang, and A.-L. Norman (2013). "Dimethyl sulfide control of the clean summertime Arctic aerosol and cloud." *Elem. Sci. Anth.* DOI: 10.12952/journal.elementa.000017.

Leaitch, W. R., A. Korolev, A. A. Aliabadi, J. Burkart, M. D. Willis, J. P. D. Abbatt, H. Bozem, P. Hoor, F. Köllner, J. Schneider, A. Herber, C. Konrad, and R. Brauner (2016). "Effects of 20–100 nm particles on liquid clouds in the clean summertime Arctic." *Atmos. Chem. Phys.* 16.17, pp. 11107–11124. DOI: 10.5194/acp-16-11107-2016.

Leaitch, W. R., L. M. Russell, J. Liu, F. Kolonjari, D. Toom, L. Huang, S. Sharma, A. Chivulescu, D. Veber, and W. Zhang (2018). "Organic functional groups in the submicron aerosol at 82.5° N, 62.5° W from 2012 to 2014." *Atmos. Chem. Phys.* 18.5, pp. 3269–3287. DOI: 10.5194/acp-18-3269-2018.

Leck, C. and E. K. Bigg (2005). "Source and evolution of the marine aerosol - A new perspective." *Geophys. Res. Lett.* 32.19. DOI: 10.1029/2005GL023651.

Lee, S.-H., D. M. Murphy, D. S. Thomson, and A. M. Middlebrook (2003). "Nitrate and oxidized organic ions in single particle mass spectra during the 1999 Atlanta Supersite Project." *J. Geophys. Res.-Atmos* 108.D7. 8471. DOI: 10.1029/2001JD001455.

Leung, F.-Y. T., J. A. Logan, R. Park, E. Hyer, E. Kasischke, D. Streets, and L. Yurganov (2007). "Impacts of enhanced biomass burning in the boreal forests in 1998 on tropospheric chemistry and the sensitivity of model results to the injection height of emissions." *J. Geophys. Res.-Atmos* 112.D10. DOI: 10.1029/2006JD008132.

Lim, H.-J., A. G. Carlton, and B. J. Turpin (2005). "Isoprene Forms Secondary Organic Aerosol through Cloud Processing: Model Simulations." *Environ. Sci. Technol.* 39.12, pp. 4441–4446. DOI: 10.1021/es048039h.

Liu, D., B. Quennehen, E. Darbyshire, J. D. Allan, P. I. Williams, J. W. Taylor, S. J.-B. Bauguitte, M. J. Flynn, D. Lowe, M. W. Gallagher, K. N. Bower, T. W. Choularton, and H. Coe (2015). "The importance of Asia as a source of black carbon to the European Arctic during springtime 2013." *Atmos. Chem. Phys.* 15.20, pp. 11537–11555. DOI: 10.5194/acp-15-11537-2015.

Liu, P., P. J. Ziemann, D. B. Kittelson, and P. H. McMurry (1995a). "Generating Particle Beams of Controlled Dimensions and Divergence: I. Theory of Particle Motion in Aerodynamic Lenses and Nozzle Expansions." *Aerosol Sci. Technol.* 22.3, pp. 293–313. DOI: 10.1080/02786829408959748.

Liu, P., P. J. Ziemann, D. B. Kittelson, and P. H. McMurry (1995b). "Generating Particle Beams of Controlled Dimensions and Divergence: II. Experimental Evaluation of Particle Motion in Aerodynamic Lenses and Nozzle Expansions." *Aerosol Sci. Technol.* 22.3, pp. 314–324. DOI: 10.1080/02786829408959749.

Liu, P. S. K., R. Deng, K. A. Smith, L. R. Williams, J. T. Jayne, M. R. Canagaratna, K. Moore, T. B. Onasch, D. R. Worsnop, and T. Deshler (2007). "Transmission Efficiency of an Aerodynamic Focusing Lens System: Comparison of Model Calculations and Laboratory Measurements for the Aerodyne Aerosol Mass Spectrometer." *Aerosol Sci. Technol.* 41.8, pp. 721–733. DOI: 10.1080/02786820701422278.

Liu, Y., J. R. Key, Z. Liu, X. Wang, and S. J. Vavrus (2012). "A cloudier Arctic expected with diminishing sea ice." *Geophys. Res. Lett.* 39.5. L05705, n/a–n/a. DOI: 10.1029/2012GL051251.

Liu, Y., C. Hu, W. Zhan, C. Sun, B. Murch, and L. Ma (2018). "Identifying industrial heat sources using time-series of the VIIRS Nightfire product with an object-oriented approach." *Remote Sens. Environ.* 204, pp. 347 –365. URL: https://doi.org/10.1016/j.rse.2017.10.019.

Lubin, D. and A. M. Vogelmann (2006). “A climatologically significant aerosol longwave indirect effect in the Arctic.” *Nature* 439, pp. 453–456. URL: http://dx.doi.org/10.1038/nature04449.

Lutsch, E., E. Dammers, S. Conway, and K. Strong (2016). “Long-range transport of NH_3, CO, HCN, and C_2H_6 from the 2014 Canadian Wildfires.” *Geophys. Res. Lett.* 43.15. 2016GL070114, pp. 8286–8297. DOI: 10.1002/2016GL070114.

Mahmood, R., K. von Salzen, M. Flanner, M. Sand, J. Langner, H. Wang, and L. Huang (2016). “Seasonality of global and Arctic black carbon processes in the Arctic Monitoring and Assessment Programme models.” *J. Geophys. Res.-Atmos.* 121.12, pp. 7100–7116. DOI: 10.1002/2016JD024849.

Marelle, L., J.-C. Raut, K. S. Law, and O. Duclaux (2018). “Current and Future Arctic Aerosols and Ozone From Remote Emissions and Emerging Local Sources - Modeled Source Contributions and Radiative Effects.” *J. Geophys. Res.-Atmos.* 123.22, pp. 12,942–12,963. DOI: 10.1029/2018JD028863.

Mauritsen, T., J. Sedlar, M. Tjernström, C. Leck, M. Martin, M. Shupe, S. Sjogren, B. Sierau, P. O. G. Persson, I. M. Brooks, and E. Swietlicki (2011). “An Arctic CCN-limited cloud-aerosol regime.” *Atmos. Chem. Phys.* 11.1, pp. 165–173. DOI: 10.5194/acp-11-165-2011.

MaxMind (2018). Last access: 10.06.2018. URL: https://www.maxmind.com/en/free-world-cities-database.

May, N. W., P. K. Quinn, S. M. McNamara, and K. A. Pratt (2016). “Multiyear study of the dependence of sea salt aerosol on wind speed and sea ice conditions in the coastal Arctic.” *J. Geophys. Res.-Atmos.* 121.15, pp. 9208–9219. DOI: 10.1002/2016JD025273.

Moffet, R. C., B. de Foy, L. T. Molina, M. J. Molina, and K. A. Prather (2008). “Measurement of ambient aerosols in northern Mexico City by single particle mass spectrometry.” *Atmos. Chem. Phys.* 8.16, pp. 4499–4516. DOI: 10.5194/acp-8-4499-2008.

Moffet, R. C. and K. A. Prather (2009). “In-situ measurements of the mixing state and optical properties of soot with implications for radiative forcing estimates.” *P. Natl. Acad. Sci.* 106.29, pp. 11872–11877. DOI: 10.1073/pnas.0900040106.

Molleker, S., F. Helleis, T. Klimach, O. Appel, H.-C. Clemen, A. Dragoneas, C. Gurk, A. Huenig, F. Köllner, F. Rubach, C. Schulz, J. Schneider, and S. Borrmann (2019). “Application of an O-ring pinch device as a constant pressure inlet for airborne sampling.” *in prep. for Atmos. Meas. Tech.*

Moore, R. H., V. A. Karydis, S. L. Capps, T. L. Lathem, and A. Nenes (2013). "Droplet number uncertainties associated with CCN: an assessment using observations and a global model adjoint." *Atmos. Chem. Phys.* 13.8, pp. 4235–4251. DOI: 10.5194/acp-13-4235-2013.

Mungall, E. L., J. P. D. Abbatt, J. J. B. Wentzell, A. K. Y. Lee, J. L. Thomas, M. Blais, M. Gosselin, L. A. Miller, T. Papakyriakou, M. D. Willis, and J. Liggio (2017). "Microlayer source of oxygenated volatile organic compounds in the summertime marine Arctic boundary layer." *P. Natl. Acad. Sci.* 114.24, pp. 6203–6208. DOI: 10.1073/pnas.1620571114.

Murphy, D. M., A. M. Middlebrook, and M. Warshawsky (2003). "Cluster Analysis of Data from the Particle Analysis by Laser Mass Spectrometry (PALMS) Instrument." *Aerosol Sci. Technol.* 37.4, pp. 382–391. DOI: 10.1080/02786820300971. eprint: https://doi.org/10.1080/02786820300971.

Murphy, D. M. (2006). "The design of single particle laser mass spectrometers." *Mass Spectrom. Rev.* 26.2, pp. 150–165. DOI: 10.1002/mas.20113.

Murphy, S. M., A. Sorooshian, J. H. Kroll, N. L. Ng, P. Chhabra, C. Tong, J. D. Surratt, E. Knipping, R. C. Flagan, and J. H. Seinfeld (2007). "Secondary aerosol formation from atmospheric reactions of aliphatic amines." *Atmos. Chem. Phys.* 7.9, pp. 2313–2337. DOI: 10.5194/acp-7-2313-2007.

NASA (2018). Last access: 29.09.2018. DOI: 10.5067/FIRMS/VIIRS/VNP14IMGT.NRT.001.. URL: https://firms.modaps.eosdis.nasa.gov.

NOAA (2018a). Last access: 01.10.2018. URL: https://www.ngdc.noaa.gov/eog/viirs/download_viirs_fire.html.

NOAA (2018b). Last access: February 2018. URL: https://data.ngdc.noaa.gov/instruments/remote-sensing/passive/spectrometers-radiometers/imaging/viirs/vnf/v21/flares/.

Najafi, M. R., F. W. Zwiers, and N. P. Gillett (2015). "Attribution of Arctic temperature change to greenhouse-gas and aerosol influences." *Nat. Clim. Change* 5, pp. 246–249. URL: http://dx.doi.org/10.1038/nclimate2524.

Nance, J. D., P. V. Hobbs, L. F. Radke, and D. E. Ward (1993). "Airborne measurements of gases and particles from an Alaskan wildfire." *J. Geophys. Res.-Atmos.* 98.D8, pp. 14873–14882. DOI: 10.1029/93JD01196.

Neubauer, K. R., M. V. Johnston, and A. S. Wexler (1998). “Humidity effects on the mass spectra of single aerosol particles.” *Atmos. Environ.* 32.14/15, pp. 2521–2529. URL: https://doi.org/10.1016/S1352-2310(98)00005-3.

Ng, N. L., M. R. Canagaratna, J. L. Jimenez, P. S. Chhabra, J. H. Seinfeld, and D. R. Worsnop (2011). “Changes in organic aerosol composition with aging inferred from aerosol mass spectra.” *Atmos. Chem. Phys.* 11.13, pp. 6465–6474. DOI: 10.5194/acp-11-6465-2011.

Nguyen, Q. T., M. Glasius, L. L. Sørensen, B. Jensen, H. Skov, W. Birmili, A. Wiedensohler, A. Kristensson, J. K. Nøjgaard, and A. Massling (2016). “Seasonal variation of atmospheric particle number concentrations, new particle formation and atmospheric oxidation capacity at the high Arctic site Villum Research Station, Station Nord.” *Atmos. Chem. Phys.* 16.17, pp. 11319–11336. DOI: 10.5194/acp-16-11319-2016.

Nguyen, Q. T., T. B. Kristensen, A. M. K. Hansen, H. Skov, R. Bossi, A. Massling, L. L. Sørensen, M. Bilde, M. Glasius, and J. K. Nøjgaard (2014). “Characterization of humic-like substances in Arctic aerosols.” *J. Geophys. Res.-Atmos.* 119.8, pp. 5011–5027. DOI: 10.1002/2013JD020144.

Nordenskiöld, A. E. (1883). “NORDENSKIÖLD ON THE INLAND ICE OF GREENLAND.” *Science* ns-2.44, p. 732. DOI: 10.1126/science.ns-2.44.732.

O’Dowd, C. D. and G. de Leeuw (2007). “Marine aerosol production: a review of the current knowledge.” *Phil. Trans. R. Soc. A* 365, pp. 1753–1774. DOI: 10.1098/rsta.2007.2043.

O’Dowd, C. D., J. A. Lowe, and M. H. Smith (1999). “Coupling sea-salt and sulphate interactions and its impact on cloud droplet concentration predictions.” *Geophys. Res. Lett.* 26.9, pp. 1311–1314. DOI: 10.1029/1999GL900231.

Orris, G., M. Cocker, P. Dunlap, J. Wynn, G. Spanski, D. Briggs, L. Gass, J. Bliss, K. Bolm, C. Yang, B. Lipin, S. Ludington, R. Miller, and M. Slowakiewicz (2014). “Potash - A global overview of evaporite-related potash resources, including spatial databases of deposits, occurrences, and permissive tracts.” *U.S. Geological Survey Scientific Investigations Report 2010–5090–S.*

Overland, J. E., K. Dethloff, J. A. Francis, R. J. Hall, E. Hanna, S.-J. Kim, J. A. Screen, T. G. Shepherd, and T. Vihma (2016). “Nonlinear response of mid-latitude weather to the changing Arctic.” *Nat. Clim. Change* 6, pp. 992–999. URL: https://doi.org/10.1038/nclimate3121.

Paasonen, P. et al. (2013). "Warming-induced increase in aerosol number concentration likely to moderate climate change." *Nature Geoscience* 6, pp. 438–442. URL: https://doi.org/10.1038/ngeo1800.

Pankow, J. F. (2015). "Phase considerations in the gas/particle partitioning of organic amines in the atmosphere." *Atmos. Environ.* 122, pp. 448 –453. URL: http://dx.doi.org/10.1016/j.atmosenv.2015.09.056.

Paris, J.-D., A. Stohl, P. Nédélec, M. Y. Arshinov, M. V. Panchenko, V. P. Shmargunov, K. S. Law, B. D. Belan, and P. Ciais (2009). "Wildfire smoke in the Siberian Arctic in summer: source characterization and plume evolution from airborne measurements." *Atmos. Chem. Phys.* 9.23, pp. 9315–9327. DOI: 10.5194/acp-9-9315-2009.

Park, K.-T., S. Jang, K. Lee, Y. J. Yoon, M.-S. Kim, K. Park, H.-J. Cho, J.-H. Kang, R. Udisti, B.-Y. Lee, and K.-H. Shin (2017). "Observational evidence for the formation of DMS-derived aerosols during Arctic phytoplankton blooms." *Atmos. Chem. Phys.* 17.15, pp. 9665–9675. DOI: 10.5194/acp-17-9665-2017.

Paxian, A., V. Eyring, W. Beer, R. Sausen, and C. Wright (2010). "Present-Day and Future Global Bottom-Up Ship Emission Inventories Including Polar Routes." *Environ. Sci. Technol.* 44.4, pp. 1333–1339. DOI: 10.1021/es9022859.

Peters, G. P., T. B. Nilssen, L. Lindholt, M. S. Eide, S. Glomsrød, L. I. Eide, and J. S. Fuglestvedt (2011). "Future emissions from shipping and petroleum activities in the Arctic." *Atmos. Chem. Phys.* 11.11, pp. 5305–5320. DOI: 10.5194/acp-11-5305-2011.

Petzold, A., B. Weinzierl, H. Huntrieser, A. Stohl, E. Real, J. Cozic, M. Fiebig, J. Hendricks, A. Lauer, K. Law, A. Roiger, H. Schlager, and E. Weingartner (2007). "Perturbation of the European free troposphere aerosol by North American forest fire plumes during the ICARTT-ITOP experiment in summer 2004." *Atmos. Chem. Phys.* 7.19, pp. 5105–5127. DOI: 10.5194/acp-7-5105-2007.

Petzold, A., J. A. Ogren, M. Fiebig, P. Laj, S.-M. Li, U. Baltensperger, T. Holzer-Popp, S. Kinne, G. Pappalardo, N. Sugimoto, C. Wehrli, A. Wiedensohler, and X.-Y. Zhang (2013). "Recommendations for reporting "black carbon" measurements." *Atmos. Chem. Phys.* 13.16, pp. 8365–8379. DOI: 10.5194/acp-13-8365-2013.

Pierce, J. R., B. Croft, J. K. Kodros, S. D. D'Andrea, and R. V. Martin (2015). "The importance of interstitial particle scavenging by cloud droplets in shaping the remote aerosol size distribution and global aerosol-climate effects." *Atmos. Chem. Phys.* 15.11, pp. 6147–6158. DOI: 10.5194/acp-15-6147-2015.

Prather, K. A. (2012). “Interactive comment on “Are black carbon and soot the same?” by P. R. Buseck et al.” *Atmos. Chem. Phys. Discuss.*

Prather, K. A. et al. (2013). “Bringing the ocean into the laboratory to probe the chemical complexity of sea spray aerosol.” *P. Natl. Acad. Sci.* 110.19, pp. 7550–7555. DOI: 10.1073/pnas.1300262110.

Pratt, K. A., S. M. Murphy, R. Subramanian, P. J. DeMott, G. L. Kok, T. Campos, D. C. Rogers, A. J. Prenni, A. J. Heymsfield, J. H. Seinfeld, and K. A. Prather (2011). “Flight-based chemical characterization of biomass burning aerosols within two prescribed burn smoke plumes.” *Atmos. Chem. Phys.* 11.24, pp. 12549–12565. DOI: 10.5194/acp-11-12549-2011.

Pratt, K. A. and K. A. Prather (2010). “Aircraft measurements of vertical profiles of aerosol mixing states.” *J. Geophys. Res.-Atmos* 115.D11. DOI: 10.1029/2009JD013150.

Pratt, K. A. and K. A. Prather (2012). “Mass spectrometry of atmospheric aerosols - Recent developments and applications. Part II: On-line mass spectrometry techniques.” *Mass Spectrom. Rev.* 31.1, pp. 17–48. DOI: 10.1002/mas.20330.

Pratt, K. A., P. J. DeMott, J. R. French, Z. Wang, D. L. Westphal, A. J. Heymsfield, C. H. Twohy, A. J. Prenni, and K. A. Prather (2009a). “In situ detection of biological particles in cloud ice-crystals.” *Nature Geoscience* 2.6, pp. 398–401. DOI: 10.1038/ngeo521.

Pratt, K. A., L. E. Hatch, and K. A. Prather (2009b). “Seasonal Volatility Dependence of Ambient Particle Phase Amines.” *Environ. Sci. Technol.* 43 (14), pp. 5276–5281. DOI: 10.1021/es803189n.

Qin, X., P. V. Bhave, and K. A. Prather (2006). “Comparison of Two Methods for Obtaining Quantitative Mass Concentrations from Aerosol Time-of-Flight Mass Spectrometry Measurements.” *Anal. Chem.* 78.17, pp. 6169–6178. DOI: 10.1021/ac060395q.

Qin, X., K. A. Pratt, L. G. Shields, S. M. Toner, and K. A. Prather (2012). “Seasonal comparisons of single-particle chemical mixing state in Riverside, CA.” *Atmos. Environ.* 59, pp. 587 –596. URL: https://doi.org/10.1016/j.atmosenv.2012.05.032.

Quantel (2008). *ICE450 Power Supply-User’s Manual.* Quantel.

Quennehen, B., A. Schwarzenboeck, J. Schmale, J. Schneider, H. Sodemann, A. Stohl, G. Ancellet, S. Crumeyrolle, and K. S. Law (2011). “Physical and chemical properties of pollution aerosol particles transported from North America to Greenland as measured during the POLARCAT summer campaign." *Atmos. Chem. Phys.* 11.21, pp. 10947–10963. DOI: 10.5194/acp-11-10947-2011.

Quennehen, B., A. Schwarzenboeck, A. Matsuki, J. F. Burkhart, A. Stohl, G. Ancellet, and K. S. Law (2012). "Anthropogenic and forest fire pollution aerosol transported to the Arctic: observations from the POLARCAT-France spring campaign." *Atmos. Chem. Phys.* 12.14, pp. 6437–6454. DOI: 10.5194/acp-12-6437-2012.

Quinn, P. K., T. L. Miller, T. S. Bates, J. A. Ogren, E. Andrews, and G. E. Shaw (2002). "A 3-year record of simultaneously measured aerosol chemical and optical properties at Barrow, Alaska." *J. Geophys. Res.-Atmos.* 107.D11. DOI: 10.1029/2001JD001248.

Quinn, P. K., G. Shaw, E. Andrews, E. G. Dutton, T. Ruoho-Airola, and S. L. Gong (2007). "Arctic haze: current trends and knowledge gaps." *Tellus B* 59.1, pp. 99–114. DOI: 10.1111/j.1600-0889.2006.00238.x.

Quinn, P. K., T. S. Bates, E. Baum, N. Doubleday, A. M. Fiore, M. Flanner, A. Fridlind, T. J. Garrett, D. Koch, S. Menon, D. Shindell, A. Stohl, and S. G. Warren (2008). "Short-lived pollutants in the Arctic: their climate impact and possible mitigation strategies." *Atmos. Chem. Phys.* 8.6, pp. 1723–1735. DOI: 10.5194/acp-8-1723-2008.

Quinn, P. K., T. S. Bates, K. Schulz, and G. E. Shaw (2009). "Decadal trends in aerosol chemical composition at Barrow, Alaska: 1976-2008." *Atmos. Chem. Phys.* 9.22, pp. 8883–8888. DOI: 10.5194/acp-9-8883-2009.

Quinn, P. K., T. S. Bates, K. S. Schulz, D. J. Coffman, A. A. Frossard, L. M. Russell, W. C. Keene, and D. J. Kieber (2014). "Contribution of sea surface carbon pool to organic matter enrichment in sea spray aerosol." *Nature Geoscience* 7, pp. 228–232. DOI: 10.1038/ngeo2092.

Radke, L. F. and P. V. Hobbs (1989). "Arctic hazes in summer over Greenland and the North American Arctic. III: A contribution from the natural burning of carbonaceous materials and pyrites." *J. Atmos. Chem.* 9.1, pp. 161–167. DOI: 10.1007/BF00052830.

Rahn, K. A., R. D. Borys, and G. E. Shaw (1977). "The Asian source of Arctic haze bands." *Nature* 268, pp. 713–715. URL: https://doi.org/10.1038/268713a0.

Rahn, K. A. and R. J. McCaffrey (1980). "ON THE ORIGIN AND TRANSPORT OF THE WINTER ARCTIC AEROSOL." *Ann. N. Y. Acad. Sci.* 338.1, pp. 486–503. DOI: 10.1111/j.1749-6632.1980.tb17142.x.

Randerson, J. T. et al. (2006). “The Impact of Boreal Forest Fire on Climate Warming.” *Science* 314.5802, pp. 1130–1132. DOI: 10.1126/science.1132075.

Rebotier, T. P. and K. A. Prather (2007). “Aerosol time-of-flight mass spectrometry data analysis: A benchmark of clustering algorithms.” *Anal. Chim. Acta* 585.1, pp. 38 –54. URL: https://doi.org/10.1016/j.aca.2006.12.009.

Reents, W. D. and M. J. Schabel (2001). “Measurement of Individual Particle Atomic Composition by Aerosol Mass Spectrometry.” *Anal. Chem.* 73.22, pp. 5403–5414. DOI: 10.1021/ac010436c.

Rehbein, P. J. G., C.-H. Jeong, M. L. McGuire, X. Yao, J. C. Corbin, and G. J. Evans (2011). “Cloud and Fog Processing Enhanced Gas-to-Particle Partitioning of Trimethylamine.” *Environ. Sci. Technol.* 45.10, pp. 4346–4352. DOI: 10.1021/es1042113.

Reilly, P. T. A., A. C. Lazar, R. A. Gieray, W. B. Whitten, and J. M. Ramsey (2000). “The Elucidation of Charge-Transfer-Induced Matrix Effects in Environmental Aerosols Via Real-Time Aerosol Mass Spectral Analysis of Individual Airborne Particles.” *Aerosol Sci. Technol.* 33.1-2, pp. 135–152. DOI: 10.1080/027868200410895.

Reitz, P., S. R. Zorn, S. H. Trimborn, and A. M. Trimborn (2016). “A new, powerful technique to analyze single particle aerosol mass spectra using a combination of OPTICS and the fuzzy c-means algorithm.” *J. Aerosol Sci.* 98, pp. 1–14. URL: https://doi.org/10.1016/j.jaerosci.2016.04.003.

Roiger, A. et al. (2015). “Quantifying Emerging Local Anthropogenic Emissions in the Arctic Region: The ACCESS Aircraft Campaign Experiment.” *B. Am. Meteorol. Soc.* 96.3, pp. 441–460. DOI: 10.1175/BAMS-D-13-00169.1.

Roth, A., J. Schneider, T. Klimach, S. Mertes, D. van Pinxteren, H. Herrmann, and S. Borrmann (2016). “Aerosol properties, source identification, and cloud processing in orographic clouds measured by single particle mass spectrometry on a central European mountain site during HCCT-2010.” *Atmos. Chem. Phys.* 16.2, pp. 505–524. DOI: 10.5194/acp-16-505-2016.

Roth, A. (2009). “Untersuchung des Einflusses der Laserwellenlänge in der Einzelpartikel-Laserablations-Aerosol-Massenspektrometrie.” MA thesis. Johannes Gutenberg-Universität Mainz.

Roth, A. (2014). “Untersuchungen von Aerosolpartikeln und Wolkenresidualpartikeln mittels Einzelpartikel-Massenspektrometrie und optischen Methoden.” PhD thesis. Johannes Gutenberg-Universität Mainz.

Russell, L. M., L. N. Hawkins, A. A. Frossard, P. K. Quinn, and T. S. Bates (2010). "Carbohydrate-like composition of submicron atmospheric particles and their production from ocean bubble bursting." *P. Natl. Acad. Sci.* 107.15, pp. 6652–6657. DOI: 10.1073/pnas.0908905107.

Sand, M., T. K. Berntsen, K. von Salzen, M. G. Flanner, J. Langner, and D. G. Victor (2016). "Response of Arctic temperature to changes in emissions of short-lived climate forcers." *Nat. Clim. Change* 6.3, pp. 286–289. URL: http://dx.doi.org/10.1038/nclimate2880.

Scalabrin, E., R. Zangrando, E. Barbaro, N. M. Kehrwald, J. Gabrieli, C. Barbante, and A. Gambaro (2012). "Amino acids in Arctic aerosols." *Atmos. Chem. Phys.* 12.21, pp. 10453–10463. DOI: 10.5194/acp-12-10453-2012.

Schade, G. W. and P. J. Crutzen (1995). "Emission of aliphatic amines from animal husbandry and their reactions: Potential source of N_2O and HCN." *J. Atmos. Chem.* 22.3, pp. 319–346. DOI: 10.1007/BF00696641.

Scharffe, D., F. Slemr, C. A. M. Brenninkmeijer, and A. Zahn (2012). "Carbon monoxide measurements onboard the CARIBIC passenger aircraft using UV resonance fluorescence." *Atmos. Meas. Tech.* 5.7, pp. 1753–1760. DOI: 10.5194/amt-5-1753-2012.

Schmale, J., J. Schneider, G. Ancellet, B. Quennehen, A. Stohl, H. Sodemann, J. F. Burkhart, T. Hamburger, S. R. Arnold, A. Schwarzenboeck, S. Borrmann, and K. S. Law (2011). "Source identification and airborne chemical characterisation of aerosol pollution from long-range transport over Greenland during POLARCAT summer campaign 2008." *Atmos. Chem. Phys.* 11.19, pp. 10097–10123. DOI: 10.5194/acp-11-10097-2011.

Schmidt, S., J. Schneider, T. Klimach, S. Mertes, L. P. Schenk, P. Kupiszewski, J. Curtius, and S. Borrmann (2017). "Online single particle analysis of ice particle residuals from mountain-top mixed-phase clouds using laboratory derived particle type assignment." *Atmos. Chem. Phys.* 17.1, pp. 575–594. DOI: 10.5194/acp-17-575-2017.

Schmidt, S. (2015). "Analyse der chemischen Zusammensetzung von Eis- und Wolkenresiduen mittels Einzelpartikel-Massenspektrometrie und Charakterisierung von Aerosolpartikeln aus anthropogenen und natürlichen Quellen." PhD thesis. Johannes Gutenberg-Universität Mainz.

Schneider, J., S. Mertes, D. van Pinxteren, H. Herrmann, and S. Borrmann (2017). "Uptake of nitric acid, ammonia, and organics in orographic clouds: mass spectrometric analyses of droplet residual and interstitial aerosol particles." *Atmos. Chem. Phys.* 17.2, pp. 1571–1593. DOI: 10.5194/acp-17-1571-2017.

Schollert, M., S. Burchard, P. Faubert, A. Michelsen, and R. Rinnan (2014). "Biogenic volatile organic compound emissions in four vegetation types in high arctic Greenland." *Polar Biol.* 37, pp. 237–249. URL: https://doi.org/10.1007/s00300-013-1427-0.

Schönwiese, C. D. (2000). *Praktische Statistik für Meteorologen und Geowissenschaftler*. 3rd ed. Gebrüder Borntraeger.

Schreiner, J., U. Schild, C. Voigt, and K. Mauersberger (1999). "Focusing of Aerosols into a Particle Beam at Pressures from 10 to 150 Torr." *Aerosol Sci. Technol.* 31.5, pp. 373–382. DOI: 10.1080/027868299304093.

Schroeder, W. and L. Giglio (2018). *NASA VIIRS Land Science Investigator Processing System (SIPS) Visible Infrared Imaging Radiometer Suite (VIIRS) 375 m & 750 m Active Fire Products: Product User's Guide Version 1.4*. Tech. rep. Department of Geographical Sciences, University of Maryland.

Schroeder, W., P. Oliva, L. Giglio, and I. A. Csiszar (2014). "The New VIIRS 375m active fire detection data product: Algorithm description and initial assessment." *Remote Sens. Environ.* 143, pp. 85 –96. URL: https://doi.org/10.1016/j.rse.2013.12.008.

Schulz, C. (2019). "Secondary organic aerosol in the pristine Amazonian atmosphere: chemical properties, formation pathways, and interactions with clouds." PhD thesis. Johannes Gutenberg-Universität Mainz.

Schulz, H., M. Zanatta, H. Bozem, W. R. Leaitch, A. B. Herber, J. Burkart, M. D. Willis, D. Kunkel, P. M. Hoor, J. P. D. Abbatt, and R. Gerdes (2019). "High Arctic aircraft measurements characterising black carbon vertical variability in spring and summer." *Atmos. Chem. Phys.* 2019.4, pp. 2361–2384. DOI: 10.5194/acp-19-2361-2019.

Schwarz, J. P. et al. (2006). "Single-particle measurements of midlatitude black carbon and light-scattering aerosols from the boundary layer to the lower stratosphere." *J. Geophys. Res.-Atmos.* 111.D16. DOI: 10.1029/2006JD007076.

Seibert, P. and A. Frank (2004). "Source-receptor matrix calculation with a Lagrangian particle dispersion model in backward mode." *Atmos. Chem. Phys.* 4.1, pp. 51–63. DOI: 10.5194/acp-4-51-2004.

Seinfeld, J. H. and S. N. Pandis (2016). *Atmospheric Chemistry and Physics: From Air Pollution to Climate Change*. John Wiley & Sons, Inc., Hoboken, New Jersey.

Serreze, M. C., A. P. Barrett, J. C. Stroeve, D. N. Kindig, and M. M. Holland (2009). "The emergence of surface-based Arctic amplification." *The Cryosphere* 3.1, pp. 11–19. DOI: 10.5194/tc-3-11-2009.

Serreze, M. C. and R. G. Barry (2011). "Processes and impacts of Arctic amplification: A research synthesis." *Global Planet. Change* 77.1, pp. 85 –96. DOI: https://doi.org/10.1016/j.gloplacha.2011.03.004.

Serreze, M. C. and J. A. Francis (2006). "The Arctic Amplification Debate." *Climatic Change* 76.3, pp. 241–264. DOI: 10.1007/s10584-005-9017-y.

Serreze, M. C., M. M. Holland, and J. Stroeve (2007). "Perspectives on the Arctic's Shrinking Sea-Ice Cover." *Science* 315.5818, pp. 1533–1536. DOI: 10.1126/science.1139426.

Sharma, S., L. A. Barrie, D. R. Hastie, and C. Kelly (1999). "Dimethyl sulfide emissions to the atmosphere from lakes of the Canadian boreal region." *J. Geophys. Res.-Atmos.* 104.D9, pp. 11585–11592. DOI: 10.1029/1999JD900127.

Sharma, S., E. Chan, M. Ishizawa, D. Toom-Sauntry, S. L. Gong, S. M. Li, D. W. Tarasick, W. R. Leaitch, A. Norman, P. K. Quinn, T. S. Bates, M. Levasseur, L. A. Barrie, and W. Maenhaut (2012). "Influence of transport and ocean ice extent on biogenic aerosol sulfur in the Arctic atmosphere." *J. Geophys. Res.-Atmos.* 117.D12209. DOI: 10.1029/2011JD017074.

Sharma, S., M. Ishizawa, D. Chan, D. Lavoué, E. Andrews, K. Eleftheriadis, and S. Maksyutov (2013). "16-year simulation of Arctic black carbon: Transport, source contribution, and sensitivity analysis on deposition." *J. Geophys. Res.-Atmos.* 118.2, pp. 943–964. DOI: 10.1029/2012JD017774.

Shaw, G. E. (1975). "The vertical distribution of tropospheric aerosols at Barrow, Alaska." *Tellus* 27.1, pp. 39–50. DOI: 10.1111/j.2153-3490.1975.tb01653.x.

Shaw, G. E. (1995). "The Arctic Haze Phenomenon." *B. Am. Meteorol. Soc.* 76.12, pp. 2403–2414. DOI: 10.1175/1520-0477(1995)076<2403:TAHP>2.0.CO;2.

Shen, X., H. Saathoff, W. Huang, C. Mohr, R. Ramisetty, and T. Leisner (2019). "Understanding atmospheric aerosol particles with improved particle identification and quantification by single-particle mass spectrometry." *Atmos. Meas. Tech.* 2019.4, pp. 2219–2240. DOI: 10.5194/amt-12-2219-2019.

Shindell, D. T. et al. (2008). “A multi-model assessment of pollution transport to the Arctic.” *Atmos. Chem. Phys.* 8.17, pp. 5353–5372. DOI: 10.5194/acp-8-5353-2008.

Shindell, D. and G. Faluvegi (2009). “Climate response to regional radiative forcing during the twentieth century.” *Nature Geoscience* 2, pp. 294–300. URL: http://dx.doi.org/10.1038/ngeo473.

Sierau, B., R. Y.-W. Chang, C. Leck, J. Paatero, and U. Lohmann (2014). “Single-particle characterization of the high-Arctic summertime aerosol.” *Atmos. Chem. Phys.* 14.14, pp. 7409–7430. DOI: 10.5194/acp-14-7409-2014.

Silva, P. J. and K. A. Prather (2000). “Interpretation of Mass Spectra from Organic Compounds in Aerosol Time-of-Flight Mass Spectrometry.” *Anal. Chem.* 72.15, pp. 3553–3562. DOI: 10.1021/ac9910132.

Silva, P. J., D.-Y. Liu, C. A. Noble, and K. A. Prather (1999). “Size and Chemical Characterization of Individual Particles Resulting from Biomass Burning of Local Southern California Species.” *Environ. Sci. Technol.* 33.18, pp. 3068–3076. DOI: 10.1021/es980544p.

Simoneit, B., J. Schauer, C. Nolte, D. Oros, V. Elias, M. Fraser, W. Rogge, and G. Cass (1999). “Levoglucosan, a tracer for cellulose in biomass burning and atmospheric particles.” *Atmos. Environ.* 33.2, pp. 173–182. URL: https://doi.org/10.1016/S1352-2310(98)00145-9.

Singh, H. B. et al. (2010). “Pollution influences on atmospheric composition and chemistry at high northern latitudes: Boreal and California forest fire emissions.” *Atmos. Environ.* 44.36, pp. 4553–4564. URL: http://www.sciencedirect.com/science/article/pii/S1352231010007004.

Sirois, A. and L. A. Barrie (1999). “Arctic lower tropospheric aerosol trends and composition at Alert, Canada: 1980-1995.” *J. Geophys. Res.-Atmos.* 104.D9, pp. 11599–11618. DOI: 10.1029/1999JD900077.

Smith, J. N., K. C. Barsanti, H. R. Friedli, M. Ehn, M. Kulmala, D. R. Collins, J. H. Scheckman, B. J. Williams, and P. H. McMurry (2010). “Observations of aminium salts in atmospheric nanoparticles and possible climatic implications.” *P. Natl. Acad. Sci.* 107.15, pp. 6634–6639. DOI: 10.1073/pnas.0912127107.

Smith, S. J., H. Pitcher, and T. Wigley (2001). “Global and regional anthropogenic sulfur dioxide emissions.” *Global Planet. Change* 29.1, pp. 99 –119. URL: https://doi.org/10.1016/S0921-8181(00)00057-6.

Snyder, J. P. (1982). *Map projections used by the U.S. Geological Survey.* Tech. rep. Report. Washington, D.C. URL: http://pubs.er.usgs.gov/publication/b1532.

Sobhani, N., S. Kulkarni, and G. R. Carmichael (2018). “Source sector and region contributions to black carbon and $PM_{2.5}$ in the Arctic.” *Atmos. Chem. Phys.* 18.24, pp. 18123–18148. DOI: 10.5194/acp-18-18123-2018.

Sodeman, D. A., S. M. Toner, and K. A. Prather (2005). “Determination of Single Particle Mass Spectral Signatures from Light-Duty Vehicle Emissions.” *Environ. Sci. Technol.* 39.12, pp. 4569–4580. DOI: 10.1021/es0489947.

Song, X.-H., P. K. Hopke, D. P. Fergenson, and K. A. Prather (1999). “Classification of Single Particles Analyzed by ATOFMS Using an Artificial Neural Network, ART-2A.” *Anal. Chem.* 71.4, pp. 860–865. DOI: 10.1021/ac9809682.

Sorensen, L. L., S. C. Pryor, G. de Leeuw, and M. Schulz (2005). “Flux divergence of nitric acid in the marine atmospheric surface layer.” *J. Geophys. Res.-Atmos.* 110.D15306. DOI: 10.1029/2004JD005403.

Sorooshian, A., V. Varutbangkul, F. J. Brechtel, B. Ervens, G. Feingold, R. Bahreini, S. M. Murphy, J. S. Holloway, E. L. Atlas, G. Buzorius, H. Jonsson, R. C. Flagan, and J. H. Seinfeld (2006). “Oxalic acid in clear and cloudy atmospheres: Analysis of data from International Consortium for Atmospheric Research on Transport and Transformation 2004.” *J. Geophys. Res.-Atmos.* 111.D23. DOI: 10.1029/2005JD006880.

Spencer, M. T., J. C. Holecek, C. E. Corrigan, V. Ramanathan, and K. A. Prather (2008). “Size-resolved chemical composition of aerosol particles during a monsoonal transition period over the Indian Ocean.” *J. Geophys. Res.-Atmos.* 113.D16 305. DOI: 10.1029/2007JD008657.

Stohl, A. (2006). “Characteristics of atmospheric transport into the Arctic troposphere.” *J. Geophys. Res.-Atmos.* 111.D11306. DOI: 10.1029/2005JD006888.

Stohl, A., C. Forster, S. Eckhardt, N. Spichtinger, H. Huntrieser, J. Heland, H. Schlager, S. Wilhelm, F. Arnold, and O. Cooper (2003). “A backward modeling study of intercontinental pollution transport using aircraft measurements.” *J. Geophys. Res.-Atmos.* 108.D12. DOI: 10.1029/2002JD002862.

Stohl, A., C. Forster, A. Frank, P. Seibert, and G. Wotawa (2005). “Technical note: The Lagrangian particle dispersion model FLEXPART version 6.2.” *Atmos. Chem. Phys.* 5.9, pp. 2461–2474. DOI: 10.5194/acp-5-2461-2005.

Stohl, A., Z. Klimont, S. Eckhardt, K. Kupiainen, V. P. Shevchenko, V. M. Kopeikin, and A. N. Novigatsky (2013). “Black carbon in the Arctic: the underestimated role of gas flaring and residential combustion emissions.” *Atmos. Chem. Phys.* 13.17, pp. 8833–8855. DOI: 10.5194/acp-13-8833-2013.

Stohl, A. (1998). “Computation, accuracy and applications of trajectories: A review and bibliography.” *Atmos. Environ.* 32.6, pp. 947 –966. URL: http://dx.doi.org/10.1016/S1352-2310(97)00457-3.

Stroeve, J. C., M. C. Serreze, M. M. Holland, J. E. Kay, J. Malanik, and A. P. Barrett (2012). “The Arctic’s rapidly shrinking sea ice cover: a research synthesis.” *Climatic Change* 110.3, pp. 1005–1027. DOI: 10.1007/s10584-011-0101-1.

Ström, J., J. Umegard, K. Torseth, P. Tunved, H.-C. Hansson, K. Holmen, V. Wismann, A. Herber, and G. König-Langlo (2003). “One year of particle size distribution and aerosol chemical composition measurements at the Zeppelin Station, Svalbard, March 2000-March 2001.” *Phys. Chem. Earth Pt. A/B/C* 28.28. The changing physical environment of Ny-Alesund Svalbard, pp. 1181 –1190. URL: https://doi.org/10.1016/j.pce.2003.08.058.

Struthers, H., A. M. L. Ekman, P. Glantz, T. Iversen, A. Kirkevåg, E. M. Mårtensson, Ø. Seland, and E. D. Nilsson (2011). “The effect of sea ice loss on sea salt aerosol concentrations and the radiative balance in the Arctic.” *Atmos. Chem. Phys.* 11.7, pp. 3459–3477. DOI: 10.5194/acp-11-3459-2011.

Stull, R. B. (1997). *An Introduction to Boundary Layer Meteorology.* Ed. by E. A. Board. Kluwer Academic Publishers. DOI: 10.1007/978-94-009-3027-8.

Su, Y., M. F. Sipin, H. Furutani, and K. A. Prather (2004). “Development and Characterization of an Aerosol Time-of-Flight Mass Spectrometer with Increased Detection Efficiency.” *Anal. Chem.* 76.3, pp. 712–719. DOI: 10.1021/ac034797z.

Suess, D. T. and K. A. Prather (1999). “Mass Spectrometry of Aerosols.” *Chem. Rev.* 99.10, pp. 3007–3036. DOI: 10.1021/cr980138o.

Sullivan, R. C. and K. A. Prather (2005). “Recent Advances in Our Understanding of Atmospheric Chemistry and Climate Made Possible by On-Line Aerosol Analysis Instrumentation.” *Anal. Chem.* 77.12, pp. 3861–3886. DOI: 10.1021/ac050716i.

Sullivan, R. C. and K. A. Prather (2007). “Investigations of the Diurnal Cycle and Mixing State of Oxalic Acid in Individual Particles in Asian Aerosol Outflow.” *Environ. Sci. Technol.* 41.23, pp. 8062–8069. DOI: 10.1021/es071134g.

Sultana, C. M., G. C. Cornwell, P. Rodriguez, and K. A. Prather (2017a). “FATES: a flexible analysis toolkit for the exploration of single-particle mass spectrometer data.” *Atmos. Meas. Tech.* 10.4, pp. 1323–1334. DOI: 10.5194/amt-10-1323-2017.

Sultana, C. M., D. B. Collins, and K. A. Prather (2017b). “Effect of Structural Heterogeneity in Chemical Composition on Online Single-Particle Mass Spectrometry Analysis of Sea Spray Aerosol Particles.” *Environ. Sci. Technol.* 51.7, pp. 3660–3668. DOI: 10.1021/acs.est.6b06399.

TSI Incorporated (2003). *Model 4140/4143 - General Purpose - Thermal Mass Flowmeter - Operation and Service Manual.* TSI Incorporated.

TSI Incorporated (2013). *Water-based Condensation Particle Counter Model 3787-Operation and Service Manual.* TSI Incorporated.

Tan, Y., A. G. Carlton, S. P. Seitzinger, and B. J. Turpin (2010). “SOA from methylglyoxal in clouds and wet aerosols: Measurement and prediction of key products.” *Atmos. Environ.* 44.39, pp. 5218 –5226. URL: https://doi.org/10.1016/j.atmosenv.2010.08.045.

Thomson, D. S., A. M. Middlebrook, and D. M. Murphy (1997). “Thresholds for Laser-Induced Ion Formation from Aerosols in a Vacuum Using Ultraviolet and Vacuum-Ultraviolet Laser Wavelengths.” *Aerosol Sci. Technol.* 26.6, pp. 544–559. DOI: 10.1080/02786829708965452.

Tjernström, M., C. E. Birch, I. M. Brooks, M. D. Shupe, P. O. G. Persson, J. Sedlar, T. Mauritsen, C. Leck, J. Paatero, M. Szczodrak, and C. R. Wheeler (2012). “Meteorological conditions in the central Arctic summer during the Arctic Summer Cloud Ocean Study (ASCOS).” *Atmos. Chem. Phys.* 12.15, pp. 6863–6889. DOI: 10.5194/acp-12-6863-2012.

Tolocka, M. P., D. A. Lake, M. V. Johnston, and A. S. Wexler (2004). “Number concentrations of fine and ultrafine particles containing metals.” *Atmos. Environ.* 38.20, pp. 3263 –3273. URL: https://doi.org/10.1016/j.atmosenv.2004.03.010.

Tremblay, S., J.-C. Picard, J. O. Bachelder, E. Lutsch, K. Strong, P. Fogal, W. R. Leaitch, S. Sharma, F. Kolonjari, C. J. Cox, R. Y.-W. Chang, and P. L. Hayes (2019). “Characterization of aerosol growth events over Ellesmere Island during the summers of 2015 and 2016.” *Atmos. Chem. Phys.* 19.8, pp. 5589–5604. DOI: 10.5194/acp-19-5589-2019.

Trimborn, A., K.-P. Hinz, and B. Spengler (2002). “Online analysis of atmospheric particles with a transportable laser mass spectrometer during LACE 98.” *J. Geophys. Res.-Atmos.* 107.D21. DOI: 10.1029/2001JD000590.

Tunved, P., J. Ström, and R. Krejci (2013). “Arctic aerosol life cycle: linking aerosol size distributions observed between 2000 and 2010 with air mass transport and precipitation at Zeppelin station, Ny-Ålesund, Svalbard.” *Atmos. Chem. Phys.* 13.7, pp. 3643–3660. DOI: 10.5194/acp-13-3643-2013.

Turquety, S., J. A. Logan, D. J. Jacob, R. C. Hudman, F. Y. Leung, C. L. Heald, R. M. Yantosca, S. Wu, L. K. Emmons, D. P. Edwards, and G. W. Sachse (2007). “Inventory of boreal fire emissions for North America in 2004: Importance of peat burning and pyroconvective injection.” *J. Geophys. Res.-Atmos.* 112.D12. DOI: 10.1029/2006JD007281.

Val Martin, M., R. A. Kahn, and M. G. Tosca (2018). “A Global Analysis of Wildfire Smoke Injection Heights Derived from Space-Based Multi-Angle Imaging.” *Remote Sensing* 10.10. DOI: 10.3390/rs10101609.

Van Neste, A., R. A. Duce, and C. Lee (1987). “Methylamines in the marine atmosphere.” *Geophys. Res. Lett.* 14.7, pp. 711–714. DOI: 10.1029/GL014i007p00711.

Van Pinxteren, M., K. W. Fomba, D. van Pinxteren, N. Triesch, E. H. Hoffmann, C. H. Cree, M. F. Fitzsimons, W. von Tümpling, and H. Herrmann (2019). “Aliphatic amines at the Cape Verde Atmospheric Observatory: Abundance, origins and sea-air fluxes.” *Atmos. Environ.* 203, pp. 183 –195. URL: https://doi.org/10.1016/j.atmosenv.2019.02.011.

VanCuren, R. A., T. Cahill, J. Burkhart, D. Barnes, Y. Zhao, K. Perry, S. Cliff, and J. McConnell (2012). “Aerosols and their sources at Summit Greenland - First results of continuous size- and time-resolved sampling.” *Atmos. Environ.* 52, pp. 82–97. URL: https://doi.org/10.1016/j.atmosenv.2011.10.047.

Wallace, J. M. and P. V. Hobbs (2006). *Atmospheric Science: An Introductory Survey*. Ed. by R. Dmowska, D. Hartmann, and H. T. Rossby. Second. Elsevier Inc.

Wandel, M. (2015). “CO-Messung in der Arktis im Rahmen der NETCARE-Kampagne.” MA thesis. Johannes Gutenberg-Universität Mainz.

Wang, X. and P. H. McMurry (2006). “A Design Tool for Aerodynamic Lens Systems.” *Aerosol Sci. Technol.* 40.5, pp. 320–334. DOI: 10.1080/02786820600615063.

Warneck, P. (2003). “In-cloud chemistry opens pathway to the formation of oxalic acid in the marine atmosphere.” *Atmos. Environ.* 37.17, pp. 2423 –2427. URL: https://doi.org/10.1016/S1352-2310(03)00136-5.

WaveMetrics (2015). *IGOR Pro Version 6.37*. WaveMetrics, Inc. URL: http://www.wavemetrics.com/.

Weiss, M., P. Verheijen, J. Marijnissen, and B. Scarlett (1997). “On the performance of an on-line time-of-flight mass spectrometer for aerosols.” *J. Aerosol Sci.* 28.1, pp. 159 –171. URL: https://doi.org/10.1016/S0021-8502(96)00067-5.

Wendisch, M. et al. (2019). “The Arctic Cloud Puzzle: Using ACLOUD/PASCAL Multi-Platform Observations to Unravel the Role of Clouds and Aerosol Particles in Arctic Amplification.” *B. Am. Meteorol. Soc.* 100.5, pp. 841–871. DOI: 10.1175/BAMS-D-18-0072.1.

Wentworth, G. R., J. G. Murphy, B. Croft, R. V. Martin, J. R. Pierce, J.-S. Côté, I. Courchesne, J.-E. Tremblay, J. Gagnon, J. L. Thomas, S. Sharma, D. Toom-Sauntry, A. Chivulescu, M. Levasseur, and J. P. D. Abbatt (2016). “Ammonia in the summertime Arctic marine boundary layer: sources, sinks, and implications.” *Atmos. Chem. Phys.* 16.4, pp. 1937–1953. DOI: 10.5194/acp-16-1937-2016.

Wenzel, R. J. and K. A. Prather (2004). “Improvements in ion signal reproducibility obtained using a homogeneous laser beam for on-line laser desorption/ionization of single particles.” *Rapid Commun. Mass Spectrom.* 18.13, pp. 1525–1533. DOI: 10.1002/rcm.1509.

Wenzel, R. J., D.-Y. Liu, E. S. Edgerton, and K. A. Prather (2003). “Aerosol time-of-flight mass spectrometry during the Atlanta Supersite Experiment: 2. Scaling procedures.” *J. Geophys. Res.-Atmos.* 108.D7. DOI: 10.1029/2001JD001563.

Willis, M. D., J. Burkart, J. L. Thomas, F. Köllner, J. Schneider, H. Bozem, P. M. Hoor, A. A. Aliabadi, H. Schulz, A. B. Herber, W. R. Leaitch, and J. P. D. Abbatt (2016). “Growth of nucleation mode particles in the summertime Arctic: a case study.” *Atmos. Chem. Phys.* 16.12, pp. 7663–7679. DOI: 10.5194/acp-16-7663-2016.

Willis, M. D., F. Köllner, J. Burkart, H. Bozem, J. L. Thomas, J. Schneider, A. A. Aliabadi, P. M. Hoor, H. Schulz, A. B. Herber, W. R. Leaitch, and J. P. D. Abbatt (2017). “Evidence for marine biogenic influence on summertime Arctic aerosol.” *Geophys. Res. Lett.* 44.12, pp. 6460–6470. DOI: 10.1002/2017GL073359.

Willis, M. D., W. R. Leaitch, and J. P. Abbatt (2018). “Processes Controlling the Composition and Abundance of Arctic Aerosol.” *Rev. Geophys.* 56, pp. 621–671. DOI: 10.1029/2018RG000602.

Wilson, T. W. et al. (2015). “A marine biogenic source of atmospheric ice-nucleating particles.” *Nature* 525, pp. 234 –238. DOI: 10.1038/nature14986.

Winiger, P., A. Andersson, S. Eckhardt, A. Stohl, I. P. Semiletov, O. V. Dudarev, A. Charkin, N. Shakhova, Z. Klimont, C. Heyes, and Ö. Gustafsson (2017).

"Siberian Arctic black carbon sources constrained by model and observation." *P. Natl. Acad. Sci.* 114.7, E1054–E1061. DOI: 10.1073/pnas.1613401114.

Xu, J.-W., R. V. Martin, A. Morrow, S. Sharma, L. Huang, W. R. Leaitch, J. Burkart, H. Schulz, M. Zanatta, M. D. Willis, D. K. Henze, C. J. Lee, A. B. Herber, and J. P. D. Abbatt (2017). "Source attribution of Arctic black carbon constrained by aircraft and surface measurements." *Atmos. Chem. Phys.* 17.19, pp. 11971–11989. DOI: 10.5194/acp-17-11971-2017.

Yang, F., H. Chen, X. Wang, X. Yang, J. Du, and J. Chen (2009). "Single particle mass spectrometry of oxalic acid in ambient aerosols in Shanghai: Mixing state and formation mechanism." *Atmos. Environ.* 43.25, pp. 3876 –3882. URL: https://doi.org/10.1016/j.atmosenv.2009.05.002.

Yang, Y., H. Wang, S. J. Smith, R. C. Easter, and P. J. Rasch (2018). "Sulfate Aerosol in the Arctic: Source Attribution and Radiative Forcing." *J. Geophys. Res.-Atmos.* 123.3, pp. 1899–1918. DOI: 10.1002/2017JD027298.

Yao, X., P. J. Rehbein, C. J. Lee, G. J. Evans, J. Corbin, and C.-H. Jeong (2011). "A study on the extent of neutralization of sulphate aerosol through laboratory and field experiments using an ATOFMS and a GPIC." *Atmos. Environ.* 45.34, pp. 6251 –6256. URL: https://doi.org/10.1016/j.atmosenv.2011.06.061.

Youn, J.-S., E. Crosbie, L. Maudlin, Z. Wang, and A. Sorooshian (2015). "Dimethylamine as a major alkyl amine species in particles and cloud water: Observations in semi-arid and coastal regions." *Atmos. Environ.* 122, pp. 250 –258. URL: http://dx.doi.org/10.1016/j.atmosenv.2015.09.061.

Yttri, K. E., C. Lund Myhre, S. Eckhardt, M. Fiebig, C. Dye, D. Hirdman, J. Ström, Z. Klimont, and A. Stohl (2014). "Quantifying black carbon from biomass burning by means of levoglucosan - a one-year time series at the Arctic observatory Zeppelin." *Atmos. Chem. Phys.* 14.12, pp. 6427–6442. DOI: 10.5194/acp-14-6427-2014.

Yu, H., R. McGraw, and S.-H. Lee (2012). "Effects of amines on formation of sub-3 nm particles and their subsequent growth." *Geophys. Res. Lett.* 39.2. L02807. DOI: 10.1029/2011GL050099.

Zanatta, M., H. Bozem, F. Köllner, P. Hoor, J. Schneider, A. Petzold, U. Bundke, K. Hayden, R. Staebler, H. Schulz, and A. B. Herber (2019). "Airborne survey of trace gas and aerosol over the Southern Baltic Sea: from clean marine boundary layer to shipping corridor effect." *submitted to Tellus B.*

Zare, A., P. S. Romer, T. Nguyen, F. N. Keutsch, K. Skog, and R. C. Cohen (2018). “A comprehensive organic nitrate chemistry: insights into the lifetime of atmospheric organic nitrates.” *Atmos. Chem. Phys.* 18.20, pp. 15419–15436. DOI: 10.5194/acp-18-15419-2018.

Zauscher, M. D., Y. Wang, M. J. K. Moore, C. J. Gaston, and K. A. Prather (2013). “Air Quality Impact and Physicochemical Aging of Biomass Burning Aerosols during the 2007 San Diego Wildfires.” *Environ. Sci. Technol.* 47.14, pp. 7633–7643. DOI: 10.1021/es4004137.

Zhang, X., K. A. Smith, D. R. Worsnop, J. Jimenez, J. T. Jayne, and C. E. Kolb (2002). “A Numerical Characterization of Particle Beam Collimation by an Aerodynamic Lens-Nozzle System: Part I. An Individual Lens or Nozzle.” *Aerosol Sci. Technol.* 36.5, pp. 617–631. DOI: 10.1080/02786820252883856.

Zhang, X., K. A. Smith, D. R. Worsnop, J. L. Jimenez, J. T. Jayne, C. E. Kolb, J. Morris, and P. Davidovits (2004). “Numerical Characterization of Particle Beam Collimation: Part II Integrated Aerodynamic-Lens-Nozzle System.” *Aerosol Sci. Technol.* 38.6, pp. 619–638. DOI: 10.1080/02786820490479833.

Zhou, L., A. Rai, and M. Zachariah (2006). “Component and morphology biases on quantifying the composition of nanoparticles using single-particle mass spectrometry.” *Int. J. Mass Spectrom.* 258.1, pp. 104 –112. URL: https://doi.org/10.1016/j.ijms.2006.07.006.

LIST OF FIGURES

LIST OF TABLES

ACRONYMS

ACLOUD	Arctic CLoud Observations Using airborne measurements during polar Day
ACP	Atmospheric Chemistry and Physics
AIMMS	Aircraft Integrated Meteorological Measurement System
ALABAMA	Aircraft-based single particle aerosol mass spectrometer
AMT	Atmospheric Measurement Techniques
a.u.	arbitrary unit
AWI	Alfred Wegener Institute
BC	black carbon
BG	Biogeoscience
BL	boundary layer
CPC	condensation particle counter
CPI	constant pressure inlet
CRISP	Concise Retrieval of Information from Single Particles
DCA	dicarboxylic acids
DEA	diethylamine
DMA	differential mobility analyzer
DMS	dimethylsulfide
DMSP	Defense Meteorological Satellite Program
DMT	Droplet Measurement Technologies
DPA	dipropylamine
EC	elemental carbon
ECCC	Environment and Climate Change Canada

ECMWF	European Centre for Medium-Range Weather Forecast
ESRL	Earth System Research Laboratory
FLEXPART	FLEXible PARTicle dispersion model
FT	free troposphere
gpdm	geopotential dekameter
GPS	Global Positioning System
Gr	Greenland
HR-ToF-AMS	high-resolution time-of-flight aerosol mass spectrometer
InGaN	indium gallium nitride
IPA	Institute for Atmospheric Physics, Mainz
LVOC	low-volatile organic compounds
MCP	multichannel plate
MODIS	Moderate Resolution Imaging Spectroradiometer
MPIC	Max Planck Institute for Chemistry
MSA	methanesulfonic acid
NASA	National Aeronautics and Space Administration
nCa	northern Canada
NCAR	National Center for Atmospheric Research
NCEP	National Centers for Environmental Prediction
Nd:YAG	neodymium-doped yttrium aluminum garnet
NETCARE	“Network on Climate and Aerosols: Addressing Key Uncertainties in Remote Canadian Environments”
NOAA	National Oceanic and Atmospheric Administration
NPF	new particle formation
nss	non-sea-spray
OC	organic carbon

OD	outer diameter
OM	organic matter
OPC	optical particle counter
PES	potential emission sensitivity
PMA	primary marine aerosol
POA	primary organic aerosol
ppb_v	parts per billion by volume
ppm_v	parts per million by volume
PSI	potential source inventory
PSL	polystyrene latex
rBC	refractory black carbon
sNA	southern North America
SOA	secondary organic aerosol
SP2	Single Particle Soot Photometer
SPMS	single particle mass spectrometer
SSMIS	Special Sensor Microwave Imager/Sounder
stdP	standard pressure
STP	standard temperature and pressure
TEA	triethylamine
TMA	trimethylamine
TMP	turbo molecular pump
TPA	tripropylamine
UCPC	ultrafine condensation particle counter
UHSAS	Ultra-High Sensitivity Aerosol Spectrometer
UofT	University of Toronto
UTC	coordinated universal time

VIIRS	Visible Infrared Imaging Radiometer Suite
VUV	vacuum ultraviolet
VOC	volatile organic compounds

PHYSICAL SYMBOLS

Symbol	Unit	Description
a	s	m/z calibration coefficient
b	$\mathrm{s\ Da^{-\frac{1}{2}}}$	m/z calibration coefficient
BD_{qualit}	-	qualitative measure of particle beam divergence
C_c	-	Cunningham slip correction factor
C_{coinc}	$\mathrm{s^{-1}}$	particle counts detected by both ALABAMA optical detection stages within a pre-defined time interval
CE	-	collection efficiency
c_{p}	$\mathrm{J\,kg^{-1}\,K^{-1}}$	specific heat capacity of air for constant pressure
$C_{\mathrm{reference}}$	$\mathrm{s^{-1}}$	particle counts detected by the reference instrument
C_0	$\mathrm{s^{-1}}$	particle counts detected by the ALABAMA first optical detection stage
$C_{>320}$	$\mathrm{s^{-1}}$	counts of particles greater than 320 nm in diameter
DE	-	detection efficiency
e	C	elementary charge
e_{v}	Pa	water vapor pressure
e_{v}^{*}	Pa	saturation vapor pressure
d_{CPI}	µm	equivalent CPI orifice diameter
d_{mob}	nm	particle mobility diameter
d_{nozzle}	mm	diameter of the last lens aperture
d_{opt}	nm	particle optical diameter

d_p	nm	particle diameter
d_{va}	nm	particle vacuum-aerodynamic diameter
f_{lens}	$\mathrm{cm^3\ s^{-1}}$	volumetric flow rate inside the lens
f_{upstream}	$\mathrm{cm^3\ s^{-1}}$	upstream volumetric flow rate
g	$\mathrm{m\,s^{-2}}$	gravity
h	m	altitude
HR	-	hit rate
k	nm	size calibration factor
L_c	µm	characteristic length
L_{v}	$\mathrm{J\,kg^{-1}}$	latent heat of condensation at 273 K and 1013 hPa
m/z	Da	ion mass to charge ratio
N	-	trials
N_{coinc}	$\mathrm{cm^{-3}}$	particle number concentration detected by both optical detection stages within a pre-defined time interval
N_{hits}	-	number of particles that are successfully ionized by the ablation laser and that create a mass spectrum
$N_{\mathrm{reference}}$	$\mathrm{cm^{-3}}$	particle number concentration monitored by the reference instrument
N_{shots}	-	number of laser shots
$N_{>5}$	$\mathrm{cm^{-3}}$	number concentration of particles greater than 5 nm in diameter
$N_{>100}$	$\mathrm{cm^{-3}}$	number concentration of particles greater than 100 nm in diameter
$N_{>320}$	$\mathrm{cm^{-3}}$	number concentrations of particles greater than 320 nm in diameter
N_0	$\mathrm{cm^{-3}}$	particle number concentration detected by the ALABAMA first optical detection stage
p	-	probability of success

p_{air}	hPa	atmospheric pressure
PF	-	fraction of the specific particle type
p_{lens}	hPa	pressure inside the aerodynamic lens
p_{upstream}	hPa	upstream pressure
q	-	probability of failure
q_{v}	kg kg^{-1}	specific humidty
RH	-	relative humidity
S_{PSL}	-	Jayne shape factor
Stk	-	Stokes number
s_{ToF}	m	ion flight path
T	K	temperature
t	s	time
TE_{Inlet}	-	inlet transmission efficiency
t_{ToF}	s	ion flight time
U	V	mass spectrometer high voltages
$upcount$	-	time counter value between the two detection events
v	m s	wind vector
V_g	m s^{-1}	gas velocity
V_{g1}	m s^{-1}	gas velocity after the gas expansion
$\mathrm{VMR}_{\mathrm{H2O}}$	$\mathrm{ppm_v}$	H_2O mixing ratio by volume
V_p	m s^{-1}	particle velocity
V_0	m s^{-1}	particle velocity before the gas expansion
X	m	particle position vector
z	-	multiple of ion charge
Δt	s	time increment
η	Pa s	coefficient of dynamic viscosity

θ	K	potential temperature
θ_e	K	pseudoequivalent potential temperature
λ	nm	wavelength
λ_g	µm	gas mean free path
ρ_p	g cm^{-3}	particle density
ρ_PSL	g cm^{-3}	PSL particle density
ρ_0	g cm^{-3}	standard particle density
$\sigma^\mathrm{abs}_{BD_\mathrm{qualit}}$	-	absolute uncertainty of the qualitative measure of particle beam divergence
σ_binomial	-	relative standard deviation of the Binomial probability distribution
σ^abs_{CE}	-	absolute uncertainty of the collection efficiency
$\sigma^\mathrm{rel}_\mathrm{coinc}$	-	relative statistical uncertainty of the particle counts detected by both ALABAMA optical detection stages
$\sigma^\mathrm{rel}_\mathrm{CPI}$	-	reproducibility of the CPI transmission efficiency
σ^abs_{DE}	-	absolute uncertainty of the detection efficiency
σ^abs_{HR}	-	absolute uncertainty of the hit rate
σ_measured	-	relative standard deviation of the measured hit rate distribution
$\sigma^\mathrm{abs}_{N_{>320}}$	cm^{-3}	absolute uncertainty of the UHSAS number concentration
σ_others	-	relative standard deviation related to instrumental issues that influence the hit rate
σ^abs_{PF}	-	absolute uncertainty of the ALABAMA particle fraction
$\sigma^\mathrm{abs}_{PF\cdot N_{>320}}$	cm^{-3}	absolute uncertainty of the ALABAMA scaled number concentration
$\sigma^{\mathrm{rel}_1}_\mathrm{reference}$	-	relative statistical uncertainty of the particle counts detected by the reference instrument

$\sigma^{\text{rel}_2}_{\text{reference}}$	-	reference instruments reproducibility
$\sigma^{\text{abs}}_{TE_{\text{Inlet}}}$	-	absolute uncertainty of the inlet transmission efficiency
$\sigma^{\text{rel}}_{\text{UHSAS}}$	-	relative statistical uncertainty of the particles counts detected by the UHSAS
$\sigma^{\text{rel}_1}_{\text{UHSAS}}$	-	instrument-related measurement efficiency derived from the UHSAS collection efficiency
$\sigma^{\text{abs}}_{upcount}$	-	absolute uncertainty of the upcount value
$\sigma^{\text{abs}}_{V_p}$	m s^{-1}	absolute uncertainty of the particle velocity
σ^{rel}_{0}	-	relative statistical uncertainty of the particle counts detected by the ALABAMA first optical detection stage
τ	µs	relaxation time

LIST OF PUBLICATIONS

The following articles and selected first author conference contributions have been published during my time as doctoral student.

PEER REVIEWED PUBLICATIONS

M. D. Willis, J. Burkart, J. L. Thomas, **F. Köllner**, J. Schneider, H. Bozem, P. M. Hoor, A. A. Aliabadi, H. Schulz, A. B. Herber, W. R. Leaitch, and J. P. D. Abbatt (2016): Growth of nucleation mode particles in the summertime Arctic: a case study, *Atmos. Chem. Phys.*, 16, 7663-7679, doi:10.5194/acp-16-7663-2016.

A. A. Aliabadi, J. L. Thomas, A. B. Herber, R. M. Staebler, W. R. Leaitch, H. Schulz, K. S. Law, L. Marelle, J. Burkart, M. D. Willis, H. Bozem, P. M. Hoor, **F. Köllner**, J. Schneider, M. Levasseur, and J. P. D. Abbatt (2016): Ship emissions measurement in the Arctic by plume intercepts of the Canadian Coast Guard icebreaker *Amundsen* from the *Polar 6* aircraft platform, *Atmos. Chem. Phys.*, 16, 7899–7916, doi:10.5194/acp-16-7899-2016.

W. R. Leaitch, A. Korolev, A. A. Aliabadi, J. Burkart, M. D. Willis, J. P. D. Abbatt, H. Bozem, P. Hoor, **F. Köllner**, J. Schneider, A. Herber, C. Konrad, and R. Brauner (2016): Effects of 20-100 nm particles on liquid clouds in the clean summertime Arctic, *Atmos. Chem. Phys.*, 16, 11107-11124, doi:10.5194/acp-16-11107-2016.

J. Burkart, M. D. Willis, H. Bozem, J. L. Thomas, K. Law, P. Hoor, A. A. Aliabadi, **F. Köllner**, J. Schneider, A. Herber, J. P. D. Abbatt, and W. R. Leaitch (2017): Summertime observations of elevated levels of ultrafine particles in the high Arctic marine boundary layer, *Atmos. Chem. Phys.*, 17, 5515-5535, doi:10.5194/acp-17-5515-2017.

M. D. Willis, **F. Köllner**, J. Burkart, H. Bozem, J. L. Thomas, J. Schneider, A. A. Aliabadi, P. M. Hoor, H. Schulz, A. B. Herber, W. R. Leaitch, and J. P. D. Abbatt (2017): Evidence for marine biogenic influence on summertime Arctic aerosol, *Geophys. Res. Lett.*, 44, 6460-6470, doi:10.1002/2017GL073359.

F. Köllner, J. Schneider, M. D. Willis, T. Klimach, F. Helleis, H. Bozem, D. Kunkel, P. Hoor, J. Burkart, W. R. Leaitch, A. A. Aliabadi, J. P. D. Abbatt, A. B. Herber, and S. Borrmann (2017): Particulate trimethylamine in the summertime Canadian high Arctic lower troposphere, *Atmos. Chem. Phys.*, 17, 13747-13766, doi:10.5194/acp-17-13747-2017.

M. Wendisch, A. Macke, A. Ehrlich, C. Lüpkes , M. Mech, D. Chechin, K. Dethloff, C. Barrientos Velasco, H. Bozem, M. Brückner, H.-C. Clemen, S. Crewell, T. Donth, R. Dupuy, K. Ebell, U. Egerer, R. Engelmann, C. Engler, O. Eppers, M. Gehrmann, X. Gong, M. Gottschalk, C. Gourbeyre, H. Griesche, J. Hartmann, M. Hartmann, B. Heinold, A. Herber, H. Herrmann, G. Heygster, P. Hoor, S. Jafariserajehlou, E. Jäkel, E. Järvinen, O. Jourdan, U. Kästner, S. Kecorius, E. M. Knudsen, **F. Köllner** et al. (2018): The Arctic Cloud Puzzle: Using ACLOUD/PASCAL Multi-Platform Observations to Unravel the Role of Clouds and Aerosol Particles in Arctic Amplification, *Bulletin of the American Meteorological Society*, 100.5, doi:10.1175/BAMSD-18-0072.1.

J. P. D. Abbatt, W. R. Leaitch, A. A. Aliabadi, A. K. Bertram, J.-P. Blanchet, A. Boivin-Rioux, H. Bozem, J. Burkart, R. Y. W. Chang, J. Charette, J. P. Chaubey, R. J. Christensen, A. Cirisan, D. B. Collins, B. Croft, J. Dionne, G. J. Evans, C. G. Fletcher, M. Gali, R. Ghahremaninezhad, E. Girard, W. Gong, M. Gosselin, M. Gourdal, S. J. Hanna, H. Hayashida, A. B. Herber, S. Hesaraki, P. Hoor, L. Huang, R. Hussherr, V. E. Irish, S. A. Keita, J. K. Kodros, **F. Köllner** et al. (2019): Overview paper: New insights into aerosol and climate in the Arctic, *Atmos. Chem. Phys.*, 19, 2527-2560, doi:10.5194/acp-19-2527-2019.

PUBLICATIONS UNDER REVIEW

H. Bozem, P. Hoor, D. Kunkel, **F. Köllner**, J. Schneider, A. Herber, H. Schulz, W. R. Leaitch, A. A. Aliabadi, M. D. Willis, J. Burkart, and J. P. D. Abbatt (2019): Characterization of Transport Regimes and the Polar Dome during Arctic Spring and Summer using in-situ Aircraft Measurements, *Atmos. Chem. Phys. Discuss.*, doi:10.5194/acp-2019-70, in review.

A. Ehrlich, M. Wendisch, C. Lüpkes, M. Buschmann, H. Bozem, D. Chechin, H.-C. Clemen, R. Dupuy, O. Eppers, J. Hartmann, A. Herber, E. Jäkel, E. Järvinen, O. Jourdan, U. Kästner, L.-L. Kliesch, **F. Köllner**, M. Mech, S. Mertes, R. Neuber, E. Ruiz-Donoso, M. Schnaiter, J. Schneider, J. Stapf, and M. Zanatta (2019): A comprehensive in situ and remote sensing data set from the Arctic CLoud Observations Using airborne measurements during polar Day (ACLOUD) campaign, *Earth Syst. Sci. Data Discuss.*, doi:10.5194/essd-2019-

96, in review.

M. Zanatta, H. Bozem, **F. Köllner**, J. Schneider, D. Kunkel, P. Hoor, G. de Faria, A. Petzold, U. Bundke, K. Hayden, R. M. Staebler, H. Schulz, and A. B. Herber (2019): Airborne survey of trace gas and aerosol over the Southern Baltic Sea: from clean marine boundary layer to shipping corridor effect, submitted to *Tellus B: Chemical and Physical Meteorology*, in review.

SELECTED FIRST AUTHOR CONFERENCE CONTRIBUTIONS

F. Köllner, J. Schneider, P. Hoor, H. Bozem: Pollution in the summertime Canadian High Arctic observed during NETCARE 2014: Investigation of origin and composition, oral presentation, *PhD conference on Earth System Science*, Mainz, March 24-27, 2015.

F. Köllner, J. Schneider, P. Hoor, H. Bozem, M. D. Willis, J. Burkart, W. R. Leaitch, J. P. D. Abbatt, A. Herber, S. Borrmann: Aerosol composition and origin of pollution in the High Arctic from aircraft measurements during NETCARE 2014, oral presentation, *European Geosciences Union General Assembly*, Vienna, April 13-17, 2015.

F. Köllner, J. Schneider, P. Hoor, H. Bozem, M. D. Willis, J. Burkart, W. R. Leaitch, J. P. D. Abbatt, A. Herber, S. Borrmann: Airborne single particle composition measurements in the Arctic summer, oral presentation, *European Aerosol Conference*, Milan, September 7-11, 2015.

F. Köllner, J. Schneider, T. Klimach, P. Hoor, H. Bozem, D. Kunkel, M. D. Willis, J. Burkart, W. R. Leaitch, J. P. D. Abbatt, A. Herber, S. Borrmann: Chemical composition of aerosol particles in the Arctic summer - Anthropogenic and biogenic influences, poster presentation awarded with the best student poster award, *1st $(AC)^3$ Science Conference on Arctic Amplification*, Bremen, March 26-28, 2017.

F. Köllner, J. Schneider, H. Bozem, P. Hoor, M. Zanatta, H. Schulz, A. Herber, U. Bundke, J. de Faria, A. Petzold, H.-C. Clemen, K. Hayden, R. Staebler, R. Brauner, and S. Borrmann: Aircraft-based single particle measurements in the Baltic Sea marine boundary layer, poster presentation, *European Aerosol Conference*, Zurich, August 27 - September 1, 2017.

F. Köllner, J. Schneider, M. D. Willis, T. Klimach, F. Helleis, P. Hoor, H. Bozem, D. Kunkel, J. Burkart, W. R. Leaitch, J. P. D. Abbatt, A. Herber,

S. Borrmann: Summertime high Arctic aerosol - Arctic regional and long-range transport influences, poster presentation, *POLAR 2018: a SCAR and IASC Conference*, Davos, June 15-26, 2018.

CONTRIBUTIONS TO THE STUDY

This study was made possible with the valuable contributions of colleagues that are acknowledged here.

In Chapter 2, experiments were carried out by myself, Christiane Schulz, and Hans-Christian Clemen, with critical feedback from Johannes Schneider. I ran the instruments and analyzed the data, with critical comments from Oliver Appel, Johannes Schneider, and Thomas Klimach. Daniel Kunkel provided the FLEXPART output. I analyzed the FLEXPART output with the help of Daniel Kunkel. Alexandre Caseiro provided data from the VIIRS Nightfire “Flares only” product. Further satellite data were downloaded by myself. I processed the satellite data to prepare emission inventory maps with the help of Alexandre Caseiro and Thomas Klimach.

In Chapter 3, the measurements were carried out by myself, with critical feedback from Andreas Hünig, Hans-Christian Clemen, and Johannes Schneider. I analyzed the data.

In Chapter 4, Jonathan Abbatt, W. Richard Leaitch and Andreas Herber designed the research project. I operated the ALABAMA onboard the research aircraft, with guidance of Johannes Schneider, Thomas Klimach, and Frank Helleis. Megan D. Willis deployed the HR-ToF-AMS and provided the data. Julia Burkart and W. Richard Leaitch operated the CPC instrument and provided the data. Andreas Herber deployed the SP2 and UHSAS instruments. Hannes Schulz provided data of the SP2 and UHSAS instruments. Heiko Bozem and Johannes Schneider carried out the CO and H_2O measurements. Heiko Bozem provided the CO and H_2O data. Amir A. Aliabadi processed the AIMMS data. I analyzed the data sets, with critical feedback from Johannes Schneider, Peter Hoor, Thomas Klimach, Daniel Kunkel, Heiko Bozem, Megan D. Willis, Jonathan Abbatt, W. Richard Leaitch, and Stephan Borrmann.

DANKSAGUNG

Die persönliche Danksagung ist in der elektronischen Version aus Gründen des Datenschutzes nicht enthalten. Ich möchte mich an dieser Stelle bei meinen Kollegen, meiner Familie und meinen Freunden für die wertvolle Unterstützung bedanken, ohne die diese Arbeit so nicht möglich gewesen wäre.